28

NASA CR-72325
R-7257

LITHIUM-FLUORINE-HYDROGEN PROPELLANT STUDY

by

H. A. Arbit, R. A. Dickerson,
S. D. Clapp, and C. K. Nagai

prepared for

NATIONAL AERONAUTICS AND SPACE ADMINISTRATION

Contract NAS3-7954

ROCKETDYNE
A DIVISION OF NORTH AMERICAN ROCKWELL CORPORATION

NASA CR-72325
R-7257.

FINAL REPORT

LITHIUM-FLUORINE-HYDROGEN PROPELLANT STUDY

by

H. A. Arbit, R. A. Dickerson,
S. D. Clapp, and C. K. Nagai

prepared for

NATIONAL AERONAUTICS AND SPACE ADMINISTRATION

22 February 1968

Contract NAS3-7954

Technical Management
NASA Lewis Research Center
Cleveland, Ohio
Liquid Rocket Technology Branch
John W. Gregory

Rocketdyne
A Division of North American Rockwell Corporation
6633 Canoga Avenue, Canoga Park, California

ACKNOWLEDGMENT

Important contributions to the conduct of the program or to the preparation of report material were made by the following personnel:

A. E. Axworthy, L. W. Carlson, D. A. Nelson, J. T. Sabol, and D. E. Zwald

FOREWORD

This report was prepared in compliance with NASA Contract NAS3-7954, entitled "Lithium-Fluorine-Hydrogen Propellant Study." Mr. J. W. Gregory, NASA Lewis Research Center, was NASA Project Manager. Rocketdyne Program Manager was Mr. E. V. Zettle, succeeded by Mr. T. A. Coultas. Technical approach and guidance of the program were directed by Mr. S. D. Clapp, who functioned as Project Engineer.

ABSTRACT

Results are reported of a program encompassing an analytical, design, and experimental effort to establish the fundamental feasibility of the fluorine/lithium/hydrogen tripropellant combination. This effort comprised: (1) a thermodynamic-kinetic analysis of the Li/F_2/H_2 system, including theoretical performance calculations, (2) studies of liquid-metal atomization and combustion, (3) design and buildup of a liquid-lithium (LLi) facility, (4) design of thrust chamber, including a fluorine-rich, hydrogen-fluorine gas generator and two lithium injectors, and (5) experimental firings of F_2/LLi/H_2. The test matrix covered a range of chamber pressure (350 to 520 psia), F_2/Li mixture ratio (2.4 to 5.2), and proportion of hydrogen (15 to 44 percent of total flowrate), and included variations in point of hydrogen addition and in chamber length. Corrected characteristic velocity efficiencies were 95 to 100 percent, showing that use of this tripropellant combination is feasible and that highly efficient combustion can be achieved.

CONTENTS

TABLES

ILLUSTRATIONS

SUMMARY

This report presents the results of an analytical and experimental investigation of the combustion characteristics of the $Li/F_2/H_2$ tripropellant combination. The primary overall program objective was to determine whether the high theoretical performance of the $Li/F_2/H_2$ combination is experimentally attainable and to investigate the necessary design requirements. Characteristic velocity (c*) efficiency of 95 to 100 percent was obtained in experimental tripropellant firings, with injector and combustion chamber designs based on the results of analytical and experimental studies of the atomization and combustion of liquid metals and of means of carrying out these processes efficiently. Nominal design point parameters were as follows:

1. Chamber pressure, 500 psia
2. F_2/Li mixture ratio, 2.74 (stoichiometric)
3. Hydrogen, 15 to 40 percent of total propellant flowrate
4. Nominal altitude thrust (30 percent H_2, $\epsilon = 60$), 2900 pounds

The program was divided into two major tasks:

I. Analysis and design

II. Combustion performance tests

The initial effort of Task I was an investigation of the chemical characteristics of the $Li/F_2/H_2$ system including an examination of the kinetics of the chemical reactions involved and detailed theoretical performance calculations. The kinetic studies showed that gas phase reactions of fluorine with hydrogen, fluorine with lithium, and lithium with hydrogen fluoride, even at the lowest temperature likely to exist in the combustion chamber, are more rapid by several orders of magnitude than the physical processes of propellant mixing and lithium vaporization. Hence combustion efficiency will be significantly affected by physical processes rather than by chemical kinetics, as is usually the case in rocket engine combustion.

Theoretical performance calculations were made for LF_2/LLi*in the mixture ratio range 2.20 to 3.30, at chamber pressures of 200 to 1000 psia and with gaseous hydrogen addition ranging from 0 to 40 percent of total propellant flowrate, as well as for LF_2/SLi*/LH_2 under similar conditions. Calculations were also made to determine the effects on performance parameters of incomplete condensation of LiF in the combustion products. Results of the computations are presented in a series of curves which show the variations in important performance parameters (I_s, c*, T_c, C_F) with proportion of hydrogen, chamber pressure, mixture ratio, and type of expansion. For LF_2/LLi, the maximum vacuum specific impulse at 500 psia chamber pressure is 458 lbf-sec/lbm at ϵ = 60. For LF_2/LLi/GH_2, the maximum vacuum specific impulse, which occurs at or near stoichiometric F_2/Li mixture ratio and with approximately 30-percent hydrogen, is 542 lbf-sec/lbm at 500-psia chamber pressure and ϵ = 60. The maximum vacuum specific impulse for LF_2/SLi/LH_2, under the same conditions, is 520 lbf-sec/lbm. Chamber pressure variation (200 to 1000 psia) has little effect on vacuum specific impulse.

The second Task I analysis and design effort involved establishment of requirements for high combustion efficiency in the LF_2/LLi/GH_2 system. It consisted of the following two parts: (1) an analytical study of lithium combustion based on a one-dimensional, vaporization rate-limited, combustion model, and (2) experimental investigations of liquid-stream penetration into gas jets and of the gas-augmented atomization of a liquid metal.

Because of the low burning rate of liquid lithium in gaseous fluorine (about one-tenth that of more common propellants), provision of very small lithium droplets is an essential requirement for high combustion efficiency. An extensive series of calculations was carried out to

*The abbreviations LLi and SLi refer to liquid and solid lithium, respectively.

establish the effect on combustion efficiency of variation in lithium droplet size, as a function of characteristic chamber length, chamber pressure, and point of hydrogen addition. It was found that a lithium droplet volume mean diameter of 20 microns would provide c* efficiency in excess of 0.96 with an F_2/Li combustion zone L* of 40 inches; 50-micron droplets require an L* of 180 inches for the same result. Curves showing the calculated effects on combustion efficiency of varying the axial point of hydrogen addition were also derived. It was found that for maximum c* efficiency the hydrogen should be injected downstream of the point of fluorine-lithium injection. However, this effect was found to be very small for small diameter lithium droplets.

Consideration of the atomization characteristics of liquid lithium showed that mean drop sizes on the order of 20 to 50 microns could be practically achieved only by gas-augmented liquid atomization. To aid in establishing specific design criteria for a gas-liquid system, a photographic study was made of the penetration of gas jets by liquid streams in a triplet element, using nitrogen and water or liquid Cerrosafe (a proprietary, low-melting-point, lead-bismuth alloy which simulates lithium). These experiments indicated that the degree of penetration is a function of liquid stream diameter, liquid/gas velocity ratio, liquid/gas density ratio, and the angle between the liquid stream and the injector face. A satisfactory empirical correlation was established.

Measurements were made of the particle sizes obtained by atomization of liquid Cerrosafe by gaseous nitrogen. Observed volume mean droplet size was adequately expressed by the Wolfe-Andersen equation, modified to account for the reduction in gas momentum due to acceleration of the atomized droplets. It was also confirmed that a conditional parameter based on the Weber and Reynolds numbers must be met to obtain the most efficient atomization.

A third effort conducted during Task I consisted of the experimental evaluation of two systems which are basic to the tripropellant thrust chamber design concept employed. The first was a high pressure gas generator in which liquid fluorine is reacted with gaseous hydrogen at high mixture ratio to produce fluorine gas at an elevated temperature. Its design consisted of separate fluorine and hydrogen injectors and a two-segment chamber, with each segment being 5 inches long. Firings of this assembly were carried out to verify that combustion efficiency in the gas generator was close to theoretical and that product gas at the desired temperature and pressure was consistently obtainable.

The second system evaluation was directed to the design, fabrication, and operation of a facility to store, heat, and deliver liquid lithium, followed by liquid lithium flow studies. The system was designed, assembled, and successfully operated. Test flows of liquid lithium through orifices of various sizes and orientations indicated that minimum orifice size for reliable free flow of lithium was 0.043-inch and that no face adherence was obtained with orifice-injector face angles of 45 degrees or larger.

The final Task I effort consisted of the design of the $F_2/Li/H_2$ thrust chamber assembly on the basis of the criteria developed. The concept consisted of the following:

1. F_2/H_2 gas generator operating at a nominal mixture ratio of about 500:1 to provide hot (960 R) gas for liquid lithium atomization
2. Lithium injector containing showerhead F_2 orifices which produced gas jets into which high-velocity liquid lithium streams were injected

3. Primary F_2/Li combustion chamber

4. Hydrogen injector

5. F_2/Li combustion product-hydrogen mixing chamber

6. Convergent-divergent nozzle

The entire assembly was uncooled and most components were graphite or graphite-lined.

The Task II (combustion performance tests) effort consisted of a series of experimental firings to establish the combustion characteristics of the F_2/Li/H_2 tripropellant combination. The results of these tests defined performance as a function of percent hydrogen added, point of hydrogen addition, and chamber length. The configurations employed are sketched below:

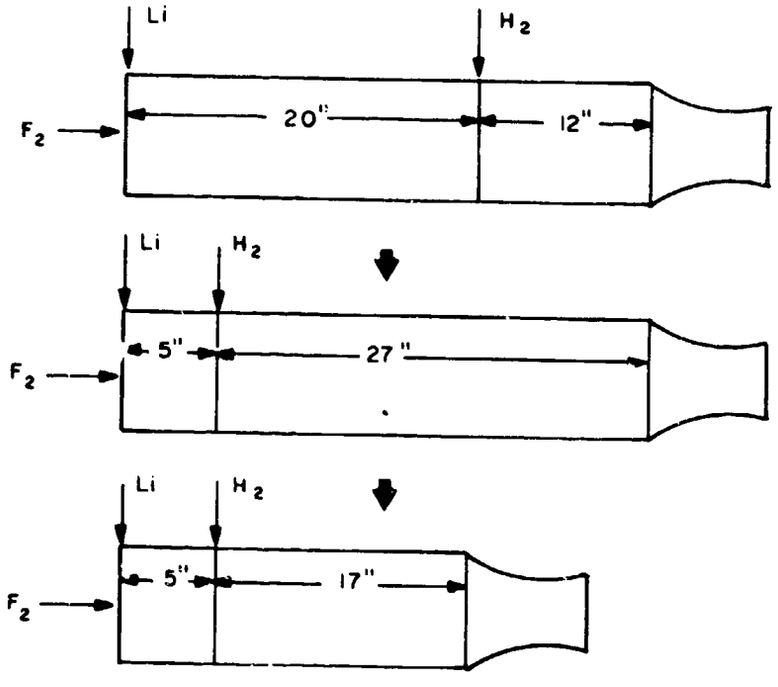

The experimental results clearly demonstrated that high combustion efficiencies can be achieved with the $F_2/Li/H_2$ tripropellant combination. Characteristic exhaust velocity efficiencies of essentially 100 percent were obtained with all three chamber configurations. In the last two, at the lowest hydrogen flowrates (15 to 20 percent of total propellant flowrate), c^* efficiency decreased to approximately 95 percent because of nonuniform distribution due to incomplete penetration of the F_2/Li combustion gas stream by the hydrogen.

INTRODUCTION

An analytical, design, and experimental program has been conducted to determine the combustion characteristics of the $Li/F_2/H_2$ propellant combination. The combustion of fluorine with a light metal such as lithium releases an extremely large amount of heat per pound; if this thermal energy is used to heat a very light working fluid such as hydrogen, a significant increase in specific impulse over that provided by bipropellant combinations is theoretically available (550-second theoretical specific impulse values are predicted). The objective of this program was to determine experimentally the combustion efficiency actually attainable with these propellants to ascertain the extent to which the desired reactions occur. A 15-month program, divided into the following two tasks, was completed: Task I was an analytical and design effort to define injector-thrust chamber design criteria for high performance; Task II consisted of experimental combustion performance testing.

During the past several years a significant amount of basic and applied combustion research has been carried out in the field of light-metal fuel additives and extended to the application of heavy metals as well. Metal additives have become standard components of various solid-propellant formulations, some of which now profitably use aluminum in quantities up to 20 percent by weight. In the liquid propellant field, effort is being oriented toward the use in the Titan II engine of aluminum in a gelled suspension with hydrazine in place of the 50-50 mixture of hydrazine (N_2H_4) and unsymmetrical dimethylhydrazine (UDMH). In this application, there is a 3-percent increase in performance and, more important, a significant increase in propellant density. In addition, the tripropellant system $Be/O_2/H_2$ has recently been studied under Air Force sponsorship.

In general, the previous multicomponent fuel studies were conducted to evaluate overall engine performance. No serious attempt was made to define injector design criteria for high combustion efficiency independent of potential performance deficiencies due to nozzle flow kinetics. Consequently, if overall performance were low, the causes of the overall inefficiency could only be postulated.

The basic premises of the present program were as follows: (1) for maximum performance with the $Li/F_2/H_2$ system, it is necessary that the lithium and fluorine be completely reacted prior to addition of hydrogen; (2) injection of hydrogen into a stream of LiF gas and subsequent attainment of thermal equilibrium do not present major problems; and therefore, (3) the most important consideration is the design of injection methods which will result in complete $Li-F_2$ reaction. The major portion of this program was consequently devoted to the investigation of means whereby high $Li-F_2$ combustion efficiency could be achieved.

A model for metal combustion (Ref. 1) was used which agrees conceptually with available hydrocarbon droplet experimental results. This model suggests that liquid metal combustion is basically a vaporization rate-limited process, complicated by the formation of a metal oxide (or fluoride) on the metal surface. This oxide layer tends to reduce liquid metal vaporization although it is considered porous. In general, the problem is aggravated if the initial drop or particle size is large, if the metal liquid vapor pressure is low, and if the oxide or fluoride melting temperature is significantly higher than that of the metal itself. Two distinct classes of metals, volatile and nonvolatile, were considered in Ref. 1 . The metals Al and Be, for example, are in the latter category. According to Ref. 1 , "the oxides of Al and Be are protective materials which adhere well to the metal surface. It is expected that an oxide

layer on the surface of these metals largely inhibits oxidation over a wide temperature range. When the surface temperature cannot rise above the melting point of the oxide, the solid shell thickens and further oxidation is inhibited." Thus, combustion of nonvolatile metals which have oxide melting temperatures higher than the metal boiling point would be very slow. Conversely, volatile metals such as lithium are characterized as follows (Ref. 1): "All of these metals have a vapor pressure of about 1 mm Hg or more at 1000 K....In view of the criterion for vapor-phase burning, it is expected that these metals can all burn in diffusion flames....Their melting points are low compared to realistic propellant flame temperatures. Accordingly, these metals should burn as liquid droplets." It is further pointed out that if large drops (80 to 100 microns) exist, some difficulty may arise due to oxide formation on the surface during the time when the comparatively large mass is being heated.

These studies indicated that efficient reaction of liquid lithium with fluorine in a rocket combustion chamber is feasible, and that its successful realization depends primarily upon the use of properly designed injection systems. To develop such systems, the same basic approach to the successful definition of injector design criteria was followed as that which has been thoroughly proved in previous performance programs (e.g., Ref. 2 and 3). Only the details of application differed. In this approach the fundamental injector spray parameters, propellant distribution and atomization, are considered to be performance controlling. Thus, for the fluorine/lithium combination, combustion efficiency will be a function of local fluorine and lithium mass and mixture distributions, as well as liquid lithium drop size. Control of the latter is considered the most critical spray requirement in the fluorine-lithium reaction. Data presented in this report indicate the necessity of achieving mean lithium droplet sizes no larger than about 20 microns for efficient combustion.

Consideration of the atomization characteristics of liquid lithium showed that simple impingement of liquid streams of practical size and velocity would not produce drop sizes small enough for realistic engine designs because of the extremely high lithium surface tension. Therefore, injector design concepts which achieve liquid atomization by use of high-velocity gas were considered. In principle, this is identical to the concept that was successfully employed in the NASA-sponsored F_2/H_2 nozzle program, in which efficiencies approaching theoretical were achieved over a mixture ratio range of 9 to 15 and a chamber pressure range of 50 to 200 psia (Ref. 2). In that case, performance was considered to be liquid fluorine vaporization-rate limited, and liquid fluorine atomization was accomplished by use of high-velocity hydrogen gas.

Lithium atomization by high-velocity hydrogen was not considered desirable because this would result in unfavorable propellant distribution, i.e., lithium drops in a hydrogen atmosphere. Instead, the concepts studied provide for generation of high-velocity F_2 and HF gases for lithium atomization. During Task I (Analysis and Design), cold-flow experiments were conducted with simulating fluids to define qualitatively the gas forces necessary to achieve 10- to 50-micron drop sizes. Hot-gas generator experiments were also carried out during this task to investigate the capability of delivering the hot-gas force necessary for atomization. These studies provided sound bases upon which injector design could proceed.

The Task II effort (Combustion Performance Tests) included determination of hot-firing c* efficiency as a function of percent hydrogen added (15 to 40 percent of total flow), hydrogen injection station, and chamber volume. The results obtained clearly demonstrated the feasibility of obtaining high combustion efficiencies with this tripropellant system.

The Task I (Analysis and Design) and Task II (Combustion Performance Tests) efforts are reported under separate headings within the text. The Task I discussion is subdivided as follows:

1. Thermodynamic and kinetic analyses of the $Li/F_2/H_2$ system
2. Analytical evaluation of $Li/F_2/H_2$ combustion
3. Liquid-metal atomization
4. Thrust chamber concept and design of components
5. Experimental evaluation of fluorine-rich gas generator
6. Liquid lithium facility and flow characterization

The Task II discussion is divided as follows:

1. Experimental facilities and procedures
2. Experimental evaluation of $Li/F_2/H_2$ combustion

TASK I

THERMODYNAMIC AND KINETIC ANALYSES OF THE $Li-F_2-H_2$ SYSTEM

REACTION KINETICS

A study was made of the kinetics of the various competing reactions involved in the $Li-F_2-H_2$ system to determine the sensitivity of combustion efficiency to the reaction rates. For purposes of this study, it was assumed that all three components are initially present and interacting. Under these conditions, it is important to ascertain to what extent lithium and hydrogen will compete for the fluorine and whether lithium would react rapidly with HF, if this were the first product formed.

Hydrogen/Fluorine Reaction

Because hydrogen and fluorine ignite hypergolically under confined conditions (Ref. 4), it might be expected that the reaction of gaseous hydrogen and fluorine would be quite rapid. However, Levy and Copeland (Ref. 5) have shown the reaction of purified gaseous fluorine and gaseous hydrogen to be slow at +230 F, with a half life of 32 seconds. They found the reaction rate under these conditions to be independent of the hydrogen concentration and proportional to the fluorine concentration (i.e., first order in fluorine). Brokaw (Ref. 6) has proposed the following energy chain mechanism to explain the results of Levy and Copeland:

$$F + H_2 \longrightarrow HF + H \qquad (1)$$

$$H + F_2 \longrightarrow \alpha HF^* + (1-\alpha)\, HF + F \qquad (2)$$

$$HF^* + F_2 \longrightarrow HF + 2F \qquad (3)$$

$$HF^* + M \longrightarrow HF + M \quad (4)$$

$$2F + M \longrightarrow F_2 + M \quad (5)$$

An energy chain mechanism has also been proposed by Kapralova, et al. (Ref. 38), whose work on fluorine/hydrogen ignition limits seems to support this postulate.

The kinetic results of Levy and Copeland do not suggest autocatalysis by the product HF, although Grosse and Kirshenbaum (Ref. 7) found it necessary to eliminate HF (and transition metal surfaces) to prevent spontaneous ignition of mixtures of hydrogen and fluorine at low temperatures.

To extrapolate the kinetic results to temperatures of interest in the present study, it is necessary to know the activation energy. Levy and Copeland (Ref. 8) present data which give a half life at 162 F of 13 minutes. This half life and their earlier value of 32 seconds at 230 F (Ref. 5) give an activation energy of 17.4 Kcal/mole. Brokaw's mechanism predicts an activation energy, E_a, equal to $2E_1+E_3-E_5-E_4$ (Ref. 6). Available estimates of E_1 are 1.5 Kcal/mole (Ref. 9) and 5.7 Kcal/mole (Ref. 10). Because the other three reactions appear to have very small activation energies, a small overall activation energy on the order of a few kilocalories is predicted from Brokaw's mechanism. However, since the rate constant for Reaction 3 represents an integrated average over all the vibrational energy levels of HF*, the activation energy of Reaction 3 may actually be large enough to permit agreement between Brokaw's mechanism and Levy's activation energy.

The lowest temperature encountered in the Li-F_2-H_2 system would be that occurring if the hydrogen and fluorine were to react to equilibrium, with the liquid lithium remaining unreacted and, together with the excess hydrogen, acting as a heat sink. This would result in a theoretical temperature of about 1400 K, with the largest proportion of hydrogen being considered (40 percent). Using an activation energy of 17.4 Kcal

to extrapolate the results of Levy and Copeland, the predicted half life at 1400 K is 2 microseconds. It thus appears that the hydrogen/fluorine reaction will be quite rapid even under the most adverse temperature conditions likely to be encountered in the combustion chamber. This would not have been the case had the activation energy been found to be much smaller. For example, a value of 5 Kcal would have led to a predicted half life of 0.3 seconds.

It is of interest that lithium vapor would be expected to inhibit the hydrogen/fluorine reaction, which is apparently a chain reaction in which fluorine atoms are one of the chain carriers. If an appreciable amount of lithium should vaporize before the hydrogen/fluorine reaction is complete, the fluorine atoms would react more readily with lithium atoms than with hydrogen molecules, thereby inhibiting the chain reaction. It is expected, however, that the reaction of hydrogen with fluorine would reach completion before the lithium is vaporized.

Lithium/HF Reaction

The above discussion suggests that the gaseous lithium atoms will find themselves in an atmosphere of HF and excess hydrogen as they evaporate from the surface of the parent liquid lithium droplets. It is of importance, therefore, that they react readily with HF if the desired reaction is to go to completion within the combustion chamber. An attempt was made to estimate the minimum rate of the reaction:

$$Li(g) + HF \longrightarrow LiF(g) + H \qquad \Delta H = -1.0 \text{ Kcal/mole} \qquad (6)$$

Exchange reactions of this type normally have activation energies on the order of 5 to 10 Kcal. Using the empirical rule of Semenov (Ref. 11), an activation energy of 11.2 Kcal/mole is obtained. At 1400 K, an error of 5 Kcal in the activation energy causes an error of only a factor of six in the estimated rate. Estimation of the pre-exponential factor is a more likely source of error, but most exchange reactions have pre-exponential factors between $10^8 T^{1/2}$ and $10^{10} T^{1/2}$ $(\text{mole-sec})^{-1}$. Therefore, the minimum value of k_6 should be approximately

$$k_6 = 10^8 T^{1/2} \exp(-11{,}000/RT) \ (\text{mole-sec})^{-1}$$

At 1400 K this estimated rate expression will give a value of 7.0×10^7 $(\text{mole-sec})^{-1}$ for k_6.

At chamber conditions of 1400 K, 500 psi, and 20 mole percent HF, the HF concentration would be 0.058 mole/liter. In this case, the maximum predicted half life of a lithium atom would be 0.2 microseconds with the value of k_6 estimated above. Even though the HF concentration will be much smaller as the reaction nears completion and a number of half lives are required to approach complete combustion of the lithium, this result indicates that the reaction of lithium with HF will be virtually complete in less than 10 microseconds even under the most adverse conditions which might be obtained (note that as the HF concentration decreases, the temperature and reaction rate increase).

It is believed that the lowest likely rate constant was used in calculating the rate of Reaction 6. If this reaction should have a very abnormally low rate for some reason, the reaction half life will be correspondingly longer, but this is very unlikely.

Fluorine/Lithium Vapor Reaction

The kinetics of the reaction of lithium vapor with fluorine has not been studied.

$$Li(g) + F_2 \longrightarrow LiF + F \qquad \Delta H = -99 \text{ Kcal/mole} \qquad (7)$$

Empirical formulas for estimating activation energies (Ref. 12) predict virtually no activation energy for Reaction 7, since a relatively weak bond is being broken and the reaction is highly exothermic. Assuming a steric factor at the low end of the "normal" range of steric factors for reactions of this type, and following the same reasoning used above for the lithium/HF reaction, the minimum rate constant for Reaction 7 should be approximately

$$k_7 = 10^8 T^{1/2} \text{ (mole-sec)}^{-1}$$

This assumes that about one collision in 100 is effective in leading to chemical reaction. At 1400 K and a fluorine concentration of 0.03 mole/liter, this predicts a lithium atom half life of only 0.006 microseconds. It thus appears that if the fluorine does not react rapidly with hydrogen for some reason (such as inhibition by Li atoms), the reaction of lithium atoms and fluorine will be very rapid even at low temperatures. The rate of this reaction will be relatively insensitive to temperature.

Condensed Lithium Reactions

A direct reaction between fluorine or HF and liquid lithium may occur at the surface of the lithium droplets. This would only be likely before

the droplet has ignited or been heated to a temperature at which it volatilizes rapidly. Otherwise, the reaction of lithium vapor will markedly deplete the concentration of oxidizer at the surface of the droplets. Reaction at the liquid surface would contribute to self-heating of the surface.

No experimental data are available on the rate of reaction of liquid lithium with HF or fluorine. It is anticipated that HF and particularly fluorine would react moderately rapidly at the liquid surface. However, the LiF layer that would form melts at 1143 K and would not be expected to reduce the rate of lithium reaction above this temperature.

Conclusions

For the concurrent reactions of gaseous fluorine, gaseous hydrogen, and liquid lithium, on the basis of available and estimated rate constants, it is concluded that the hydrogen/fluorine reaction would be very rapid even at the lowest temperature likely to exist in the combustion chamber, with predicted half life of about 2 microseconds at 2520 R (1400 K). As the lithium vaporizes, it will react extremely rapidly with the HF (predicted half life of about 0.2 microseconds at 2520 R) to form LiF. If the lithium vaporizes before HF formation is complete, the lithium may inhibit further HF formation; under these conditions lithium vapor will react nearly instantaneously with fluorine to form LiF (predicted half life of about 0.006 microseconds at 2520 R). In any event, the equilibrium condition following lithium vaporization is that the fluorine is nearly completely reacted with the lithium rather than with the hydrogen. Further, within the certainty of the estimated rate constants, the desired reactions will proceed much more rapidly than the physical processes of mixing and lithium vaporization, so that the latter will be the limiting factors in the attainment of complete combustion; reaction kinetics will not significantly affect combustion efficiency.

The experimental procedure adopted in the present investigation was to permit the fluorine and lithium to react prior to addition of hydrogen, at combustion zone temperatures of about 9800 R. However, although addition of all three propellants at the same axial position would result in substantially lower theoretical combustion temperatures (5500 to 5400 R, depending upon the proportion of hydrogen), they are still high enough so that combustion efficiency will not be affected by reaction kinetics.

THEORETICAL PERFORMANCE ANALYSES

Theoretical performance calculations for the Li F_2 and Li F_2 H_2 systems were made with the Rocketdyne N-Element computer program (Ref. 13), in which the propellants are reacted isenthalpically at a specified pressure to form atomic and molecular species in thermal and chemical equilibrium, defined by minimizing the Gibbs free energy of the system. The most recent JANAF propellant property tabulations are used for input data.

The combustion process is irreversible, and therefore non-isentropic, but all other nonequilibrium effects (chemical kinetics, transport processes, wall effects, etc.) are excluded. After combustion, the gaseous products expand by ideal, one-dimensional, isentropic flow through a nozzle to a specified exit pressure. Continuous chemical, thermal, kinetic, and phase equilibria are maintained among all species and phases. Temperature, pressure, density, velocity, and composition are uniform across any section normal to the velocity gradient. The nozzle is assumed to be fed from an infinite, stagnant, chamber and to discharge in parallel flow, so that calculated specific impulse is maximized.

In addition to the shifting equilibrium calculations, the model permits assumption of frozen composition; that is, chemical composition may be frozen in the chamber or at any point in the expansion, downstream of which the combustion product composition and phases remain invariant at the freezing point values.

Performance calculations were made to cover the LF_2/LLi mixture ratio range of 2.0 to 3.4 at chamber pressures of 200 to 1000 psia, with the addition of various amounts of hydrogen ranging from 0 to 40 percent of the total tripropellant flowrate. Limited calculations were also made with solid lithium injected at 36 R with liquid hydrogen. Auxiliary calculations included some in which no condensation of LiF was permitted, and others in which only extremely small amounts of hydrogen were present, as would be the case in experimental Li/F_2 firings (where F_2/H_2 is employed in the gas generator at very high mixture ratios).

Results of the theoretical performance computations are presented in a series of curves which show the variations in important performance parameters at specified conditions of chamber pressure, mixture ratio, and type of expansion. The data are then compared to establish the effects on the various performance parameters of chamber pressure, mixture ratio, proportion of hydrogen present, type of expansion, propellant state at injection, and incomplete condensation of LiF.

LF_2/LLi Performance Calculations

Results of the first series of calculations (Table 1), for liquid fluorine at 153 R and liquid lithium at 960 R, are illustrated in Fig. 1 through 4. The range of chamber pressure is 200 to 500 psia, and the range of F_2/Li

mixture ratio is 2.0 to 3.4. Maximum theoretical c* occurs at a mixture ratio of approximately 2.2 at 500 psia and 2.0 at 200 psia. On the other hand, chamber temperature, vacuum specific impulse, and thrust coefficient reach maxima at, or very near, the stoichiometric mixture ratio (2.74). As shown in Fig. 3, maximum vacuum specific impulse at 500 psia chamber pressure is 450 lbf-sec/lbm at an expansion ratio of 40 and 488 lbf-sec/lbm at an expansion ratio of 300.

Previous calculations of theoretical performance parameters for the liquid lithium/liquid fluorine propellant combination were published by NACA in 1951 (Ref. 14). Enthalpies of formation used for those calculations were -3.030 Kcal/mole for LF_2 (153 R), and 2.305 Kcal/mole for LLi (1000 R). Both frozen and shifting equilibrium performances were computed, for 300 psia chamber pressure and expansion to 1 atmosphere. Two sets of computations were made: one in which the combustion products (Li, F, LiF, Li^+, F^-, e^-) included ionized substances, and the other in which only nonionized combustion gases were considered (Li, F, LiF). It was found that the effects of ionization on the performance parameters are negligible.

Propellant inlet conditions for the performance calculations of the present study (LF_2 at 153 R and LLi at 960 R) were comparable to those of Ref. 14. The combustion products considered were Li, F, LiF, Li_2, and Li_2F_2. Although the last two species were not included in the computations of Ref. 14, they are present in only very small amounts (mole fractions less than 0.01), so that the inlet conditions and combustion products in both sets of calculations are comparable. It is therefore possible to compare the results obtained (Fig 5 and 6). Shifting equilibrium c* and I_s reported in Ref. 14 are somewhat higher than those calculated in the present study, but values of frozen composition c* and C_F in both computations are very close. Since the present calculations are based on newer thermochemical data and were obtained with the most recent modification of the N-Element computer program, they are believed to be the more reliable.

An amount of hydrogen equivalent to F_2/H_2 mixture ratios of 300 to 500 was expected to be used for reaction with fluorine in the gas generator upstream of the lithium injector in the experimental Li/F_2 firings of this investigation. Therefore, theoretical performance calculations were made which included these proportions of hydrogen to provide a base for comparison of experimental results. It was found that inclusion of such small amounts of hydrogen resulted in very minor changes in the performance parameters. The changes, for F_2/Li mixture ratio of 2.74 and chamber pressure of 250 psia, are shown in Fig. 7 and amount to about 0.5 percent for c* and I_s.

$LF_2/LLi/GH_2$ Performance Calculations

An extensive series of performance calculations was carried out for the LF_2(153 R)/LLi(960 R)/GH_2(537 R) tripropellant combination. The various parameters are illustrated in a series of curves which are listed in Table 2 and shown in Fig. 8 through 44. Important results are summarized as follows:

1. At 500 psia chamber pressure and with 15 to 40 percent added hydrogen (Fig. 8), vacuum specific impulse is maximum at, or very near, the stoichiometric F_2/Li mixture ratio (2.74); variation of specific impulse with mixture ratio above the stoichiometric point is more pronounced at the higher hydrogen levels. Optimum percentage hydrogen, which varies with mixture ratio and expansion ratio, is 30 to 35 percent at $\epsilon = 40$ (Fig. 8), decreasing to 24 to 28 percent at $\epsilon = 500$ (Fig. 10). Maximum vacuum specific impulse at 500 psia chamber pressure is 535 lbf-sec/lbm (F_2 Li MR = 2.74, H_2: 35 percent) at $\epsilon = 40$ (Fig. 8),

571 lbf-sec lbm (F_2 Li MR = 2.74, H_2: 30 percent) at ϵ = 300 (Fig. 9), and 578 lbf-sec lbm (F_2 Li MR = 2.74, H_2: 28 percent) at ϵ = 300 (Fig. 10). Chamber pressure variation in the range of 400 to 1000 psia has a small effect on vacuum specific impulse at ϵ = 40 (Fig. 14) and slightly larger effect at ϵ = 300 (Fig. 15); in either case, the changes at the higher percentages of hydrogen are nearly negligible. Differences between shifting equilibrium and frozen composition values of vacuum specific impulse decrease with increasing percentage of hydrogen (Fig. 22). At mixture ratio 2.74 and ϵ = 40, the approximate difference is 55 lbf-sec/lbm at 25 to 30 percent hydrogen, 37 lbf-sec/lbm at 35-percent hydrogen, and 19 lbf-sec/lbm at 40-percent hydrogen.

2. Characteristic exhaust velocity (c*) peaks at stoichiometric mixture ratio with the higher percentages of hydrogen (25 to 40 percent) but not at 15-percent hydrogen (Fig. 23). At 500 psia chamber pressure, mixture ratio 2.74, and 40-percent hydrogen, maximum c* is 9191 ft/sec with shifting equilibrium (Fig. 23), and 9035 ft/sec with frozen composition (Fig. 24); corresponding maxima at 1000 psia chamber pressure are 9233 ft/sec (Fig. 26) and 9118 ft/sec (Fig. 27).

3. Similar to c*, chamber temperature also peaks at the stoichiometric mixture ratio with the higher percentages of added hydrogen (30 to 40 percent) but not with lesser amounts (Fig. 28). The substantial heat absorption capability of the hydrogen is shown by the chamber temperatures at 2.74 MR and 500 psia chamber pressure in the absence of hydrogen (9814 R, Fig. 2), with 15-percent hydrogen (5436 R, Fig. 29), and with 40-percent hydrogen (3526 R, Fig. 29).

4. Vacuum thrust coefficients (C_F) at expansion ratios of 40 to 500 (Fig. 31, 32, 33) are generally maximum at the stoichiometric mixture ratio with 25 to 35 percent added hydrogen, but not outside this hydrogen addition range. As with specific impulse, the differences between shifting equilibrium and frozen composition values of vacuum thrust coefficient are more pronounced with 15- to 30-percent hydrogen addition than at higher hydrogen percentage levels (Fig. 40).

5. The mass fraction of condensed species in the chamber increases with increasing percent added hydrogen, with decreasing mixture ratio, and with increasing chamber pressure (Fig. 41, 42). In the nozzle, condensation is complete at an expansion ratio that decreases with increasing percent hydrogen; for example, with 25-percent added hydrogen, at 500-psia chamber pressure and 2.74 F_2/Li mixture ratio, maximum condensation (75 weight percent) is reached at ϵ = 300, but with 40-percent hydrogen at the same chamber pressure and mixture ratio, maximum condensation (60 weight percent) is reached at ϵ = 3 (Fig. 43).

A limited number of computations were made to estimate the effect on thrust chamber parameters of incomplete LiF condensation in the combustion chamber. Decreasing the amount of heat available for raising the hydrogen temperature would result in lowered chamber temperature, characteristic exhaust velocity and specific impulse. The effect is shown in Fig. 45 and 46. The abscissa represents the actual weight percent of condensed LiF as a fraction of the theoretical condensed weight percent. These effects are largest with 40-percent hydrogen addition (with 15- to 25-percent hydrogen, there is no LiF condensation in the chamber at 500 psia chamber pressure and 2.74 F_2/Li mixture ratio). In the extreme case of no LiF condensation, with 40-percent hydrogen, chamber temperature decrease would be approximately 8.5 percent, c* decrease, approximately 4.4 percent, and I_s (vac, ϵ = 40) decrease, about 6.2 percent.

$LF_2/SLi/LH_2$ Performance Calculations

A set of theoretical performance calculations was carried out to establish the effects of injecting the lithium as a solid at liquid hydrogen temperature instead of as a heated liquid. The tripropellant combination employed was LF_2(155 R)/SLi(36 R)/LH_2(36 R), at a single chamber pressure (500 psia). Results are illustrated in a series of curves which are listed in Table 5 and shown in Fig. 47 through 75. They are briefly summarized as follows:

1. Maximum theoretical vacuum specific impulse occurs at or near the stoichiometric F_2 Li mixture ratio for all conditions of percentage hydrogen addition and expansion area ratio, as with liquid lithium (Fig. 47, 48, and 49). Optimum percentage hydrogen decreases from about 30 at ϵ = 40 to about 25 at ϵ = 500 (Fig. 50, 51, and 52). Maximum vacuum specific impulse at 500 psia chamber pressure is 512 lbf-sec/lbm (F_2 Li MR = 2.74, H_2: 30 percent) at ϵ = 40 (Fig. 50), 550 lbf-sec/lbm (F_2 Li MR = 2.74, H_2: 25 percent) at ϵ = 500 (Fig. 51), and 558 lbf-sec/lbm (F_2 Li MR = 2.74, H_2: 25 percent) at ϵ = 500 (Fig. 52), which represent decreases of about 4 percent from the liquid lithium gaseous hydrogen system. Differences between shifting equilibrium and frozen composition vacuum specific impulse are nearly identical for the SLi/LH_2 and LLi/GH_2 combinations (Fig. 22 and 59).

2. Maximum characteristic velocity occurs at the stoichiometric F_2/Li mixture ratio with 25- to 40-percent added hydrogen, but is above mixture ratio 4 with 15-percent hydrogen (Fig. 60). At 500 psia chamber pressure and F_2 Li mixture ratio of 2.74, maximum c* (8750 ft/sec) occurs with 35-percent added hydrogen for shifting equilibrium (Fig. 60) but with 40-percent hydrogen for frozen

(8582 ft/sec, Fig. 61). Maximum c* in both cases was with 40-percent hydrogen for the LLi/GH_2 system (Fig. 23 and 24). The difference in c* between the LLi/GH_2 and SLi/LH_2 systems is approximately 5 percent.

3. Variation of chamber temperature with F_2/Li mixture ratio and with percent hydrogen (Fig. 63 and 64), at 500-psia chamber pressure, is the same in both systems. Decrease in temperature of the injected lithium and hydrogen is reflected in chamber temperature decreases of about 4 percent with 15-percent added hydrogen, 3 percent with 30-percent added hydrogen, and 8 percent with 40-percent added hydrogen.

4. Vacuum thrust coefficients of the SLi/LH_2 system differ very slightly from those of the LLi/GH_2 system. The abrupt drop in C_F at about 25-percent added hydrogen is evident in both cases, for F_2/Li mixture ratios below stoichiometric (Fig. 65, 66, and 67). Again, the difference between shifting equilibrium and frozen composition C_F decreases significantly with increasing percentage of hydrogen (Fig. 73).

5. Because of the lower chamber temperatures occurring with the SLi/LH_2 system, the percentage of condensed mass in the chamber (Fig. 74) is somewhat greater than in the LLi/GH_2 case under comparable conditions (Fig. 41). Similarly, maximum condensation occurs in the nozzle at a lower expansion ratio with SLi/LH_2 (Fig. 75) than with LLi/GH_2 (Fig. 43).

ANALYTICAL EVALUATION OF LITHIUM-FLUORINE-HYDROGEN COMBUSTION

Design of a $LF_2/LLi/GH_2$ rocket engine requires information regarding: (1) the mechanism by which lithium burns in a fluorine and/or fluorine-hydrogen combustion product environment, and (2) the design parameters which affect the reaction completion. Accordingly, present models of liquid metal combustion were reviewed, and it was determined that for small lithium droplet sizes, the rate-limiting mechanism inhibiting complete combustion would be the liquid lithium vaporization rate.

With this as a basis, a modified, one-dimensional, computer program based on a vaporization rate-limited combustion model was used to predict characteristic exhaust velocity efficiency as a function of engine design variables (contraction area ratio and chamber length), operating chamber pressure, amount and location of hydrogen addition, and lithium droplet size. These computations suggested that c* efficiency is extremely sensitive to drop size and chamber residence time (L*), with a lesser but significant dependency upon hydrogen injection location and amount. The predicted effect of pressure was minor. Consideration of the lithium combustion mechanism suggested that the dependency of c* efficiency upon drop size may be greater than predicted because the combustion of larger drops may not be vaporization rate-limited.

LITHIUM-FLUORINE COMBUSTION MECHANISM

Brzustowski and Glassman (Ref. 1) have observed that liquid metals which have. (1) vapor pressures of 1 mm Hg or more at 1900 K, (2) boiling points much lower than the corresponding oxide boiling point, (3) low melting points compared to the flame temperature, and (4) porous oxides tend to

burn with vapor-phase diffusion flames. These conditions are satisfied by lithium burning in fluorine because: (1) the vapor pressure of lithium is greater than 1 mm Hg at 1000 K, (2) the fluoride boiling point is 3050 F as opposed to the 2450 F boiling point of liquid lithium, (3) the melting point of liquid lithium is low (360 F), and (4) the Pilling-Bedworth ratio* of 0.7 indicates a porous fluoride.

On the basis of reasoning similar to that presented in Ref. 1 , the following theoretical mechanism is suggested for combustion of lithium droplets injected into a Li-F_2 combustion chamber:

1. Upon injection, the liquid lithium droplet is considerably below its boiling point, and fluorine diffuses to the surface of the droplet where it reacts to form a porous layer of LiF.

2. The droplet continues to react as the fluorine diffuses through the porous LiF layer. The reaction heat quickly causes the droplet to heat up to the melting point of LiF, at which point the latter becomes a molten layer coating the lithium droplet.

3. Only small amounts of LiF have been formed on the droplet to this point so that the molten LiF layer is thin, particularly on the upstream stagnation point of the droplet during acceleration in the combustion gas stream. Chemical reaction continues by diffusion of fluorine through the thin liquid layer.

4. As the temperature of the droplet increases, the vapor pressures of both the lithium and the LiF increase. Because the LiF is exposed to the gas phase, it gradually evaporates.

5. The liquid lithium becomes exposed to the gaseous fluorine atmosphere and has significant vapor pressure, so that it begins to burn in a diffusion flame around the droplet. The burning is now much more rapid than before.

*The Pilling-Bedworth ratio is the ratio of the volume of metal oxide or fluoride formed to the volume of metal reacted with oxygen or fluorine. When this number is less than unity, the oxide or fluoride is porous (Ref. 1, p 50).

6. The droplet becomes further heated until its temperature approaches the lithium boiling point, and the burning rate of the droplet reaches a quasi-steady state.

It is important to note that the theoretical mechanism described above is applicable only to small droplets of lithium, which have high ratios of surface area to mass, so that the molten LiF layer formed is thin and easily evaporated in step 4. On large droplets, with lower ratios of surface area to mass, the molten LiF layer formed in steps 1, 2, and 3 is relatively thick, and it physically inhibits the heat-producing reaction of lithium and fluorine; this results in the layer actually increasing in thickness rather than evaporating as in step 4. For further clarification, the large and small drop combustion mechanisms are schematically illustrated in Fig. 76.

It is interesting to note that if all of the heat of the Li-F_2 reaction were used to heat a 500 F lithium droplet to its boiling point, approximately 2 percent of its mass would be reacted with fluorine. This would result in a layer of LiF on the droplet with an average thickness of approximately 1.5 percent of the droplet diameter (actually, somewhat more LiF will be formed, because of heat losses from the droplet during the heating period). For initial droplet sizes of 1, 5, 10, 30, 60, and 100 microns, a 1.5-percent layer of LiF has a thickness of 0.015, 0.075, 0.15, 0.45, 0.9 and 1.5 microns, respectively. If a 1-micron-thick layer of LiF is arbitrarily selected as the maximum thickness which will allow a droplet to burn by the small droplet mechanism, then droplets smaller than approximately 70 microns will burn by the mechanism illustrated in Fig. 76-A, and larger droplets will burn by the mechanism of Fig. 76-B.

Although maximum droplet size for reaction as a small drop is not known, the determining factor will be the amount of LiF formation on the droplet surface. Greater quantities of LiF will be formed if:

1. A solid rather than liquid is injected. A larger time interval will elapse prior to steady-state combustion (time required to reach the metal boiling point).
2. The atmosphere contains only dilute concentrations of fluorine. Under this condition, the rate-limited chemical reactions discussed previously (specifically, steps 1, 2, and 3) will be slow, and greater quantities of LiF formation are necessary to achieve droplet heating because of increased heat losses from the droplet to the surroundings during the extended heating period.
3. The surrounding atmosphere is cold. Again, additional LiF must be formed to compensate for heat losses.

Thus, if the lithium is injected as a solid particle into a cold, dilute atmosphere of fluorine, it will have a greater tendency to burn by the large droplet mechanism. On the contrary, if the lithium is injected as a molten droplet into a hot, concentrated fluorine atmosphere, it will have a greater tendency to burn by the small droplet mechanism. Therefore, which of the two mechanisms prevails depends not only upon the size of the particle, but also upon the injection temperature of the lithium, the concentration of fluorine, and the prevailing temperature in the chamber.

MODEL OF THE LITHIUM DROPLET COMBUSTION MECHANISM

Brzustowski and Glassman (Ref. 15) have proposed an analytical model for the vaporization rate-limited combustion of liquid metal droplets, which resembles the models developed for propellants such as hydrocarbons (Ref. 16 through 19), except that effects of thermal radiation to the droplets and the possibility of condensed products in the combustion zone around the droplet were considered. If the effects of thermal radiation to the droplet are not included in the combustion analysis, the model of Ref. 15 becomes very similar to those of Ref. 16 through 19. A schematic description of the single droplet burning model is given in Fig. 77.

The equations (Ref. 15) used in the present study to model single metal-droplet burning under stagnant gas conditions are:

$$W = \frac{\ell n\ (1 + B)}{1 - D_A/D_B} \qquad (1)$$

with

$$\frac{D_B}{D_A} = 1 + \frac{\ell n\ (1 + B)}{\beta \beta_0} \qquad (2)$$

Data used to calculate droplet burning rates by Eq. 1 and 2 are given in Table 4, which lists all the parameters required except for the temperature of the reaction zone surrounding the droplet, T_B. In some instances, this temperature has been taken as equal to the metallic oxide boiling point for metals burning in air (Ref. 15). However, for lithium burning stoichiometrically in gaseous fluorine, it has been calculated that no condensed products are produced and therefore T_B should not be equal to the condensation temperature of LiF. Furthermore, the possibility of LiF condensation is decreased in the present case because the gaseous fluorine

will be preheated during gassification in the gas generator and by the early stages of combustion with lithium. For these reasons, the value of T_B was calculated separately by the following expression (Ref. 18):

$$T_B = \frac{3.76T_c + 64{,}200\left[\left(1 + Y_{o,c}/2.74\right)^{3.76} - 1\right]}{3.76\left(1 + Y_{o,c}/2.74\right)^{3.76}} \qquad (3)$$

The theoretical derivation upon which Eq. 3 is based neglects the effects of combustion product dissociation so that it tends to give values of T_B which are somewhat high, but this, in turn, compensates for the earlier assumption of no radiant heat transfer from the reaction zone to the liquid droplet.

If the droplet has reached its equilibrium temperature and the surrounding conditions do not change, the stagnation burning rate, k_s', remains constant throughout the combustion of the droplet and is given by the following expression (Ref. 15):

$$-\frac{d\left(D_A^2\right)}{dt} = k_s' = \frac{8\bar{\lambda}W}{\rho_L \bar{C}_p} \qquad (4)$$

With the data given in Table 4 and Eq. 1, 2, 3, and 4, the burning rate constant for single lithium droplets under stagnation conditions was calculated as:

$$\left(k_s'\right)_{Li} \cong 0.00044 \text{ in}^2/\text{sec} \qquad (5)$$

For cases in which hydrogen is added to the lithium-fluorine system, it was assumed that the total amount of hydrogen is added at a given axial location, and that it attains instantaneous equilibrium with the other species present. Addition of hydrogen results in the formation of HF, which also diffuses to the lithium droplet and reacts with lithium vapor.

The higher diffusivity of the HF molecule (compared to F_2) tends to be offset by the formation of increased amounts of combustion products which must diffuse in a countercurrent direction away from the vapor phase reaction zone surrounding the lithium droplets. The primary effect of hydrogen addition, therefore, is the dilution and the decreased temperature of the reactant atmosphere. The addition of hydrogen affects the droplet combustion rate primarily as shown in Eq. 3. A 20 to 30 percent decrease in k'_s for lithium droplet combustion was generally found to occur for the amounts of hydrogen addition (15 to 40 percent) considered when all three propellants are added at the same point.

DESCRIPTION OF THE COMPUTER PROGRAM

The single droplet burning rate constant, k'_s, is directly applicable to the original version of the Rocketdyne combustion model (Ref. 20). Only two minor changes to the model were required. One was the incorporation of Eq 3, and the other concerned alteration of the computer program to consider a three-propellant combination rather than the original two-propellant combination.

The combustion model considers the liquid propellants to be distributed into several droplet size groups, with all droplets in each group having the same diameter. The propellants were distributed into three size groups at the injection point by selection of the volume mean diameter, D_{30}, and use of a Nukiyama-Tanasawa distribution.

The following major processes are considered in the model: (1) droplet vaporization under forced convection, (2) droplet drag and acceleration,

and (3) compressible flow dynamics of combustion gases. These three processes are interrelated and result in "bootstrap" combustion in the rocket engine combustion chamber. Droplet vaporization increases the gas velocity, and increased gas velocity increases convective heat transfer to, and vaporization of, the droplets. As a balancing factor, increased gas velocity causes greater droplet acceleration and hence shorter residence time in the combustion chamber.

For droplet vaporization under forced convection, the program computes an increased droplet burning rate constant by applying a convective heat transfer factor to the stagnation burning rate constant:

$$k' = k'_s \left(1 + 0.3\ Re^{1/2}\ Pr^{2/3}\right) \qquad (6)$$

Droplet drag and acceleration are accounted for by use of a standard drag equation, together with drag coefficients specifically applicable to liquid droplets (Ref. 20):

$$\frac{dV_D}{dt} = \frac{3}{4} C_D \frac{\rho_g}{\rho_D} \left(V_g - V_D\right) \left|V_g - V_D\right| \qquad (7)$$

$$C_D = 27\ Re^{-0.84} \qquad Re < 80$$

$$C_D = 0.271\ Re^{0.217} \qquad 80 < Re < 10^4$$

$$C_D = 2.0 \qquad Re > 10^4$$

The compressible flow dynamics of the combustion gases are handled by classical methods (Ref. 21), except that the interchange of momentum between the compressible combustion gases and the liquid droplets is considered (Ref. 20).

The combustion model used considers one-dimensional, steady-state, rocket engine combustion. It takes no account of the ignition processes, nor does it consider the combustion which occurs in the poorly mixed (two-dimensional) regions near the injector face. This version of the program requires the following boundary conditions:

1. Conditions at the start of the well-mixed, one-dimensional zone.
   a. Propellant flowrate
   b. Droplet size distributions and velocities
   c. Combustion gas velocity
2. Sonic gas velocity at the throat

The computer program starts calculation with the first boundary condition. It then applies the appropriate equations, in finite difference form, to determine the combustion processes which occur in the chamber by calculations at short increments (about 0.05 inch) until the throat is reached.

The final results of the computations define the amount of lithium vaporized as a function of pertinent variables such as drop-size, chamber length, etc. Assuming that the amount vaporized equals the amount burned, characteristic exhaust velocity efficiency is expressed as a function of the amount of burned and unburned propellants:

$$\eta_{c^*} = \left[\frac{\dot{W}_{\text{burned}}}{\dot{W}_{\text{injected}}}\right] \left[\frac{c^*_{\text{burned}}}{c^*_{\text{injected}}}\right] \qquad (8)$$

For the $Li/F_2/H_2$ propellant combination, the fluorine and hydrogen are considered to be injected as gaseous propellants and are therefore assumed to be 100 percent burned in all cases. The only unburned propellant which enters into the calculation of η_c^* by Eq. 8 is any lithium which does not become vaporized in passing through the combustion chamber.

For all of the combustion model calculations, it was assumed that the well-mixed zone begins 2.5 inches downstream of the injector face, at which point 15 percent of the lithium is reacted and the velocity of all droplets is 30 ft/sec (Fig. 78). The combustion gas velocity assumed at the 2.5-inch location is consistent with a F_2/Li mixture ratio of 2.74, fluorine injected in the gaseous state, and 15 percent of the lithium reacted at that point. For cases in which hydrogen was assumed to be injected upstream of the 2.5-inch location, its presence was also included in the assumed gas velocity at 2.5 inches, to satisfy the mass continuity equation. The hydrogen injection velocity was assumed to have no effect on the combustion gas momentum because the specific direction in which the hydrogen can be injected is not fixed. At the point of injection, the hydrogen was assumed to be instantaneously mixed and completely reacted with the other gaseous species present.

Propellant injection rates were estimated so that the portion which reacted would result in sonic gas velocity with the desired throat area. If the propellants burned more completely or less completely than anticipated, the computer program automatically adjusted the contraction ratio to the proper value. If the calculated contraction ratio was not sufficiently close to the desired value, the propellant injection rates were adjusted, and the entire set of calculations was repeated.

The somewhat arbitrary assumptions of 15 percent lithium reaction and uniform conditions at the 2.5-inch location do not profoundly affect the final results of the combustion model calculation. If, in fact, the lithium is 15 percent reacted at 1.25-inches downstream of the injector rather than 2.5 inches, then the same overall result may be obtained by

merely constructing a combustion chamber 1.25 inches shorter. On the other hand, if the true distance is 5 inches rather than 2.5 inches, then a chamber 2.5 inches longer than anticipated would be needed.

The relationship between c* efficiency and percentage of lithium burned is illustrated in Fig. 79, which shows that incomplete lithium vaporization has relatively little effect on η_{c*} when hydrogen is present, compared to the case for zero percent hydrogen. Losses in c* are small when hydrogen is present because it can react with the unused fluorine. If none of the lithium were to vaporize and react, c* efficiency would be entirely determined by the reaction between fluorine and hydrogen. In the $Li/F_2/H_2$ combustor as presently conceived, fluorine and hydrogen are injected as gases; therefore, it is likely that the F_2/H_2 reaction will reach equilibrium. Figure 80 shows the η_{c*} which would be obtained if the lithium were partially reacted and the F_2/H_2 reaction were complete. For hydrogen addition in excess of about 7 percent, the shaded region in Fig. 80, in which lithium reaction is incomplete, represents an η_{c*} range of approximately 20 percent.

The characteristics of the $Li/F_2/H_2$ propellant combination shown in Fig. 79 and 80 are important in interpreting the combustion model results, reported herein as c* efficiencies.

COMPUTER PROGRAM RESULTS AND DISCUSSION

Table 5 lists the results of the combustion model calculations in terms of the following parameters: injector-to-throat chamber length, liquid lithium volume mean droplet diameter, chamber pressure, distance of point of hydrogen addition from the injector face, amount of hydrogen added (expressed as weight percent of the total propellant flowrate), chamber contraction ratio, chamber characteristic length, percentage of lithium reacted before reaching the throat, and c* efficiency. For all the cases listed in Table 5, the F_2/Li injection mixture ratio was 2.74.

The calculated efficiencies given in Table 5 for lithium volume mean droplet sizes of 100, 150, and 200 microns may not be realistic, since these large droplets very likely do not burn by the vaporization rate-limited process which is characteristic of smaller sizes. Nevertheless, the vaporization rate-limited process was assumed to occur even for these large droplets, and the calculations are included in Table 5 to show the detrimental effects of large droplet size on combustion efficiency. The large sizes will probably give even lower combustion efficiencies than indicated, because they may actually burn by the slower mechanism.

Figure 81 displays most of the data from Table 5 for the case of zero-percent hydrogen on the basis of characteristic chamber length (L*), which is a convenient parameter because it effectively normalizes the various chamber lengths and chamber contraction ratios to a single plot. The parametric curves represent lithium volume mean droplet sizes (with Nukiyama-Tanasawa distribution) from 20 to 200 microns. It is apparent that lithium volume mean droplet sizes must be less than 50 microns to achieve efficient combustion with a practical chamber L*.

Figure 82 shows the effect of injecting hydrogen at the Li/F_2 injector face. The addition of small amounts of hydrogen actually results in increased η_{c*}, which is a result of the F_2/H_2 reaction; the increase occurs even though less lithium is reacted. Hydrogen addition decreases the Li/F_2 flame temperature and thereby retards the lithium vaporization process.

Figure 83 shows the effect of adding hydrogen 5-inches downstream of the Li/F_2 injector. Comparison of Fig. 82 and 83 reveals that as much as 4 percent gain in η_{c*} is obtained by moving the hydrogen injection point downstream to the 5-inch location. This gain occurs because the absence

of hydrogen near the injector face results in an increased flame temperature, and thereby accelerates the lithium vaporization. Downstream hydrogen injection also gives slower gas velocities near the Li/F_2 injector face, which results in a longer residence time for the lithium droplets and hence their more complete vaporization.

The effect of increasing the total chamber length to 15 inches, with hydrogen injection at the 10-inch location, is shown in Fig 84. The 5-inch increase in upstream zone length, where $Li-F_2$ combustion in the absence of hydrogen occurs, results in η_{c*} gains of approximately 2 percent. The effect of an additional 5-inch increase in upstream zone length is shown in Fig 85, in which overall chamber length is increased to 20 inches and hydrogen is injected at 15 inches. Comparison with Fig 84 shows gain in η_{c*} of only 1 percent or less due to the 5-inch increase.

The effect of increasing zone length downstream of the hydrogen injection point by 10 inches (by increasing the overall chamber length to 30 inches while retaining the hydrogen injection point at 15 inches) is shown in Fig 86, which indicates that even with lithium droplet sizes as large as 50 microns, it is possible to obtain 99 percent combustion efficiency.

Figure 87 shows the effect of adding hydrogen at the Li/F_2 injector face in a 20-inch-long combustion chamber. Commparison with Fig. 85 shows that hydrogen injection at this point results in up to 4 percent decrease in η_{c*} compared to injection at the 15-inch location. Figure 88 shows that combustion efficiency is not a strong function of chamber pressure.

LIQUID-METAL ATOMIZATION

The static burning rate of liquid lithium in a gaseous fluorine atmosphere is only about one-tenth that of conventional storable and cryogenic propellants. To compensate for this inherently lower burning rate, the mean diameter of the liquid-lithium droplets must be approximately one-third that of more common propellants for equivalent combustion in chambers of comparable size.

Atomization of liquid lithium is relatively difficult because of its high surface tension (approximately 395 dynes/cm) compared to that of other liquid propellants (approximately 25 dynes/cm). Mean drop size in liquid sprays is a square root function of the liquid surface tension, so that under normalized injection conditions the mean drop size of liquid-lithium droplets would be about four times that of more conventional propellants. Rocketdyne experience (Ref. 22) with conventional self-impinging doublet injectors for molten sodium indicated that a mean drop size of approximately 180 microns was produced when extremely small (0.0135-inch diameter) orifices were employed at high injection velocities (about 200 ft/sec). Because of its physical properties, liquid lithium injected under similar conditions would produce mean drop sizes about twice this value. It was therefore evident that a much more efficient atomization technique would be required to produce the small lithium droplet sizes required for high combustion efficiency.

GAS-LIQUID ATOMIZATION

Experience with gas-liquid atomization techniques indicated that the use of high-velocity gas for aerodynamic atomization would probably provide the lithium drop size range required for efficient burning. With the

present tripropellant combination, either fluorine, hydrogen, or a combination of the two could be considered for use as the atomizing gas. Use of hydrogen alone would result in low flame temperatures and, therefore, slow vaporization and combustion of the lithium droplets. Addition of a small amount of fluorine to the hydrogen to generate higher-temperature gases would result in an increase in lithium burning efficiency. However, the need to vary the amount of hydrogen in combination with the fluorine and lithium would be accompanied by significant changes in the resulting lithium dropsize. As a more desirable alternative, therefore, gaseous fluorine derived by precombustion of a small amount of hydrogen with the liquid fluorine was selected as the most feasible atomizing gas. A specific advantage of this method is that the density and temperature of the gas can easily be varied by changing the pressure and mixture ratio in the gas generator. To maintain high lithium combustion temperature, the bulk of the hydrogen would be added downstream of the fluorine-lithium combustion zone.

A proven technique for gas-liquid atomization is the employment of an injector design in which a central showerhead gas jet is used to provide shear atomization of a pair of impinging liquid streams (Ref. 2, 23). Compared to the case of atomization by the mechanical impingement of two or more liquid streams, a basically different liquid breakup mechanism prevails when a liquid stream is exposed to high-velocity gases (Ref. 24, 25). In the latter case, very small wavelength capillary waves are induced on the surface of the liquid body; these grow in amplitude and eventually shear loose into small discrete droplets.

The mean droplet size resulting from the breakup of a single large drop in a high-velocity gas flow into discrete, finely atomized, smaller droplets is given by the following expression (Ref. 26):

$$\left[D_{30}\right] = \left[\frac{136\mu_L \, \sigma_L^{3/2} \, D_L^{1/2}}{\rho_L^{1/2} \, \rho_g^{2} \, \Delta V_g^{4}}\right]^{1/3} \qquad (9)$$

Equation 9 is an expression for the mean droplet size which can be expected under somewhat idealized conditions, namely: (1) the original spherical liquid droplet, of diameter D_L, is essentially at rest before the atomization process occurs; (2) only a single droplet is exposed to a relatively large amount of gas so that there is essentially no gas velocity degradation during the entire atomization process due to the acceleration of the fine droplets; and (3) the gas flow is enclosed in a duct so that no gas momentum is lost due to interactions with the surrounding media. The D_{30} symbol is bracketed in Eq. 9 because of the ideal conditions associated with its derivation.

To estimate the droplet size produced by injection of a liquid stream into a high-velocity gas jet, the characteristic diameter, D_L, in Eq. 9 was replaced by the liquid jet orifice diameter, D_L. Secondly, a correction was made for the loss of gas velocity due to the acceleration of the fine particles which are produced. The assumptions required for this correction are: (1) the droplets produced are sufficiently small so that they are instantaneously accelerated to the gas velocity, and (2) the atomization process is a steady-state process so that the liquid being atomized at any point is subjected to a gas velocity determined by its initial velocity and the amount of liquid which has been atomized and accelerated upstream of that point. With these assumptions, the gas velocity at any position can be approximated by a momentum balance:

$$\Delta V_g = \Delta V_g^{\,o} \left[\frac{\dot{W}_g}{\dot{W}_g + \dot{W}_L} \right] \tag{10}$$

Assuming that Eq. 9 and 10 apply to any given differential portion of the atomization process, the number of droplets, d_N, produced when an amount of liquid, $d\dot{W}_L'$, is atomized, may be expressed by:

$$d_N = \frac{d\,\dot{W}_L'}{\frac{\pi}{6}\,\rho_L} \left[\frac{\rho_L^{1/2}\,\rho_g^{2}\,\left(\Delta V_g^{\,o}\right)^4 \left(\frac{\dot{W}_g}{\dot{W}_L + \dot{W}_g} \right)^4}{136\,\mu_L\,\sigma_L^{3/2}\,D_L^{1/2}} \right] \tag{11}$$

Equation 11 can be integrated to obtain the total number of droplets produced, N, when the amount of liquid atomized, $\dot{W}_L'$, is equal to the total amount of liquid injected, $\dot{W}_L$. The result is

$$N = \frac{3\,\dot{W}_g}{2\pi\rho_L}\left[\frac{(1+\dot{W}_L/\dot{W}_g)^3-1}{(1+\dot{W}_L/\dot{W}_g)^3}\right]\left[\frac{\rho_L^{1/2}\,\rho_g^{2}\,(\Delta V_g^{\,o})^4}{136\mu_L\,\sigma_L^{3/2}\,D_L^{1/2}}\right] \qquad (12)$$

The volume mean droplet diameter produced by the overall atomization process is given by:

$$D_{30} = \left[\frac{\dot{W}_L}{\frac{\pi}{6}\rho_L N}\right]^{1/3} = \left[\frac{3\,\dot{W}_L/\dot{W}_g}{1-\left(1+\frac{\dot{W}_L}{\dot{W}_g}\right)^{-3}}\right]^{1/3}\left[\frac{136\mu_L\,\sigma_L^{3/2}\,D_L^{1/2}}{\rho_L^{1/2}\,\rho_g^{2}\,(\Delta V_g^{\,o})^4}\right]^{1/3} \qquad (13)$$

If jet spreading (gas divergence) effects are unimportant, Eq. 13 is an expression for the volume mean droplet size produced. It will be shown that it does, in fact, reasonably predict experimentally measured droplet sizes. If jet spreading effects are large, they may be estimated and applied by appropriate reduction of the relative gas velocity, $\Delta V_g^{\,o}$.

It is convenient to express Eq. 13 in the following short form:

$$D_{30} = \phi\, D_{30}^{\,o} \qquad (14)$$

where

$$\phi = \left[\frac{3\left(\dot{W}_L/\dot{W}_g\right)}{1-\left[1+\left(\dot{W}_L/\dot{W}_g\right)\right]^{-3}}\right]^{1/3}$$

and

$$D_{30}^{\,o} = \left[\frac{136\mu_L\,\sigma_L^{3/2}\,D_L^{1/2}}{\rho_L^{1/2}\,\rho_g^{2}\,(\Delta V_g^{\,o})^4}\right]^{1/3}$$

D_{30}^{o} in Eq. 14 is the droplet size which would be produced if there were no gas velocity decrease due to momentum exchange between the gas and the atomized droplets. Hence, ϕ is the increase in droplet size which results from the finite ratio of gas to liquid. Figure 89 is a plot of the ϕ factor as a function of the $\dot{W}_L/\dot{W}_g$ ratio. As $\dot{W}_L/\dot{W}_g$ approaches zero, ϕ approaches unity; it does not become significantly greater than unity until the ratio $\dot{W}_L/\dot{W}_g$ exceeds about 0.1.

Equation 14 does not completely express the breakup processes which occur, since the limiting condition at which the aerodynamic breakup of liquids ceases must also be considered. It has been shown (Ref.27) that the aerodynamic mechanism of liquid breakup will prevail only under the following condition:

$$\frac{We}{\sqrt{Re}} \geq 1.0 \qquad (15)$$

That is to say, the aerodynamic breakup mechanism described by Eq. 9 occurs and the results expressed by Eq. 14 are valid if the condition described by Eq.15 is first met. If the condition of Eq. 15 is marginal, aerodynamic breakup may start, but the gas velocity will dissipate sufficiently during the process to stop it. Therefore, Eq. 14 may not be valid when Eq. 15 is marginally true. It should be noted that the latter was obtained for application to spherical droplets, but has here been applied to cylindrical liquid streams.

JET PENETRATION

A basic tenet of the aerodynamic atomization expression (Eq. 14) is that the liquid stream is wholly exposed to the high-velocity gas. For a triplet injector element, maximum initial exposure of the liquid surface area

occurs when the streams are able to penetrate to the center of the gas jet. Full penetration results in the most effective use of the available gas momentum. An additional desirable feature derived from full penetration by the liquid streams is the relative improvement in the mixing of gas and liquid. Without full liquid penetration, a gas-rich condition exists within the core, resulting in degradation of combustion efficiency. Because of the criticality of having good penetration of the gas jet, a brief experimental program was conducted to define the parameters which affect this process.

APPARATUS AND PROCEDURE

A schematic drawing of a triplet injector element, with the liquid streams penetrating completely to the center of the gas jet, is shown in Fig. 90. This condition is described by:

$$X_p = D_g/2 \qquad (16)$$

Figure 91 is a schematic of the apparatus used to study jet penetration at ambient pressures. Photographs were taken of flow tests with injection conditions ranging from nonpenetration to complete penetration. The gas used was nitrogen, the flowrate of which was measured by a choked orifice. Water and Cerrosafe* were the liquids used.

The tests covered a relatively large range (0.125 to 1.50 inches) of gas jet diameter. Two liquid stream diameters, 0.040 and 0.060 inch, were used. The angle of the liquid streams with respect to the injector face was maintained constant to limit the number of test injectors. It is desirable to minimize this angle since smaller angles give better jet penetration; 45 degrees was chosen because it is close to the smallest angle which can be used without causing backsplashing of liquid onto the injector

*Cerrosafe properties are given in Table 7.

face. The nitrogen density was 0.066 lb/ft^3 (ambient pressure and temperature) for the majority of the tests; however, four test series were conducted at elevated pressures with nitrogen density as high as 1.21 lb/ft^3. The higher densities correspond roughly to the fluorine gas densities used in the Li-F_2 injector. Gas velocities were varied from 380 to 1100 ft/sec (Mach 1.0) with two liquid densities: 62.3 lb/ft^3 (water) and 590 lb/ft^3 (Cerrosafe metal alloy). The liquid Cerrosafe tests were carried out because these data would be of interest in connection with droplet size distribution tests. Water, on the other hand, has a density more comparable to that of lithium and is more easily handled than Cerrosafe; it was therefore used for the majority of the tests. The critical liquid velocities (i.e., those required for penetration of the liquid stream to the center of the gas jet) were obtained by suitably adjusting the liquid ΔP in each individual test.

Results and Discussion

Test data for the jet penetration experiments are given in Table 6, and typical photographs are shown in Fig. 92. Figure 92-A shows liquid-stream impingement in the absence of gas flow through the showerhead orifice of the triplet element; Fig. 92-B shows a condition in which the liquid streams do not have adequate velocity for gas jet penetration, and Fig. 92-C illustrates the condition in which the liquid streams have sufficient velocity to penetrate to the center of the gas jet.

The data obtained from the cold-flow jet penetration studies indicate that the physical mechanism primarily responsible for the limitation of liquid-stream penetration into a flowing gas jet is the aerodynamically caused breakup of the penetrating stream into small fragments. Such disintegration of the liquid streams is apparent from the test photographs

such as Fig.92-B and 92-C. Breakup of the liquid stream results in droplets which are much smaller than the original diameter of the cylindrical stream. These small droplets are very rapidly accelerated by the gas jet, and their velocities therefore become almost identical to the gas velocity very soon after they are formed. The rapid acceleration of the small droplets effectively prevents further liquid penetration.

Since breakup of the liquid stream is the predominant mechanism limiting jet penetration, correlation of the experimental data was based on the "flight time" of the liquid (defined as the time during which it is exposed to the high-velocity gas flow), and the calculated time required for the jet to break up due to the aerodynamic forces. The flight time of the liquid is given by the following equation:

$$t_f = \frac{X_p}{V_L \cos\theta} \tag{17}$$

For the breakup time of the cylindrical liquid stream, the following expression, derived and experimentally verified for application to the breakup of relatively large spherical liquid droplets into small droplets (Ref. 26), was used:

$$t_b = \frac{D_L}{V_g} \left(\frac{\rho_L}{\rho_g}\right)^{1/2} \tag{18}$$

The value of t_b given by Eq. 18 is the time between the first exposure of the liquid to the gas jet and the start of actual liquid breakup. This "dead time," or preparation time, is a result of the necessity to first generate disturbances (capillary waves) on the surface of the original liquid droplets. When the disturbances are critically large, liquid breakup begins. The time required for completion of the liquid breakup is approximately equal to the initial preparation period. The total time from initial exposure of the liquid to the gas to the completion of the

breakup process is therefore about twice the value of t_b given by Eq. 18 . Since this equation was originally developed to be applicable to liquid droplets rather than to cylindrical liquid streams, some modifications to it might be required to account for the differences between the two. However, because breakup time was used only as an empirical correlating parameter, no consideration was given to the geometrical difference between spheres and cylinders.

Equation 17 gives the exposed flight time of the liquid stream, which is equal to its total breakup time (or slightly more, due to continued penetration of the gas jet by the atomized liquid even after the actual cylindrical liquid stream has been completely broken up). For any particular situation, then, it should be expected that t_f will be slightly more than $2t_b$.

Values of t_f and t_b are given in Table 6 and are plotted in Fig. 93 where, in view of the approximate nature of this type of data, they are well correlated by the equation

$$t_f = 2.5\ t_b \tag{19}$$

The coefficient 2.5 is consistent with the expectation that it should be slightly larger than 2.

Combination of Eq. 17 through 19 gives:

$$\frac{X_p}{D_L} = 2.5\left[\frac{\rho_L\ V_L^2}{\rho_g\ V_g^2}\ \cos^2\theta\right]^{1/2} \tag{20}$$

Equation 20 essentially expresses the experimental results of the jet penetration studies.

In another series of experiments, schlieren photographs were taken of two opposing 0.10-inch-diameter helium jets penetrating into a gaseous nitrogen jet exhausting from a 2.0-inch-diameter tube, to aid in development of design criteria for the hydrogen injector. Details are given in a subsequent section of this report. The data from these experiments were used to evaluate a coefficient for an equation of the same form as Eq. 20:

$$\frac{X_p}{D_{He}} = 3.2 \left[\frac{\rho_{He} V_{He}^2}{\rho_{N_2} V_{N_2}^2} \cos^2 \theta \right]^{1/2} \qquad (21)$$

where cos θ was 1.0. The numerical coefficient, 3.2, is close to the coefficient (2.5) found for liquid-stream penetration into a gaseous jet. This was not unexpected since the aerodynamic forces greatly overwhelm the surface tension and viscous properties of the liquids so that inertial resistance remains as the primary factor to resist breakup.

EXPERIMENTAL STUDY OF LIQUID-METAL ATOMIZATION

Following determination of the conditions required for efficient penetration of a gas jet by a liquid stream, the more basic problem of attaining a high degree of liquid lithium atomization was investigated. The objective of this study was to determine the validity of the atomization equation of Wolfe and Andersen (Ref. 26) for specific practical applicability to the design of the gaseous fluorine/liquid lithium injector.

The basic Wolfe-Andersen atomization equation has never been experimentally verified for liquids of very high surface tension such as liquid lithium. In particular, experimental verification was required of the modified

Wolfe-Andersen equation derived herein for the case in which only a limited amount of gas is available for the liquid atomization. Experiments were therefore carried out to verify these atomization expressions, using a suitable simulant for liquid lithium.

Apparatus and Procedure

Cerrosafe* was used as lithium simulant for the droplet-size measurements. This had two advantages: (1) after atomization, the metal droplets which were formed were easily frozen and collected, and (2) Cerrosafe has high surface tension (400 dynes/cm, measured in this laboratory) approximately equal to that of lithium. No data are available for the viscosity of Cerrosafe. However, the viscosities of most liquid metals at their melting points are in the approximate range of 1 to 3 centipoise. It was assumed for computational purposes that Cerrosafe has a viscosity of 1 centipoise. Volume change data are included in Table 7 to show that no significant error is introduced by the assumption that solid particles are the same size as the liquid droplets from which they are formed.

Figure 94 is a schematic representation of the apparatus used for the liquid-metal atomization droplet size measurement studies. Cerrosafe was contained in a tank immersed in water maintained at approximately 200 F to ensure that the alloy was molten. The outlet of the Cerrosafe tank was connected through a valve to the triplet injector manifold supplying the liquid doublet orifices. Gaseous nitrogen was supplied to the element through an orificed line as indicated.

*Cerrosafe properties are given in Table 7

The spray produced by the triplet element was directed into a collection vessel, the bottom of which was covered with water. Cerrosafe droplets were exposed to ambient-temperature gas during their descent and were solidified when they entered the collection vessel, although some of the larger droplets probably did not freeze until actually contacting the water layer. After each test the Cerrosafe particles in the collection vessel were sampled for photomicrography. A mechanical shutter was provided between the triplet injector element and the collection vessel to divert the spray during the transient portions of the tests. Cerrosafe flowrates were calculated from the injection pressure drop ($C_D = 0.7$), and nitrogen flowrates were calculated from the pressure drop across a choked orifice.

Two triplet element injectors were used for the droplet size tests. Both had 0.060-inch-diameter liquid doublet orifices inclined 45 degrees to the injector face. The showerhead gas orifice diameter was 1.0 inch for one injector and 1.50 inch for the other. Preliminary experiments had shown 0.060-inch liquid orifices to be approximately the lowest usable size; intermittent plugging occurred with smaller diameters due to formation of oxides and other slag. The relatively large gas orifices were necessary to obtain sufficient total gas momentum without choking the flow of the ambient-pressure nitrogen at the orifice exit. Figure 95 is a photograph of a typical Cerrosafe atomization test.

The solidifed Cerrosafe droplets sampled from the collection vessel were air-dried and a portion of the sample was photomicrographed at magnifications ranging from 35 to 200 X, depending on the relative droplet sizes in the sample. A typical photomicrograph is shown in Fig. 96. It was found that collected particles smaller than 40 to 50 microns resembled chrome-plated spheres, whereas larger droplets were somewhat distorted from the spherical shape.

To measure droplet sizes from the photomicrographs, a transparent sheet was placed across the photograph in a random orientation. The transparent sheet had a very thin line scribed upon it, and the diameters of all droplets images which touched the scribed line were measured and recorded. The process was repeated until a minimum of 200 individual droplet images were measured. A weighting factor, equivalent to the inverse of the diameter, is applied to each droplet counted when mean diameters are calculated from such image measurements (Ref.28). The defining equation for mean droplet size, in terms of the measured droplet images, is:

$$D_{qp} = \left[\frac{\sum_{i=1}^{M} \frac{1}{D_i} (D_i)^q}{\sum_{i=1}^{M} \frac{1}{D_i} (D_i)^p} \right]^{\frac{1}{q-p}} \qquad (22)$$

A computer program was written to sort the droplet measurements according to size and to calculate the mean droplet sizes for values of q and p from 0 to 6 inclusive. The mean droplet size of greatest interest is the volume mean droplet size, D_{30}, obtained when $q = 3$ and $p = 0$:

$$D_{30} = \left[\frac{\sum_{i=1}^{M} \frac{1}{D_i} (D_i)^3}{\sum_{i=1}^{M} \frac{1}{D_i}} \right]^{1/3} \qquad (23)$$

Another factor calculated for the droplet sprays was G(D), the total volume fraction of the spray contained in droplets with diameter less than D:

$$G(D) = \frac{\sum_{D_i=0}^{D} \frac{1}{D_i} (D_i)^3}{\sum_{D_i=0}^{\infty} \frac{1}{D_i} (D_i)^3} \qquad (24)$$

The volume distribution of the spray is obtained by graphical differentiation of G(D).

The weighting factor, $1/D_i$, has been retained separately in Eq.22 through 24 to emphasize its presence.

It is apparent from Eq. 23 and 24 that the larger-diameter image measurements are the most important in the determination of D_{30} and G(D). The measurement technique employed tends to increase the frequency of measurements at the large end of the droplet size spectrum, and although the higher frequency of measurements at the large end is accounted for by the weighting factor, this in turn improves the accuracy of the summations of the larger droplets at the expense of the smaller. Since the large end of the size spectrum is the most significant, a definite advantage is gained by measuring only droplets which touch a randomly positioned line.

The following expression (Ref. 29) was used to estimate the accuracy of D_{qp}, defined by Eq. 22, as a function of measured particle sizes.

$$\text{Error in } D_{qp} = \frac{\pm(1962)}{\sqrt{M\,(q-p)}} \left[\frac{\sum_{i=1}^{M} (D_i)^{2(p-1)}}{\left\{\sum_{i=1}^{M} (D_i)^{(p-1)}\right\}^2} + \frac{\sum_{i=1}^{M} (D_i)^{2(q-1)}}{\sum_{i=1}^{M} (D_i)^{(q-1)}} - \frac{2\sum_{i=1}^{M} (D_i)^{(p+q-2)}}{\sum_{i=1}^{M} (D_i)^{(p-1)} \sum_{i=1}^{M} (D_i)^{(q-1)}} \right]^{1/2} \qquad (25)$$

Equation 25 gives the estimated maximum error in D_{qp} at the 95-percent confidence level which occurs because a finite number, M, of droplets are counted; it does not include errors from other sources (sampling technique, experimental errors, etc.). The measured D_{30} values are estimated (Eq. 25) to have errors ranging from 6 to 16 percent.

Experimental Results and Discussion

Eleven experiments were carried out to obtain dropsize measurements for comparison with the sizes predicted by the atomization equations described above. The salient parameters varied during this study were the Weber to Reynolds number ratio (Eq. 13) and the quantity of gas available per pound of liquid to be atomized. The effect of the latter parameter was evaluated in terms of the parameter ϕ (Eq. 14). In general, the data obtained showed that the measured dropsizes agreed reasonably well with the calculated sizes and that a critical $We/\sqrt{Re}$ ratio exists below which the derived equations were not applicable.

The experimental conditions and results are presented in Table 8. The parameter P included in this table represents the calculated percentage of liquid-stream penetration into the gas jet (P = 100 represents

penetration to the center of the gas jet). Values in excess of 100 percent mean that the liquid streams possess more than the necessary velocity to penetrate to the center and therefore collide.

The data obtained show that triplet (liquid-gas-liquid) element atomization is a somewhat complex phenomenon. Typical data were plotted to illustrate the overall droplet mass distribution as a function of dropsize. Figure 97 shows the distributions obtained when ϕ was > 2.0 (test 52), < 1.9 (test 41), and ~ 1.9 (tests 42 and 48). With the largest values of ϕ, fairly broad, flat-shaped curves typically resulted, whereas with the smallest values of ϕ much sharper curves were produced. In the intermediate ϕ range the distribution curves have a double-peak shape. These results are consistent with those which would be predicted since larger values of ϕ are caused by reduction in the quantity of gas available for atomization. Because of this, a greater gas velocity gradient downstream of the injection point occurs. The broader range of relative gas-to-liquid velocity thus created results in a larger dropsize range.

Three tests (42, 43, and 44) were conducted in which the $We/\sqrt{Re}$ ratio was less than, or near, unity. The distribution obtained in run 42 is shown in Fig. 97. It can be seen that a very broad dropsize range was produced under these conditions, and as shown in Table 8, the experimental mean dropsizes were much larger than calculated. In view of these observations, it seems apparent that a different mechanism of atomization occurred.

The calculated value of the penetration parameter, P, was over 80 percent for 10 of the 11 experiments. Within this range, the penetration parameter should have negligible effects on the dropsize characteristics measured. However, one experiment (test 40) was conducted in which the penetration parameter was reduced to 45 percent, but the values of calculated and measured mean dropsizes remained similar. The rather

small influence of the degree of penetration on dropsize might be expected, since a 2:1 change in the penetration parameter only causes an 8-percent change in the value of ϕ. This small change occurs because, with 50-percent penetration, 75-percent of the gas flowrate is involved in the liquid atomization. These results indicate that penetration will probably influence propellant distribution more significantly than it does the degree of atomization.

In summary, the experimental data show that the gas-liquid atomization equation developed (Eq. 14) is applicable to the design of the gaseous fluorine-liquid lithium injector. Further, application of this equation is limited to cases in which the $We/\sqrt{Re}$ ratio is greater than unity.

THRUST CHAMBER CONCEPT AND DESIGN OF COMPONENTS

The tripropellant thrust chamber concept developed in this program was based on the premise that lithium/fluorine combustion should be completed prior to hydrogen addition and subsequent achievement of thermal equilibrium. Thus, in essence, a two-stage system was employed, in the first of which hot LiF was formed (theoretical temperature = 9800 R, molecular weight = 26), followed by hydrogen addition resulting in reduced temperature (3500 to 5400 R) and molecular weight (5 to 9). Component designs were to be flexible to the extent that variations in upstream and downstream chamber volume could be made so that the combustion and mixing volumes required for high efficiency could be defined experimentally. Potentially, in the limit, the design would allow the determination of the basic necessity for a two-stage system as opposed to injection of all propellants in the same vicinity.

The basis upon which the Li/F_2 injector was to be designed depended upon the results of calculations based on the analytical combustion model and on the simulated lithium atomization and propellant distribution criteria obtained in the cold-flow atomization study. In summary, the combustion model results indicated that a maximum volume mean lithium drop size of about 20 microns was required for high performance. The cold-flow data showed that to achieve this drop size, gas atomization of the liquid lithium would be required. Accordingly, the lithium injector concept which was developed consisted of the injection of lithium streams into high-velocity gas jets. These gas jets were to be obtained by use of a fluorine-rich gas generator upstream of the lithium injector.

A conceptual illustration of the thrust chamber assembly is shown in Fig. 98. A schematic scale drawing of the actual assembly is presented in Fig. 99.

Nominal design operating conditions for the system were:

Mixture ratio, F_2/Li = 2.74

Hydrogen added, percent = 15 to 40 of total flowrate

Chamber pressure, psia = 500

Sea level thrust, lbf = 2000

Design criteria and descriptions of the various components are discussed below.

GAS GENERATOR DESIGN

The gas generator concept arose from the need to supply hot (500 to 1000 F), pressurized (400 to 700 psi) fluorine to the Li/F_2 injector to obtain a high degree of lithium atomization. It was recognized that a convenient way of obtaining such hot gas was to react liquid fluorine with a very small amount of hydrogen, at mixture ratios which would produce the desired gas temperatures. Figure 100 shows the variation of LF_2/GH_2 combustion gas temperature in the mixture ratio range 200 to 500 at chamber pressures of 400 to 1000 psia. Corresponding shifting-equilibrium c* values are shown in Fig. 101. Within the mixture ratio range of interest (300 to 500), the small amount of HF which would be present in the gas generator output would not significantly alter its properties from those of pure fluorine. The gas generator assembly is

shown schematically in Fig. 102. It consisted of separate hydrogen and fluorine injectors, two identical chamber sections, and a nozzle plate. Design details and the function of each of the components are discussed below.

Hydrogen Injector

Since the hydrogen flowrate into the gas generator was necessarily very small (0.005 to 0.009 lb/sec), use of hydrogen injection momentum to atomize the liquid fluorine, as in a triplet element, was not practical. The hydrogen was injected through nine 0.0135-inch, showerhead orifices drilled on a 2-inch basic diameter. Design pressure drop through these small orifices (square entrances) was such that flow of ambient-temperature hydrogen through them was sonic. The injector was fabricated from OFHC copper (Fig. 103).

Fluorine Injector

Liquid fluorine was injected through 36 circumferential, self-impinging doublet elements arranged around the inner diameter of the stainless-steel injector (Fig. 104) and forming radially directed sprays which intersected the hydrogen jets. The orifice diameter was 0.026 inch and the impingement angle was 60 degrees; design pressure drop at the nominal fluorine flowrate of 2.74 lb/sec was 250 psi, and injection velocity was 110 ft/sec. Cold flow of the hydrogen-fluorine injector combination with water and nitrogen as propellant simulants, at relative momenta approximating those in a hot firing, is shown in a photograph (Fig. 105) which indicates a good degree of liquid atomization.

Combustion Chamber

The function of the combustion chamber was to permit interaction of the fluorine and hydrogen and to provide uniform gas properties at the chamber exit. Calculations made with the one-dimensional, vaporization rate-limited combustion model previously discussed showed that combusion would be complete within a 5-inch chamber length for 80-micron fluorine droplets, and within 10 inches for 120-micron droplets. These droplet sizes are of the order of magnitude produced by the 0.026-inch impinging fluorine streams. Hence, a chamber consisting of two identical 5-inch sections was designed to permit use of either 5 or 10-inch chamber lengths. Since gas temperatures within the combustion chamber are relatively low, 1018 carbon steel was selected as the material of construction. To promote gas mixing within the chamber, perforated stainless-steel mixing plates were welded at the center of each section. Experimental temperature data showed that they effectively increased the degree of combustion gas uniformity.

Nozzle Plate

The stainless-steel nozzle plate (Fig. 106) was both a model of the injector into which the gas generator output was to be directed and an exit nozzle for control of chamber pressure during gas generator evaluation tests. For firings at 400 to 500-psia chamber pressures, the nozzle plate contained thirteen 0.185-inch orifices. A plate with seven 0.213 orifices was used for tests at 700 psia. Figure 107 shows the gas generator components in order of assembly, with only one of the chamber sections.

LITHIUM/FLUORINE INJECTOR

The Li/F_2 injector was the most important component of the thrust chamber because of its profound effect upon combustion efficiency. Since its design posed several unique problems, two distinct designs were completed: (1) a triplet pattern (two lithium streams impinging into a showerhead fluorine gas jet) and (2) a doublet pattern (one lithium stream injected into a showerhead gas jet). The design requirements, i.e., the necessity for gas atomization and for adequate liquid penetration into the gas jet, were the same in both cases.

The major differences between the two injectors were the method and material of construction. The triplet, which was considered functionally superior in terms of providing a more uniform propellant distribution, was, by necessity, fairly complex and required machinable metal construction. The durability of this design was unknown and it was limited to temperature levels which the selected metal (stainless steel) was capable of withstanding. The doublet design was based upon the assumption that the heat flux rates encountered would be too severe for common metals, and therefore a simplified design which permitted the use of a more thermally compatible material would be necessary. For this reason, the doublet design employed graphite as construction material and it was used for the major portion of the experimental program.

Triplet Injection Pattern

Liquid lithium and gaseous fluorine were injected through triplet elements with the outer liquid lithium streams intersecting at a 90 degree angle over a central fluorine gas orifice. As a result of data obtained during the lithium flow studies (described in detail in the

Liquid Lithium Flow Characterization section), 0.043-inch-diameter lithium orifices were selected for a seven-element injector; the design pressure drop at nominal flowrate (1.00 lb/sec) was 275 psi (C_D = 0.8).

Results obtained in the metal atomization studies reported in a preceding section indicated that the triplet element should be sized so that the outer liquid metal streams would have sufficient momentum to penetrate the central gas jet completely (i.e., to its center). Application of this criterion for optimum atomization showed that complete penetration is difficult to achieve at high gas velocities; a compromise is required between high gas velocities, which produce finely atomized metal droplets, and low gas velocities, which ensure complete penetration and hence efficient aerodynamic contact between gas and liquid. Thus, high gas velocity results in the production of finely atomized metal droplets for that portion of the liquid which penetrates the gas jet. The degree of penetration may be so low, however, that a substantial fraction of the liquid does not contact the gas and is therefore very poorly atomized.

The following three equations were utilized to predict the behavior of the triplet injector:

$$\frac{\rho_g V_g D_g^2}{2 \rho_L V_L D_L^2} = 2.74 \qquad (26)$$

$$\frac{X_p}{D_L} = 2.5 \left[\frac{\rho_L V_L^2}{\rho_g V_g^2}\right]^{1/2} \cos \theta \qquad (20)$$

$$D_{30} = \phi \left[\frac{136 \mu_L \sigma_L^{3/2} D_L^{1/2}}{\rho_L^{1/2} \rho_g^2 \Delta V^4}\right]^{1/3} \qquad (14)$$

Equation 26 is a continuity equation which expresses the F_2/Li injection mixture ratio as the ratio of the weight flowrates through the single fluorine orifice and the two lithium orifices of the triplet injector element. Equation 20 was developed in the cold flow portion of this program; it describes the penetration of the liquid lithium streams into the central showerhead fluorine jet. Equation 14 is a modified form of the Wolfe-Anderson equation (Ref. 26) which was verified in the cold-flow portion of this program; it expresses the lithium droplet size as a function of the injection conditions and propellant properties. Factors which must be considered in the use of these equations were discussed in the section of this report which deals with liquid metal atomization.

Results obtained with Eq.14, 20, and 26 are presented in Fig. 108A and 108B,, which show the predicted extent of lithium stream penetration into the fluorine jet and the predicted volume mean droplet size of the atomized lithium, respectively. (It should be noted that 50-percent penetration in Fig. 108 represents penetration to the gas jet centerline.) Lithium is injected at 0.0714 lb/sec/orifice through 0.043-inch orifices inclined at an angle of 45 degrees to the face. The effects of variable fluorine injection temperature and orifice diameter and of variable chamber pressure are indicated. It is apparent that larger fluorine orifices allow better jet penetration along with increasing droplet size; the increased degree of penetration is beneficial whereas the increased drop size is detrimental. Conversely, smaller fluorine orifice diameters produce smaller droplet sizes but increasingly poor jet penetration. The selected size for the design chamber pressure (500 psia) was 0.272 inch. This size represents the approximate optimum design condition for liquid penetration to the gas jet centerline and minimized drop size for the nominal gas generator design operating temperature of 1000 R.

Triplet Material Selection. The most satisfactory materials for hot gaseous fluorine service are nickel, monel, copper, aluminum, and, to a

lesser degree, the 300-series austenitic stainless steels (Ref. 30). For liquid lithium service, available data (Ref. 31 and 32) indicate that the best materials are pure iron, stainless and carbon steels, and certain refractory metals (molybdenum, tantalum, columbium); nickel and nickel alloys are probably satisfactory for temperatures under 600 F, while copper, aluminum, and their alloys have poor resistance to attack by molten lithium.

Selection of the injector material involved a number of tradeoffs, not only because of conflicting compatibility properties but also on account of relative cost, availability, ease of machining, and high-temperature strength. Consideration of these factors led to the selection of stainless steel (321) as the basic injector material, with nickel as the best alternate. Materials bordering on state-of-the-art development were not considered as candidates because of scarcity of compatibility data and generally excessive cost and delivery lead time. The relatively low thermal conductivity of stainless steel was a recognized disadvantage in this application with regard to both preliminary heatup time and firing duration capability. For the latter reason, an injector design was developed which allows protection of most of the injector face from the combustion gases during firing (described below).

Triplet Injector Heating. To heat the injector to 500 F and keep it at this temperature prior to firing, heater rods (3-kilowatt total capacity) arranged in a radial pattern around the injector center were provided. Although some injector heating was obtained from the hot gaseous fluorine as well as from hot helium purge gas prior to the flow of lithium, these were auxiliary heat sources, not adequate in themselves to satisfy total injector heating requirements.

Triplet Injector Face Thermal Protection. The extremely hot (~9800 R) combustion gases in the recirculation zone imposed a requirement for thermal protection of the injector face. Such protection was provided

by inclusion of a 0.75-inch layer of carbon cloth/phenolic resin ablative over the entire face of the injector except for minimum areas around the propellant orifices. The carbon cloth layers in the ablative were oriented parallel to the injector face. This ablative protector could be replaced after each firing series if necessary.

Photographs of the triplet injector and its components are presented as follows: Fig. 109 shows the inlets to the seven fluorine gas orifices; Fig. 110 is a face view of the triplet injector with the protective ablative face plate installed; Fig. 111 and 112 are face and back views of the ablative plate, respectively; and Fig. 113 shows the triplet injector with the face plate removed.

Doublet Injection Pattern

The lithium/fluorine injector is subjected to extremely severe chemical and thermal environments. On the inlet side, it is exposed to fluorine gas at temperatures up to 800 F and pressures up to 700 psi, as well as to liquid lithium at 500 F and 500 to 800 psi; at its face, combustion chamber temperature may be as high as 9800 R for firing durations up to 8 seconds. No common metal can withstand these conditions without protective devices such as thermal resistive coatings or ablative shields, and the adequacy of such protectors is questionable. Better results might be obtained with refractory metals, but not enough is known of their compatibilities to justify their high cost and difficulty of fabrication.

Of the nonmetallic materials, possible candidates are graphite, ceramic oxides, or metal carbides. Graphite was selected as the material for the alternate injector design, for the following reasons:

1. Experience with graphite in combustion chambers and nozzles with fluorine and other fluorinated oxidizers has been generally satisfactory, although experimental conditions to date have not been as severe as those to which the lithium injector might be subjected.

2. Various properties of graphite are favorable for this application (high thermal conductivity, good resistance to thermal shock, chemical inertness, ease of machining).

3. The common ceramics and carbides have one or more disadvantages which, at present, rate them below graphite for use as injector material (lack of appropriate compatibility data, brittleness, variable porosity, difficulty of machining, high cost).

Use of triplet elements in the first Li/F_2 injector required fairly elaborate internal manifolding which could be eliminated by conversion to LLi/GF_2 doublets. Calculations of the degree of penetration of the fluorine gas jet by the liquid lithium stream and of the mean droplet sizes of the atomized lithium indicated that acceptable levels of both parameters could be obtained with a doublet injection element. Thus, for an 8-element injector with fluorine orifice diameter of 0.297 inch and lithium orifice diameter of 0.055 inch, under the injection conditions for firings at 500-psia chamber pressure, the calculated degree of gas jet penetration was approximately 85 percent, and calculated mean lithium droplet diameter was approximately 10 microns.

Fluorine from the gas generator was injected through showerhead orifices. Liquid lithium was injected through individual tubes to each element through orifices inclined at 45 degrees to the injector face. The tubes were 321 stainless steel and were fed from a manifold outside the injector body. This assembly is shown in Fig. 114. Figure 115 is a face view of the injector.

The external lithium manifold was close-coupled to the lithium/fluorine injector and was heated by Thermwire heating cable wrapped around it. The lithium inlet tubes were not electrically heated within the injector body but were heated instead by passage of hot helium purge gas through them immediately before the lithium flow. Calculations showed that the inner surfaces of the tubes could be heated to about 500 F by flowing helium gas at 800 F through them for 4 seconds at normal purge gas pressure. This was confirmed experimentally by embedding a tube in a block of graphite, heating it by a 4-second flow of helium at 800 F, and then flowing liquid lithium through it without difficulty. Preheating of the tubes by conduction from the heated manifold provides added assurance of temperature attainment.

COMBUSTION CHAMBER

Chamber Geometry

Design criteria for the F_2/Li combustion chamber were established from results of calculations based on the Lambiris-Combs one-dimensional, steady-state combustion model (Ref. 20). Assembled results of these calculations are shown in Fig. 81, which present η_{c*} of the F_2/Li system as a function of L* and mean lithium droplet size.

At 500-psia chamber pressure, lithium combustion occurs primarily in the first chamber section (item 7, Fig. 99). The actual residence time of the propellants in the first chamber section is nearly constant and independent of the amount of hydrogen injected or the throat size, provided the chamber pressure and the flowrates of fluorine and lithium are constant. Consequently, computation of effective L* for the first chamber section was based on the throat area which would give 500-psia chamber pressure when

fired at the nominal F_2/Li ratio (2.74) and total propellant weight flowrate (3.74 lb/sec), with zero hydrogen injection. As described below, the throat area required was 1.75 sq in.; with a 5-inch chamber diameter, this corresponds to a contraction ratio of approximately 11 and an effective L* of 180 inches.

It is apparent from Fig. 81 that increasing the effective L* of the first chamber section beyond 180 inches results in only minor gains in calculated combustion efficiency, even with lithium droplet sizes as large as 50 microns, whereas decreasing L* below 180 inches has an increasingly adverse effect. Hence, the 180-inch value, corresponding to a chamber length of 15 inches, was selected for the first chamber section. The 5-inch, second chamber section was designed to allow changes to be made in the overall L* during the experimental program by permitting use of 5-, 15-, or 20-inch combustion chamber lengths; the latter is shown in Fig. 99.

Chamber Materials

The F_2/Li combustion chamber upstream of the hydrogen injector is subjected to extremely high-temperature combustion products. Heat transfer calculations with the Bartz equation (Ref. 33) indicated that uncooled copper chamber sections would be satisfactory for 10-second firings. However, Rocketdyne experience with fluorine and other fluorinated oxidizers has shown that heat flux near the injector face is frequently much higher than values calculated from the Bartz equation and may, in fact, approach that at the nozzle throat. It has also been found that under these conditions and in the absence of water, ATJ graphite gives excellent service. Hence, this material was chosen for the combustion chamber sections in the form of 1.5-inch-thick cylindrical liners.

Compressible, porous graphite washers were used to accommodate stresses associated with thermal expansion of the graphite liners in the axial direction and asbestos sheet in the radial direction. Steel pressure shells were used for both chamber sections.

HYDROGEN INJECTOR

The hydrogen injector should introduce gaseous (ambient) hydrogen into the flowing F_2/Li combustion gases in such a manner that efficient mixing occurs in the chamber section downstream of the injector. This implies a requirement for maximum unformity of hydrogen distribution across the chamber, which may be satisfied by use of tranversely directed orifices arranged so that each one directly opposes another across the chamber. The impingement point of each pair of jets then becomes, in effect, a hydrogen injection point from which diffusion and turbulent mixing may begin. The principal advantage of this simple concept is its capability of providing uniform mixing without use of projections into the high-temperature gas stream.

Jet Penetration

The hydrogen injection concept was based on the premise that each of the gaseous hydrogen jets would be able to penetrate the F_2/Li combustion gases and impinge upon its opposing jet. To verify the penetration capability of gas jets, cold-flow schlieren photographs were taken to observe the penetration characteristics of high-velocity (650, 1300, and 2600 ft sec), 0.1-inch-diameter, helium jets into a low-velocity (155 and 310 ft sec), 2.0-inch-diameter gaseous nitrogen stream.

The schlieren experiments were used as a design basis for the hydrogen injector. Since it was uncertain whether jet breakup or jet turning is the limiting factor for gas jet penetration, methods based on both these phenomena were used to scale the He/GN_2 cold-flow results to the $H_2/(Li\text{-}F_2)$ hot firing situation. If jet turning were the limiting factor, the cold-flow results indicated that all hydrogen jets would penetrate the Li/F_2 combustion gas stream and form the patterns indicated in Fig. 116. This corresponds to a condition in which the hydrogen mass injection rate is 15 percent or more of the total propellant flowrate. On the other hand, if jet breakup were the limiting factor, the hydrogen injection rate must be at least 22 percent of the total propellant weight flowrate to produce the same results. The percentage of hydrogen injection required for complete penetration, therefore, is between 15 and 22 percent.

The hydrogen injector is expected to be an efficient mixing device at the higher hydrogen injection rates (22 to 40 percent); at the lower injection rates (15 to 22 percent) the mixing efficiency might possibly drop because the opposing hydrogen jets may not be ideally cylindrical but rather elongated and distorted when they impinge. Acceptance of possibly less satisfactory hydrogen jet penetration at the lower injection rates was the preferred choice over the following two alternatives:

1. Use of higher hydrogen injection velocities. The resultant flows at the higher injection rates would raise the requisite hydrogen supply pressure to prohibitive levels and, in addition, would produce underexpanded, "bushy" hydrogen jets.
2. Use of fewer hydrogen orifices, with increased diameter. This would provide better jet penetration capability, as indicated by Eq. 21. To maintain the same hydrogen injection velocity, a smaller number of orifices would be required. This would result in fewer hydrogen jet impingement points, which might degrade mixing efficiency.

Hydrogen Injector Design

The hydrogen injector design consisted of a ring-shaped copper segment with the same inside diameter as the combustion chamber and containing 64 transversely directed, 0.10-inch diameter orifices. The orifices were arranged in 32 directly opposing pairs (each of the 32 impingement points located approximately at the centroid of an area equal to 1/32 of the total chamber cross section) on four diameters separated by 0.4 inch, and successively rotated 45 degrees, as indicated in Fig. 117.

Estimation of the heat transfer rate to the hydrogen injector face and of the cooling capability of the hydrogen flow through the injector orifices indicated marginal face cooling in four injector areas where a relatively large gap between injection orifices exists. To improve this situation, eight 0.052-inch-diameter holes were provided for additional cooling on the upstream edge of the injector.

A copper spacer similar to the hydrogen injector, fitted with pressure taps but without orifices, was fabricated for use between the combustion chamber and the nozzle section in the F_2/Li firings.

MIXING CHAMBER

The function of the mixing chamber is to ensure that the hydrogen is uniformly mixed with the F_2/Li combustion products and that thermal equilibrium is attained. The material of construction was OFHC copper. Copper is suitable here because the temperature decreases markedly (from ~9800 to ~4000 R) after hydrogen is added.

NOZZLE SECTION

Selection of Throat Areas

The experimental firing program plan included variations in hydrogen flowrate over the range 15 to 40 percent of total flow. The planned variations in propellant flowrates in these firings required corresponding variations in throat area to maintain desired chamber pressures (Fig. 118). Ideally, a separate nozzle with the proper throat area would be constructed for each test condition. However, it is practical to utilize only a small number of nozzles to cover the range of test conditions. At some test conditions, therefore, chamber pressure or flowrate will be slightly different from the nominal values because the exact size nozzle is not used.

The criteria for selection of the nozzle throat areas were maintenance of chamber pressure at 500 psia and of total fluorine plus lithium flowrate at 3.74 lb/sec, corresponding to 1.0 lb/sec lithium flowrate at the design F_2/Li mixture ratio (2.74). The 500-psia chamber pressure criterion conformed to program plan requirements. The constant lithium flowrate criterion resulted from the need to maintain high lithium injector pressure drop and injection velocity to promote a high degree of atomization by the gaseous fluorine.

At a test condition consisting of a given F_2/Li ratio and hydrogen percentage, assumption of constant characteristic exhaust velocity results in the following proportionality:

$$\frac{P_c}{\dot{W}_{tot}} \propto \frac{1}{A_t}$$

Furthermore, since the F_2/Li ratio and percentage hydrogen are fixed for a given test condition, the total flowrate is proportional to the lithium flowrate, and the proportionality above becomes

$$\frac{P_c}{\dot{W}_{Li}} \propto \frac{1}{A_t}$$

A sufficient number of throats should be used such that the fraction $P_c/\dot{W}_{Li}$ would not vary significantly from its nominal value. For the test conditions required, the maximum variation in $P_c/\dot{W}_{Li}$ was calculated as a function of the number of throat areas to be constructed. These results are presented in Fig. 119, which shows that if two throat areas were used, the variation in $P_c/\dot{W}_{Li}$ from the nominal value would be approximately ±24 percent. Distributed evenly between chamber pressure and lithium flowrate, this means that the entire range of conditions could be tested within approximately a ± 12-percent variation in chamber pressure about the nominal 500 psia, and a ± 12-percent variation in $\dot{W}_{Li}$ about the nominal 1.0 lb/sec. If three throats were constructed, $P_c/\dot{W}_{Li}$ can stay within ±16.5 percent of the nominal value. A considerable gain (7.5 percent) is obtained in changing from two to three throats. With four throats, $P_c/\dot{W}_{Li}$ can stay within ±12.3 percent of the nominal value, a further gain of only 4.2 percent.

Three nozzles were fabricated; throat dimensions were as follows:

Nozzle	Throat Diameter, inches	Throat Area, $in.^2$	Contraction Ratio
1	1.48	1.72	11.5
2	1.74	2.38	8.3
3	2.05	3.30	5.9

The range for each of the three nozzles is shown in Fig. 120. Each has a ±16.5 percent variation of $P_c/\dot{W}_{Li}$ from the nominal value when used at the extremes of its range; when used at the middle portions of the ranges, the variation in $P_c/\dot{W}_{Li}$ from nominal would be less and, in fact, would at one point be zero.

Selection of Nozzle Material

The criterion to be met in the selection of nozzle material was the requirement that test duration should be at least 4.0 seconds (preferably longer to allow greater test sequence flexibility). Candidate nozzle materials, on the basis of substantial Rocketdyne experience with fluorinated oxidizers, were copper and graphite.

A transient heat transfer analysis was carried out on the nozzle; the Bartz equation (Ref. 33) was used to calculate throat heat transfer coefficients, and the techniques given in Ref. 34 were used to obtain the transient solution of the time-dependent heat conduction equation. It was assumed for these calculations that initial temperature of the copper nozzle was 100 F and that maximum run duration corresponded to the time required for the inside surface temperature to reach 1250 F. Figure 121, which summarizes the results for the copper nozzle, shows that maximum run duration would be about 2.2 seconds. Since this is considerably below the desired level, copper was rejected as a possible nozzle material. The variation of allowable operating time of the copper nozzle over the total range of hydrogen addition is quite small due to the fact that throat heat flux decreases by only about 35 percent as the amount of hydrogen increases from 0 to 40 percent and chamber temperature decreases correspondingly from 9800 to 3500 R. Heat flux remains relatively constant despite the wide variation in gas temperature primarily because of the compensating change in gas heat capacity (0.40 B/lb-R to 1.93 B/lb-R).

Rejection of copper as the nozzle material pointed to the selection of graphite in its place. The graphite nozzle heat transfer analysis was the same as for the copper nozzle except that initial temperature was assumed to be 500 F and final inside surface temperature to be 4000 F. The first assumption is conservative, although hot gaseous fluorine from the fluorine gas generator would raise the nozzle temperature above ambient. Figure 122 presents the transient heat transfer analysis results for the cases of 0-, 10-, and 20-percent hydrogen addition. Hydrogen addition of 10 percent or more easily allows run durations in excess of 4.0 seconds at chamber pressure of 500 psia; however, only short runs are possible when no hydrogen is added at 500-psia chamber pressure. Fig. 123, obtained from the same analysis, shows that lower initial graphite temperatures result in only relatively small increases in allowable run duration, even when the nozzle is prechilled to -200 F.

The nozzle section of the thrust chamber (Fig. 99) consisted of an ATJ graphite liner enclosed in a steel shell. A compressible, porous graphite washer and an asbestos outer liner were included, as in the chamber sections, to accommodate thermal stresses. The steel shell was tapered to retain and seal the liner.

EXPERIMENTAL EVALUATION OF FLUORINE-RICH GAS GENERATOR

A fluorine-rich gas generator was designed to provide the high-velocity gases which accomplish liquid lithium atomization. The nominal design operating conditions were 700-psia chamber pressure and 500:1 F_2/H_2 mixture ratio. Since this was a new type of gas generator, it was considered necessary to carry out a series of experiments to ensure its proper operation.

Accordingly, sixteen experiments were conducted, with the following objectives:

1. To demonstrate feasibility;
2. To investigate the effects of varying operating conditions on hardware durability and gas temperature. The operating variables were to be F_2/H_2 mixture ratio, chamber pressure, and duration;
3. To investigate the effects of thrust chamber geometry and thermal condition. The geometric variables to be studied were chamber length and the presence of mixing plates. The thermal condition of the exit plate (which simulated the stainless-steel triplet injector) was varied by preheating this component. This variable was investigated primarily because of the dependency of fluorine-steel compatibility on metal temperature.

The gas generator experimental conditions and performance results are summarized in Table 9. Performance was monitored by measuring chamber

pressure and propellant flowrates and computing the resultant characteristic exhaust velocities and also by measurement of gas temperatures with thermocouples inserted into the combustion chamber through the mating flange just upstream of the exit plate. Three thermocouples were located in the same plane at differing radial positions: (1) centerline of the chamber (2 inches from the wall) (2) 1-1/4 inches from the wall, and (3) 1/4 inch from the wall.

The first three tests were short-duration runs intended to check out the hardware and design concept. These firings conclusively established the feasibility of utilizing a fluorine gas generator to provide a hot fluid for atomizing liquid lithium jets. Combustion gas temperature was not measured, however, due to thermocouple burnouts. Prior to the second series of tests, a mixing plate was installed in the first chamber segment to provide a more uniform radial gas temperature profile.

The second test series (runs 4 to 6) was intended to verify long-duration capability of the gas generator at design mixture ratio and to provide reliable measurements of c* performance and combustion gas temperature. A maximum duration of 10.6 seconds was attained and no hardware damage resulted. Performance measurements consistently exceeded theoretical values, but this may be attributed to imprecision of hydrogen flowrate measurements, reflected in the determination of mixture ratio. Measured gas temperature is the average of three thermocouple readings, and for tests 5 and 6 compares very favorably with theoretical predictions. These results indicate that the hydrogen reacted completely and that all of the liquid fluorine was vaporized.

The first six gas generator tests employed a 10-inch long chamber. In the first three, no gas mixer was installed in the first 5-inch chamber

segment. Three additional tests (7 through 9) were carried out in which only the 5-inch chamber (containing the mixer) was employed to determine combustion efficiency in the short chamber; also, lower mixture ratios were used to obtain higher gas temperatures. No difficulties were experienced in these 10-second firings, and there was no hardware damage. Performance efficiency remained at 100 percent within the precision limitation of the very low hydrogen flowrate measurements. In the 5-inch chamber, measured gas temperature downstream of the mixer showed approximately a 20-percent spread from the lowest value (at the center of the chamber) to the highest (at a point 1/4 inch from the wall); this compares to an average 10-percent spread in the 10-inch chamber. In all cases, average gas temperature is close to theoretical. A mixer plate was then installed in the second chamber section also, and subsequent radial variations were less than 5 percent.

The effects of chamber pressure and mixture ratio on hardware durability and gas temperature were determined during tests 10 through 16. The chamber pressure range was approximately 350 to 720 psia; the mixture ratio range was about 370 to 660. In addition, during the last three tests (14 through 16), the exit plate was preheated to about 500 F (simulating the triplet injector firing condition) to determine whether a fluorine-steel compatibility problem would occur.

As indicated in Table 9 , the performance of the gas generator followed the theoretical trends in terms of changes in temperature with mixture ratio over the ranges of chamber pressure and mixture ratio covered and no hardware damage was observed. The final resulting plot of temperature vs mixture ratio is presented in Fig. 124, which shows excellent agreement between experimentally observed temperatures and the theoretical values.

These experiments demonstrated the gas generator chamber geometry and operating conditions required for the production of (essentially) gaseous fluorine at high temperatures and pressures over long durations, and hence its feasibility for the $F_2/Li/H_2$ firings.

LIQUID LITHIUM FACILITY AND FLOW CHARACTERIZATION

The objectives of this subtask were first to design and build a facility for storing, heating, and delivering liquid lithium to the experimental thrust chambers, and then to conduct a series of lithium flow tests to check the operation of the various system components and to characterize the flow of liquid lithium through small orifices.

LIQUID LITHIUM FACILITY

Design, installation, and operational checkout of a liquid lithium system for use in experimental rocket motor firings constituted an important part of the overall program. Major system requirements were as follows:

1. Capability for storage of at least 20 pounds of liquid lithium
2. Capability for system heating, to melt solid lithium and to maintain the liquid at equilibrium temperature of 500F
3. Capability for liquid lithium flow control and flowrate measurement
4. Provision of a heated helium purge gas subsystem
5. Capability of pressurization to 1000 psi with filtered, moisture- and oxygen-free helium

Austenitic stainless steel (304) was selected as the basic structural material for the lithium system because it is compatible with hot liquid lithium, has suitable structural and thermal properties, and is readily available and machineable. The installed system, illustrated schematically in Fig 125, consists of the following major components.

Lithium Tank

This is a 4-foot length of 6-inch, schedule 80, 304 stainless-steel pipe, with welded, ASA, ring-sealed, flanged ends. The tank volume is approximately 6.7 gallons. It is ASME coded and approved for 1145 psi at 600 F. A boss in the tank wall near the lower flange accommodates an immersion thermocouple. The upper flange contains a single port to which both the pressurization and vent systems are joined, and the lower flange has a single outlet port.

Valves

The three valves (lithium main, purge, and vent) which might contact liquid lithium are special, 1-inch, bellows-sealed, globe valves constructed entirely of 300-series stainless steels*. The valve seat is machined directly into the body to eliminate the need for a valve seat insert. The other two system valves (pressurizing valve and freeze water valve) are conventional Annin globe valves.

Flow Line

The 1-inch line (304 stainless steel, schedule 10) between the lithium tank and main valve has welded joints to eliminate leakage hazards, and is U-shaped to compensate for thermal changes. An in-line, stainless-steel screen filter (0.018-inch mesh) is installed in the main flow-line downstream of the main valve and purge line connection point.

*Manufactured by Wm. Powell Co., Cincinnati, Ohio

Flowmeter

Lithium flowrate is measured by a magnetic flowmeter (MSA Model FM-4) welded into the flow line. The flowmeter consists essentially of a 1-inch, schedule 10, 304 stainless-steel pipe within a permanent 890-gauss magnet. The d-c voltage generated by flow of lithium through the line is a direct measure of the flowrate. Suitable heating elements, a chromel-alumel thermocouple, and complete insulation are integral parts of the flowmeter unit.

The original design of the lithium system included a turbine flowmeter in the line between the magnetic flowmeter and the main valve. During preliminary tests, however, reliable flowrate measurements could not be obtained with the turbine meter, hence it was not used in the present investigation.

Freeze Jacket

An emergency "freeze" jacket around an 8-inch section of the line, with inlet and outlet ports for water flow, is included in the lithium line downstream of the magnetic flowmeter. In the event of line or valve failure downstream of the jacket during lithium flow, a plug of solid lithium can be formed in the line by water-cooling of the jacketed section.

Helium Purification System

To avoid introduction of significant amounts of impurities (such as water, oxygen, or particulate matter) into the lithium system with the

pressurant gas, a dryer (artificial Zeolite molecular sieve), a de-oxygenator (heated copper turnings), and a 10-micron filter are included in the helium supply line.

Check Valves

Specially designed stainless-steel ball check valves incorporating Inconel tension springs downstream of possible lithium flow are used in the lithium system.

Purge Gas System

The purge gas heater consists of a 4-foot length of 2-inch-diameter schedule 40, stainless-steel pipe filled with 0.25-inch steel balls. It supplies 500 F minimum helium for at least 10 seconds at nominal flowrates when initially heated to about 1000 F.

Heating System

Heating of the lithium system is accomplished by means of externally mounted electrical resistance heaters. Radiant-type heaters are used for the tank (Lindberg "Hevi-Duty", Model 50731) and for the purge gas line (Lindberg Model 50031). The lower tank flange, flow line and main valve are heated by wrap-around cable (Chromalox "Thermwire", Type TWM-20) embedded in "Thermon" heat conducting cement, and the lower tank flange is also heated by "Calrod" cartridge units. The helium de-oxygenator is heated by two 500-watt Watlow "Firerod" cartridge units.

For control purposes the heater electrical system is divided into four sections: one 230-volt, 3-phase, 12 kw source and three 120-volt, single-phase, 3 kw sources. The power from each source is varied independently by means of manually controlled variable transformers. Heatup rates are reproduced by current control through each transformer. The power sources terminate in plug-in connectors at the test stand to permit convenient tie-in of the heating units.

Thermocouples are used to monitor temperatures at various points of the lithium system. These include two immersed in the liquid (one in the tank and one immediately upstream of the injector) and nine externally welded to the tank body, lower tank flange, magnetic flowmeter, flow line (2), main valve, purge gas heater, purge gas line, and delivery line to the injector. Two of the thermocouples are used for automatic temperature control of the magnetic flowmeter (Foxboro "Rotax" controller) and the main valve (Wheelco controller).

The heated portion of the lithium system is insulated with fiberglass insulation overwrapped with aluminum foil. The entire system is mounted on a frame to make it portable for cleaning or storage. The system, with upper tank flange removed, is shown in Fig. 126 and 127.

Lithium System Loading and Operation

Lithium is purchased in the form of 1-pound or 2.7-pound cylindrical ingots individually packed in cans in an inert atmosphere. The cans

are opened and the tank is loaded with the desired number of ingots in an argon atmosphere. A small amount of metallic sodium (0.5 weight percent) is added between the ingots to improve the wetting capabilities of the lithium (proper line wetting is essential for accurate operation of the magnetic flowmeter).

System heating begins at the tank and the lower tank flange. After these reach approximately 300 F, the line and the main valve are successively heated. The purge gas heaters are activated simultaneously with those of of the main valve. When the lithium system reaches approximately 500 F and the purge gas heater reaches about 1000 F, the power inputs are reduced to maintenance levels. Starting at ambient temperature, about 3 hours are required to accomplish the heating process. The helium line de-oxygenator is heated from ambient to 500 F in about 30 minutes.

System pressurization and pressure regulation are carried out with motorized loaders and dome-type regulators in the customary manner.

LIQUID LITHIUM FLOW TESTS

A series of lithium flow tests was conducted with two primary objectives: (1) to make operational checks of the various lithium system components and procedures, and (2) to study the flow of lithium through orifices whose diameters and discharge inclinations typified those of a hot-firing injector.

The experimental series consisted of the following eight tests:

Test Number	Description
1 and 2	Flow at tank pressure and flowrate equal to those of anticipated hot firings
3 through 7	Flow through single orifices into argon-filled vessels
8	Flow through a single, self-impinging doublet element into argon-filled vessel

Lithium System Checkout

The lithium system loading and operational procedures were found to be generally satisfactory. Details of the various subsystem and component functions are described below.

Valves. Operation of the bellows valves was satisfactory although some installation difficulty was experienced in obtaining leak-free seals at the serrated rings between the upper and lower valve bodies. Opening time of the lithium main valve when pressurized to 750 psi was about 85 msec; closing time was about 40 msec.

Although the main valve functioned satisfactorily, it was found that if there was an extended time period (over ten days) between valve actuations unpredictable valve behavior occurred. Under these circumstances, excessive valve opening time delays (1 second or greater) were encountered, especially during the first attempt at valve opening. This problem was circumvented by system heatup on the day preceding the actual test

firing, and actuating the valve until the opening and closing times were as noted above.

Heaters. The heaters and heater controls functioned satisfactorily and predictably.

Flowmeters. Flowrates indicated by the magnetic flowmeter were in good agreement with rates calculated from orifice C_D values obtained from water calibrations and rates estimated from catch tank weight increases.

The turbine flowmeter produced excellent water calibration results and appeared to be functioning properly when it was installed in the lithium line. During the flow tests, however, its behavior was very erratic; the output would usually peak at the start of the flow, then immediately return to zero. Although the meter was not used, its removal from the system was impractical and it was left in place.

Purge Gas System. The purge gas heater functioned satisfactorily.

System Operation. Procedures for lithium loading, system pressurization, and conducting purge gas and lithium flow tests were found to be satisfactory.

Lithium Flow Test Results

A three-step test procedure was initiated following system warm-up to 525 ±25 F (with purge gas heater at 1000 ±50 F). This consisted of the following: purge gas flow (2 to 5 seconds), lithium flow (3 to 9 seconds), and purge gas cycling.

Tests No. 1 and 2. These tests were made at lithium flowrate (1 lb/sec) and tank pressurization level (750 psi) equivalent to those expected in the hot firings. Test objectives were to check valve operation and lithium flow under these conditions. A 1/2-inch line terminating in a suitably-sized orifice was positioned downstream of the main valve. In Test No. 1, the lithium flow was directed into a covered, 25-gallon steel drum in which an argon atmosphere was maintained; in Test No. 2, the lithium was allowed to flow out to atmosphere (igniting after emergence from the line). No anomalies were encountered in these tests, and it was concluded that the system was capable of furnishing lithium at the temperature and flowrate needed for the experimental firings.

Tests No. 3 and 7. These tests were made to obtain photographic recording of liquid lithium flow through orifices of various sizes and orientations, primarily to aid in providing design criteria for the lithium injector. Stainless-steel injector segments were used, each of which contained three identical nonimpinging orifices (Fig. 128). Cartridge heating elements (500 w) were fastened to the test segments to heat them to 500 F. The injector segment being tested was placed in a covered, 6 x 12 x 26-inch, steel catch tank, between two Lucite windows, one for backlighting and one for photography (Fastax camera, 800 to 1000 frames per second, Kodak Ektachrome EF-7242 film). A stream of argon was maintained through the catch tank, prior to and during the lithium flows.

At a 300-psi pressure differential, it was found that steady flow at approximately the calculated rates could be maintained through 0.043-inch orifices but that sustained steady flow was not obtained through 0.031-inch orifices. This may have been due to blockage by solid particles of lithium oxide or nitride, since two of the three orifices were found

closed after the test. With the 0.043-inch orifices, discharge angles of 45 and 90 degrees with respect to the segment face gave free-flowing streams, while a 30 degree angle produced noticeable adherence of lithium to the face. A typical lithium flow test (Segment No. 15, d = 0.043 in, α = 90 degrees) is shown in Fig 129.

As a result of these tests and of lithium injection requirements for minimum orifice sizes consistent with full, non-adhering flow at ΔP of about 300 psi, orifices of 0.043-in diameter and 45 degrees inclination were selected for the first lithium injector.

Test No. 8. The final lithium flow test of the series was made with a single, self-impinging doublet element (orifice diameter = 0.043 inch, impingement angle = 90 degrees). The purpose of this test was to obtain photographic visualization of the spray formed by the lithium streams, for qualitative comparison with that typical of impinging Cerrosafe streams, since experimental results derived from the latter were the bases for important lithium injector design criteria. The lithium spray was directed into an argon-filled vessel fitted with Lucite windows, and strobe-lighted motion pictures (1000 frames per second, 1 microsecond flash per frame) were taken. Figure 130 shows enlarged single frames of both lithium and Cerrosafe sprays. Similar primary atomization into ligaments and large drops is evident, lending support to the application of Cerrosafe droplet size correlations to lithium atomization.

TASK II

EXPERIMENTAL FACILITIES AND PROCEDURES

TEST FACILITY

Since a detailed description of the liquid lithium system has been given previously, only the fluorine and hydrogen facilities will be discussed in the present section. The experimental firings were carried out at the Propulsion Research Area of SSFL. A schematic diagram of the fluorine system, which is rated at 3000 psi, is shown in Fig. 131. Fluorine gas, supplied from a manifolded system of fifteen, 6-pound, GF_2 cylinders, is liquefied in an LN_2-jacketed condenser and fed to a jacketed, 15-gallon, cylindrical run tank. A dip-leg tank outlet is used, leading to a jacketed shutoff valve and delivery line. A jacketed, three-way, main valve and a jacketed line between the valve and the injector ensure delivery of liquid fluorine to the oxidizer manifold.

The hydrogen system (Fig. 132) consists of two branches, one to the gas generator (with flowrates of 0.005 to 0.009 lb/sec) and the other to the main combustion chamber (0.7 to 2.5 lb/sec). Each branch includes three parallel valves and venturi meters. By successive operation of these valves, several discrete hydrogen flowrates, both to the gas generator and to the main chamber, can be obtained in the course of a single firing. This capability of obtaining several data points per run proved to be of substantial value in the course of the experimental program.

INSTRUMENTATION

Instrumentation locations are schematically indicated in Fig. 133. The particular transducers used for the various types of measurement are described below.

Thrust

The thrust chamber mount was supported on flexures which allowed free movement parallel to the engine axis, restrained in the thrust direction by a Baldwin-Lima-Hamilton double-bridge load cell (Model U-382).

Pressure

All pressures were measured with bonded strain gage transducers (Taber Teledyne Series 206). Chamber pressures were determined at several axial locations both in the gas generator and in the main combustor. At each location 2, 3, or 4 circumferential pressure taps were manifolded together, and the manifold pressure was measured. The other pressure measurements shown in Fig.133 were made with close-coupled transducers at each location.

Flowrate

Hydrogen. Hydrogen flowrates were measured with sonic venturi meters (Flow-Dyne Model Series V-16).

Fluorine. Two turbine flowmeters in series (Fischer-Porter Model RF-1-50) were used to measure volumetric fluorine flowrates.

Temperature

Fluorine. Liquid fluorine temperature was measured by two shielded, platinum resistance bulbs (Rosemount Model 176) immersed in the liquid stream, one upstream of the first flowmeter and the other downstream of the second.

Hydrogen. Temperatures in the venturi plena were measured with iron-constantan thermocouples.

Chamber. Temperatures in the gas generator chamber and in the wall of the combustion chamber were measured with chromel-alumel thermocouples.

Data Recording

Pressure, temperature, and flow measurements were recorded on tape during each firing by means of a Beckman Model 210 Data Acquisition and Recording System. This system acquires analog data from the transducers, which it converts to digital form in binary-coded decimal format. The latter are recorded on tapes for computer processing.

The Beckman Data Acquisition Unit sequentially samples the input channels at a rate of 5625 samples per second. Programmed computer output consists of tables of time vs parameter value (in engineering units), printed out as either the instantaneous values at approximately 10-millisecond intervals during the firing or as average values over prespecified time slices, together with calibration factors, prerun and postrun zero readings, and related data. The same computed results are also machine plotted and displayed as CRT outputs on appropriately scaled and labeled grids.

Primary data recording for these firings was on the Beckman 210 system. In addition, the following auxiliary recording systems were employed:

1. An 8-channel Brush Mark 200 recorder was used in conjunction with the Beckman unit to establish time intervals for data reduction and for quick-look information at the most important parameters.
2. A CEC, 36-channel, direct-reading oscillograph was used as backup for the Beckman 210 System for indication of possible oscillatory combustion and for precise recording of firing-event timing.
3. Direct-inking graphic recorders were used to set prerun propellant supply pressures, for monitoring fluorine system chilldown and lithium system heating, to provide quick-look information, and as secondary backup to the Beckman and oscillograph recorders.

CALIBRATION PROCEDURES

Transducer calibrations were used not only to obtain appropriate factors for test data reduction, but also to develop statistical histories of each transducer so that estimates of short- and long-term deviations could be made and probable error bands calculated (see Appendixes B and C for detailed discussions). The calibration methods used for the various types of transducers are described below.

Thrust

The thrust-measuring load cell was calibrated in-place. A permanently mounted, manually operated, hydraulic force cell was employed which deflected the load cell exactly as did the engine, through a yoke-tension rod system. Known loads were applied to the force cell through a Morehouse compression-type, temperature-compensated, proving ring calibrated by the National Bureau of Standards (NBS).

Pressure

Pressure transducers were calibrated by mounting them on stand manifolds in which pressures were read with high-precision Heise Bourdon-tube gages. The latter were calibrated periodically on Ruska dead-weight testers with weights traceable to NBS standards.

Flowrate

Fluorine. Calibrations of the turbine flowmeters to obtain volume flowrates as functions of rotational speeds were made with water. Transfer of these cycles-per-gallon factors to liquid fluorine usage requires application of corrections which allow for the differences in temperature

and viscosity between water and LF_2. The temperature correction (70 to -310 F), which is a function of meter material and not of meter size, has been estimated as 1.005 (Ref. 35) and 1.009 (Ref. 36), average: 1.007. The viscosity correction, which is a boundary layer phenomenon and therefore depends on flowmeter size, was estimated as 0.992 (1-inch meter, Ref.35), so that the net correction applicable to the water calibration factors was (1.007 x 0.992), or 0.999. This was within the readability limits of meter output and was therefore considered negligible. Hence, volumetric flow factors determined with ambient-temperature water were used for liquid fluorine without correction.

Hydrogen. The sonic venturi meters were calibrated with hydrogen by the manufacturer.* Mass flowrate was determined from the following equation:

$$\dot{W} = \frac{KP}{\sqrt{T}}$$

The calibrations established curves which gave values of K as functions of gas pressure and temperature at the venturi inlet. The flow coefficient curves were calculated from the ASME equations (Ref. 37).

Calibration procedures for the pressure and temperature sensors used in conjunction with the venturi meters are described in other parts of this section.

*Flow-Dyne Engineering, Inc., 3701 W. Vickery St., Fort Worth, Texas 76107

Lithium. The magnetic flowmeter was calibrated for lithium by the manufacturer* to establish the variation of the flowrate factor (gpm/mv output) with temperature. A Leeds & Northrup Type K potentiometer was used to calibrate the amplification-recording circuits.

Temperature

Resistance Thermometers. Resistance of the platinum thermometers used in the LF_2 line was converted to millivolt output by a triple-bridge system. This was calibrated by substituting a decade resistance box for the sensor, and setting it at various resistances corresponding to a temperature-resistance calibration supplied by the manufacturer** for each instrument. These precision platinum resistance sensors have no significant calibration drift. They were checked upon receipt by immersion in liquid nitrogen and liquid oxygen; temperature readings were correct within the limits of readability.

Thermocouples. Thermocouples were used on the basis of the standard NBS millivolt/temperature tables. Thermocouple recorders were electrically calibrated.

Calibration Frequency

The thrust load cell was calibrated immediately before every firing. Pressure transducers were calibrated at intervals dictated by the Measurement Analysis Program (Appendix B). The magnetic flowmeter, fluorine flowmeters, venturi meters, and resistance thermometers were calibrated just before the start of the experimental firings.

*MSA Research Corp., Evans City, Pa.
**Rosemount Engineering Co., 4900 West 78th Street, Minneapolis 24, Minn.

FIRING PROCEDURES

Fluorine System Passivation

Prior to assembly, fluorine system components were thoroughly cleaned in accordance with standard prescribed procedures (Ref. 30). Passivation of the assembled system (to main oxidizer valve) by provision of protective fluoride films on exposed surfaces was carried out as follows: low-pressure gaseous fluorine was introduced into the system and maintained for successive 15-minute periods at 5, 10, and 15 psi; finally, 20 psi was maintained for several hours.

The feed line-thrust chamber system downstream of the main valve was passivated immediately before firing by flowing fluorine through the system for several short intervals of time.

Run Procedure

Prerun and postrun zeros were taken with the fluorine and lithium inlet lines at run temperatures (-310 and 600 F, respectively) to avoid line temperature effects on thrust zero-point readings.

Firings were controlled by an automatic electronic timer; the sequencing is indicated in Fig. 134. For the gas generator both startup and shutoff were oxidizer-rich, while in the main combustion chamber there was a hydrogen lead (over the lithium) at startup and a corresponding hydrogen lag at shutoff. The purpose of the preliminary hot helium purge was to heat the lithium injector tubes. The three steps in the main hydrogen flow indicate operation of the three main valves for attainment of three discrete run levels.

EXPERIMENTAL EVALUATION OF LITHIUM-FLUORINE-HYDROGEN COMBUSTION

The original Task II experimental program plan consisted of two phases: Phase I, involving F_2/Li injector design characterization and Phase II, involving evaluation of tripropellant performance.

The objectives of Phase I were to confirm that performance efficiency was a function of the degree of lithium atomization and to define injector design criteria in terms of F_2 gas jet momentum and orifice size under actual hot-firing conditions. These data were to be used for final design of an injector with demonstrated high performance so that if tripropellant inefficiencies were observed, the losses would not be erroneously attributed to incomplete formation of lithium fluoride.

The objective of Phase II was to evaluate tripropellant performance as a function of chamber volume, percent hydrogen added, and hydrogen injection station. These tests were to be conducted at optimum F_2/Li mixture ratio (2.74) and nominal chamber pressure of 500 psia. Thus, the primary objective of Phase II was to determine the efficiency of the hydrogen-combustion gas mixing process as a function of the above-mentioned variables.

However, because of operational difficulties and initial hardware damage, no significant data were obtained in Phase I and it was necessary to proceed directly to Phase II without the injector design information desired from Phase I. However, the lithium/fluorine injector design that was employed, which was based entirely upon cold-flow and analytical results, proved to be satisfactory. It produced nearly theoretical F_2/Li combustion efficiency.

Each of the eleven firings conducted is separately discussed in the section below. This is followed by a general discussion and graphical display of the experimental results.

EXPERIMENTAL RESULTS

Individual Test Descriptions, Phase I

Run No. 1. The objectives of this test were to check out the facility and to evaluate the F_2/Li triplet injector design. Target conditions and parameters for this firing were as follows:

Chamber Length, inches (injector face to start of nozzle convergence)	= 17
$\dot{W}_{LF_2}$, lb/sec	= 2.74
$\dot{W}_{LLi}$, lb/sec	= 1.00
$\dot{W}_{GH_2}$, lb/sec	= 0.0055
MR (F_2/H_2)	= 495
MR (F_2/Li)	= 2.74
T_{GG}, R	= 960
P_{GG}, psia	= 370
P_c, psia	= 235 (90 percent η_{c*})
F, lbf	= 1045 (90 percent η_{I_s})

The planned firing sequence was to consist of: (1) gas generator operation for 3 seconds, (2) combined gas generator and F_2/Li firing for 2 seconds, and (3) an additional 2.5 seconds of gas generator operation only. Both the lithium purge (hot helium) and a GN_2 purge through the chamber pressure taps were to be on throughout the firing, except during portion (2).

Prior to the firing, the fluorine manifold and injector were passivated by pressurizing the LF_2 tank and opening the fluorine main valve for three 1-second intervals. The firing was initiated with an oxidizer-rich

startup of the gas generator; fluorine flowrate (3.2 lb/sec), hydrogen flowrate (0.006 lb/sec), gas generator chamber pressure (355 psia), and temperature (910 R) were close to targeted values when steady-state conditions were reached (in ~2 seconds). After 3 seconds of gas generator operation, during which a hot helium purge was maintained through the lithium system, the lithium purge valve was closed. The lithium main valve was programmed to open simultaneously. However, there was no indication that it did open; the lower valve stem-travel microswitch was not actuated nor was any lithium flow shown by the magnetic flowmeter. For 2 seconds, therefore, the lithium purge was off and the gas generator was in operation without mainstage combustion. At the end of this time the lithium purge valve was opened (with the programmed simultaneous closing of the lithium main valve), whereupon a burnthrough occurred in the lithium injector and the test was manually terminated.

Significant damage from the burnthrough was confined to the lithium injector, which was irreparable. Examination of the lithium injector showed that about one-third of the face was burned completely through to the back, and that reaction probably began in the manifold. On the part that was not burned through, the fluorine orifices were eroded into cone-shaped openings with bases at the face, indicating that this burning progressed from the gas side into the main injector body. When the lithium delivery line was removed, traces of lithium nitride were found near its exit, indicating that a small amount of lithium had passed through the lithium main valve, even though the travel microswitches on the valve stem had not been actuated and the magnetic flowmeter showed no discernible lithium flow.

The following appears to be the most probable course of events preceding the injector burnthrough: when the lithium purge was shut off and the lithium main valve did not simultaneously open, gaseous fluorine diffused into the lithium injector manifold; the lithium valve opening was delayed until just before the signal to close was given so that the stem was barely

lifted from its seat; the very small amount of lithium which passed through the valve was atomized by the helium purge which immediately followed it and was carried into the lithium manifold, where ignition with the fluorine already present resulted in the burnthrough.

Several postrun checks of the lithium valve were made to investigate its operation since its physical removal for inspection was impractical. In the earlier lithium flow tests, time elapsed from open signal impulse until actuation of the lower valve stem microswitch (indicating start of opening) was ~120 milliseconds; time between lower and upper microswitch actuations (considered to be the valve opening time) was approximately 85 milliseconds. This compares with the delay of nearly 2 seconds observed in the F_2/Li firing. To investigate the timing of the valve, it was cycled a number of times on the day following the firing. The timings observed during these cyclings indicated that several cyclings of the valve were needed to establish normal operational timing after a period of inactivity, possibly because of initial delays in the functioning of the bellows around the valve stem. They also pointed to a requirement for establishment of normal valve timing by cycling the valve immediately prior to a firing.

Run No. 2. The following changes were made in the test procedures to avoid possible recurrence of the lithium valve malfunction and injector burnthrough:

1. After warmup of the lithium system to 500 F, the lithium main valve was cycled three times (with lithium flow to atmosphere), in the last two of which the time elapsed from valve signal to valve liftoff (130 milliseconds) and from valve liftoff to open position (85 milliseconds) were in the normal range.
2. Temperatures of the preheated lithium injector and of the helium purge gas were reduced from 550 to 450 F and from 1000 to 700 F, respectively, to lessen the possibility of ignition of the injector body by fluorine.

3. Closing of the lithium purge valve was slaved to actuation of the upper microswitch on the stem of the lithium main valve so that purge pressure would be maintained until the main valve was fully open.

4. A sampler circuit was installed to check the load cell output at a programmed instant in the firing so that the run would be cut if thrust were below a preset level.

5. Automatic run cut could also be triggered by discontinuity in a fine wire wound around the oxidizer system and injector such as would be caused by a serious fluorine leak.

Target conditions for the second firing were the same as for run No. 1.

Because of contact malfunction in one of the channels of the electronic timer used to sequence firing functions, two attempted firings preceded the actual test. The timer malfunction in the two aborted runs resulted in premature closing of the fluorine valve during gas generator operation prior to opening of the lithium valve. This was followed by automatic cutoff by the thrust sampler circuit 0.3 second after opening of the lithium valve. Run No. 2 was carried out following rectification of the timer malfunction and sequencing occurred as programmed. This firing was manually terminated after 1.5 seconds of lithium flow when failure of a check valve in the fluorine purge system released some fluorine into the test pit.

Postfiring examination of hardware, test data, and motion pictures showed that the center portion of the lithium injector was burned out, and that this burnout occurred during the first part of the run before lithium valve opening. Consequently, no usable performance data were obtained. The posttest examination also indicated that the premature closing of the fluorine valve in the preceding two firing attempts resulted in high-temperature transients which subjected the gas generator chamber and the

lithium injector to substantial overheating. Although no external hardware damage was visible after these attempts, close inspection was not possible because of the presence of lithium in the chamber and nozzle as well as on the test pit floor. Hence, the condition of the lithium injector after the aborted tests is not known.

Run No. 3. Test objectives and target run conditions for the third firing were the same as for the first two. In this firing, however, the graphite-core, doublet-pattern lithium injector was used because a triplet was not available.

Prerun preparations included the customary lithium system heatup and cycling of the lithium main valve to ensure proper functional timing. It was observed at test start, during operation of the gas generator, that the fluorine flowrate was significantly below the expected level. The run was therefore manually cut after 2.5 seconds of F_2 H_2 firing (prior to opening of the lithium main valve). No hardware damage occurred.

Examination of the liquid nitrogen system used to chill the fluorine system and a series of blowdowns using liquid oxygen as fluorine simulant indicated that the liquid nitrogen flowrate through the jacket around the fluorine line between the tank and main valve was not adequate on exceptionally hot days to prevent partial gassification of fluorine within the line. Suitable modifications were accordingly made in the liquid nitrogen system to permit attainment of a sufficient degree of line chill even during hot-weather conditions.

Run No. 4. This was the first firing in which F_2 Li combustion data were obtained. Target run conditions and test sequence were the same as in previous runs; the graphite-core, doublet-pattern injector was used.

The firing was cut by the thrust sampler circuit at the 5.3-second point, after 0.8 second of lithium flow, because thrust had not reached the preset minimum level. This was due to low lithium flowrate, as shown in the tabulation below. The table gives expected and observed levels of operating parameters during both the preliminary gas generator operation and the F_2/Li firing. The agreement between targeted and experimental values is good in all cases except for lithium flowrate and, hence, for the F_2/Li mixture ratio.

Parameter	Gas Generator Alone		Gas Generator and Lithium Flow	
	Target	Experimental	Target	Experimental
Liquid Fluorine Flowrate, lb/sec	2.97	2.85	2.74	2.60
Gaseous Hydrogen Flowrate, lb/sec	0.0055	0.0054	0.0055	0.0054
F_2/H_2 Mixture Ratio	537	528	493	482
Liquid Lithium Flowrate, lb/sec			1.00	0.25
F_2/Li Mixture Ratio			2.74	10.4
Gas Generator Pressure, psia	290	303	314	311
Gas Generator Temperature, R	870	850	960	
Chamber Pressure, psia			235	109
Thrust, pounds			1045	400
Experimental Characteristic Velocity, ft/sec			4090	
Theoretical Characteristic Velocity, ft/sec			4400	
Uncorrected Characteristic Velocity Efficiency, percent			93	

The graphite injector body was intact after the firing, and the fluorine orifices were not significantly enlarged. Six of the eight lithium delivery tubes in the injector were found to be plugged with solidified lithium after the firing. Analysis of the contents of the plugged tubes showed a significant degree of lithium contamination (approximately 4 percent).

To remove the contaminants, which had accumulated during repeated contact of molten lithium with impurities, the lithium system was emptied and thoroughly cleaned. In addition, a series of tests was carried out to determine whether the blockage resulted from clogging of the tubes by contaminants in the lithium or from inadequate heating of the tubes prior to the firing. Blowdowns with both hot helium and lithium were made through the ring manifold and lithium injector tubes. The manifold was preheated electrically, while the delivery tubes were preheated prior to lithium flow with a heated helium purge. These experiments indicated that the tubes were adequately heated by the hot purge gas under firing conditions (5-second flow of 1000 F helium). At this time, an in-line, stainless-steel, screen filter (0.018-inch mesh) was installed in the lithium delivery line to remove any residual impurities.

Although lithium flow was delivered through only two of the eight injector tubes, which resulted in poor propellant distribution, F_2, Li combustion efficiency was over 90 percent, indicating promise of high combustion efficiency under design operating conditions.

Individual Test Descriptions, Phase I'

Run No. 5. At this point in the program, the decision was made to proceed to the Phase II tripropellant firings, in which the graphite doublet injector would be used. It was recognized that the previous failures of the triplet injector were attributable to facility malfunctions rather than to its design. However, the doublet injector appeared to be capable of performing quite adequately and was apparently more durable. Target test conditions for run No. 5 were as follows:

P_c = 500 psia

F_2 Li MR = 2.74

H_2 Addition, (percent of total flow) = 40

The thrust chamber configuration employed (Fig. 135) was that shown schematically in Fig. 99, i.e., gas generator chamber, doublet injector, 20-inch combustion chamber, hydrogen injector, 10-inch mixing chamber, and nozzle.

During the first second of gas generator operation, the fluorine flowrate was nearly at the targeted value, but it then declined to about half the targeted value for the remainder of the firing. Posttest examination of run data and procedures indicated inadequate chilling of the fluorine injector, with consequent two-phase flow through the orifices, as the cause of the low fluorine flowrate. The insufficient chilling was attributed to the GN_2 purge maintained through the fluorine injector during the chilldown period. The pretest purging procedure was modified for later firings.

The lithium flowrate was at the targeted level during the first 80 milliseconds of mainstage, after which it increased significantly to a point substantially higher than the calibration range of the magnetic flowmeter. This increase in lithium flowrate was due to burning of the orifice tips of the lithium delivery tubes and to low chamber pressure resulting from the decreased fluorine flowrate. In spite of the unfavorable degree of lithium atomization and the poor distribution resulting from the very low F_2/Li mixture ratio (1.05), corrected c* efficiency was approximately 94 percent.

Hardware damage resulting from this firing was relatively minor and included burning of the inner core of the main hydrogen injector (copper) and hydrogen mixing chamber (copper), erosion of the graphite core of the lithium injector, and burning of the stainless-steel gas generator chamber wall immediately upstream of the lithium injector.

Run No. 6. Targeted parameters for this firing were the same as those for Run No. 5. Hardware modifications prior to the test included substitution of a graphite (for copper) hydrogen injector core (Fig. 136), a graphite liner in the copper mixing section, and a graphite mixer plate and liner in the

downstream half of the second gas generator chamber (nearest the lithium injector). In addition, the lithium injection tubes were recessed about 1/8 inch from the face of the injector to provide a measure of protection from the hot chamber gases.

The test was completed successfully. Observed parameter values are compared to the corresponding targets in the following tabulation. Details of the computational procedures and corrections applied are given in Appendix A.

Run No. 6	Target	Actual
$\dot{W}_{LF_2}$, lb/sec	2.52	2.59
$\dot{W}_{LLi}$, lb/sec	0.94	1.08
$\dot{W}_{GH_2}$ (main), lb/sec	2.26	2.15
$\dot{W}_{GH_2}$ (gas generator), lb/sec	0.0055	0.0055
F_2/Li MR	2.68	2.40
H_2, percent	40	37.0
Gas Generator Pressure, psia	535	489
Chamber Pressure, psia	490	449
Thrust, pounds	2360	2185
η_{c^*} (corr), percent		100.0
η_{I_s} (meas), percent		91.5

Posttest hardware examination showed that the orificed ends of the lithium injection tubes were burned away and that there was substantial erosion of the stainless-steel portion of the gas generator upstream of the graphite insert. The burning of stainless steel adjacent to graphite had been generally observed during these firings. This suggested initiation of fluorine-steel reaction by the heat of surface reactions of fluorine with graphite. To minimize the possibility of stainless steel burning in subsequent firings, nickel liners were installed in the first gas generator

chamber to act as a buffer between the graphite in the downstream chamber and the stainless-steel fluorine injector.

Run No. 7. Thrust chamber geometry and target run conditions for Run No. 7 were the same as for Run No. 6 except for the percent hydrogen added. In this case, two hydrogen flowrates were planned during the test, by use of the parallel hydrogen feed system previously described. In addition, the lithium injection tubes were recessed further from the injector face (about 1/2 inch) to increase their service time beyond 1 second.

Both of the planned steps were achieved and c* efficiency remained high: step 1, H_2 = 24 percent, corrected c* efficiency = 100 percent; step 2, H_2 = 20 percent, corrected c* efficiency = 101 percent.

Run No. 8. The test objective of Run No. 8 was to determine the influence of hydrogen injection station on performance. Accordingly, the hydrogen injector was moved forward 15 inches. The resulting chamber configuration consisted of (1) the gas-generator plus lithium injector, (2) a 5-inch-long F_2/Li combustion zone (previous length was 20 inches), (3) the hydrogen injector, and (4) a 27-inch-long mixing chamber (previous length was 12 inches). The target run conditions included three discrete hydrogen flowrates, corresponding to 15, 25, and 35 percent of total propellant flowrate.

The test was successfully completed and data points for all three hydrogen flow conditions were obtained. Performance remained high (η_{c^*} >97 percent).

Run No. 9. The test objective of Run No. 9 was to determine the effect of chamber length on performance. To accomplish this, the downstream mixing chamber length used in Run No. 8 was reduced from 27 to 17 inches. The target run conditions and remaining thrust chamber geometry remained unchanged. The test was successfully completed; three hydrogen flow conditions

were evaluated. However, the measured lithium flowrates indicated that four of the eight injector tubes had plugged either at or prior to test start, because the indicated flowrate, although constant, was only about 60 percent of the target value. In spite of the resulting high F_2/Li mixture ratio and attendant nonuniform mixture ratio distribution (i.e., lithium was not injected into four of the GF_2 jets), performance remained high.

Runs No. 10 and 11. Subsequent flow checks and two additional attempted firings (Runs No. 10 and 11) revealed that the lithium main value was the cause of the difficulty. During Run No. 10, the main valve failed to open properly (the opening time was about 750 milliseconds compared to 150 milliseconds observed in previous tests) and all injection tubes were plugged. Continued investigation revealed that not only was valve operation unpredictable, but significant leakage was occurring across the valve seat and becoming more severe with time. Initially, the valve only leaked under pressure; later, however, valve leakage was observed as soon as the lithium was liquified, even without tank pressurization.

Since the lithium injecter tubes were heated by hot purge gas, the presence of liquid lithium in the run line downstream of the main valve would result in tube plugging (lithium would be carried into the injector tubes before they could be adequately heated). No additional tests were attempted.

Data Summary

Performance levels were established on the basis of c* efficiencies obtained from measurements of chamber pressure and thrust with applicable corrections for energy losses, throat area changes, and departures from ideal, inviscid, one-dimensional flow. Details of the procedures used for these computations and for estimation of the correction factors are given in Appendix A.

A measurement error analysis was carried out (Appendix C) to obtain estimates of the uncertainty intervals associated with the determinations of $\left[\eta_{c*}\right]_{P_c}$ and $\left[\eta_{c*}\right]_F$. This analysis indicated the following typical error bands at the 2σ (95 percent) confidence level:

$$\text{For } \left[\eta_{c*}\right]_{P_c} : \pm 1.0 \text{ percent}$$

$$\left[\eta_{c*}\right]_F : \pm 1.3 \text{ percent}$$

A summary of the experimental performance data is presented in Table 10.

Note that η_{I_s} (meas) is the observed specific impulse (corrected to vacuum); multiplication of this efficiency by φ_{TOTAL} gives c* efficiency based on thrust.

The values of c* (theo) and I_s(theo) were obtained from theoretical performance calculations carried out for each individual set of run conditions. This avoided errors arising from the triple interpolations that would otherwise be required (for P_c, MR, and percent H_2).

The good agreement between $\left[\eta_{c*}\right]_{P_c}$ and $\left[\eta_{c*}\right]_F$ is shown in Fig. 137, in which only minor departures from the ideal 45-degree line are evident.

DISCUSSION OF EXPERIMENTAL RESULTS

The nine separate experimental conditions covered in runs No. 6 through 9 provided a total of 18 performance data points, nine each for c* efficiency based on chamber pressure and on thrust. Correlations of these data with analytical predictions of the degree of lithium atomization, fraction of lithium vaporized and burned, and uniformity of propellant distribution are presented in this section.

The fundamental requisite for the practical feasibility of the $F_2/Li/H_2$ tripropellant combination is that all, or nearly all, of the injected lithium be vaporized and burned. A series of curves showing predicted c* efficiency for varying percentages of lithium vaporized as a function of percent hydrogen, at nominal chamber pressure and F_2/Li mixture ratio, is presented in Fig. 138. They were calculated by the methods discussed in preceding sections of this report. Superimposed on these curves are the experimentally observed c* efficiencies. It is apparent that in all cases the injected lithium is essentially completely reacted with the fluorine, and the combustion products are uniformly mixed with the hydrogen; hence the fundamental feasibility of the $F_2/Li/H_2$ system is established.

The results illustrated in Fig. 138 also point up the fact that separate determination of F_2/Li combustion efficiency, originally planned as Phase I of the experimental firing program, was not essential since overall efficiencies on the order of 100 percent were obtained. Consequently, bypassing of the F_2/Li firings was not detrimental to achievement of program objectives.

The nine experimental firing conditions cover a range of chamber pressure (348 to 523 psia) within which the predicted effect of chamber pressure on c* efficiency is negligibly small (Fig. 88). Further, the variation of F_2/Li mixture ratio included in these firings (2.4 to 5.2) also has negligible predicted effect on c* efficiency as shown in Fig. 139. For these reasons, the significant variables in the tripropellant firings

conducted were: (1) percentage of hydrogen, (2) point of hydrogen addition, and (3) chamber length.

The cylindrical portion of the experimental thrust chambers (i.e., the length between the lithium injector and start of nozzle convergence) included the F_2/Li combustion chamber section, the 2-inch-wide hydrogen injector, and the mixing chamber between the hydrogen injector and the nozzle. (For convenience, the hydrogen is considered to be added at a single axial point, and the width of the hydrogen injector is included in the length of the mixing chamber section). The first six tests used a 32-inch chamber. In the first three, hydrogen was added at 20 inches from the lithium injector (giving a 20-inch F_2/Li combustion chamber); in the second three, hydrogen was added at 5 inches from the lithium injector (giving a 5-inch F_2/Li combustion chamber). The final three tests employed a 22-inch chamber with hydrogen addition at 5 inches.

Each of these three chamber configurations will be separately discussed in the following paragraphs in terms of the degree of lithium atomization and hydrogen mixing efficiency.

The results of the first three tests are plotted in Fig. 140 together with the c* efficiencies estimated for lithium mean droplet sizes of 30 and 70 microns. Corrected c* efficiency was essentially 100 percent over the hydrogen addition range of 19 to 37 percent of total propellant flowrate. These results indicate that a high degree of lithium atomization was obtained (<30-micron mean droplet size) in all three cases.

Figure 141 presents the results of the second set of three tests, with the hydrogen addition point moved 15 inches upstream. Again, c* efficiencies of nearly 100 percent were obtained except at the lowest percentage of hydrogen, where c* efficiency was 95.5 percent. The decrease in performance at this point is due to incomplete penetration of the F_2/Li combustion gas by the hydrogen, as discussed in the design portion of this report, with resulting poor distribution.

Results of the third set of firings, in which the 5-inch F_2/Li combustion chamber length was retained while the mixing chamber length was decreased to 17 inches, are shown in Fig. 142. Again, c* efficiencies of essentially 100 percent were obtained except at the lowest percentage of hydrogen, where incomplete penetration occurred. The difference in c* efficiency at the 19-percent hydrogen level between the 20- and 5-inch F_2/Li combustion chamber length configurations (Fig. 140 and 142) indicates that completeness of penetration of the hydrogen at this level is marginal and, in addition, that the 20-inch chamber ensured completeness of the F_2/Li reaction and consequent greater combustion gas uniformity at the hydrogen injector than did the 5-inch F_2/Li chamber.

Figure 143 shows the effect of F_2/Li combustion chamber length on predicted c* efficiency (with three total chamber lengths) for a lithium mean droplet size of 30 microns and 25-percent hydrogen addition at 500-psia chamber pressure and 2.74 F_2/Li mixture ratio. Observed c* efficiencies with the three thrust chamber configurations employed are also shown. With actual lithium mean droplet sizes indicated to be less than 30 microns, predicted c* efficiency at zero F_2/Li combustion chamber length (i.e., all three propellants injected at the same axial point) is over 95 percent even with the 12-inch overall chamber length.

CONCLUDING REMARKS

The experimental results of this program clearly demonstrate that essentially complete combustion can be obtained with the $F_2/Li/H_2$ tripropellant combination, and confirm the validity of the criteria upon which the designs of the thrust chamber components were based.

Program experience showed that no major difficulties are involved in the simultaneous use of a cryogenic and a heated liquid-metal propellant, provided careful attention is paid to operating procedures. It was also found that adequate material compatibility for the $F_2/Li/H_2$ system may be obtained without recourse to exotic materials.

Although combustion efficiencies were high in the thrust chamber configurations employed, several simplifying modifications remain to be experimentally investigated, such as:

1. Use of smaller volume chambers (The results of the present program indicate that high c* efficiencies may be obtained with significantly shorter chambers than were employed because of the small lithium droplet sizes produced by gas-augmented atomization.)
2. Use of nonreactive gas for lithium atomization; i.e., use of a fuel-rich, instead of an oxidizer-rich, gas generator (This would minimize combustion at the injector face and the hazards of premature fluorine-lithium interaction.)
3. Avoidance of difficulties inherent in the use of a liquid-metal valve by employing alternate methods of lithium flow control (e.g., rupture disks)

With the attainability of high combustion efficiency demonstrated, the next important step in determining the practical feasibility of the $F_2/Li/H_2$ combination is an experimental investigation of nozzle efficiency

because to achieve the high theoretical specific impulse of the tripropellant system, both c* and C_F efficiencies must be high. Such studies of the nozzle flow process are particularly essential when, as in the case of $F_2/Li/H_2$, expansion of a two-phase system is involved.

REFERENCES

1. Brzustowski, T. A. and I. Glassman, "Spectroscopic Investigation of Metal Combustion," Progress in Astronautics and Aeronautics, Vol. 15, Heterogeneous Combustion, Academic Press, New York, N. Y., 1963, 41-74.
2. Arbit, H. A. and S. D. Clapp, Fluorine-Hydrogen Performance Evaluation, Phase I, Part I: Analysis, Design, and Demonstration of High-Performance Injectors for the Liquid Fluorine-Gaseous Hydrogen Propellant Combination, NASA CR-54978, Prepared for NASA by Rocketdyne, a Division of North American Aviation, Inc., Canoga Park, California, July 1966.
3. Technical Documentary Report No. TR 65-107, Performance Characteristics of Compound A/Hydrazine Propellant Combination, Rocketdyne, a Division of North American Aviation Inc., Canoga Park, California, May 1965, CONFIDENTIAL.
4. Corbett, A. D. et al., Hypergolic Ignition at Reduced Pressure, Report No. AFRPL-TR-65-105, Edwards Air Force Base, California, July 1965, CONFIDENTIAL.
5. Levy, J. B. and B. K. W. Copeland, "The Kinetics of the Thermal, Hydrogen-Fluorine Reaction. I. Magnesium Reactor," J. Phys. Chem., Vol. 67, 2156-2159 (1963).
6. Brokaw, R. S., "A Suggested Mechanism for the Hydrogen-Fluorine Reaction," J. Phys. Chem., Vol. 69, 2488-2489 (1965).
7. Grosse, A. V. and A. D. Kirshenbaum, "The Premixed Hydrogen-Fluorine Flame and its Burning Velocity," J. Amer. Chem. Soc., Vol. 77, 5012-5013 (1955).
8. Levy, J. B. and B. K. W. Copeland, "The Kinetics of the Hydrogen-Fluorine Reaction. II. The Oxygen-Inhibited Reaction," J. Phys. Chem., Vol. 69, 408-416 (1965).
9. Mayer, S. W., L. Schieler, and H. S. Johnston, "Computation of High-Temperature Rate Constants for Bimolecular Reactions of Combustion Products," Eleventh Symposium (International) on Combustion, The Combustion Institute, Pittsburgh Pennsylvania 1967, 837-844.

10. Wilde, K. A., "Numerical Study of Hydrogen-Fluorine Kinetics in Nozzles," A.I.A.A. Journal, Vol. 2, 374-376 (1964).

11. Semenov, N. N., Some Problems in Chemical Kinetics and Reactivity, Vol. I, Princeton University Press, Princeton, N. J., 1958.

12. Laidler, K. J. and J. C. Polanyi, "Theories of the Kinetics of Bimolecular Reactions," Progress in Reaction Kinetics, Vol. 3, G. Porter, Editor, Pergamon Press, New York (1965), 1-61.

13. Gerhauser, J. M. and R. J. Thompson, Jr., Theoretical Performance Evaluation of Rocket Propellants, Report No. R-5802, Rocketdyne, a Division of North American Aviation, Inc., Canoga Park, Calif., August 1964.

14. Gordon, S. and V. N. Huff, "Theoretical Performance of Lithium and Fluorine as a Rocket Propellant," NACA Research Memorandum RM-E51C01, May 1951.

15. Brzustowski, T. A. and I. Glassman, "Vapor-Phase Diffusion Flames in the Combustion of Magnesium and Aluminum. I. Analytical Developments," Progress in Astronautics and Aeronautics, Vol. 15, Heterogeneous Combustion, Academic Press, New York, 1963, 75-116.

16. Godsave, G. A. E., "Studies of the Combustion of Drops in a Fuel Spray - The Burning of Single Drops of Fuel," Fourth Symposium (International) on Combustion, Williams & Wilkins Co., Baltimore, 1953, 818-830.

17. Spalding, D. B., "The Combustion of Liquid Fuels," Fourth Symposium (International) on Combustion, Williams & Wilkins Co., Baltimore, 1953, 847-864.

18. Goldsmith, M., and S. S. Penner, "On the Burning of Single Drops of Fuel in an Oxidizing Atmosphere," Jet Propulsion, Vol. 24, 245-251, (1954).

19. Wise, H., J. Lorrell, and B. J. Wood, "The Effects of Chemical and Physical Parameters on the Burning Rate of a Liquid Droplet," Fifth Symposium (International) on Combustion, Reinhold Publishing Corp., New York, 1955, 132-141.

20. Lambiris, S., L. P. Combs, and R. S. Levine, Stable Combustion Processes in Liquid Propellant Rocket Engines, Fifth Colloquium of the Combustion and Propulsion Panel, Advisory Group for Aeronautical Research and Development, NATO, Braunschweig, Germany, April 1962.

21. Shapiro, A. H., The Dynamics and Thermodynamics of Compressible Fluid Flow, Vol. I, The Ronald Press Co., New York, 1953.

22. Nurick, W. H., J. D. Seader, and T. A. Coultas, "Transient Heat Transfer from a Liquid Metal Spray Impinging on a Vertical Surface," Chemical Engineering Progress Symposium Series, Vol. 61, No. 59, 1965, 127-137.

23. Heckert, B. J. and S. D. Clapp, Preliminary Study of Liquid Atomization by a Gas, RR 65-22, Rocketdyne, a Division of North American Aviation, Inc., Canoga Park, California, April 1965.

24. Mayer, E., "Theory of Liquid Atomization in High Velocity Gas Streams," ARS Journal, Vol. 31, 1783-1785 (1961).

25. Weiss, M., and C. Worsham, "Atomization in High Velocity Airstreams," ARS Journal, Vol. 29, 252-259 (1959).

26. Wolfe, H. E. and W. H. Andersen, "Kinetics, Mechanism, and Resultant Droplet Sizes of the Aerodynamic Breakup of Liquid Drops," Report No. 0395-04(18)SP, Aerojet-General Corporation, Downey, California, April 1964.

27. Rabin, E., A. R. Schallenmueller, and R. B. Lawhead, "Displacement and Shattering of Propellant Droplets," Rocketdyne, a Division of North American Aviation, Inc., Final Summary Report for AFOSR, Washington, D.C., Report No. TR 60-75, March 1960.

28. Calderbank, P. H. and J. Rennie, "The Physical Properties of Foams and Froths Formed on Sieve-Plates," Trans. Inst. Chem. Engr. (Gt. Britain), Vol. 40, 3-12, 1962.

29. Webb, S. R., Statistical Treatment of Mean Diameters from Droplet Size Distribution, Stat. Memo 67-1, Rocketdyne, a Division of North American Aviation, Inc., Canoga Park, California, 16 February 1967.

30. Design Handbook for Liquid Fluorine Ground Handling Equipment, Technical Report AFRPL-TR-65-133, Air Force Rocket Propulsion Laboratory, Edwards Air Force Base, California, August 1965.

31. Lyon, R. N., Editor, Liquid Metals Handbook, Report No. NAVEXOS P-733 (Rev.), Atomic Energy Commission and Department of the Navy, Washington, June 1952.

32. Stang, J. H. et al., Compatibility of Liquid and Vapor Alkali Metals with Construction Materials, DMIC Report No. 227, Battelle Memorial Institute, Columbus, Ohio, 15 April 1966.

33. Bartz, D. R., "A Simple Equation for Rapid Estimation of Rocket Nozzle Convective Heat Transfer Coefficients," Jet Propulsion, Vol. 27, 49-51, January 1957.

34. Hatch, J. E. et al., Graphical Presentation of Difference Solutions for Transient Radial Heat Conduction in Hollow Cylinders with Heat Transfer at the Inner Radius and Finite Slabs with Heat Transfer at One Boundary, NASA Technical Report R-56, 1960.

35. Grey, J., "Calibration of Turbine Flowmeters for Cryogenic Operations," ARS Journal, Vol. 30, February 1960, pages 192 to 193.

36. Bulletin for Model 10C1510 and 10C1511 Turbine Flowmeters, Division 1, Fischer & Porter Company, Warminster, Pennsylvania, Publication No. 14815, 13.

37. A.S.M.E. Research Committee on Fluid Meters, Fluid Meters---Their Theory and Application, Fifth Edition, American Society of Mechanical Engineers, New York, 1959, 81.

38. Kapralova, G. A., E. M. Trofimova, and A. E. Shilov, "Upper Ignition Limit in the Reaction of Fluorine with Hydrogen," Kinetika i Kataliz, Vol. 6, #6, 977-981 (1965), Translated in Kinetics and Catalysis, Vol. 6, 884-888 (1965).

39. Weatherford, W. D., Jr., J. C. Tyler and P. M. Ku, Properties of Inorganic Energy-Conversion and Heat-Transfer Fluids for Space Applications, WADD Technical Report 61-96, Aeronautical Systems Division, AFSC, USAF, Wright-Patterson Air Force Base, Ohio, November 1961.

NOMENCLATURE

A = area

B = transfer number = $\overline{C}_p\ (T_B - T_A)/\Delta H_v$

c^* = characteristic velocity

c^*_{burned} = theoretical c^* at the mixture ratio corresponding to the burned propellants

$c^*_{injected}$ = theoretical c^* at the mixture ratio corresponding to the total amount of all propellants injected

C_p = gas-phase heat capacity

C_D = drag coefficient or discharge coefficient

D = diameter

D_{30} = volume mean droplet diameter

D_i = measured droplet image size of i^{th} droplet

D_{qp} = generalized mean droplet size

D_o = binary diffusion coefficient of oxidizer

$\mathcal{O}_o$ = dimensionless molar flux of oxidizer

$$= \left[\eta_{stoich} \,/\, \overline{\overline{Le}}\right]\left[\int_o^{P_{o,c}} \frac{d\,P_c}{P - P_o\,(1 - \alpha\, M_{stoich})}\right]$$

f_{total} = total correction factor applicable to measured P_c

F = thrust

ΔH_v = latent heat of vaporization

K = flow coefficient for sonic venturi meter

k' = burning rate constant corrected for convection

k'_s = stagnation burning rate constant

L^* = characteristic chamber length

$\overline{\overline{Le}}$ = Lewis number = $\overline{\overline{\lambda}} / (\overline{\overline{D}}_o \rho \overline{\overline{C}}_p / RT)$

M = total number of droplets counted (Eq. 22)

M_{stoich} = moles of gaseous product per mole of oxidizer

N = number of droplets

p = exponent expressing nature of mean droplet size (Eq. 22)

P = pressure

P_c = chamber pressure

P_o = partial pressure of oxidizer

Pr = Prandtl number

q = exponent expressing nature of mean droplet size (Eq. 22)

R = gas constant

Re = Reynolds number = $D_L \rho_g (\Delta V)/\mu_L$

t = time

t_b = breakup time (Eq. 18)

t_f = flight time (Eq. 17)

T = temperature

V = velocity

ΔV = relative gas-liquid velocity

$\dot{w}_s$ = molar vaporization (burning) rate of droplet

W = dimensionless droplet burning rate = $\dot{w}_s \overline{C}_p / 2\pi\overline{\lambda} D_A$

$\dot{W}$ = weight flowrate

$\dot{W}_{burned}$ = total weight flowrate of all propellants injected minus weight flowrate of propellants remaining unburned at the throat

$\dot{W}_{injected}$ = total weight flowrate of all propellants injected

We = Weber number = $D_L \rho_g (\Delta V)^2/\sigma_L$

X_p = penetration distance of liquid stream into gas jet

$Y_{o,c}$ = weight fraction oxidizer in the gaseous phase

α = fraction of product vaporized

β = diffusivity ratio = $\overline{C}_p \overline{\overline{\lambda}}/\overline{\overline{C}}_p \overline{\lambda}$

η_{c*} = characteristic velocity efficiency

η_{I_s} = specific impulse efficiency

η_{stoich} = stoichiometric coefficient (moles of lithium per mole of fluorine)

$(\eta_{c*})_F$ = characteristic velocity efficiency based on measurement of thrust

$(\eta_{c*})_{P_c}$ = characteristic velocity efficiency based on measurement of chamber pressure

θ = angle between liquid stream and injector face

λ = thermal conductivity

μ = viscosity

ρ = density

σ = surface tension

ϕ = defined in Eq. 14

φ_{total} = total correction factor applicable to measured thrust

Subscripts

A, B, C, = locations A, B, and C, respectively, of Fig. 77

D = droplet

g = gas

GG = gas generator

L = liquid

t = throat

Superscripts

$\overline{\overline{}}$ = value in zone BC (Fig. 77)

$\overline{}$ = value in zone AB (Fig. 77)

o = initial condition

TABLE 1

LF_2 (153 R) /LLi (960 R) PLOTTED THEORETICAL PERFORMANCE PARAMETERS

Fig. No.	Ordinate	Abscissa	Expansion	Plotted Parameter	Constant Parameters
1	c*	M.R.	Shifting	P_c	
2	F_c	M.R.		P_c	
3	I_s (vac)	M.R.	Shifting	P_c	$\epsilon = 40$, $\epsilon = 300$
4	C_F	M.R.	Shifting	P_c	$\epsilon = 40$, $\epsilon = 300$

TABLE 2

LF_2 (153 R) /LLi (960 R) /GH_2 (537 R) PLOTTED THEORETICAL PERFORMANCE PARAMETERS

Fig. No.	Ordinate	Abscissa	Expansion	Plotted Parameter	Constant Parameters
8	I_s (Vac)	M.R., F_2/Li	Shifting	H_2, %	P_c = 500 psia, ϵ = 40
9	↑	M.R., F_2/Li	↑	H_2, %	↑ ϵ = 300
10	↑	M.R., F_2/Li	↑	H_2, %	↑ ϵ = 500
11	↑	H_2, %	↑	M.R., F_2/Li	↑ ϵ = 40
12	↑	H_2, %	↑	M.R., F_2/Li	↑ ϵ = 300
13	↑	H_2, %	↑	M.R., F_2/Li	↓ ϵ = 500
14	↑	H_2, %	↑	P_c	F_2/Li M.R. = 2.74, ϵ = 40
15	↑	H_2, %	↑	P_c	F_2/Li M.R. = 2.74, ϵ = 300
16	↑	ϵ	↑	H_2, %	P_c = 500 psia, F_2/Li M.R. = 2.00
17	↑	↑	Frozen	↑	P_c = 500 psia, F_2/Li M.R. = 2.00
18	↑	↑	Shifting	↑	P_c = 500 psia, F_2/Li M.R. = 2.74
19	↑	↑	Frozen	↑	P_c = 500 psia, F_2/Li M.R. = 2.74
20	↓	↓	Shifting	↓	P_c = 500 psia, F_2/Li M.R. = 3.40

TABLE 2

(Continued)

Fig. No.	Ordinate	Abscissa	Expansion	Plotted Parameter	Constant Parameters
21	I_s (vac)	ϵ	Frozen	H_2, %	P_c = 500 psia, F_2/Li M.R. = 3.40
22	ΔI_s (vac)	ϵ	Shift-Frozen	H_2, %	P_c = 500 psia, F_2/Li M.R. = 2.74
23	c*	M.R., F_2/Li	Shifting	H_2, %	P_c = 500 psia
24	↑	M.R., F_2/Li	Frozen	H_2, %	P_c = 500 psia
25	↑	H_2, %	Shifting	M.R., F_2/Li	P_c = 500 psia
26	↓	H_2, %	Shifting	P_c	F_2/Li M.R. = 2.74
27	↓	H_2, %	Frozen	P_c	F_2/Li M.R. = 2.74
28	T_c	M.R., F_2/Li		H_2, %	P_c = 500 psia
29	↑	H_2, %		M.R., F_2/Li	P_c = 500 psia
30	↓	H_2, %		P_c	F_2/Li M.R. = 2.74
31	C_F (vac)	M.R., F_2/Li	Shifting	H_2, %	P_c = 500 psia, ϵ = 40
32	↑	M.R., F_2/Li	Shifting	H_2, %	P_c = 500 psia, ϵ = 300
33	↑	M.R., F_2/Li	Shifting	H_2, %	P_c = 500 psia, ϵ = 500
34	↓	H_2, %	Shifting	M.R., F_2/Li	P_c = 500 psia, ϵ = 40

TABLE 2

(Continued)

Fig. No.	Ordinate	Abscissa	Expansion	Plotted Parameter	Constant Parameters
35	C_F(vac)	H_2, %	Shifting	M.R., F_2/Li	P_c = 500 psia, ϵ = 300
36	↕	↕	↕	M.R., F_2/Li	P_c = 500 psia, ϵ = 500
37				P_c	F_2/Li M.R. = 2.74, ϵ = 40
38		ϵ		H_2, %	P_c = 500 psia, F_2/Li M.R. = 2.74
39		ϵ	Frozen	H_2, %	P_c = 500 psia, F_2/Li M.R. = 2.74
40	ΔC_F(vac)	ϵ	Shift-Frozen	H_2, %	P_c = 500 psia, F_2/Li M.R. = 2.74
41	Cond. %	H_2, %	Shifting	M.R., F_2/Li	P_c = 500 psia
42	Cond. %	H_2, %	Shifting	P_c	F_2/Li M.R. = 2.74
43	Cond. %	ϵ	Shifting	H_2, %	P_c = 500 psia, F_2/Li M.R. = 2.74
44	Cond. %	ϵ	Shifting	H_2, %	P_c = 1000 psia

TABLE 3

LF_2 (153 R) /SLi (36 R) /LH_2 (36 R) PLOTTED THEORETICAL PERFORMANCE PARAMETERS

Fig. No.	Ordinate	Abscissa	Expansion	Plotted Parameter	Constant Parameters
47	I_s(vac)	M.R., F_2/Li	Shifting	H_2, %	P_c = 500 psia, ϵ = 40
48	I_s(vac)	M.R., F_2/Li	Shifting	H_2, %	P_c = 500 psia, ϵ = 300
49	I_s(vac)	M.R., F_2/Li	Shifting	H_2, %	P_c = 500 psia, ϵ = 500
50	I_s(vac)	H_2, %	Shifting	M.R., F_2/Li	P_c = 500 psia, ϵ = 40
51	I_s(vac)	H_2, %	Shifting	M.R., F_2/Li	P_c = 500 psia, ϵ = 300
52	I_s(vac)	H_2, %	Shifting	M.R., F_2/Li	P_c = 500 psia, ϵ = 500
53	I_s(vac)	ϵ	Shifting	M.R., F_2/Li	P_c = 500 psia, F_2/Li M.R. = 2.00
54	I_s(vac)	ϵ	Frozen	M.R., F_2/Li	P_c = 500 psia, F_2/Li M.R. = 2.00
55	I_s(vac)	ϵ	Shifting	M.R., F_2/Li	P_c = 500 psia, F_2/Li M.R. = 2.74
56	I_s(vac)	ϵ	Frozen	M.R., F_2/Li	P_c = 500 psia, F_2/Li M.R. = 2.74
57	I_s(vac)	ϵ	Shifting	M.R., F_2/Li	P_c = 500 psia, F_2/Li M.R. = 3.40
58	I_s(vac)	ϵ	Frozen	M.R., F_2/Li	P_c = 500 psia, F_2/Li M.R. = 3.40
59	ΔI_s(vac)	ϵ	Shift-Frozen	M.R., F_2/Li	P_c = 500 psia, F_2/Li M.R. = 2.74

TABLE 3

(Continued)

Fig. No.	Ordinate	Abscissa	Expansion	Flotted Parameter	Constant Parameters
60	c*	M.R., F_2/Li	Shifting	H_2, %	P_c = 500 psia
61	c*	M.R., F_2/Li	Frozen	H_2, %	P_c = 500 psia
62	c*	H_2, %	Shifting	M.R., F_2/Li	P_c = 500 psia
63	T_c	M.R., F_2/Li		H_2, %	P_c = 500 psia
64	T_c	H_2, %		M.R., F_2/Li	P_c = 500 psia
65	C_F	M.R., F_2/Li	Shifting	H_2, %	P_c = 500 psia, ϵ = 40
66	C_F	M.R., F_2/Li	Shifting	H_2, %	P_c = 500 psia, ϵ = 300
67	C_F	M.R., F_2/Li	Shifting	H_2, %	P_c = 500 psia, ϵ = 500
68	C_F	H_2, %	Shifting	M.R., F_2/Li	P_c = 500 psia, ϵ = 40
69	C_F	H_2, %	Shifting	M.R., F_2/Li	P_c = 500 psia, ϵ = 300
70	C_F	H_2, %	Shifting	M.R., F_2/Li	P_c = 500 psia, ϵ = 500
71	C_F	ϵ	Shifting	H_2, %	P_c = 500 psia, F_2/Li M.R. = 2.74
72	C_F	ϵ	Frozen	H_2, %	P_c = 500 psia, F_2/Li M.R. = 2.74
73	ΔC_F	ϵ	Shift-Frozen	H_2, %	P_c = 500 psia, F_2/Li M.R. = 2.74
74	Cond.%	H_2, %	Shifting	M.R., F_2/Li	P_c = 500 psia
75	Cond.%	ϵ	Shifting	H_2, %	P_c = 500 psia, F_2/Li M.R. = 2.74

TABLE 4

DATA USED TO CALCULATE LITHIUM DROPLET BURNING RATE

Term	Value	Comments
T_A	3900 R	Boiling point of lithium at 500 psia (Ref. 39)
$\bar{\lambda}$	1.9×10^{-6} $\frac{\text{Btu}}{\text{sec-ft-F}}$	Thermal conductivity of gas in zone AB (Fig. 77)
$\bar{\bar{C}}_p$	1.2 $\frac{\text{Btu}}{\text{lb-F}}$	Heat capacity of F_2-Li combustion products
$\bar{\bar{\lambda}}$	21.2×10^{-6} $\frac{\text{Btu}}{\text{sec-ft-F}}$	Thermal conductivity of F_2-Li combustion products
η_{stoich}	2.0	Moles of Li/mole F_2
M_{stoich}	2.44	Moles of gaseous product per mole of oxidizer
$P_{o,c}$	0.25	Assumed constant at this intermediate value
$\bar{C}_p$	0.7 Btu/lb-R	Heat capacity of gas in zone AB (Fig. 77)
ΔH_v	7,600 Btu/lb	Heat of vaporization of lithium at 3900 R (Ref. 39)
$\bar{\bar{Le}}$	1.0	Lewis number

TABLE 5

RESULTS OF COMBUSTION MODEL COMPUTATIONS (F_2/Li M.R. = 2.74)

Case No.	L, inches	(D_{30})Li, microns	P_c, psia	x_{B_2}, inches	B_2, percent	Contraction Ratio	L*, inches	Percent Li Reacted	η_{c^*}, percent
1	10.0	10	500		0	7.25	64.7	100	100
2	↓	20	↓		↓	3.74	34.0	93.3	97.6
3		↓				5.27	47.4	95.4	98.4
4	10.5					7.14	67.3	96.3	98.6
5	10.0					7.25	64.7	96.7	98.8
6	↓					9.66	85.8	98.2	99.4
7		30				3.74	34.0	84.6	94.2
8		↓				5.27	47.4	87.5	95.3
9	10.5					7.14	67.3	90.6	96.5
10	10.0					7.25	64.7	90.5	96.5
11	↓					9.66	85.8	92.8	97.4
12		40				4.03	36.5	78.2	91.7
13		↓				5.54	49.7	81.5	93.0
14	10.5					7.14	67.3	84.3	94.1
15	10.0					7.25	64.7	84.1	94.1
16	↓					10.09	89.5	87.0	95.1
17		50				3.91	35.5	71.2	88.4
18		↓				10.09	89.5	82.0	93.2
19	↓					7.25	64.7	78.3	91.7
20	10.5	↓				10.09	89.5	82.0	93.2
21	10.0	100				7.25	64.7	56.3	79.5
22	10.0	150				6.82	60.9	44.3	70.0
23	9.8	200				4.80	41.3	37.6	62.7
24	15.0	10				7.25	100.9	100	100
25	↓	20				↓	↓	98.8	99.6
26		30						94.6	98.1
27		40						89.3	96.1
28		50						84.5	94.2
29	↓	100				7.36	↓	64.3	84.7
30	14.8	150				5.11	70.5	51.3	75.7
31	14.8	200				5.11	70.5	43.7	69.4
32	17.2	60				7.20	116.1	83.7	93.9
33	20.0	20				7.24	137.0	99.6	99.9
34	↓	30				4.033	76.8	93.6	97.7
35		↓				5.54	105.1	95.3	98.3
36						7.24	137.0	96.8	98.9
37	↓	↓				10.07	201.9	98.2	99.3
38	20.0	40				4.15	79.1	88.0	95.5
39	↓	↓				5.54	105.1	90.6	96.6
40						7.24	137.0	92.7	97.3
41						10.07	201.9	95.0	98.3
42		50				4.15	79.1	82.9	93.5
43		↓				5.80	110.0	85.9	94.7
44						7.24	137.0	88.3	95.7
45						11.07	220.5	91.5	96.9
46		100				7.24	137.0	69.4	87.3
47		150				8.27	156.3	56.4	79.6
48	↓	200	↓		↓	8.27	156.3	47.9	73.1
49	30.1	30				4.10	123.2	96.3	98.7
50	30.0	30				5.50	159.4	97.8	99.3
51	30.1	40				4.10	123.2	92.3	97.2
52	30.0	↓				5.50	159.4	94.4	98.0
53	30.0					7.36	212.9	96.0	98.6
54	30.1	50	↓		↓	4.10	123.2	87.7	95.5

TABLE 5
(Concluded)

Case No.	L, inches	$(D_{30})_{Li}$, microns	P_c, psia	x_{H_2}, inches	H_2, percent	Contraction Ratio	L*, inches	Percent Li Reacted	η_{c^*}, percent
55	30.0	50	500		0	5.84	169.2	96.5	96.5
56	10.0	20		0	7	7.25	64.7	91.6	98.6
57	9.9				15	7.25	64.0	89.9	98.4
58	↓	↓			30	7.25	64.0	87.7	97.6
59					40	7.73	68.1	86.8	97.4
60	10.0	30			7	7.25	64.7	79.8	96.5
61	9.9				15	7.73	68.1	77.3	96.2
62	↓				30	7.73	68.1	74.9	95.1
63				↓	40	7.73	68.1	74.2	94.5
64	10.0			5	15	7.25	64.7	89.8	98.4
65	↓	↓		5	30	↓	↓	89.8	98.1
66		40		0	15			65.9	94.1
67		↓		↓	30			63.9	92.7
68					40			63.3	91.0
69				5	15			82.9	97.2
70				5	30			83.8	96.9
71		50		0	15			57.3	92.2
72		↓		0	30			55.7	90.9
73				5	15	7.73	68.9	77.9	96.4
74	↓	↓		5	30	7.73	68.9	78.2	95.8
75	15.0	30		10	15	7.25	101.0	95.2	99.2
76	↓	30		↓	30	↓	↓	95.7	99.1
77		40			15			90.3	98.5
78		40			30			91.5	98.3
79		50			15			86.2	97.8
80		50		↓	30	↓	↓	87.2	97.5
81	20.0	20		0	15	7.24	137.0	97.5	99.6
82	↓	20		↓	30	↓	↓	96.5	99.3
83		30			15			90.2	98.4
84		↓		↓	30			88.0	97.7
85				15	15			97.5	99.7
86		↓		15	30	↓	↓	98.0	99.5
87		40		0	15	7.72	146.0	81.4	97.0
88		↓		0	30	7.72	146.0	79.0	96.0
89				15	15	7.24	137.0	93.9	99.0
90				15	30	7.24	137.0	95.0	99.0
91		50		0	15	7.72	146.0	73.1	95.5
92		↓		0	30	7.72	146.0	70.9	94.3
93				15	15	7.24	137.0	90.2	98.4
94	↓			↓	30	7.24	137.0	91.4	98.3
95	30.0	30			15	7.36	212.9	98.8	99.5
96	↓	30			30	↓	↓	98.9	99.7
97		40			15			96.3	99.3
98		40			30			96.4	99.3
99		50			15			93.1	98.9
100		50		↓	30	↓	↓	93.5	98.7
101	10.0	20	200		0	7.25	64.7	95.5	98.4
102	20.0	40	200			↓	137.0	90.4	96.5
103	10.0	20	350				64.7	96.4	98.8
104	10.0	40	↓			7.73	68.9	83.6	93.8
105	20.0	20				7.24	137.0	99.5	99.8
106	20.0	40					137.0	98.1	97.1
107	10.0	20	650				64.7	97.0	98.9
108	20.0	40	650		↓	↓	137.0	93.2	97.6

TABLE 6

TRIPLET ELEMENT JET PENETRATION TESTS: CONDITIONS FOR LIQUID STREAM PENETRATION TO CENTER OF GAS JET

Test No.	D_g, inches	D_L, inches	ρ_g, lb/ft^3	V_g, ft/sec	ρ_L, lb/ft^3	V_L, ft/sec	$\frac{D_g}{2V_L \cos\theta}$, seconds	$\frac{D_L}{V_g}\sqrt{\frac{\rho_L}{\rho_g}}$, seconds
21	0.242	0.60	0.066	840	62.3	35	0.41×10^{-3}	0.18×10^{-3}
22	0.242	0.60	↓	660	↓	28	0.51	0.23
23	0.242	0.60		1100		44	0.32	0.14
24	0.125	0.40		1690		36	0.21	0.10
25	0.125	0.40		610		20	0.27	0.17
27	0.250	0.40		380		27	0.55	0.27
28	0.250	0.40		630		35	0.42	0.16
29	0.250	0.40		870		51	0.29	0.12
30	0.250	0.40		990		54	0.27	0.10
31	0.250	0.40		1100		57	0.26	0.09
36	1.50	0.60		1090	590	69	1.28	0.42
48	1.00	0.60		1090	590	44	1.34	0.42
104	0.238	0.60	1.21	600	62.3	72	0.20	0.06
111	0.238	0.60	1.04	990	↓	92	0.15	0.04
131	0.238	0.60	0.94	520		85	0.17	0.08
135	0.238	0.60	0.75	500		72	0.20	0.08

TABLE 7

PHYSICAL PROPERTIES OF CERROSAFE* AND LITHIUM

Property	Cerrosafe	Lithium
Specific Gravity at 68 F	9.4	0.53
Melting Range, F	160 - 190	357
Liquid Surface Tension at Melting Point, dyne/cm	400	395
Volume Change (Liquid to Solid), percent	-2.0	---
Volume Change (Growth After Solidification), percent	0.5	---
Composition, percent:		
Bismuth	42.5	
Lead	37.7	
Tin	11.3	
Cadmium	8.5	

*Manufactured by Cerro Sales Corporation, New York, N. Y.

TABLE 8

DROPLET DISTRIBUTION DATA, ATOMIZATION OF CERROSAFE WITH NITROGEN IN A LIQUID-GAS-LIQUID TRIPLET ELEMENT

Test No.	D_g, inches	D_L, inches	V_g, ft/sec	V_L, ft/sec	$\dot{W}_L/\dot{W}_g$	ϕ	P, percent	$\frac{We}{\sqrt{Re}}$	D_{30}, microns	$[D_{30}]_{exp}$, microns	$[D_{30}]_{calc}$, microns
40	1.50	0.06	1080	37	0.88	1.46	45	2.6	9.3	17.6	13.5
41	1.50	0.06	860	60	1.80	1.79	93	1.8	12.6	15.1	22.6
42	1.50	0.06	635	60	2.47	1.95	126	1.1	19.0	79.1	37.0
43	1.50	0.06	480	49	2.65	2.01	137	0.7	27.7	75.4	55.8
44	1.50	0.06	640	49	1.99	1.84	103	1.1	19.0	72.2	34.9
48	1.00	0.06	1090	44	2.38	1.94	81	2.6	9.2	16.6	17.8
49	1.00	0.06	1090	47	2.54	1.98	87	2.6	9.2	12.5	18.3
50	1.00	0.06	940	37	2.30	1.92	78	2.0	11.2	9.2	21.4
51	1.00	0.06	940	56	3.50	2.20	118	2.0	11.2	24.2	24.5
52	1.00	0.06	760	37	2.85	2.05	97	1.5	14.9	25.8	30.6
53	1.00	0.06	1090	59	3.19	2.12	108	2.6	9.2	33.2	19.6

TABLE 9

GAS GENERATOR DATA SUMMARY

Test No.	Duration, seconds	Chamber length, inches	Mixing Plates	Chamber Pressure, psia	Total Flowrate, lb/sec	Mixture Ratio	η_{c*}, percent	Gas Temperature, R	Theoretical Gas Temperature, R	Remarks
1	0.6	10	None	432	3.06	620	108			Test objective of tests 1, and 2, and 3: checkout facility and hardware. (Thermocouples were burned away.)
2	1.7	10	None	452	2.97	490	101			
3	2.8	10	None	458	3.06	500	100			
4	3.1	10	1	441	2.93	510	102	820	930	Test objective of tests 4, and 5, and 6: verify duration capability of hardware at design mixture ratio.
5	6.1	10	1	430	2.74	480	102	970	990	
6	10.6	10	1	456	3.07	540	103	880	870	
7	10.0	5	1	464	3.00	510	104	1010	930	Test objective of tests 7, and 8, and 9: investigate effects of chamber length and mixture ratio
8	10.0	5	1	428	2.48	410	103	1240	1170	
9	10.0	5	1	398	2.09	340	99	1490	1410	
10	4.6	10	2	716	3.16	570	92	1380	1290	Test objective: investigate effect of chamber pressure
11	4.0	10	2	591	3.26	610	98	740	760	Test objectives of tests 11, and 12, and 13: investigate effects of chamber pressure and mixture ratio produced by stepwise changes in hydrogen flowrate during a continuing firing
	0.6			616	3.18	550	98	800	850	
12	1.6	10	2	598	3.70	660	92	710	690	
	1.7			634	3.38	580	98	840	810	
	1.1			660	3.16	510	99	920	930	
13	1.6	10	2	563	3.19	560	92		850	
	1.7			597	3.02	490	93	950	970	
14	7.5	10	2	554	1.79	440	97	1010	1080	Test objectives of tests 14, and 15, and 16: determine hardware durability as function of chamber pressure and mixture ratio when end plate is heated to 500 F
15	7.5	10	2	587	1.65	370	97	1230	1290	
16	7.5	10	2	607	3.00	410	97	1110	1170	

TABLE 10

DATA SUMMARY

Parameter	Run No.										
	4	5	6	7	7	8	8	8	9	9	9
			Step No.								
				1	2	1	2	3	1	2	3
Combus. Chan., inches	17	20	20	20	20	5	5	5	5	5	5
Mixing Chan., inches		12	12	12	12	27	27	27	17	17	17
P_c, psia	109	311	446	481	453	384	453	523	348	418	490
F_{vac}, pounds			2185	2317	2190	1887	2230	2563	1741	2107	2439
A_t, $in.^2$	3.33	3.35	3.40	3.43	3.43	3.47	3.47	3.47	3.49	3.49	3.49
$\dot{w}_{IF_2}$, lb/sec	2.60	1.26	2.59	3.85	3.83	3.52	3.42	3.21	3.31	3.19	2.90
$\dot{w}_{ILi}$, lb/sec	0.25	1.20	1.08	1.10	1.07	1.08	1.07	0.94	0.64	0.63	0.61
$\dot{w}_{GH_2}$(main), lb/sec		2.16	2.15	1.54	1.20	0.82	1.40	2.43	0.95	1.62	2.79
$\dot{w}_{GH_2}$(GG), lb/sec	0.0054	0.0055	0.0055	0.0056	0.0056	0.0056	0.0056	0.0056	0.0055	0.0055	0.0055
$\dot{w}_p$, lb/sec	2.855	4.626	5.826	6.496	6.106	5.426	5.896	6.586	4.906	5.446	6.306
F_2 Li Mixture Ratio	10.4	1.05	2.40	3.50	3.58	3.26	3.20	3.41	5.17	5.06	4.75
H_2, percent		46.8	37.0	23.8	19.7	15.2	23.8	37.0	19.4	29.9	44.3
c*(uncorr), ft/sec	4090	7246	8431	8171	8187	7901	8578	8866	7965	8618	8725
c*(theo), ft/sec	4400	8003	9006	8715	8661	8409	8718	9093	8578	8761	8833
η_{c^*}(uncorr), percent	93.0	90.5	93.6	93.8	95.2	94.0	96.4	97.5	92.9	98.4	98.8
f_{TOTAL}*	1.02	1.04	1.068	1.064	1.062	1.014	1.007	1.009	1.017	1.012	1.013
$[\eta_{c^*}]_{P_c}$(corr), percent	94.9	94.1	100.0	99.8	101.1	95.3	99.1	98.4	94.5	99.6	100.1
$t_{s,vac}$(meas), seconds			375	357	359	348	378	389	355	387	387
$t_{s,vac}$(theo), seconds			410	397	392	383	397	413	390	401	401
η_{I_s}(meas), percent			91.5	89.9	91.6	90.9	95.2	94.2	91.0	96.5	96.5
ϕ_{TOTAL}**			1.105	1.104	1.098	1.051	1.039	1.044	1.054	1.035	1.043
$[\eta_{c^*}]_{F}$(corr), percent			101.1	99.2	100.6	95.5	98.9	98.3	95.9	99.9	100.6

*f_{TOTAL} total correction factor applicable to measured P_c

$f_P\ f_{TR}\ f_{DIS}\ f_{HL}$ (cf. Appendix A)

**ϕ_{TOTAL} total correction factor applicable to measured thrust

$\phi_{DIV}\ \phi_{TR}\ \phi_{HL}$ (cf. Appendix A)

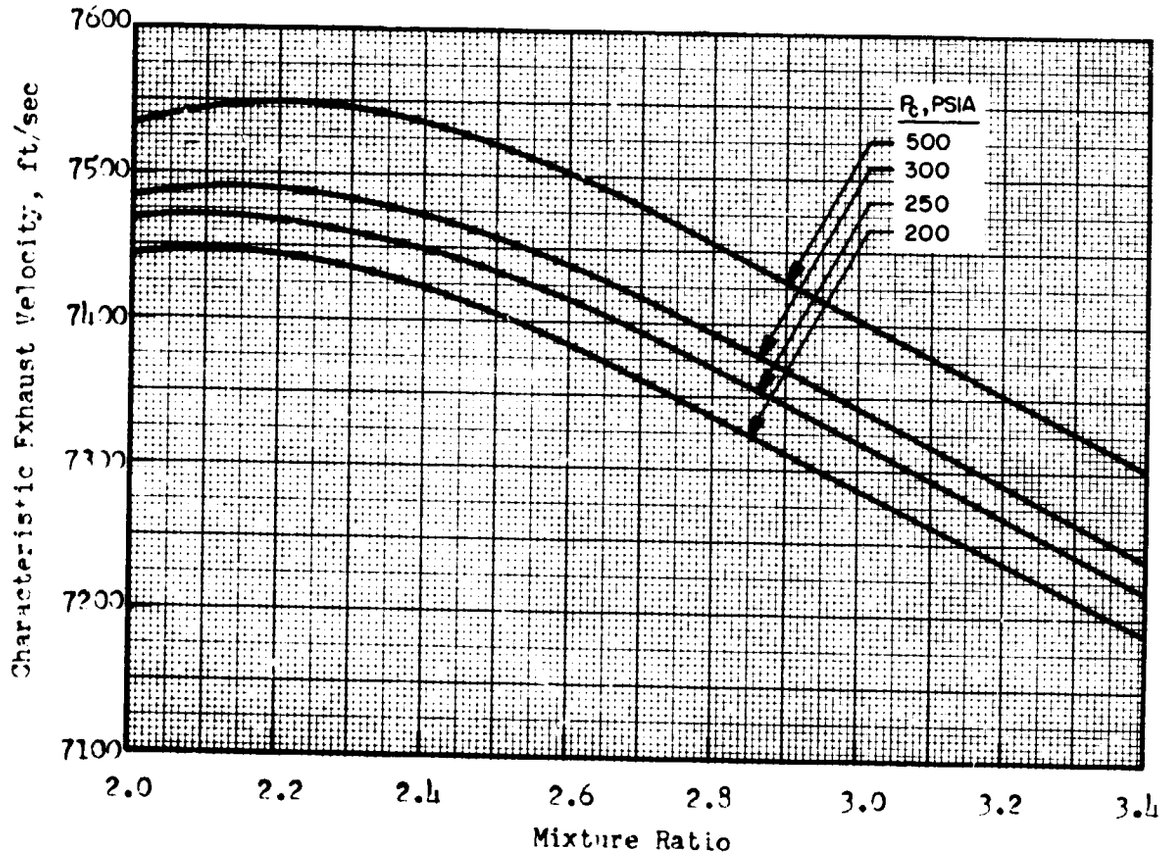

Figure 1. Variation of c* (Shifting Equilibrium) with Mixture Ratio at Indicated Chamber Pressures, LF_2 (153 R)/LLi (960 R).

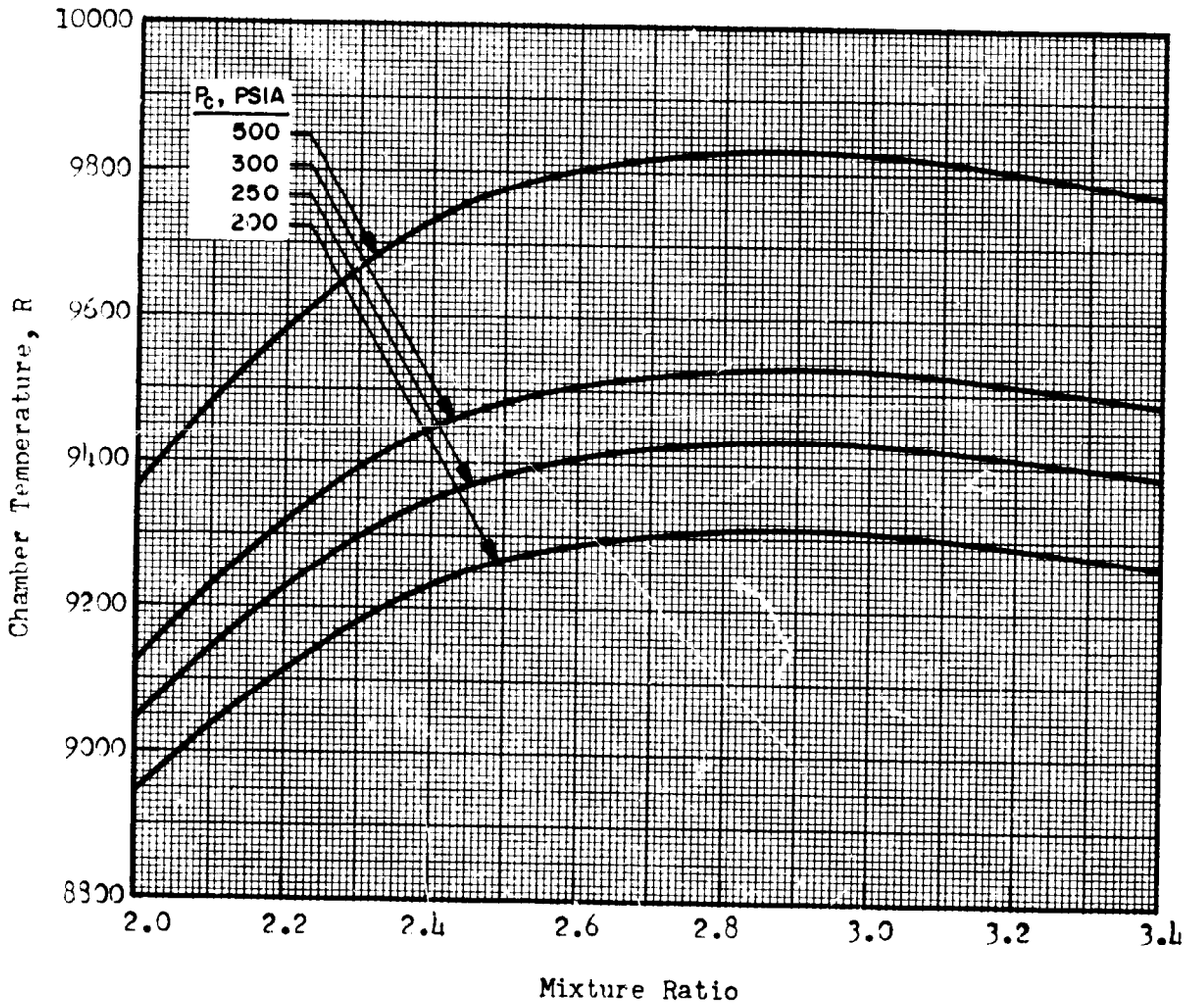

Figure 2. Variation of Chamber Temperature with Mixture Ratio at Indicated Chamber Pressures, LF_2 (153 R)/LLi (960 R).

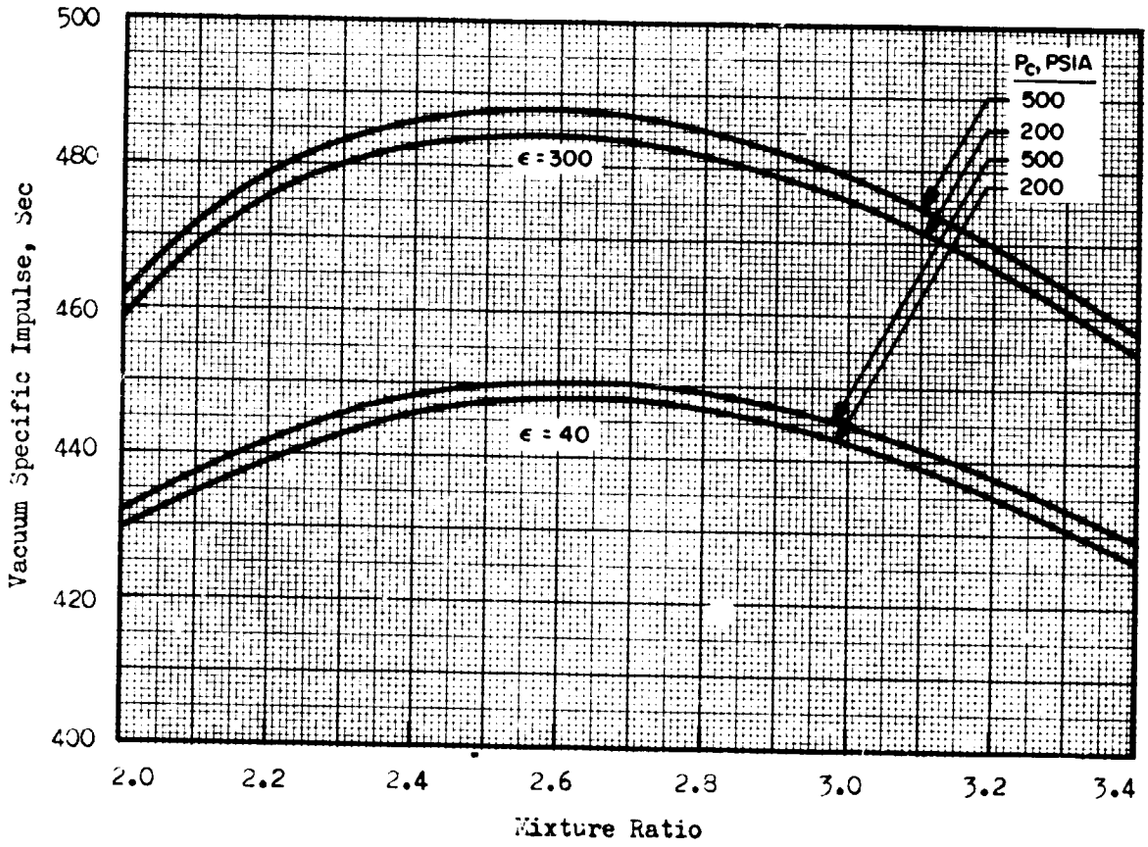

Figure 3. Variation of Vacuum Specific Impulse (Shifting Equilibrium) with Mixture Ratio at Indicated Chamber Pressures and Expansion Ratios, LF_2 (153 R)/LLi (960 R).

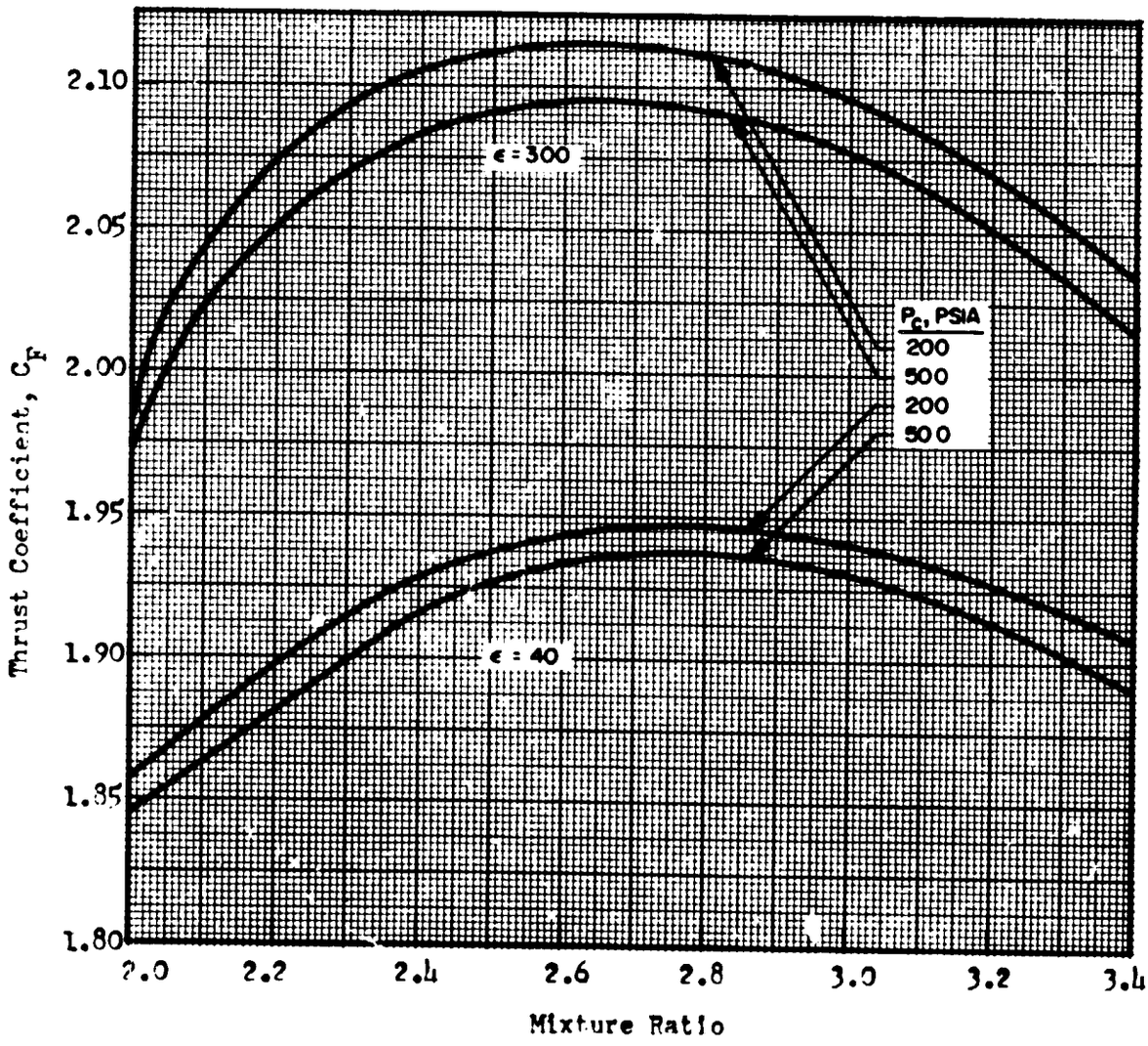

Figure 4. Variation of Thrust Coefficient (Shifting Equilibrium) with Mixture Ratio at Indicated Chamber Pressures and Expansion Ratios, LF_2 (153 R)/LLi (960 R).

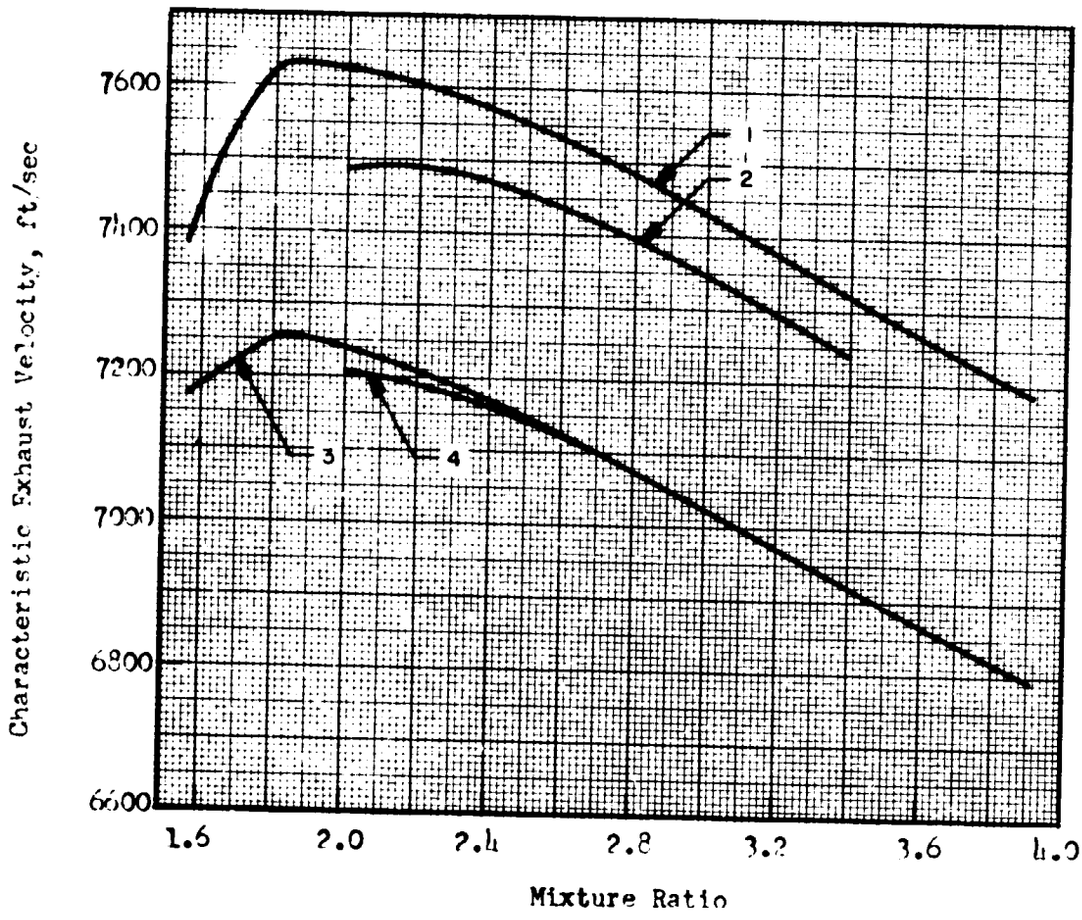

Figure 5. Variation of c* with Mixture Ratio at P_c = 300 psia, LF_2 (153 R)/LLi (960 R),
Curve 1: Shifting Equilibrium, Ref. 14
Curve 2: Shifting Equilibrium, Present Study
Curve 3: Frozen Composition, Ref. 14
Curve 4: Frozen Composition, Present Study

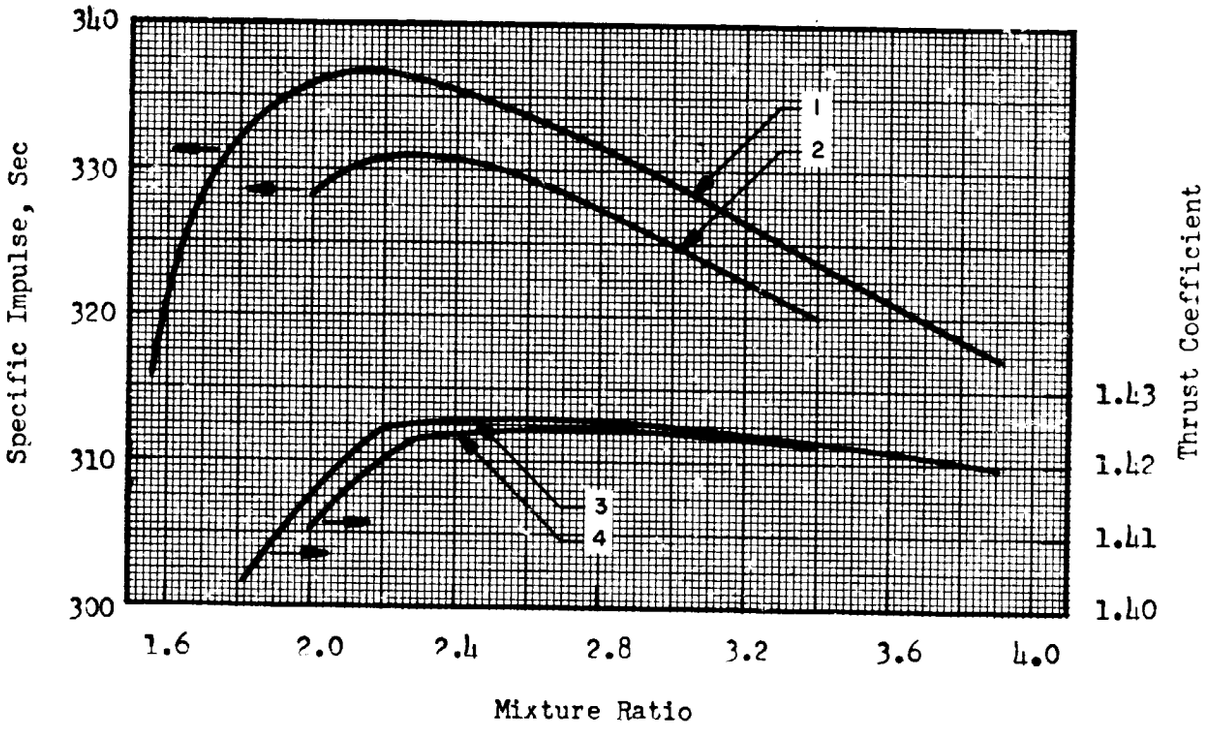

Figure 6. Variation of Specific Impulse and Thrust Coefficient with Mixture Ratio, LF_2 (153 R)/ LLi (960 R), P_c = 300 psia, Shifting Equilibrium, Expansion to one Atmosphere.

Curves 1 and 3: Ref. 14

Curves 2 and 4: Present Study

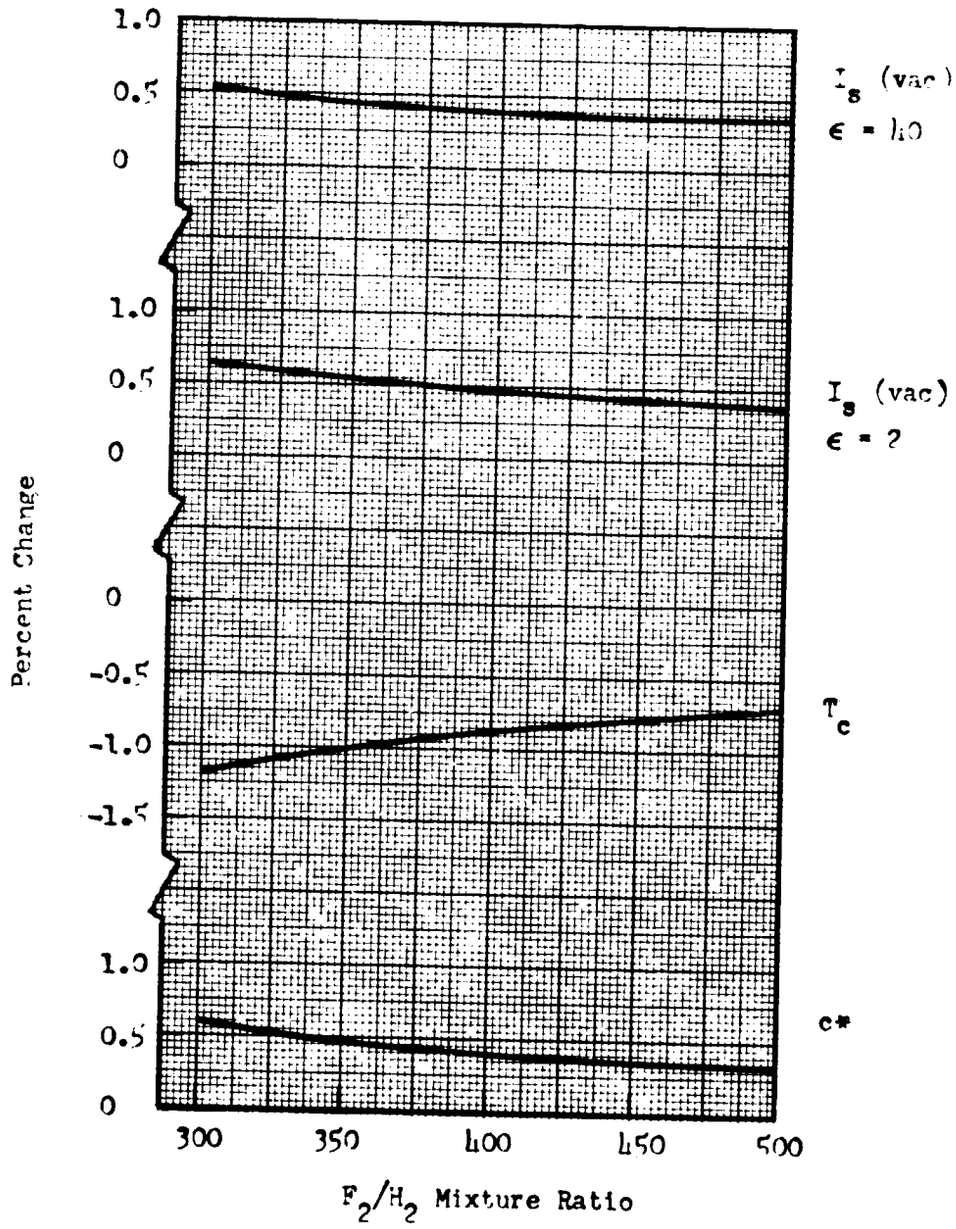

Figure 7. Percent Change in Indicated Parameters from Zero Hydrogen Condition to Indicated F_2/H_2 Mixture Ratio, LF_2 (153 R)/LLi (960 R), P_c = 250 psia, F_2/Li M.R. = 2.74.

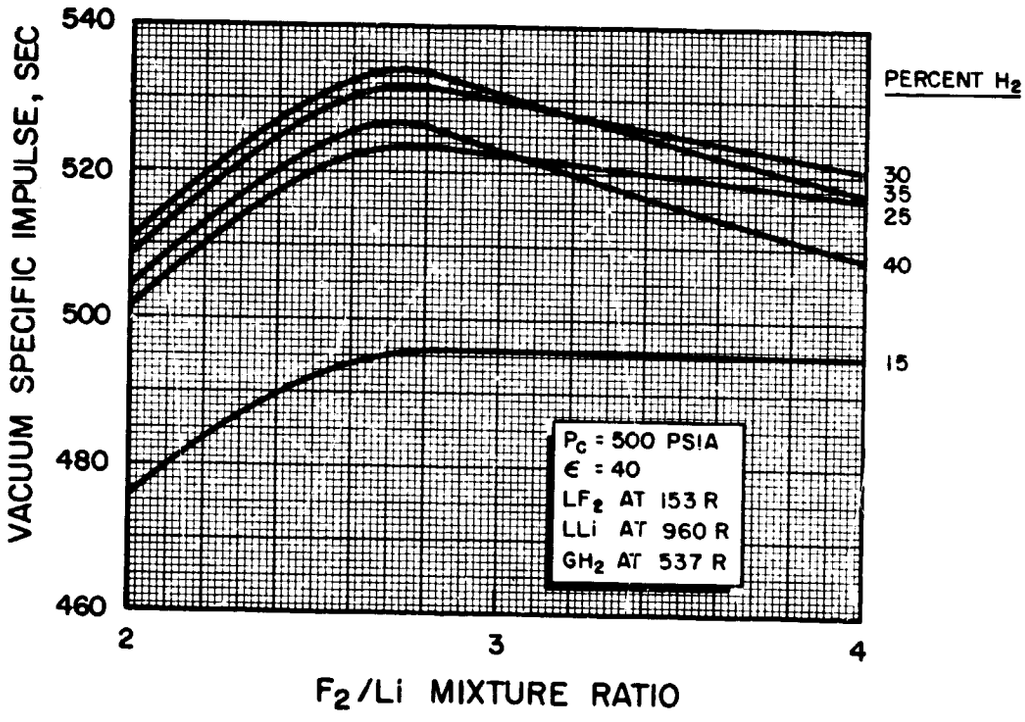

Figure 8. Variation of Vacuum Specific Impulse (Shifting Equilibrium) with F_2/Li Mixture Ratio at Indicated Percentages of Hydrogen, Chamber Pressure, and Expansion Ratio, LF_2(153 R)/LLi(960 R)/GH_2(537 R)

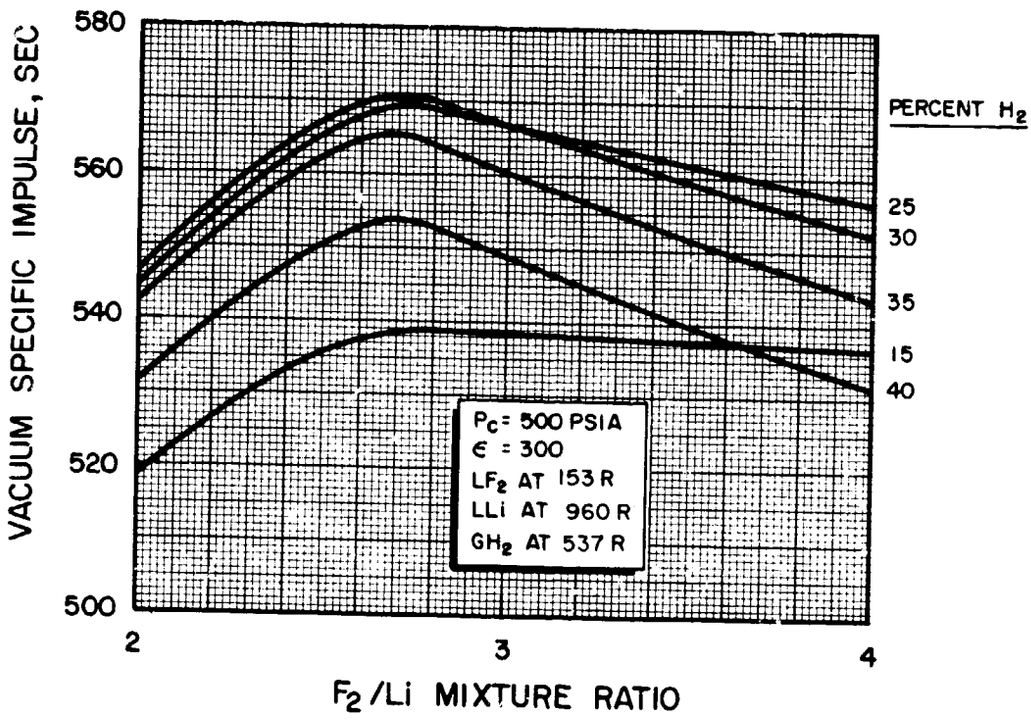

Figure 9. Variation of Vacuum Specific Impulse (Shifting Equilibrium) with F_2/Li Mixture Ratio at Indicated Percentages of Hydrogen, Chamber Pressure, and Expansion Ratio, LF_2(153 R)/LLi(960 R)/GH_2(537 R).

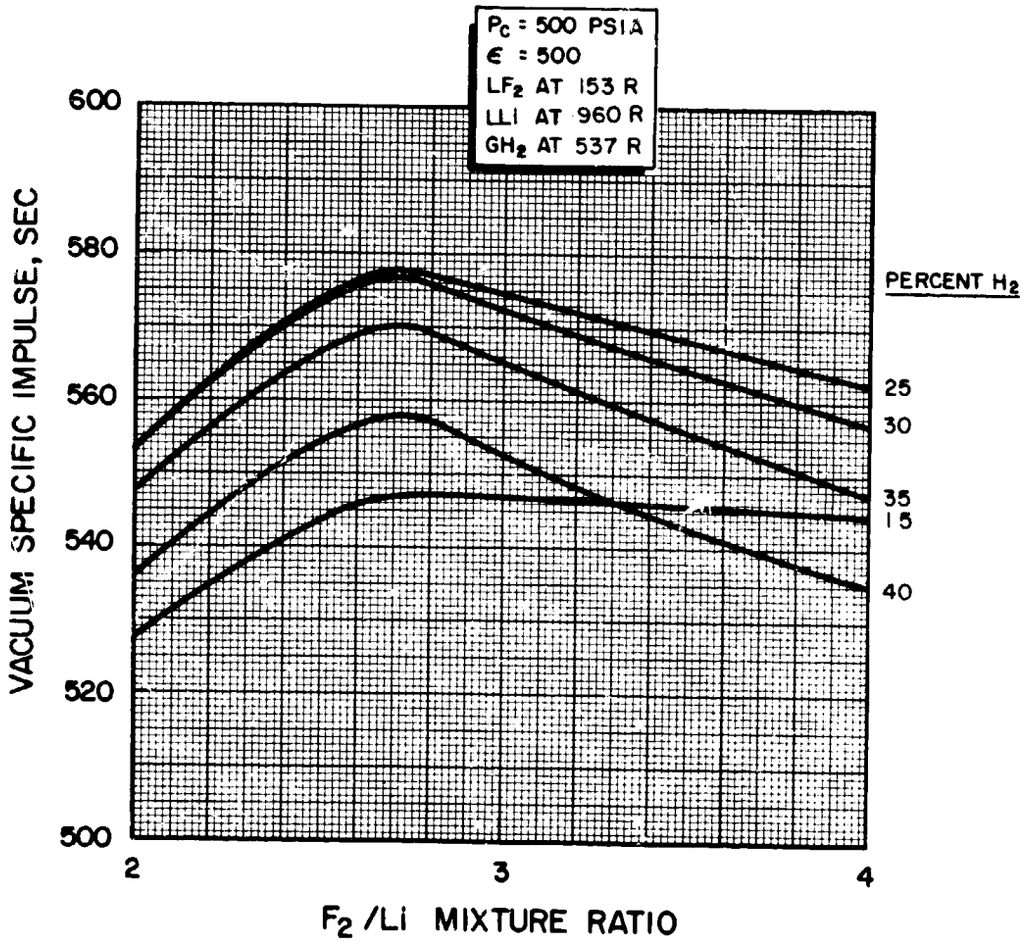

Figure 10. Variation of Vacuum Specific Impulse (Shifting Equilibrium) with F_2/Li Mixture Ratio at Indicated Percentages of Hydrogen, Chamber Pressure, and Expansion Ratio, LF_2(153 R)/LLi(960 R)/GH_2(537 R).

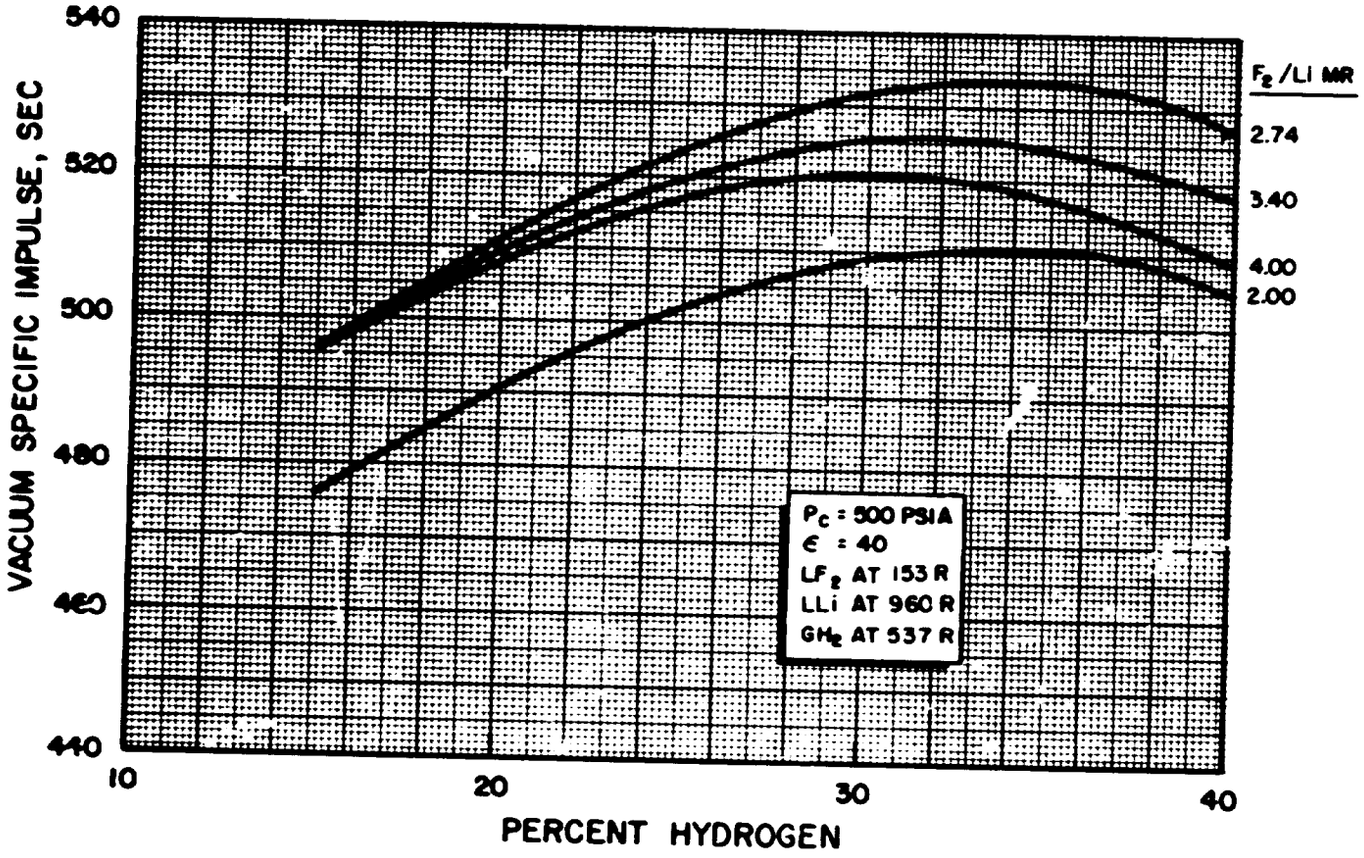

Figure 11. Variation of Vacuum Specific Impulse (Shifting Equilibrium) with Percent Hydrogen, at Indicated F_2/Li M.R., Chamber Pressure, and Expansion Ratio, LF_2(153 R)/LLi(960 R)/GH_2(537 R)

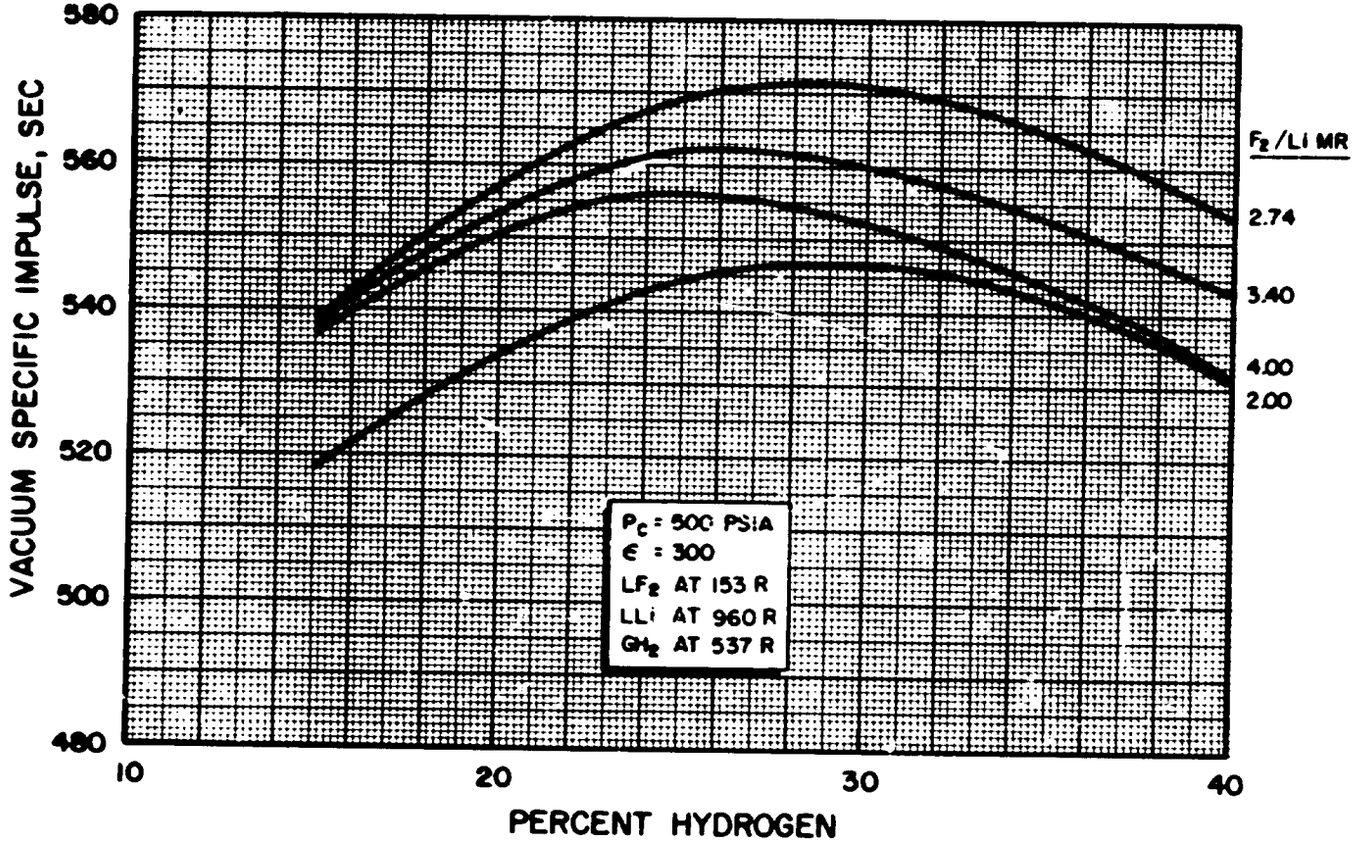

Figure 12. Variation of Vacuum Specific Impulse (Shifting Equilibrium) with Percent Hydrogen, at Indicated F_2/Li M.R., Chamber Pressure, and Expansion Ratio, LF_2(153 R)/LLi(960 R)/GH_2(537 R).

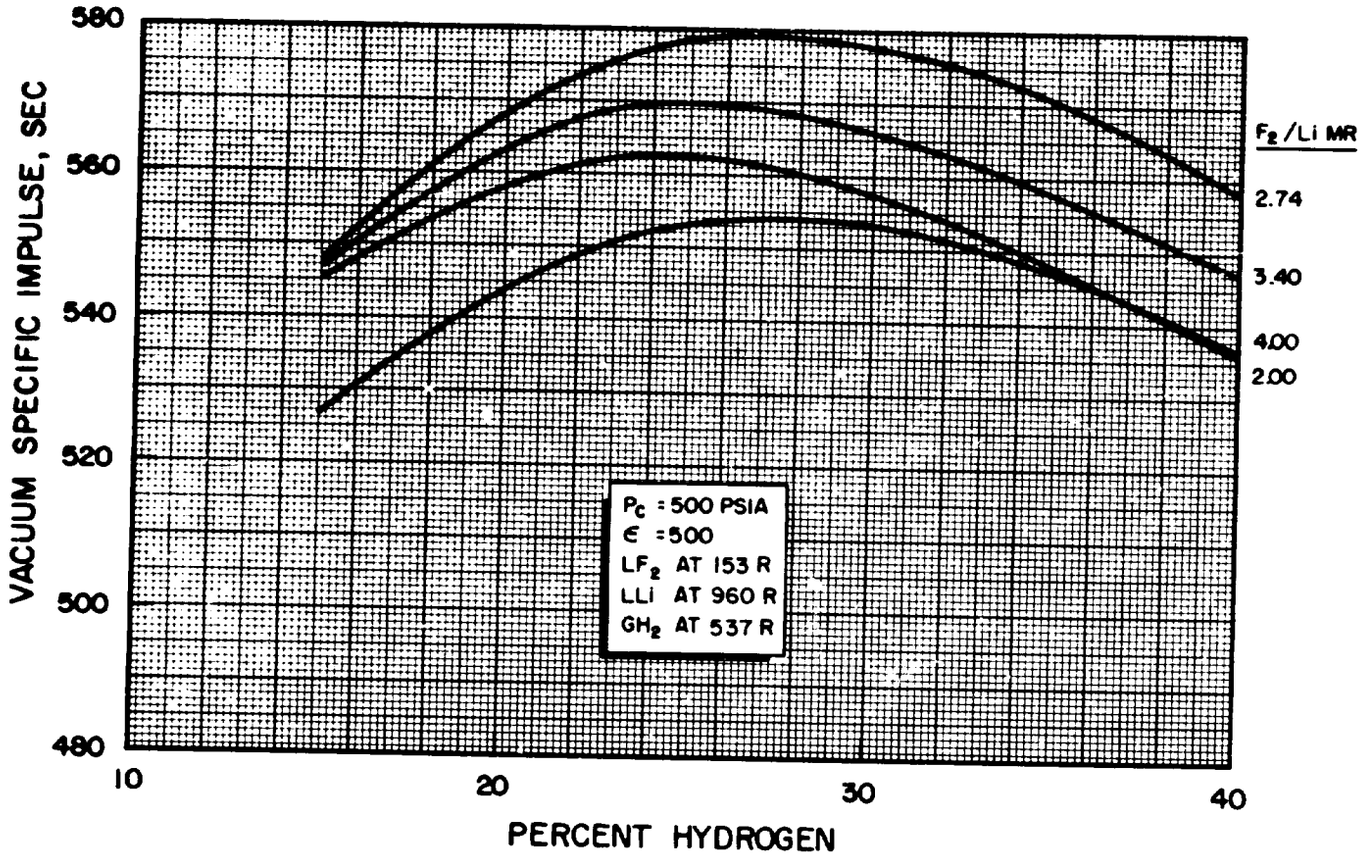

Figure 13. Variation of Vacuum Specific Impulse (Shifting Equilibrium) with Percent Hydrogen at Indicated F_2/Li M.R., Chamber Pressure, and Expansion Ratio, LF_2(153 R)/LLi(960 R)/GH_2(537 R).

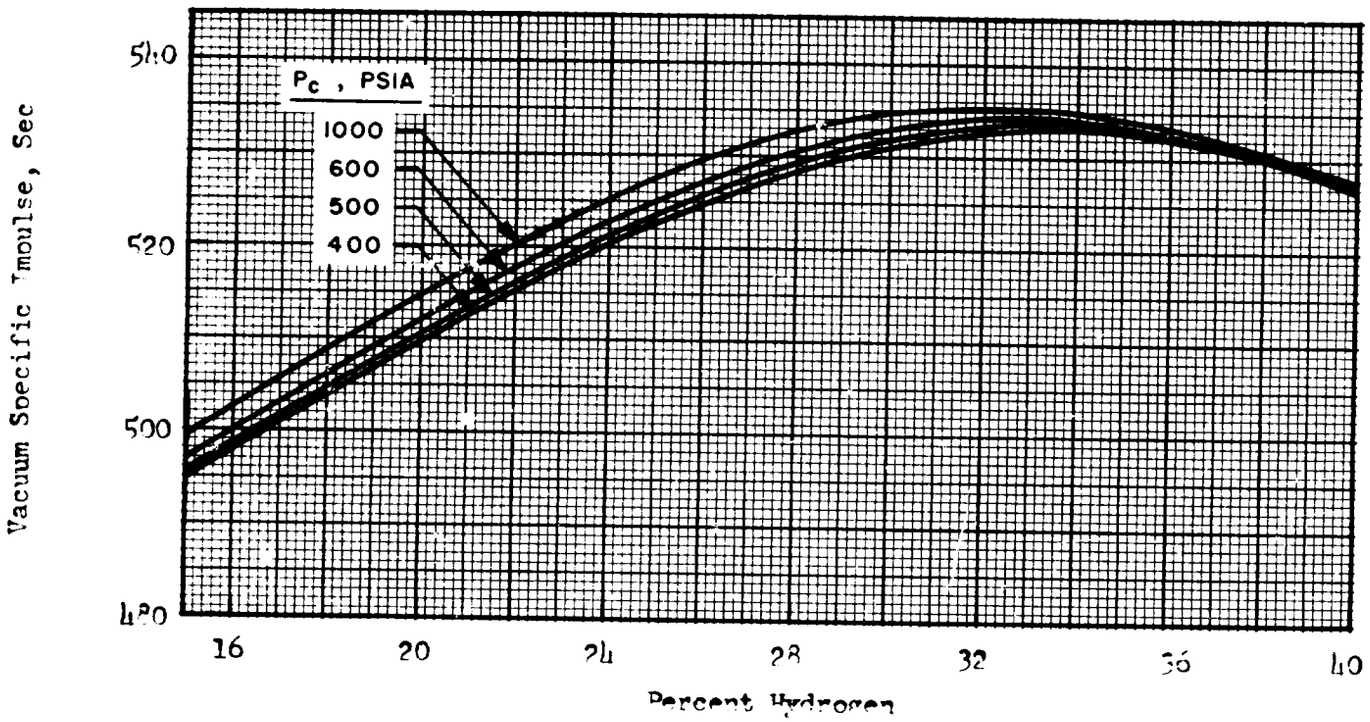

Figure 14. Vacuum Specific Impulse (Shifting Equilibrium) as Function of Percent Hydrogen at Indicated Chamber Pressures, F_2/Li M.R. = 2.74, ϵ = 40.
LF_2(153 R)/LLi(960 R)/GH_2(537 R).

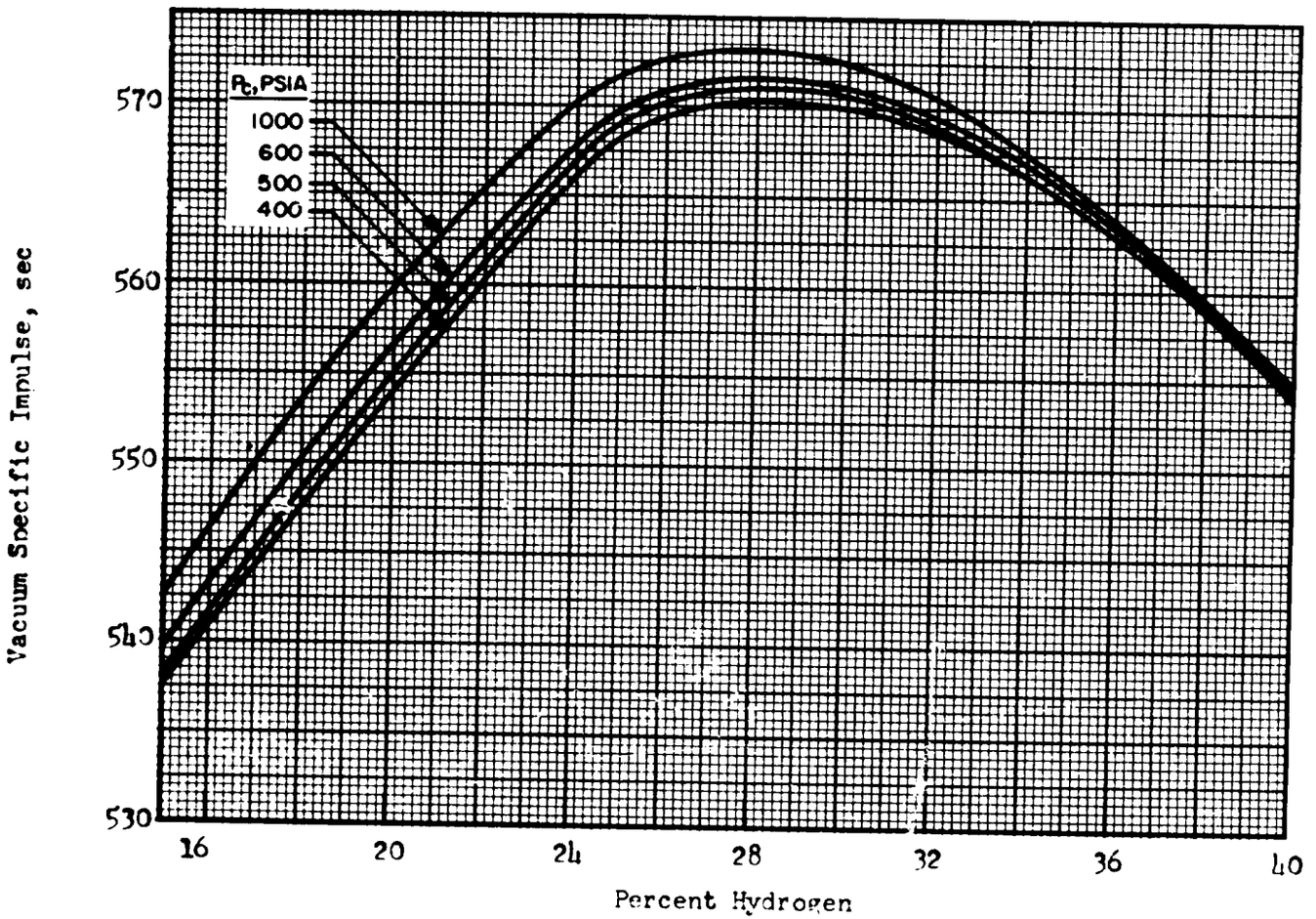

Figure 15. Vacuum Specific Impulse (Shifting Equilibrium) as a Function of Percent Hydrogen at Indicated Chamber Pressures, F_2/Li M.R. = 2.74, ϵ = 300. LF_2(153 R)/LLi(960 R)/GH_2(537 R).

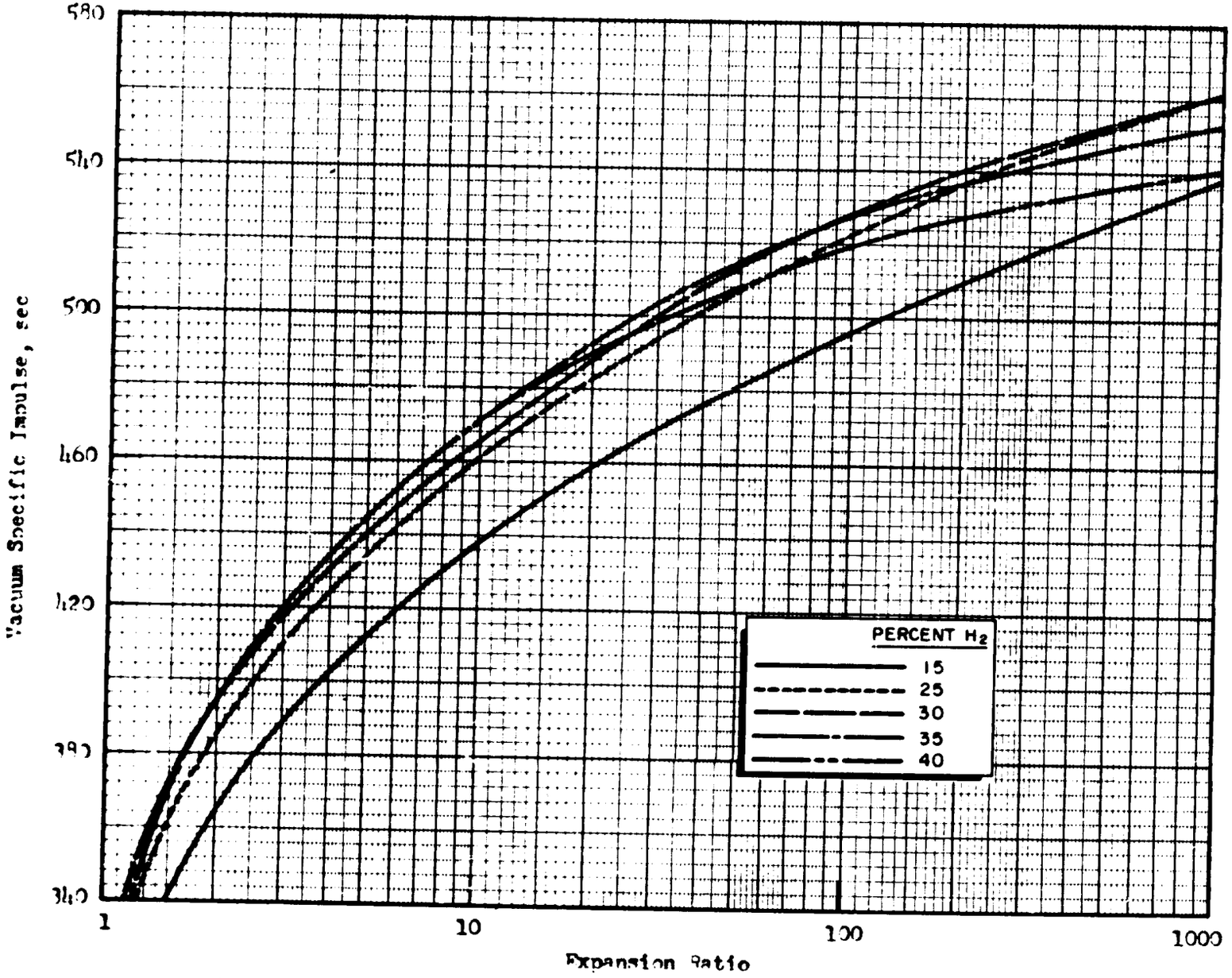

Figure 16. Variation of Vacuum Specific Impulse (Shifting Equilibrium) with Expansion Ratio at P_c = 500 psia, F_2 / Li M.R. = 2.00, and Indicated Percent Hydrogen, LF_2(153 R) / LLi(960 R) / GH_2(537 R).

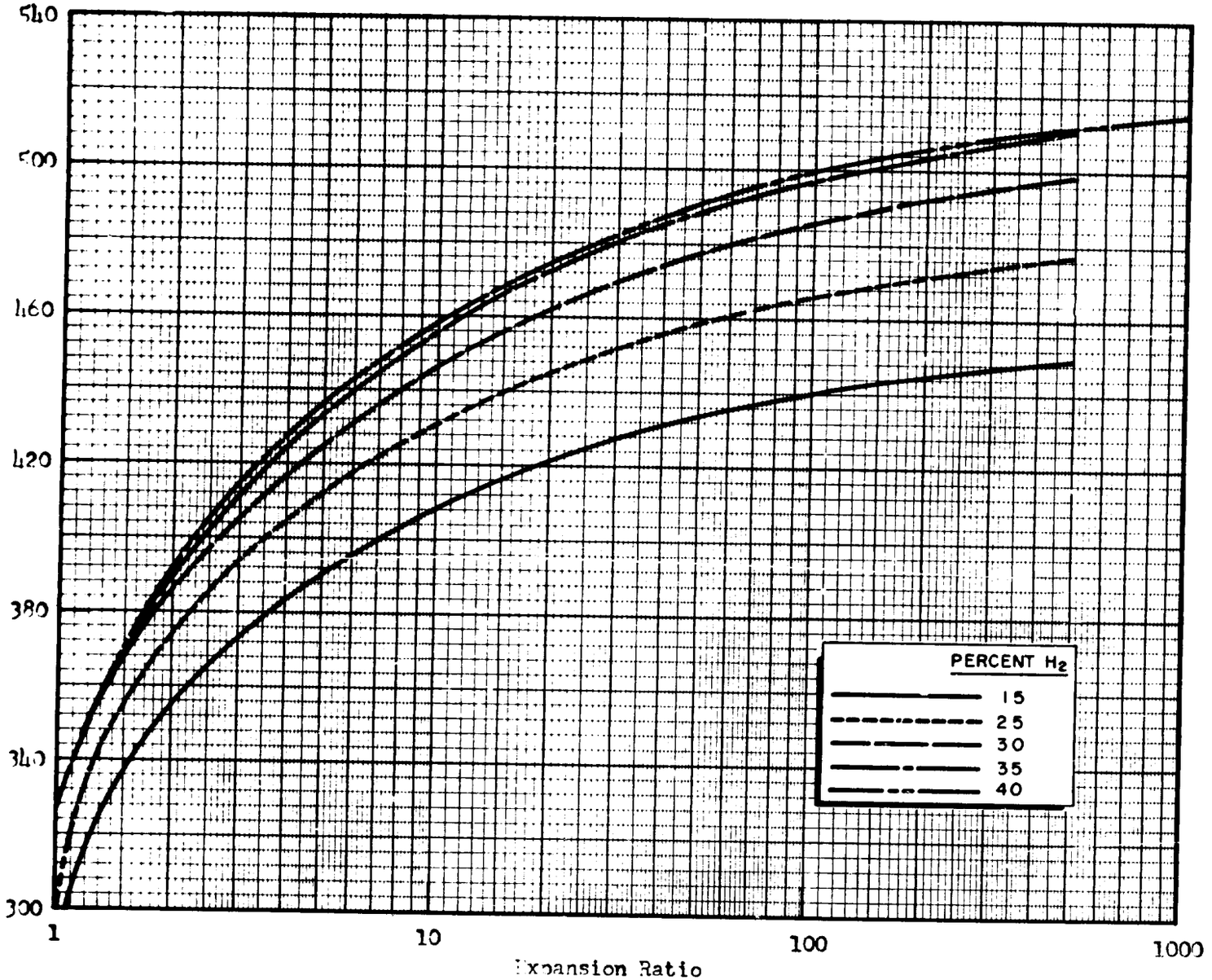

Figure 17. Variation of Vacuum Specific Impulse (Frozen Composition) with Expansion Ratio at P_c = 500 psia, F_2/Li M.R. = 2.00, and Indicated Percent Hydrogen, LF_2(153 R)/LLi(960 R)/GH_2(537 R).

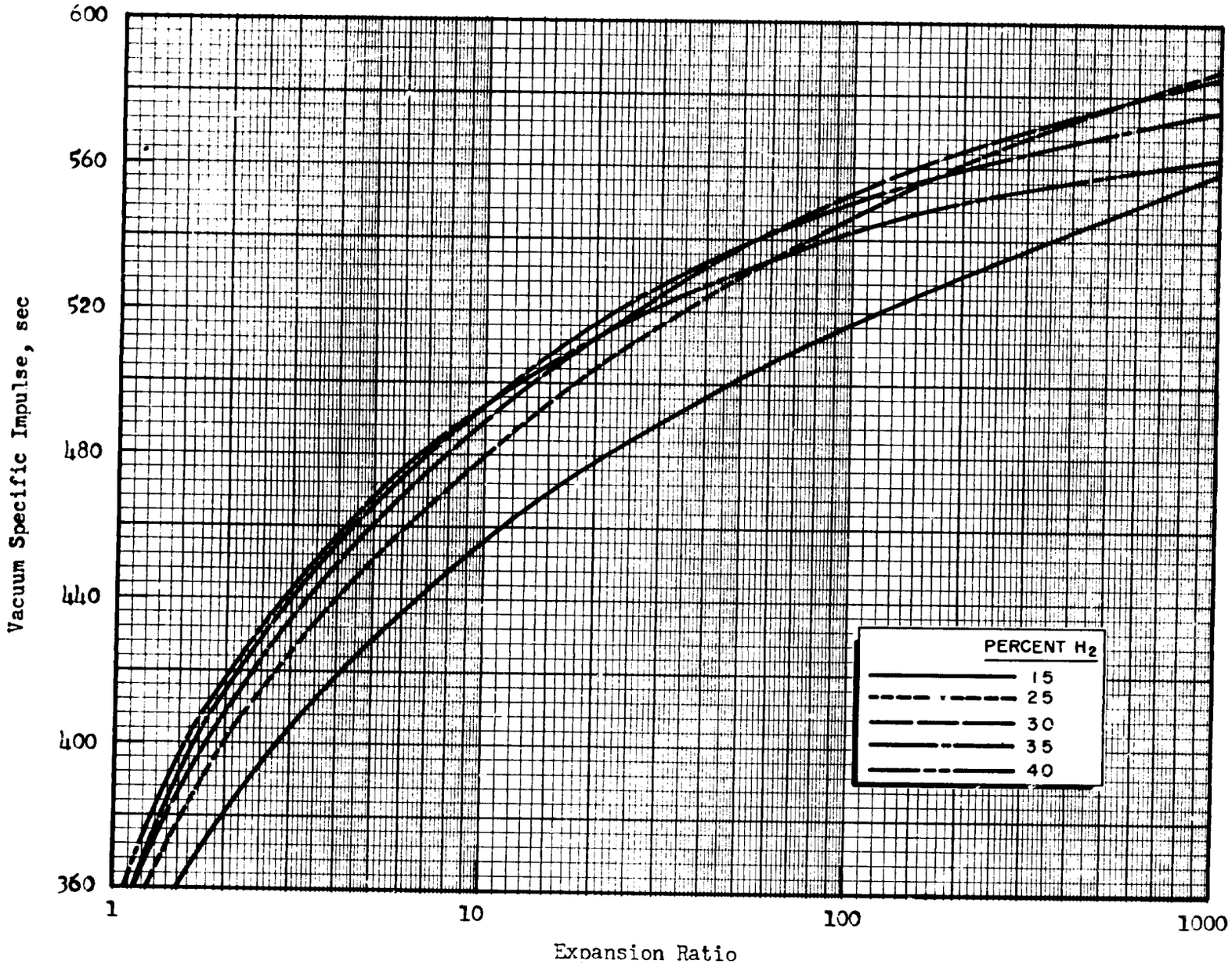

Figure 18. Variation of Vacuum Specific Impulse (Shifting Equilibrium) with Expansion Ratio at P_c = 500 psia, F_2/Li M.R. = 2.74, and Indicated Percent Hydrogen, LF_2(153 R)/LLi(960 R)/GH_2(537 R).

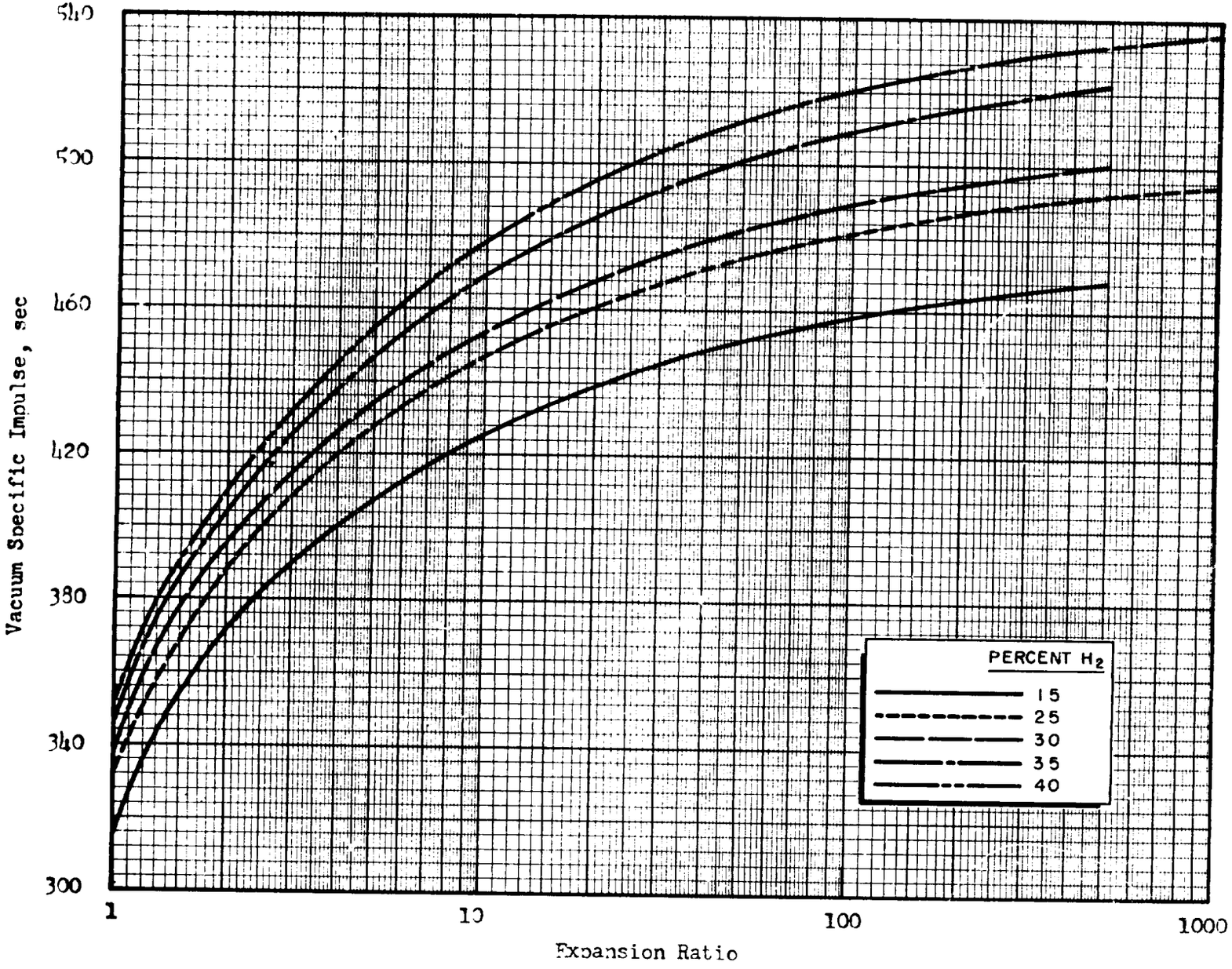

Figure 19. Variation of Vacuum Specific Impulse (Frozen Composition) with Expansion Ratio at P_c = 500 psia, F_2/Li M.R. = 2.74, and Indicated Percent Hydrogen, LF_2(153 R)/LLi(960 R)/GH_2(537 R).

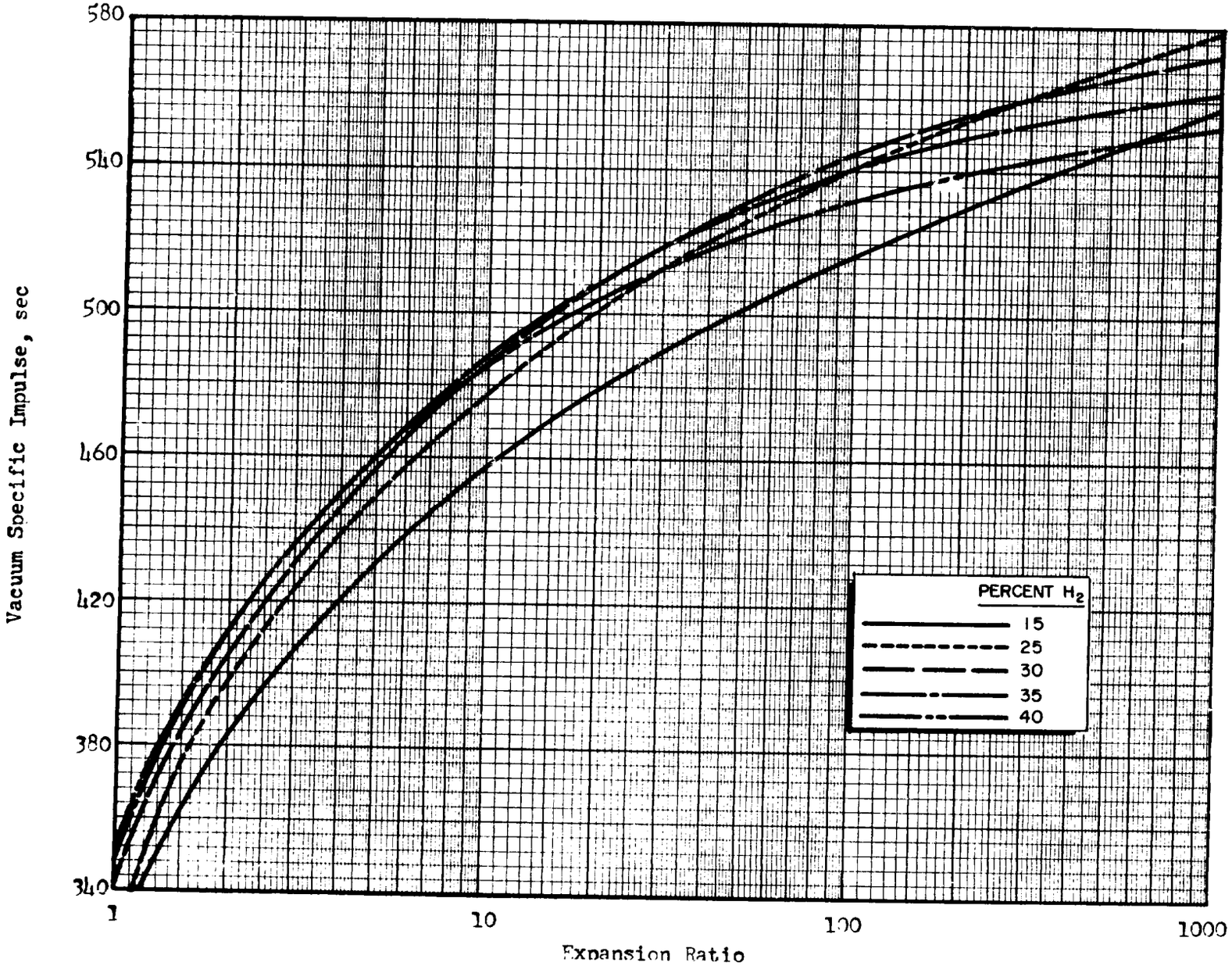

Figure 20. Vacuum Specific Impulse (Shifting Equilibrium) as Function of Expansion Ratio at Indicated Percent Hydrogen. P_c = 500 psia, F_2/Li M.R. = 3.40. LF_2(153 R)/LLi(960 R)/GH_2(537 R).

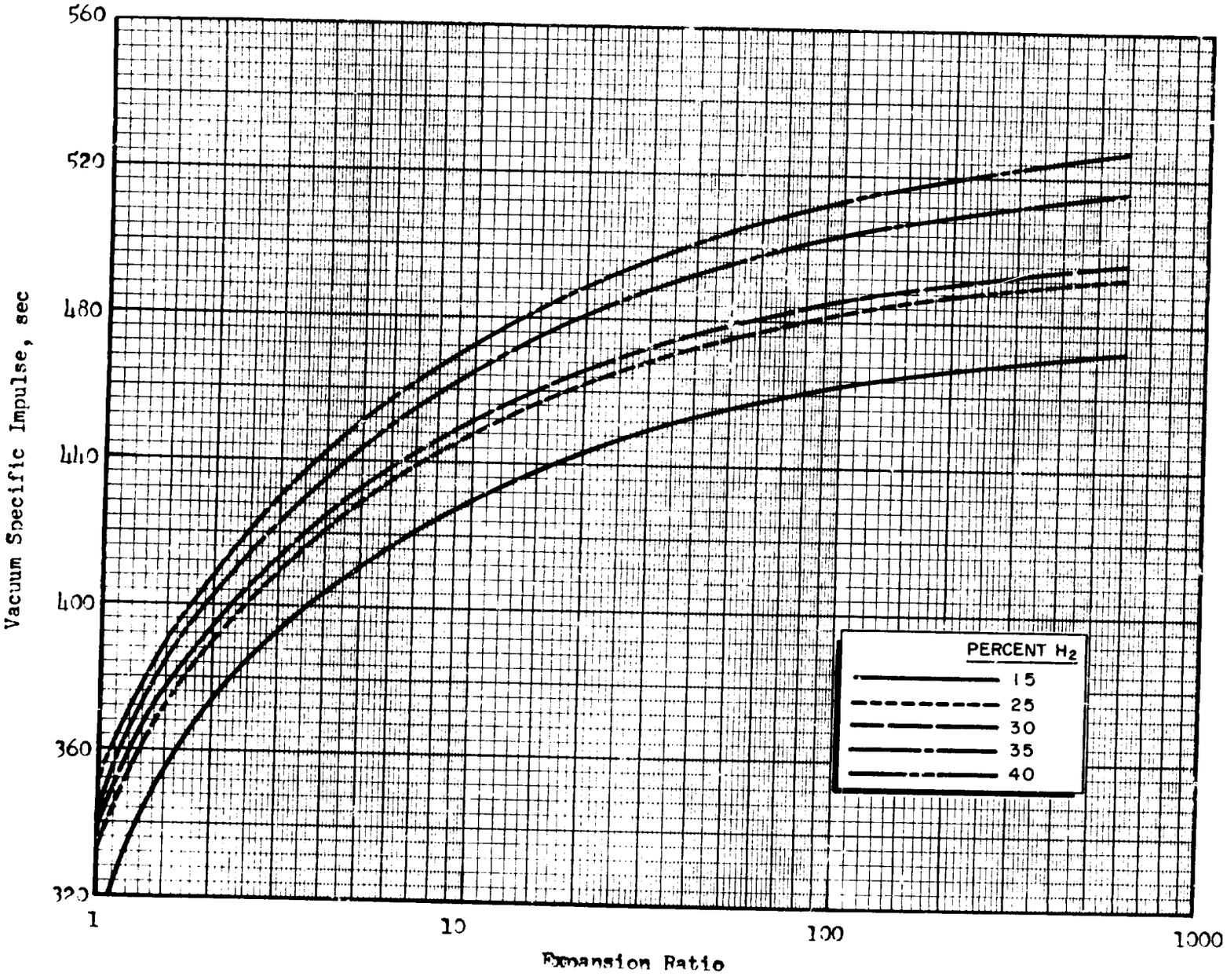

Figure 21. Vacuum Specific Impulse (Frozen Composition) as Function of Expansion Ratio at Indicated Percentages of Hydrogen. P = 500 psia, F_2/Li M.R. = 3.40. LF_2(153 R)/LLi (960 R)/GH_2(537 R).

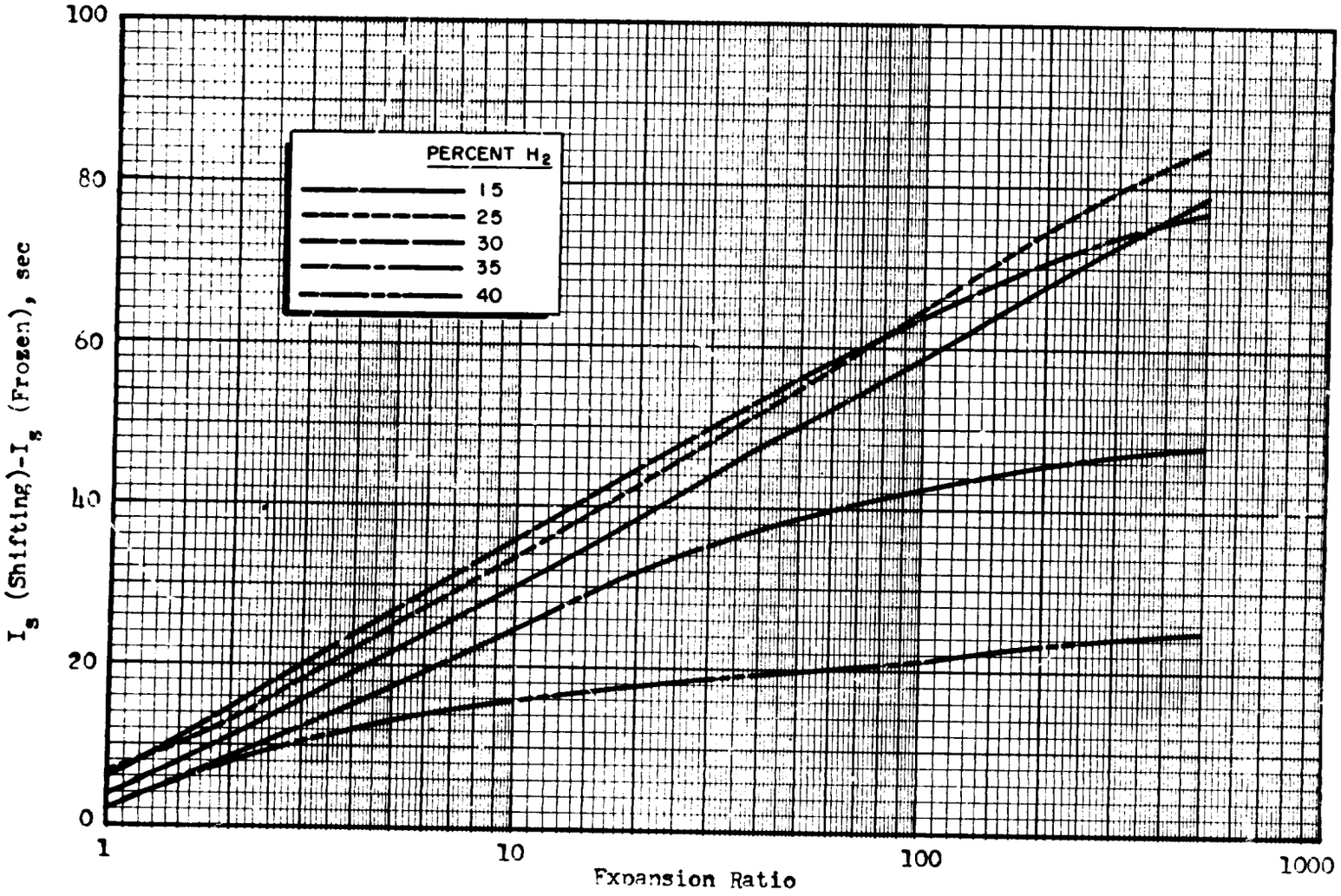

Figure 22. Difference between Shifting Equilibrium and Frozen Composition Vacuum Specific Impulse at Indicated Percentages of Hydrogen. P_c = 500 psia, F_2/Li M.R. = 2.74. LF_2(153 R)/LLi(960 R)/GH_2(537 R).

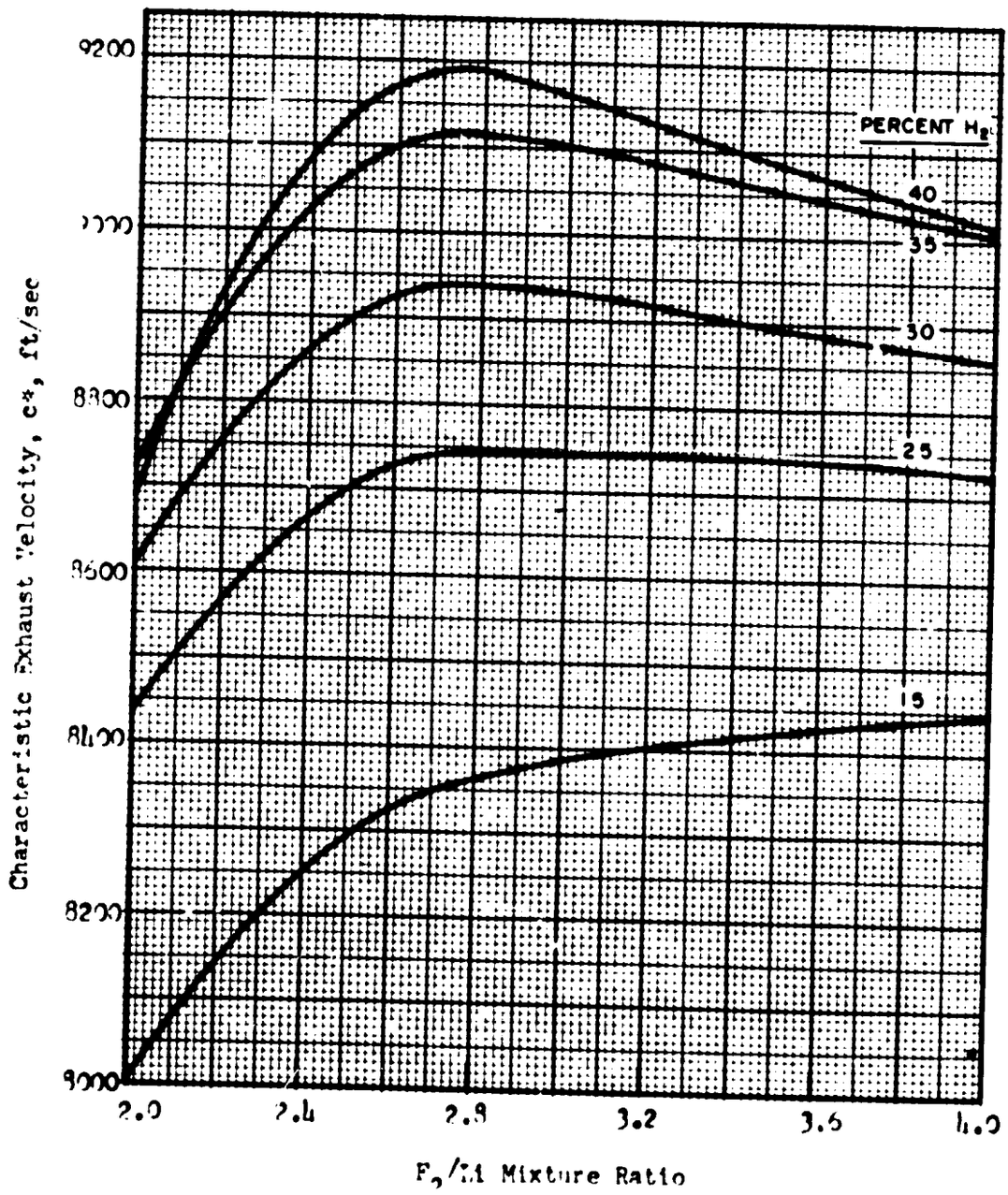

Figure 23. Variation of c* (Shifting Equilibrium) with F_2/Li Mixture Ratio at P_c = 500 psia and Indicated Percentages of Hydrogen, LF_2(153 R)/Li(960 R)/GH_2(537 R).

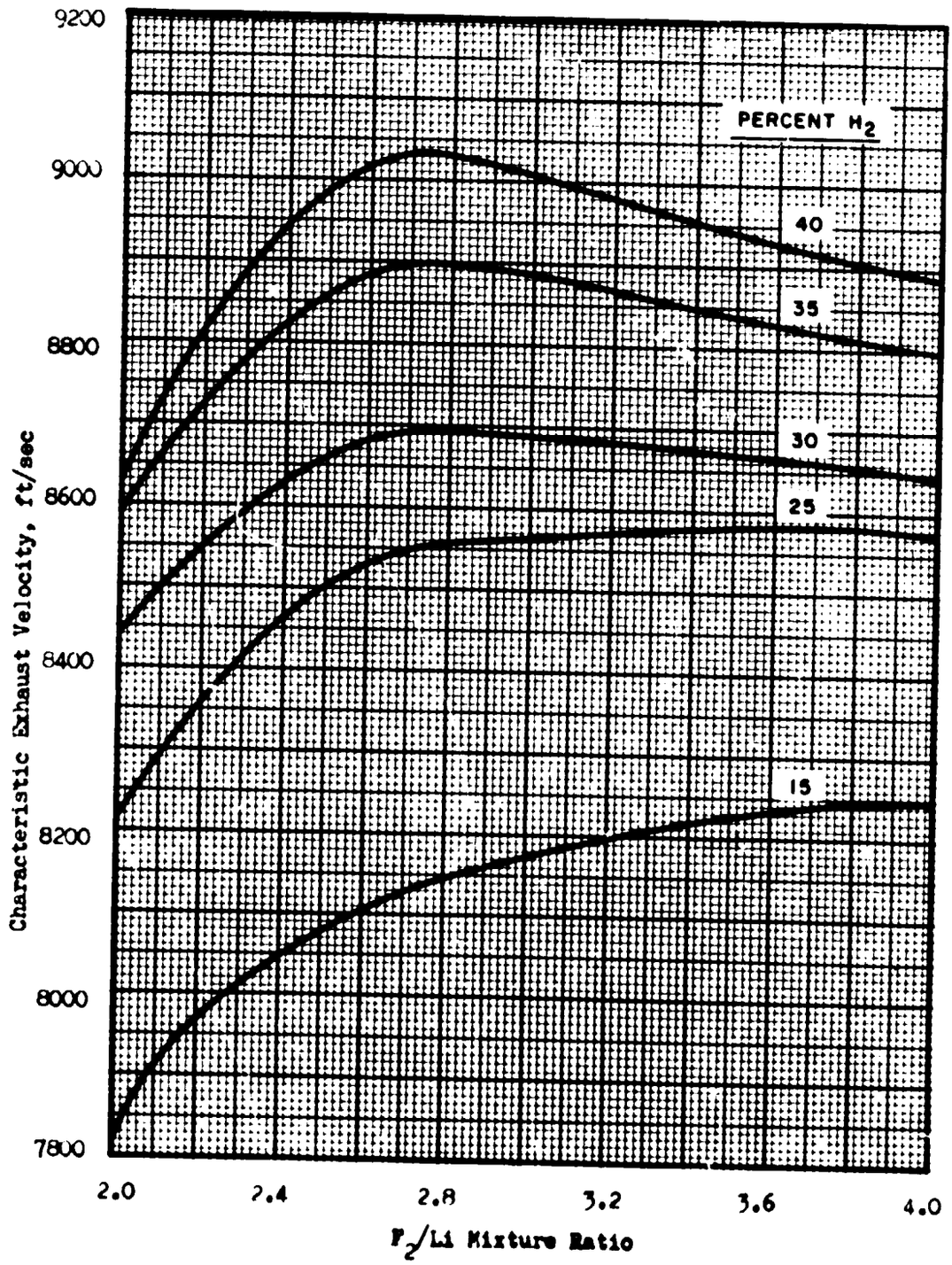

Figure 24. Variation of c* (Frozen Composition) with F_2/Li Mixture Ratio at Indicated Percent Hydrogen, P_c = 500 psia, LF_2(153 R)/LLi(960 R)/GH_2(537 R).

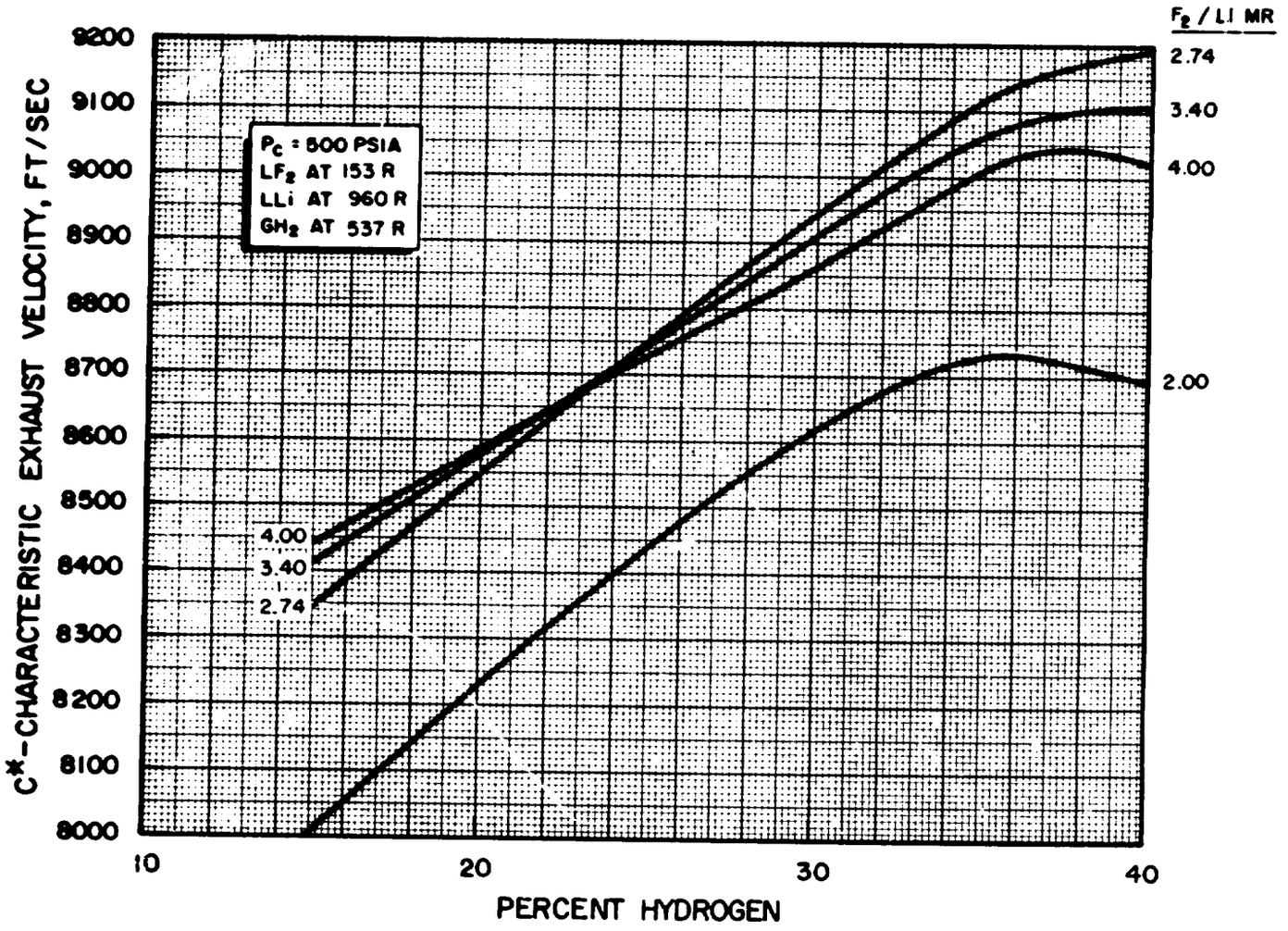

Figure 25. Variation of c* (Shifting Equilibrium) with Percent Hydrogen at Indicated F_2/Li M.R. and Chamber Pressure, LF_2(153 R)/LLi(960 R)/GH_2(537 R).

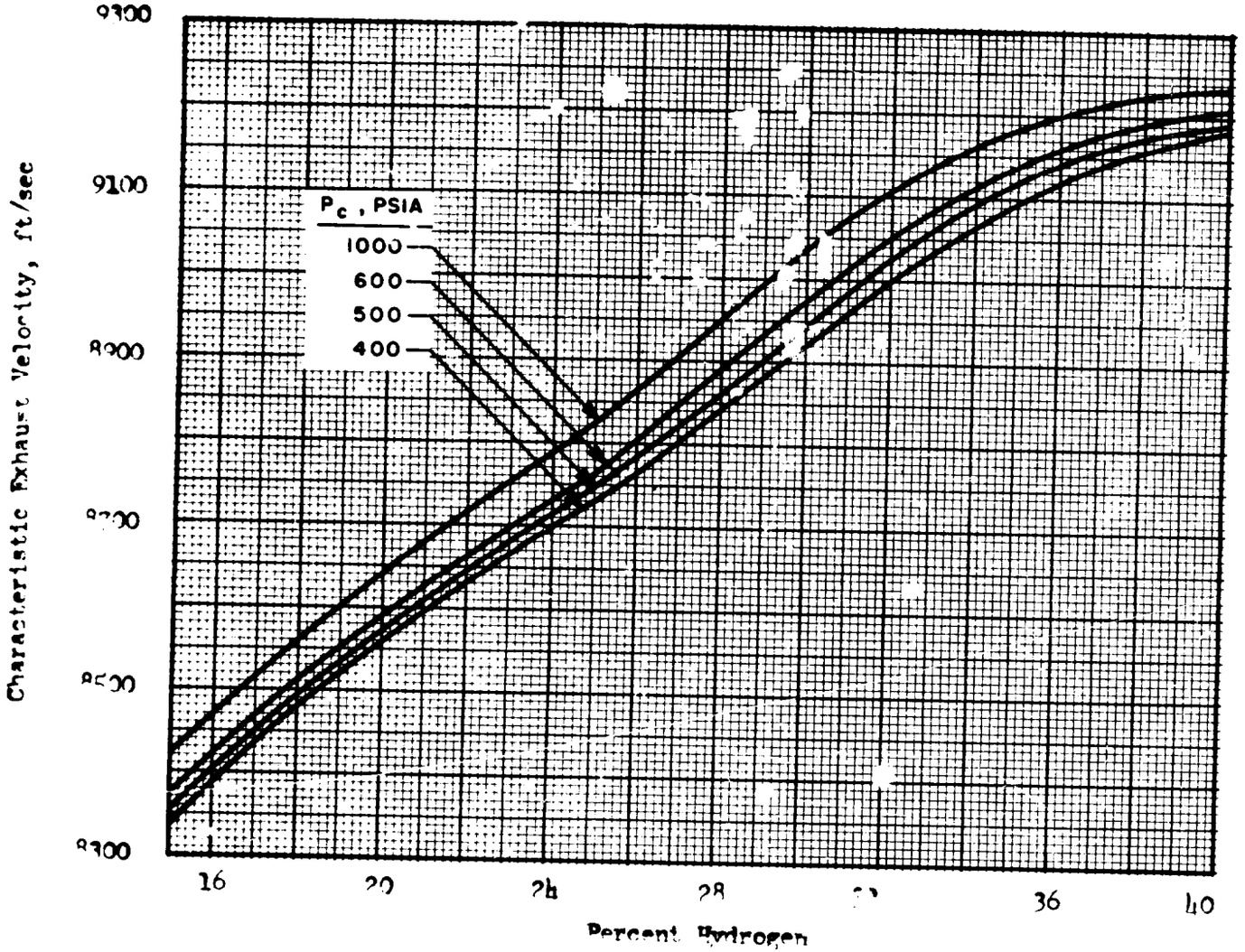

Figure 26. Variation of c* (Shifting Equilibrium) with Percent Hydrogen at Indicated Chamber Pressures, F_2/Li M.R. = 2.74. LF_2(153 R)/LLi(960 R)/GH_2(537 R).

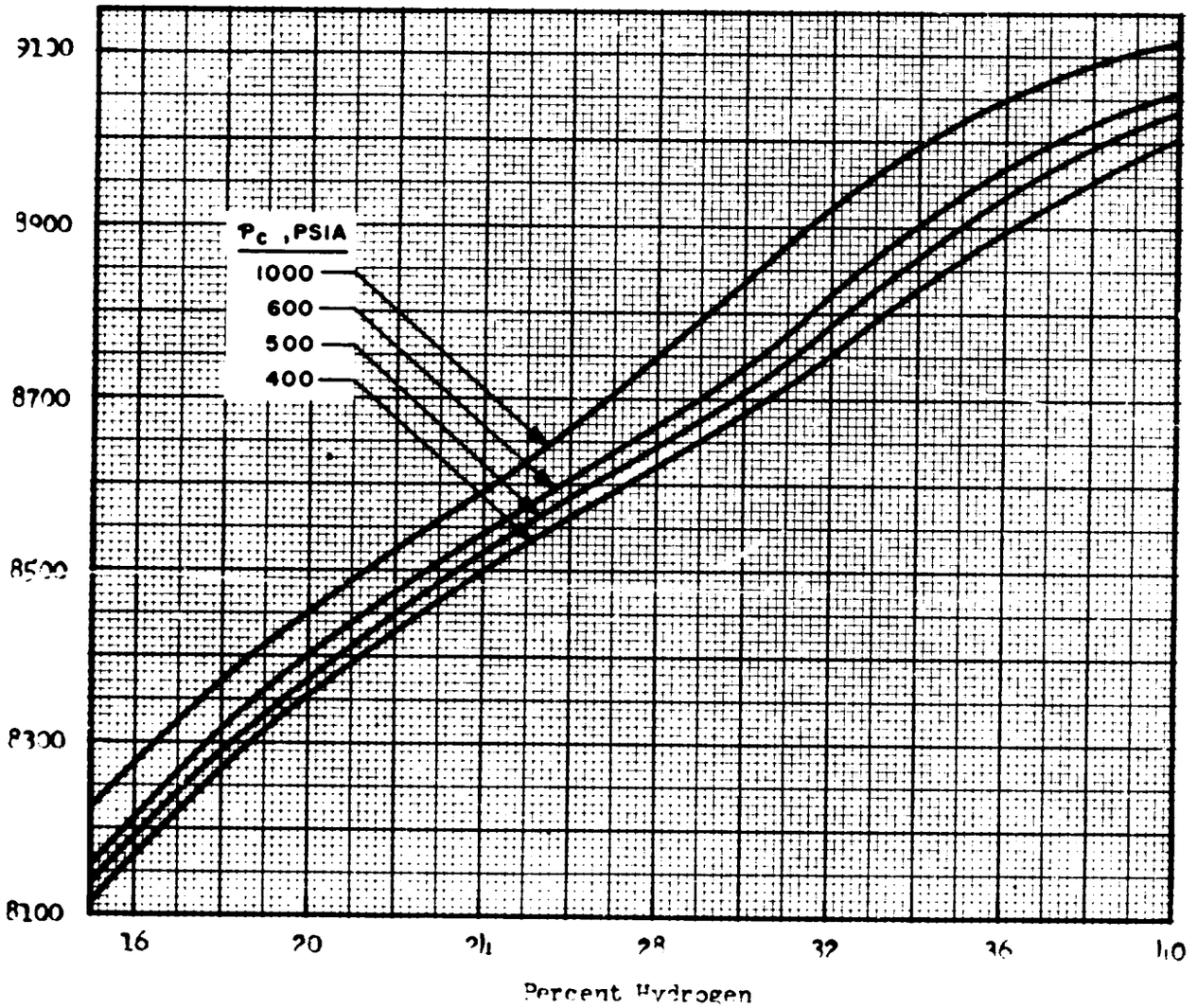

Figure 27. Variation of c_s (Frozen Composition) with Percent Hydrogen at Indicated Chamber Pressures, F_2/Li M.R. = 2.74. LF_2(153 R) /LLi(960 R)/GH_2(537 R).

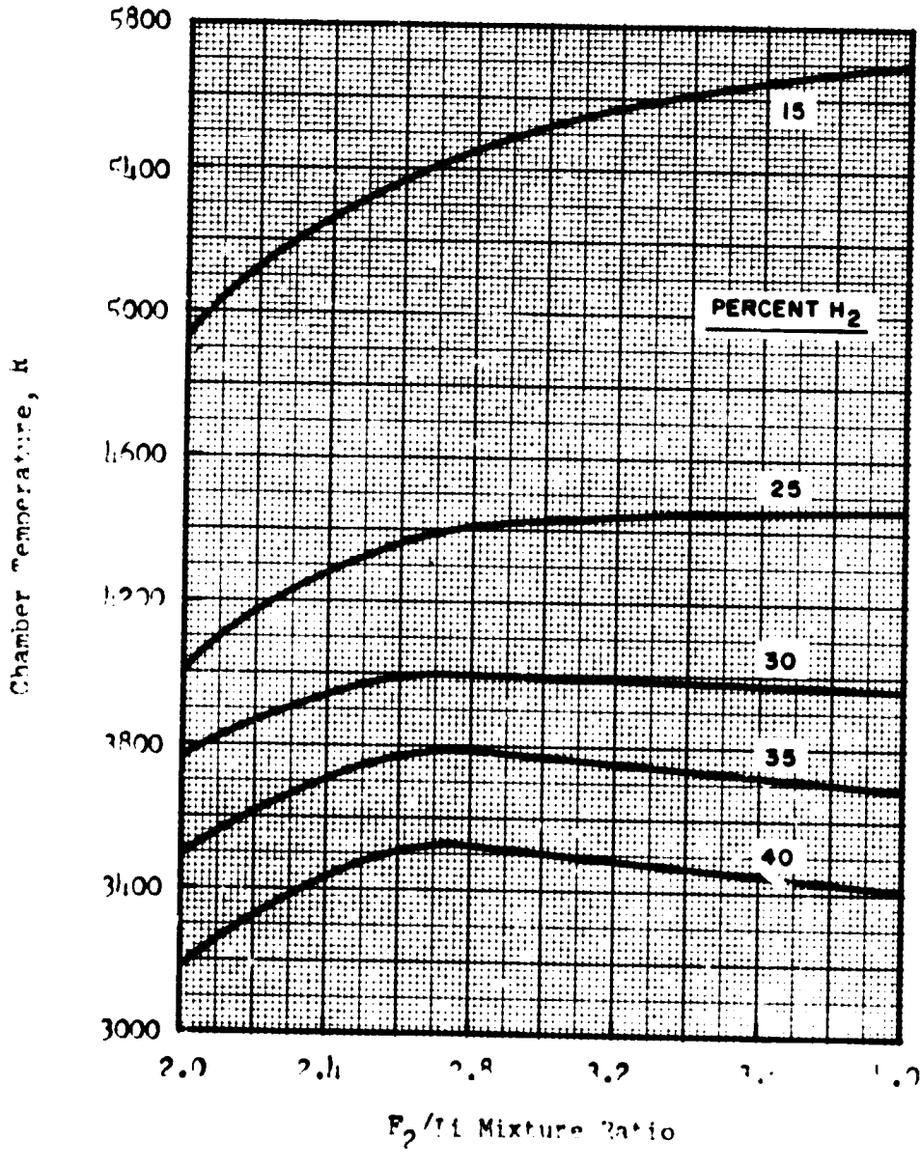

Figure 28. Variation of Chamber Temperature with F_2/Li Mixture Ratio at Indicated Percent Hydrogen, P_c = 500 psia. LF_2(153 R)/LLi(960 R)/GH_2(537 R).

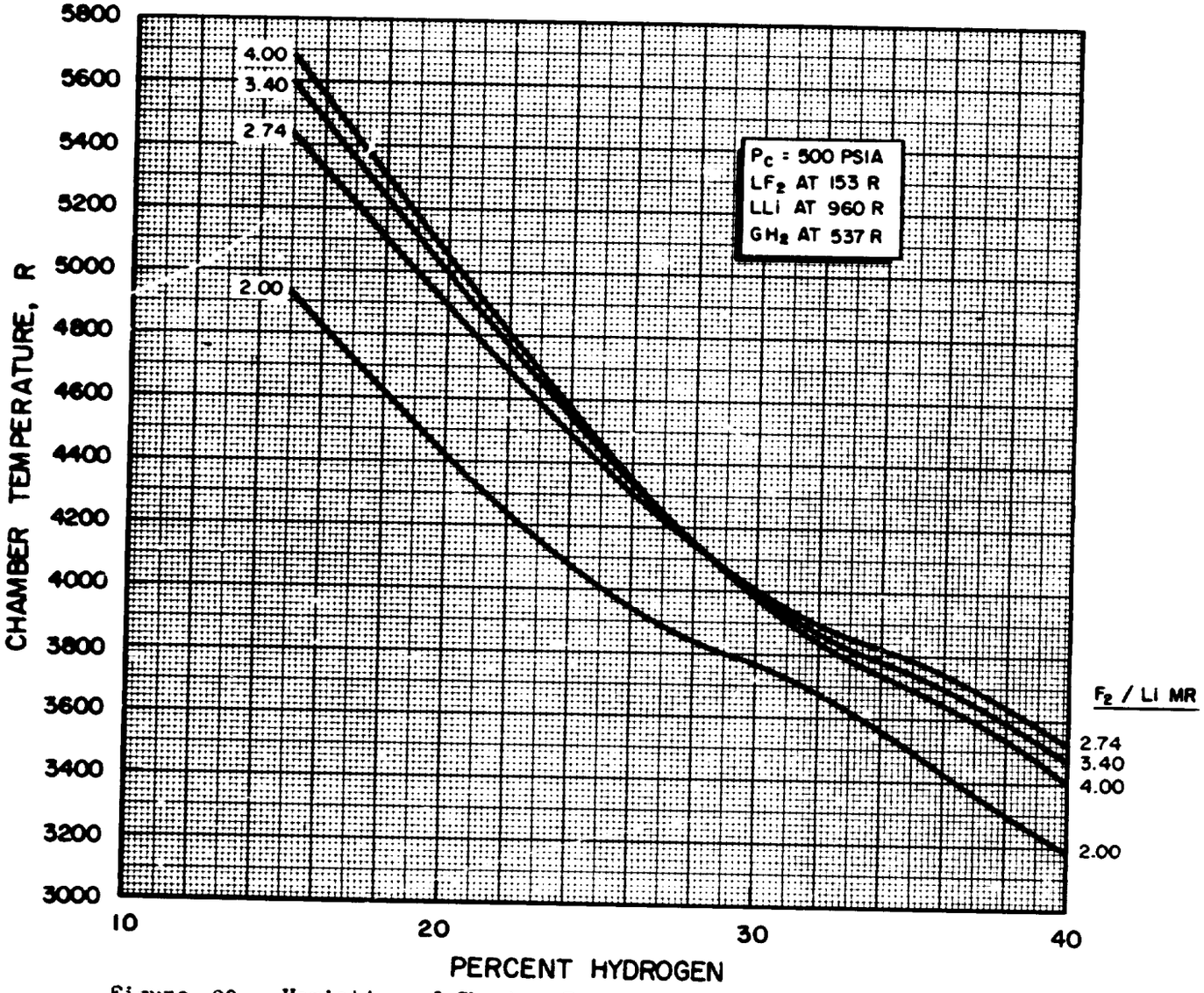

Figure 29. Variation of Chamber Temperature with Percent Hydrogen at Indicated Chamber Pressure, LF_2(153 R)/LLi(960 R)/GH_2(537 R).

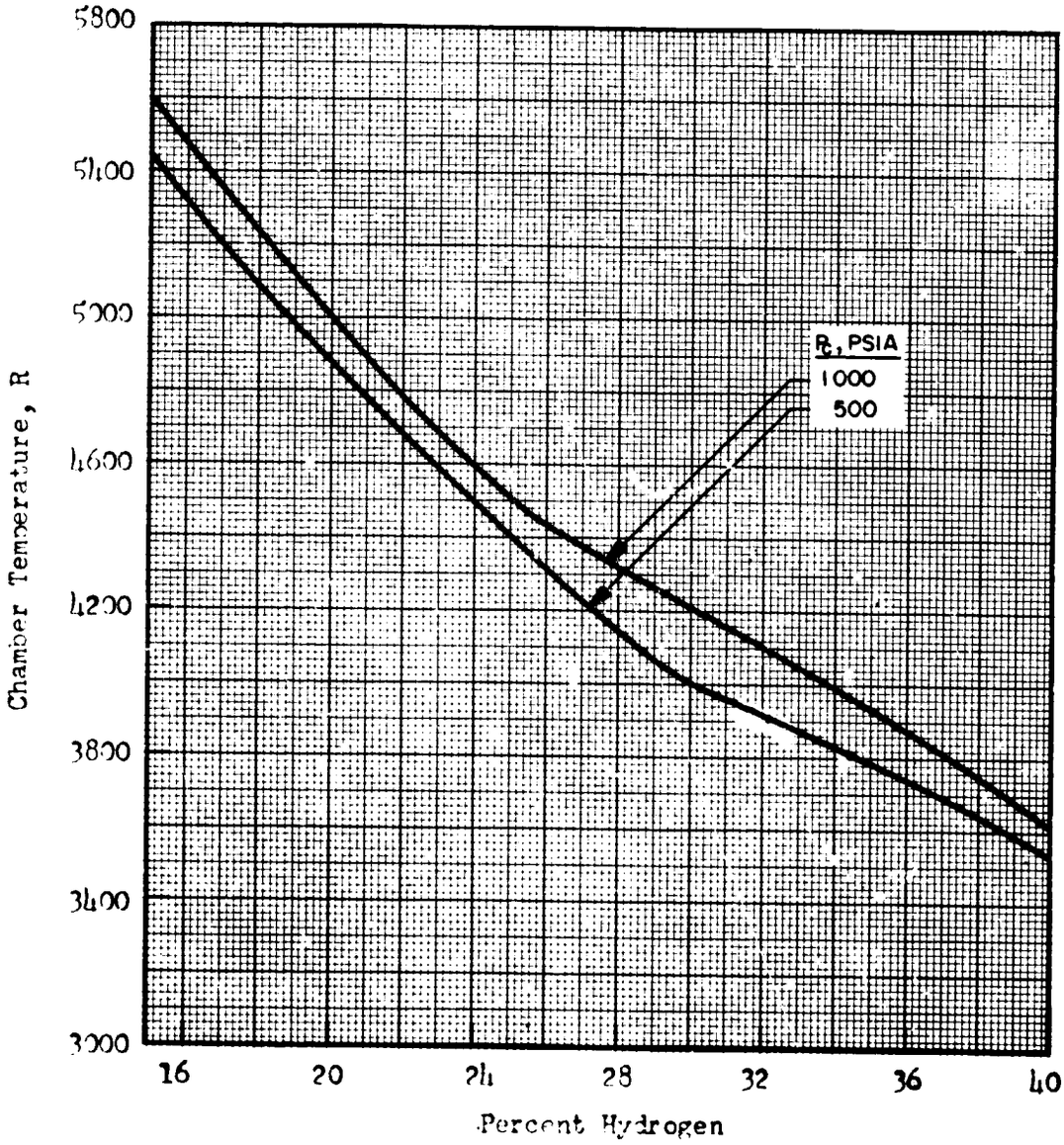

Figure 30. Chamber Temperature as Function of Percent Hydrogen at Indicated Chamber Pressures. LF_2(153 R)/LLi(960 R)/GH_2(537 R).

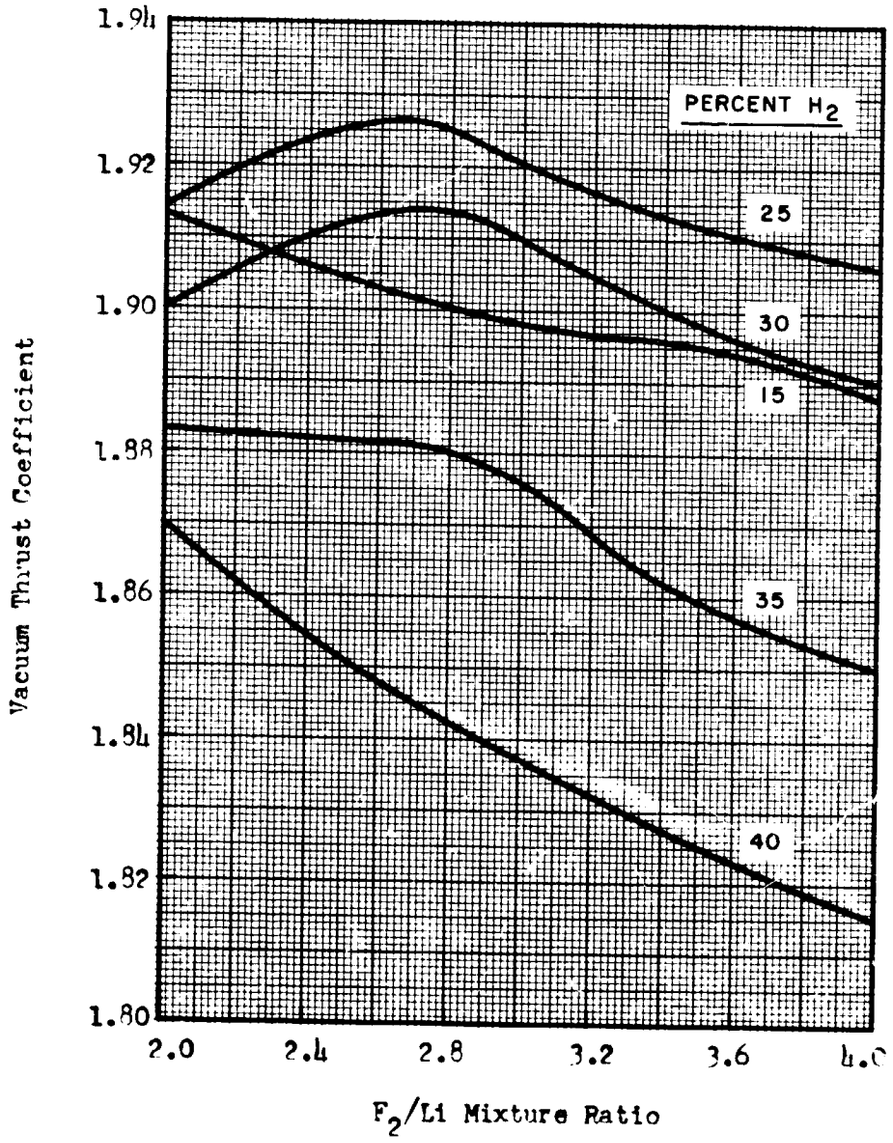

Figure 31 . Variation of Vacuum Thrust Coefficient (Shifting Equilibrium) with F_2/Li Mixture Ratio at Indicated Percent Hydrogen, P_c = 500 psia, ϵ = 40. LF_2(153 R)/LLi(960 R)/GH_2(537 R).

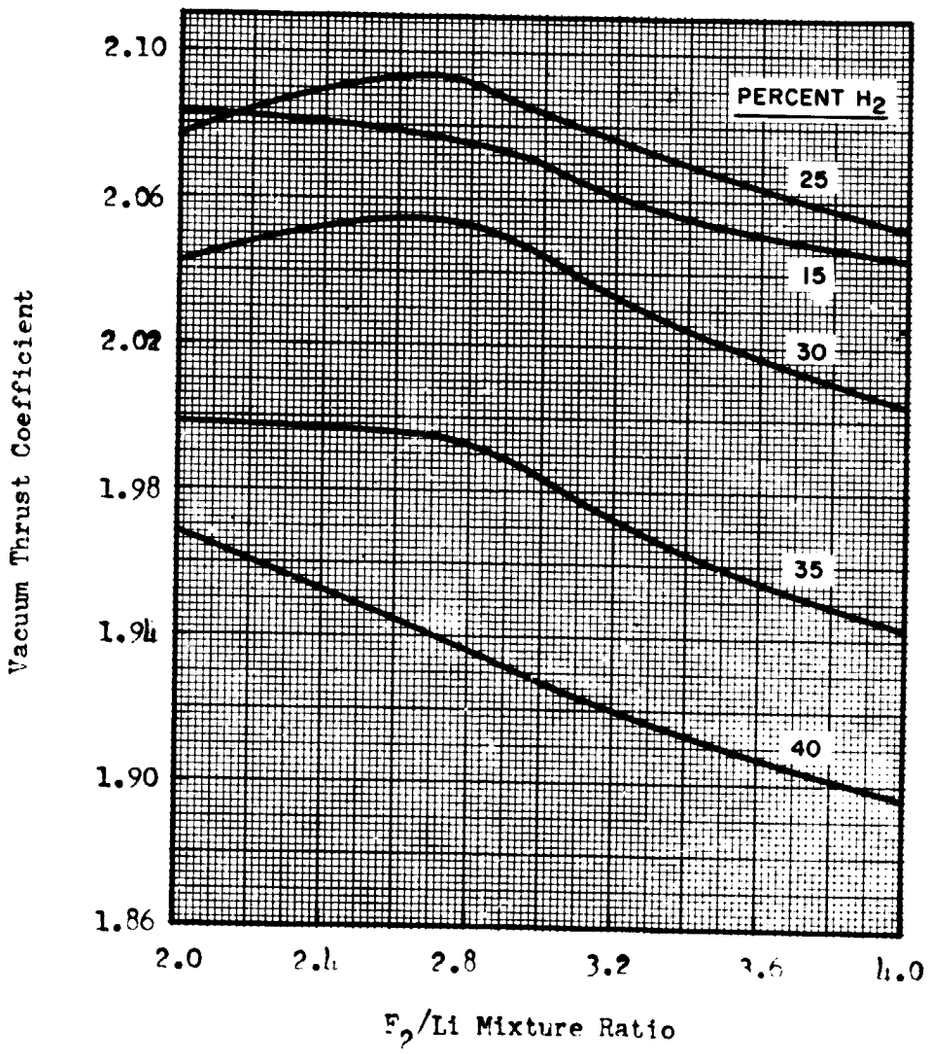

Figure 32 . Variation of Vacuum Thrust Coefficient (Shifting Equilibrium) with F_2/Li Mixture Ratio at Indicated Percent Hydrogen, P_c = 500 psia, ϵ = 300. LF_2(153 R)/LLi(960 R)/GH_2(537 R).

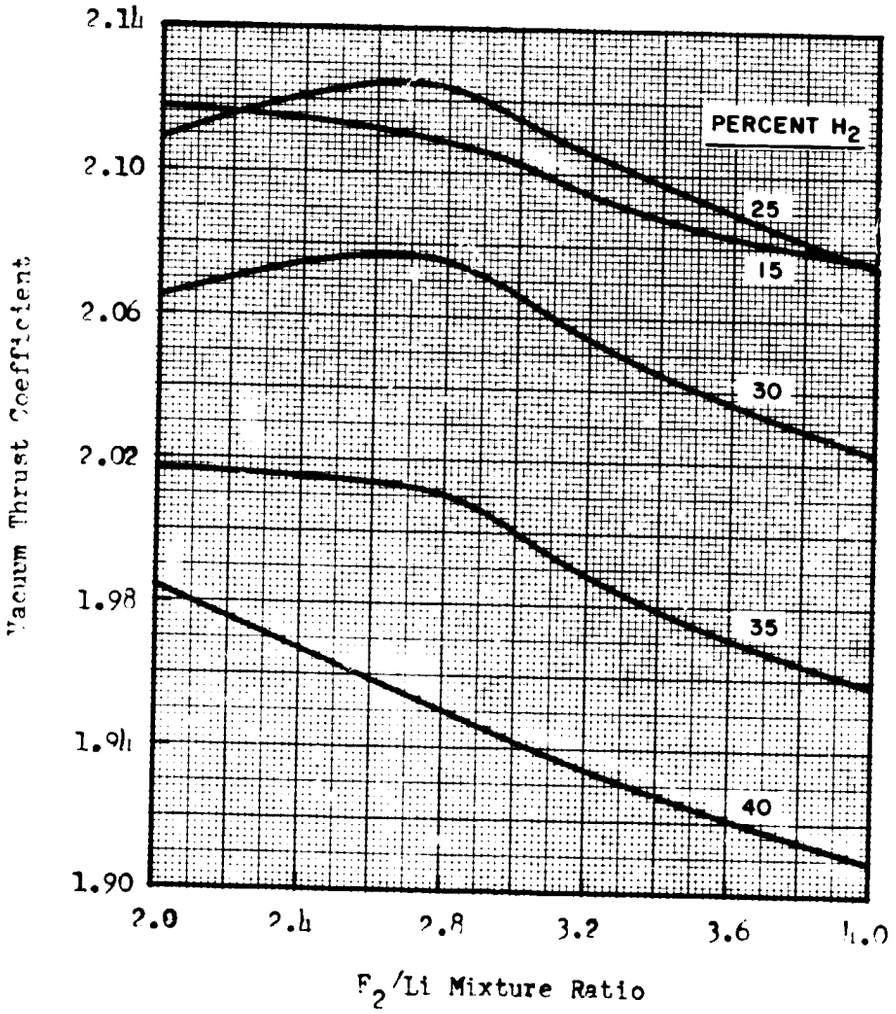

Figure 33. Variation of Vacuum Thrust Coefficient (Shifting Equilibrium) with F_2/Li Mixture Ratio at Indicated Percent Hydrogen, P_c = 500 psia, ϵ = 500. LF_2(153 R)/LLi(960 R)/GH_2(537 R).

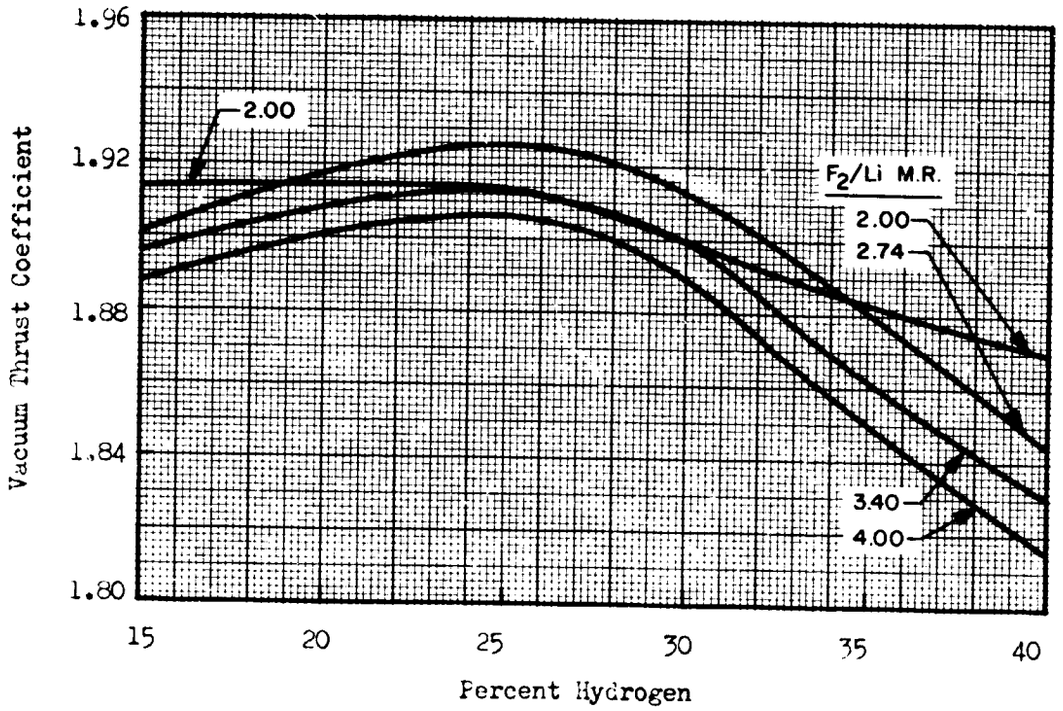

Figure 34. Variation of Vacuum Thrust Coefficient (Shifting Equilibrium) with Percent Hydrogen at Indicated F_2/Li Mixture Ratio, p_c = 500 Psia, ϵ = 40 LF_2(153 R)/LLi(960 R)/GH_2(537 R).

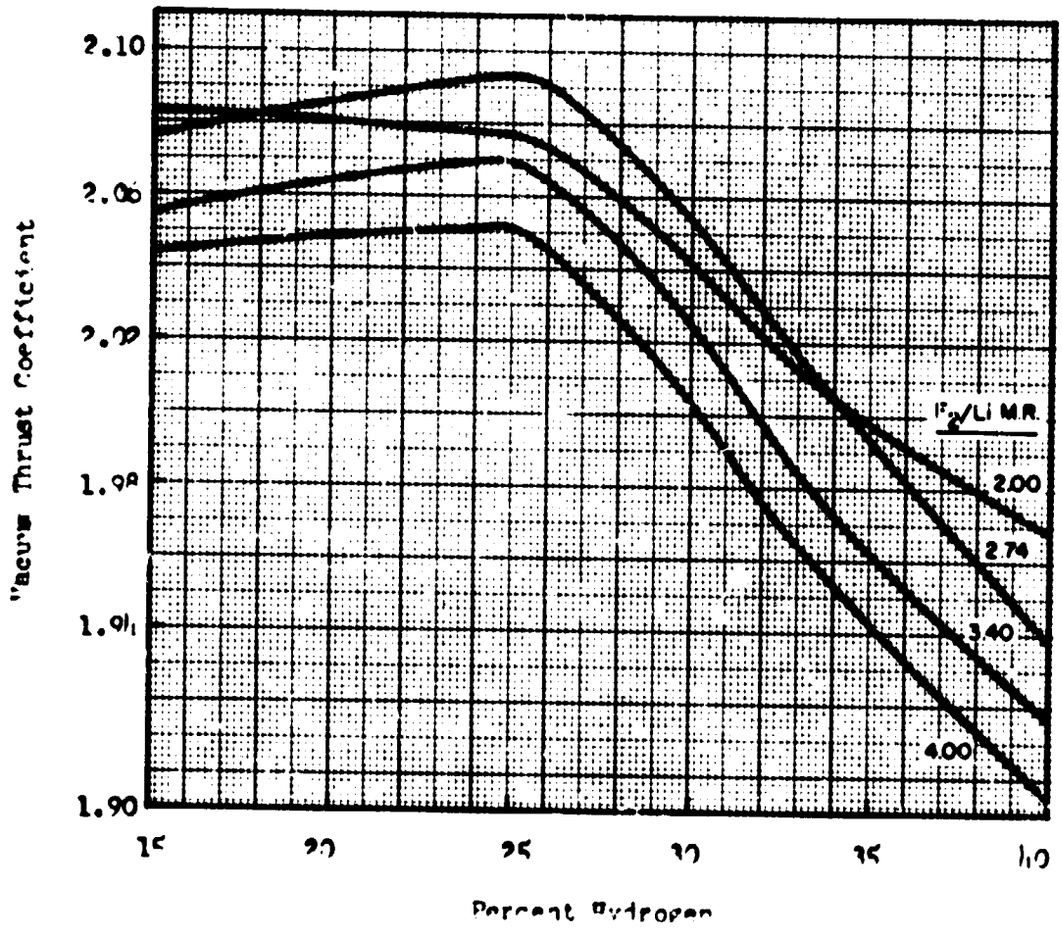

Figure 35. Variation of Vacuum Thrust Coefficient (Shifting Equilibrium) with Percent Hydrogen at Indicated F_2/Li Mixture Ratio, P_c = 500 psia, ϵ = 100. LF_2 (153 R) Li (960 R) GH_2 (537 R).

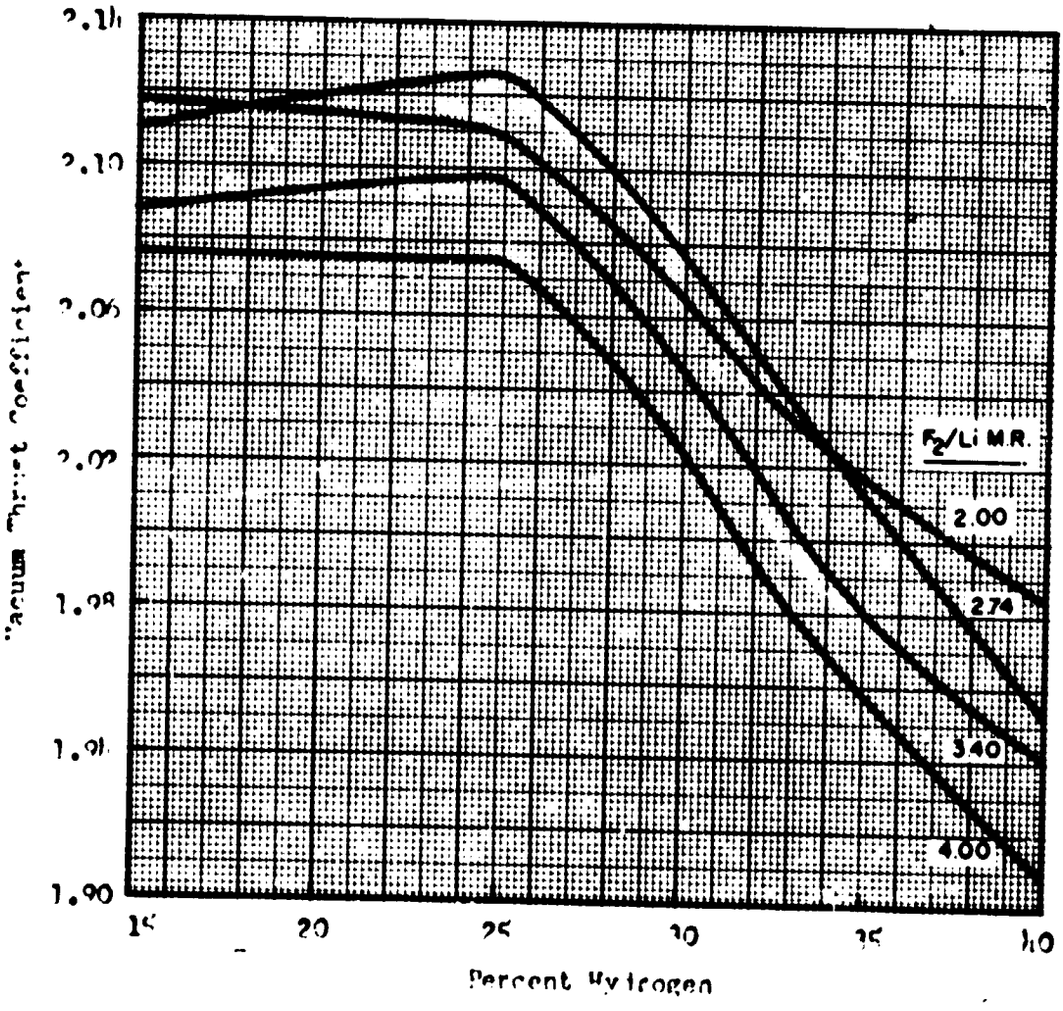

Figure 36. Variation of Vacuum Thrust Coefficient (Shifting Equilibrium) with Percent Hydrogen at Indicated F_2/Li Mixture Ratio. P_c = 500 psia, ϵ = 500, LF_2(155 R) / Li (960 R) / GH_2(537 R).

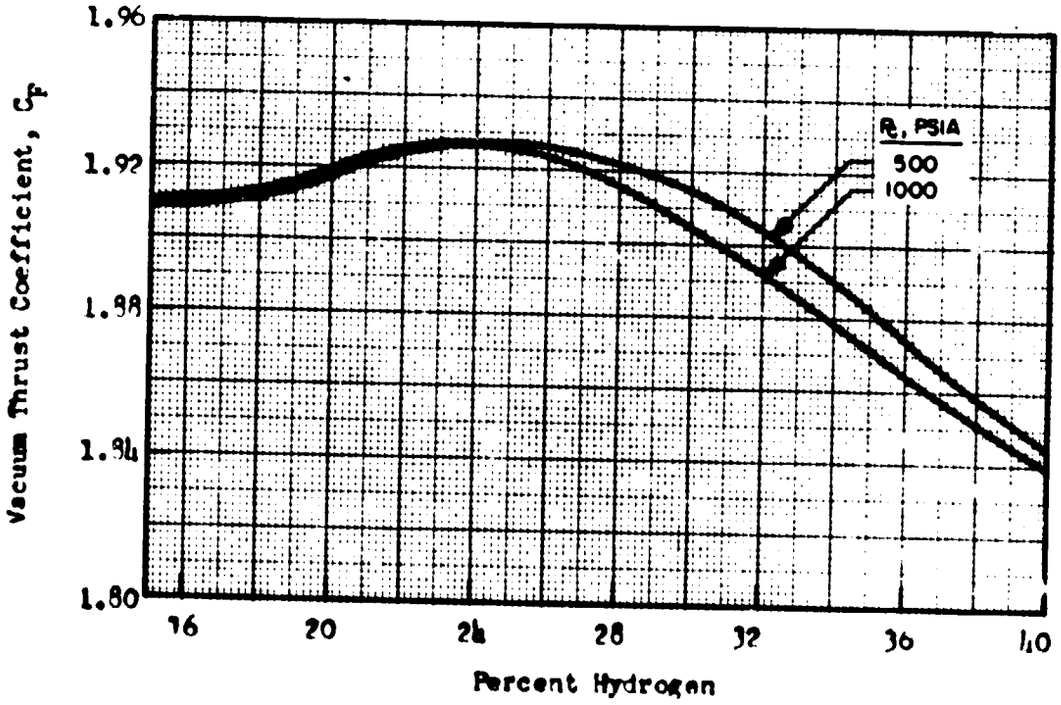

Figure 37. Vacuum Thrust Coefficient, C_F, as Function of Percent Hydrogen at Indicated Chamber Pressures, F_2/Li M.R. = 2.74, ϵ = 40, LF_2(153 R)/LLi(960 R)/GH_2(537 R).

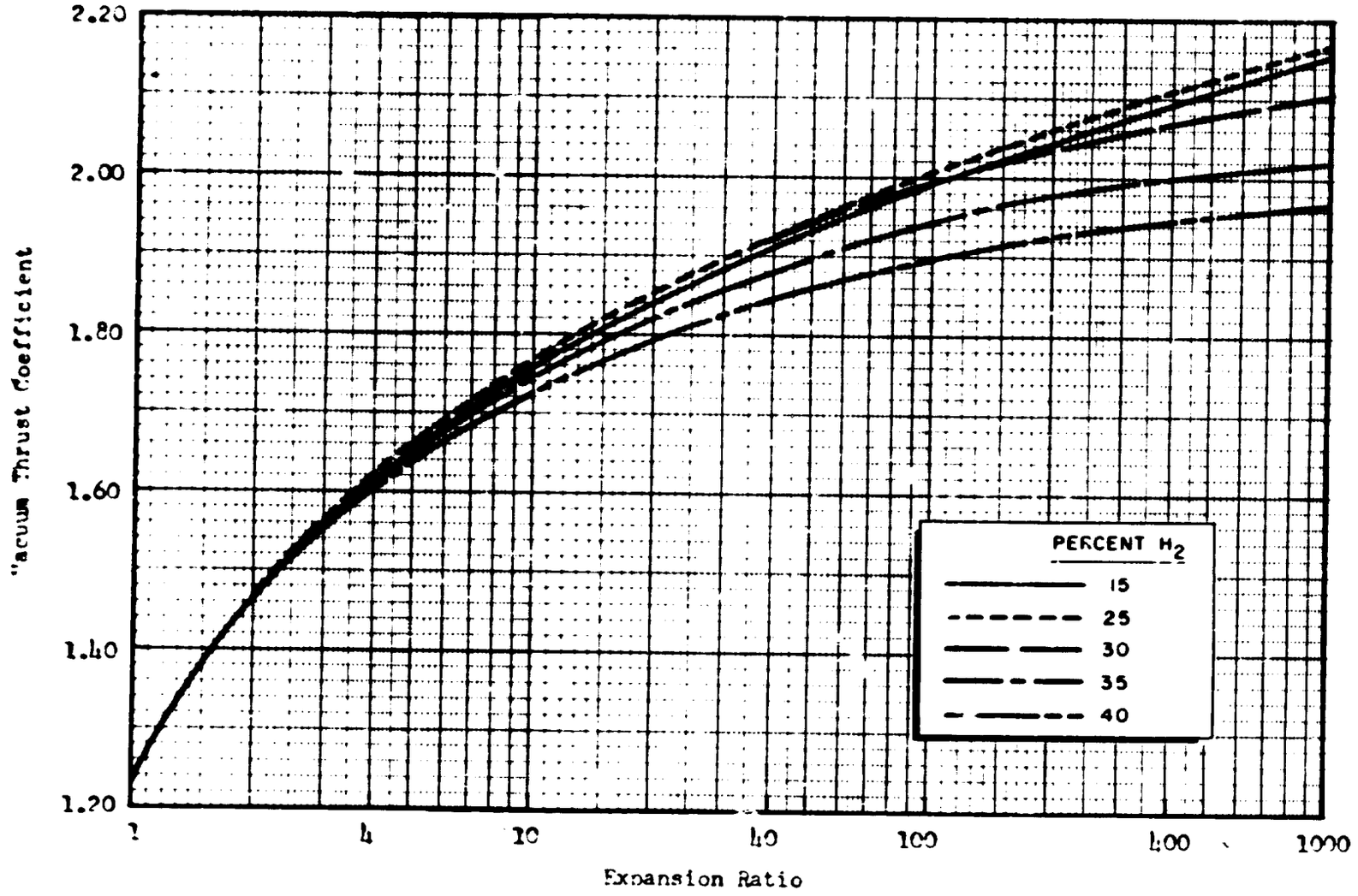

Figure 38. Vacuum Thrust Coefficient (Shifting Equilibrium) as Function of Expansion Ratio at Indicated Percent Hydrogen, P_c = 500 psia, F_2/Li M.R. = 2.74. LF_2(153 R) Li(960 R) GH_2(537 R).

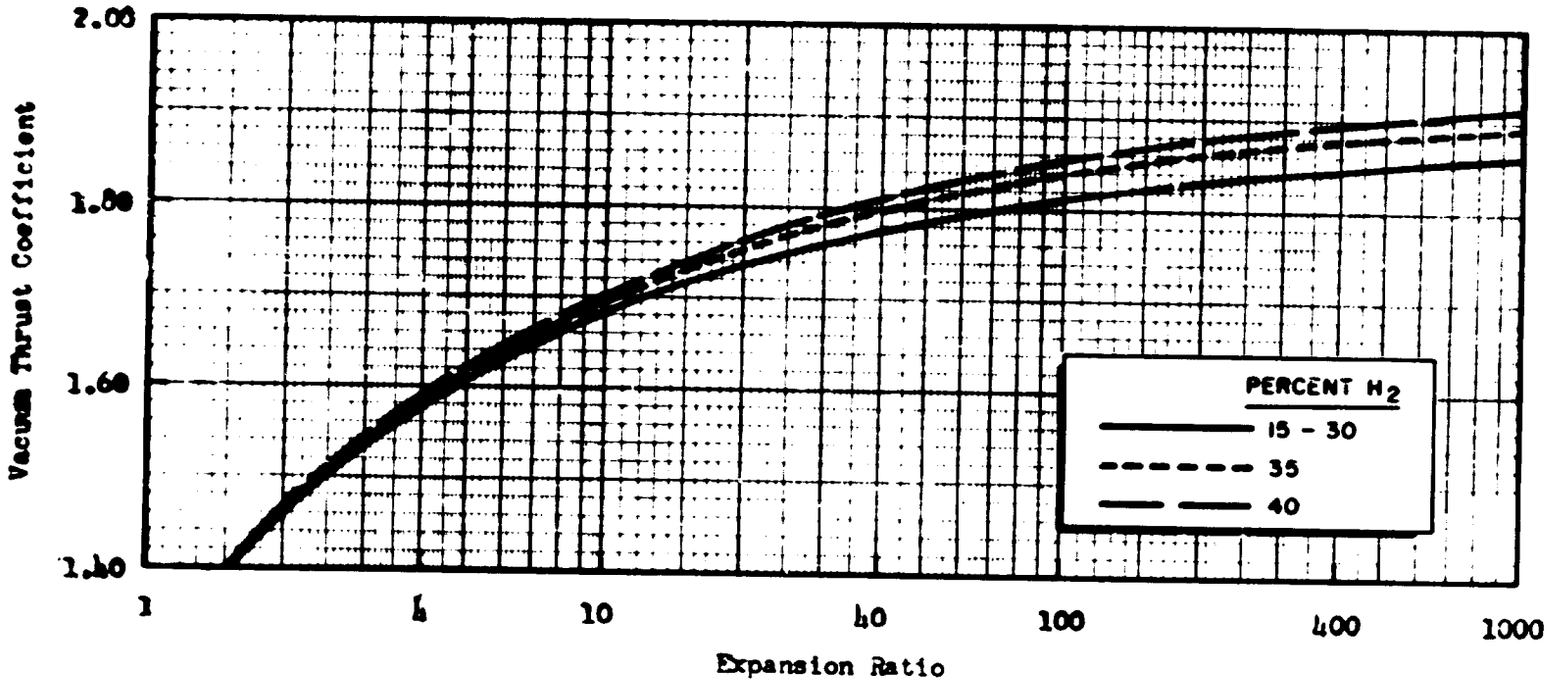

Figure 39. Vacuum Thrust Coefficient (Frozen Composition) as Function of Expansion Ratio at Indicated Percent Hydrogen. P_c = 500 psia, F_2/Li M.R. = 2.74. LF_2(153 R)/LLi(960 R)/GH_2(537°R).

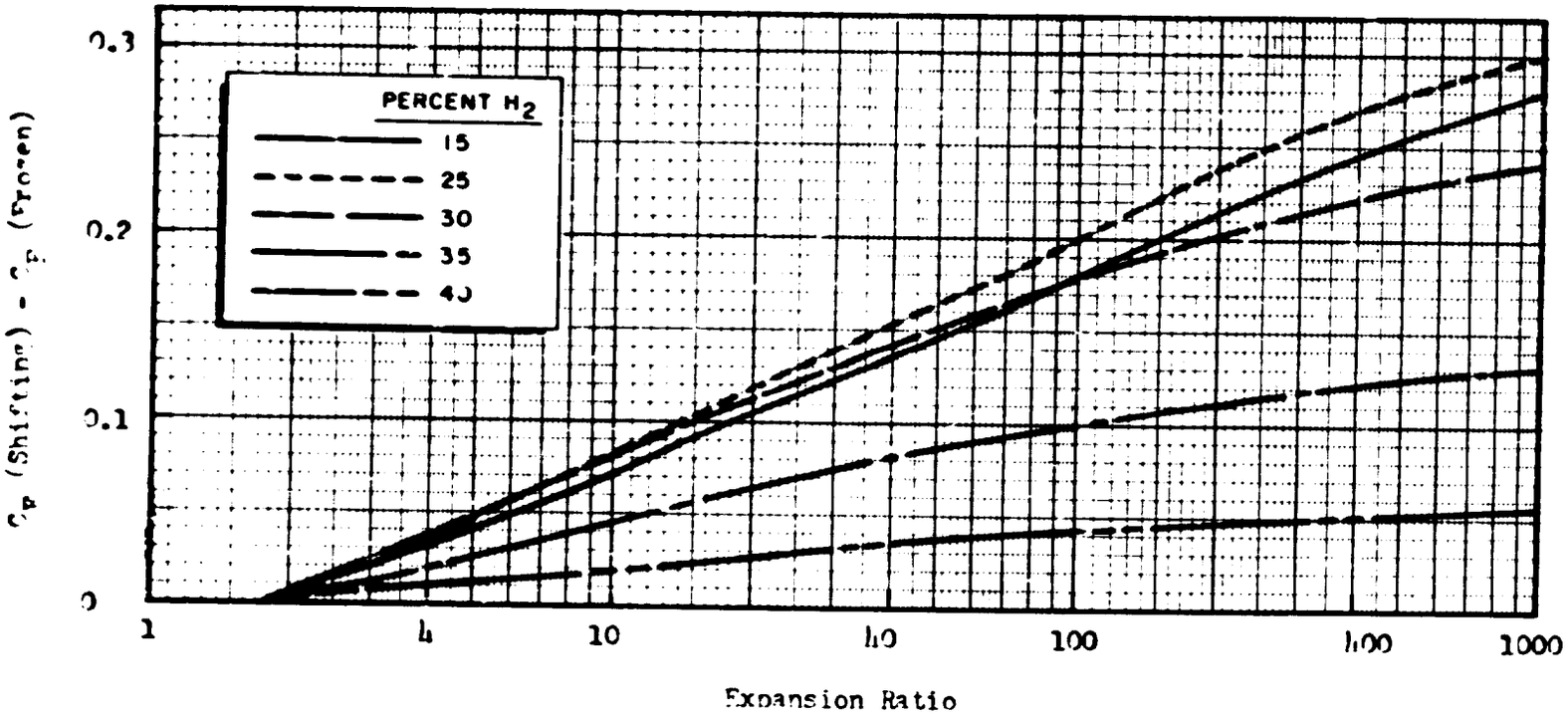

Figure 40. Difference Between Shifting and Frozen Vacuum Specific Impulse as Function of Expansion Ratio at Indicated Percent Hydrogen. P_c = 500 psia, F_2/Li M.R. = 2.74. LF_2(153 R)/LLi(960 R)/GH_2(537 R).

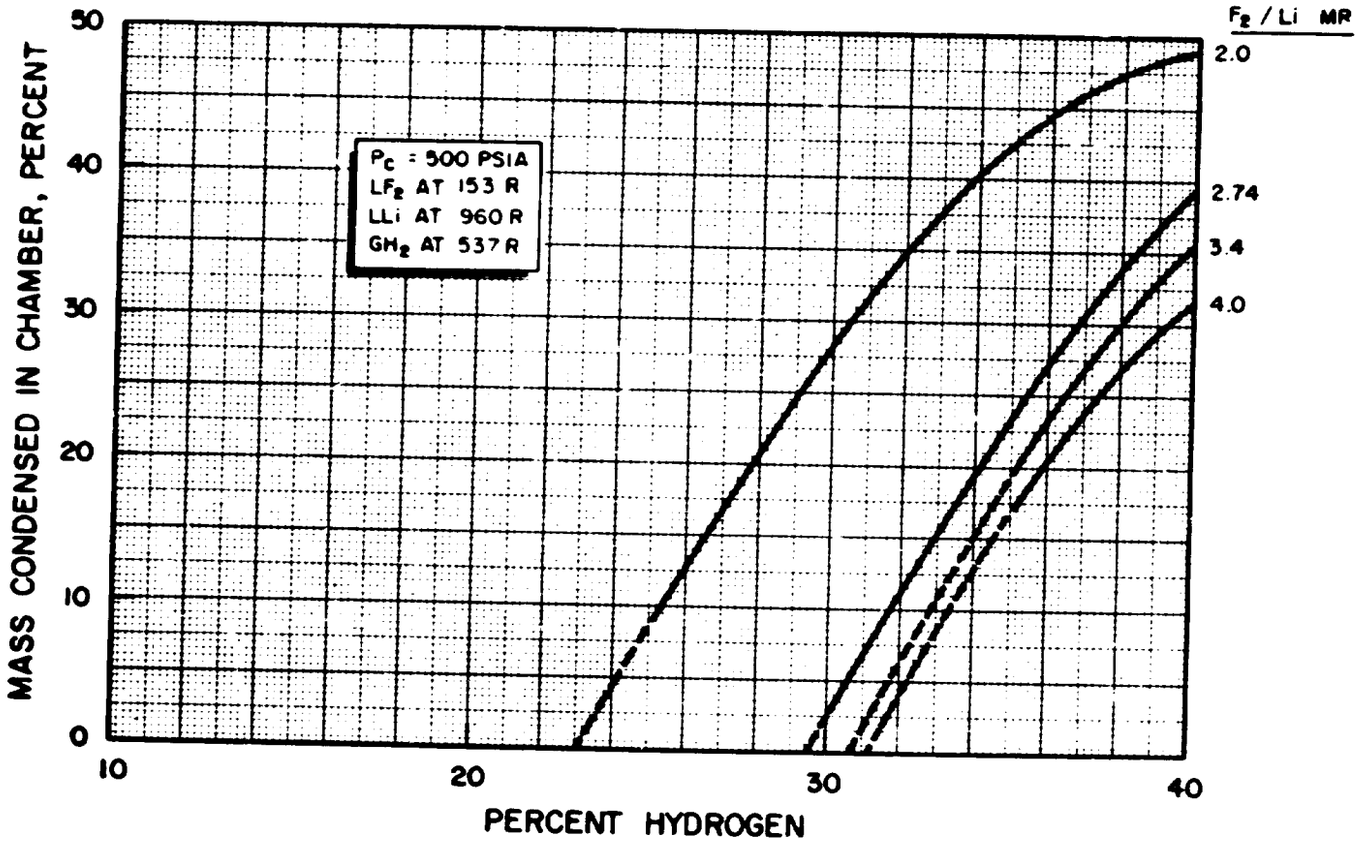

Figure 41. Weight Percent Condensed in Chamber as Function of Percent Hydrogen, at Indicated F_2/Li M.R. and Chamber Pressure, LF_2(153 R)/LLi(960 R)/GH_2(537 R).

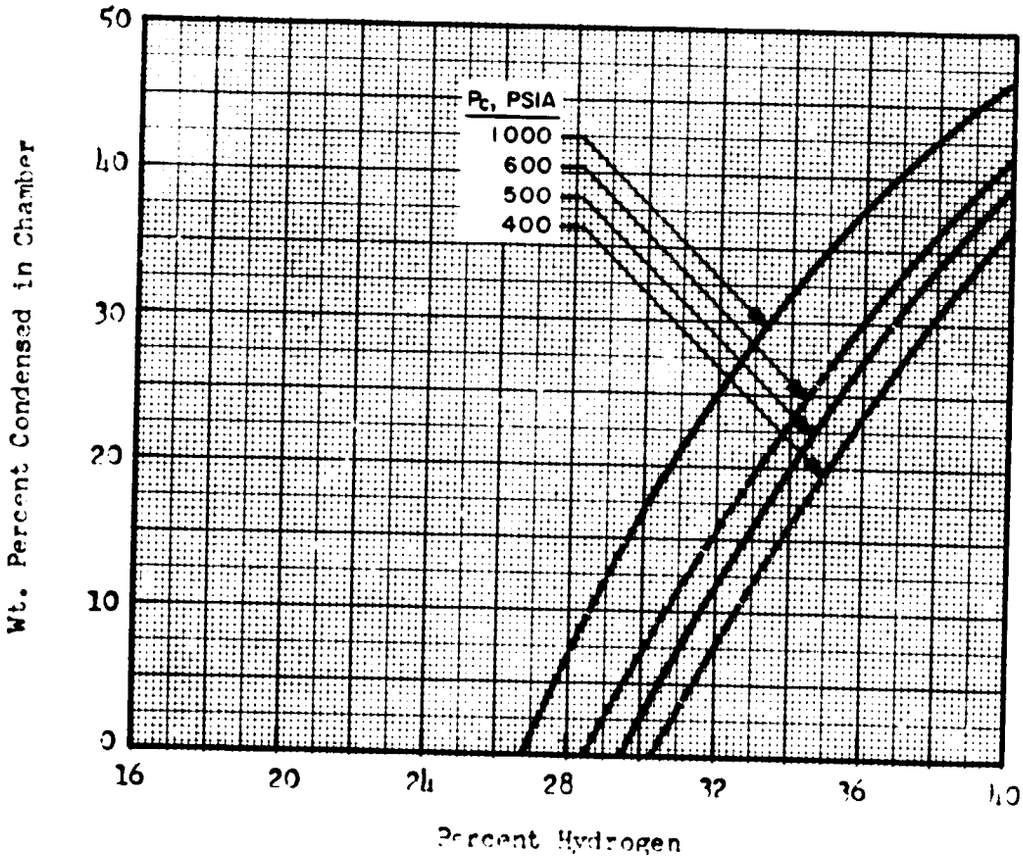

Figure 42. Weight Percent of Condensed Phase in the Chamber as Function of Percent Hydrogen, at Indicated Chamber Pressures.
F_2/Li M.R. = 2.74.
LF_2(153 R)/LLi(960 R)/GH_2(537 R).

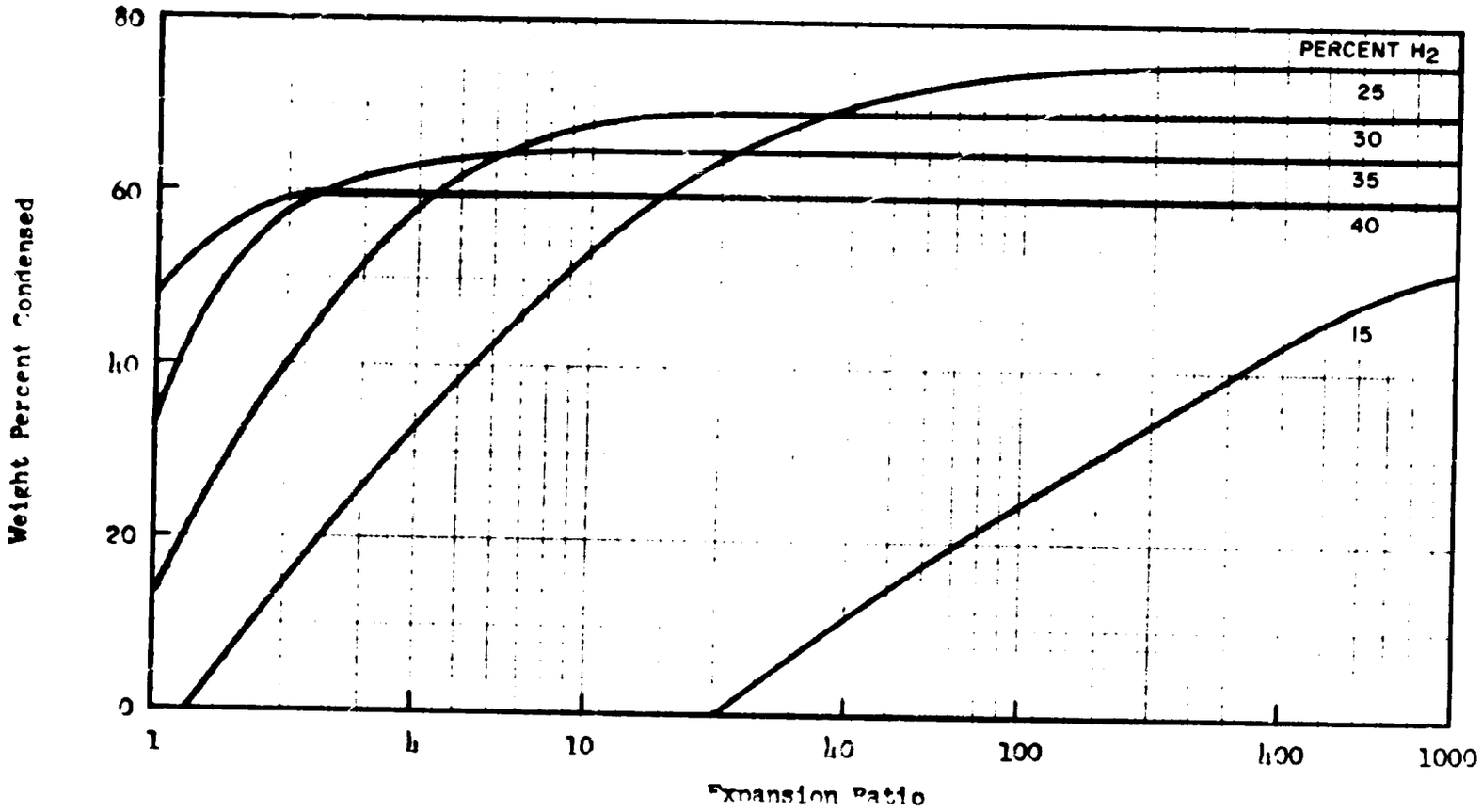

Figure 43. Weight Percent of Condensed Phase as Function of Expansion Ratio at Indicated Percent Hydrogen. P_c = 500 psia, F_2/Li M.R. = 2.74. LF_2(153 R)/LLi(960 R)/GH_2(537 R).

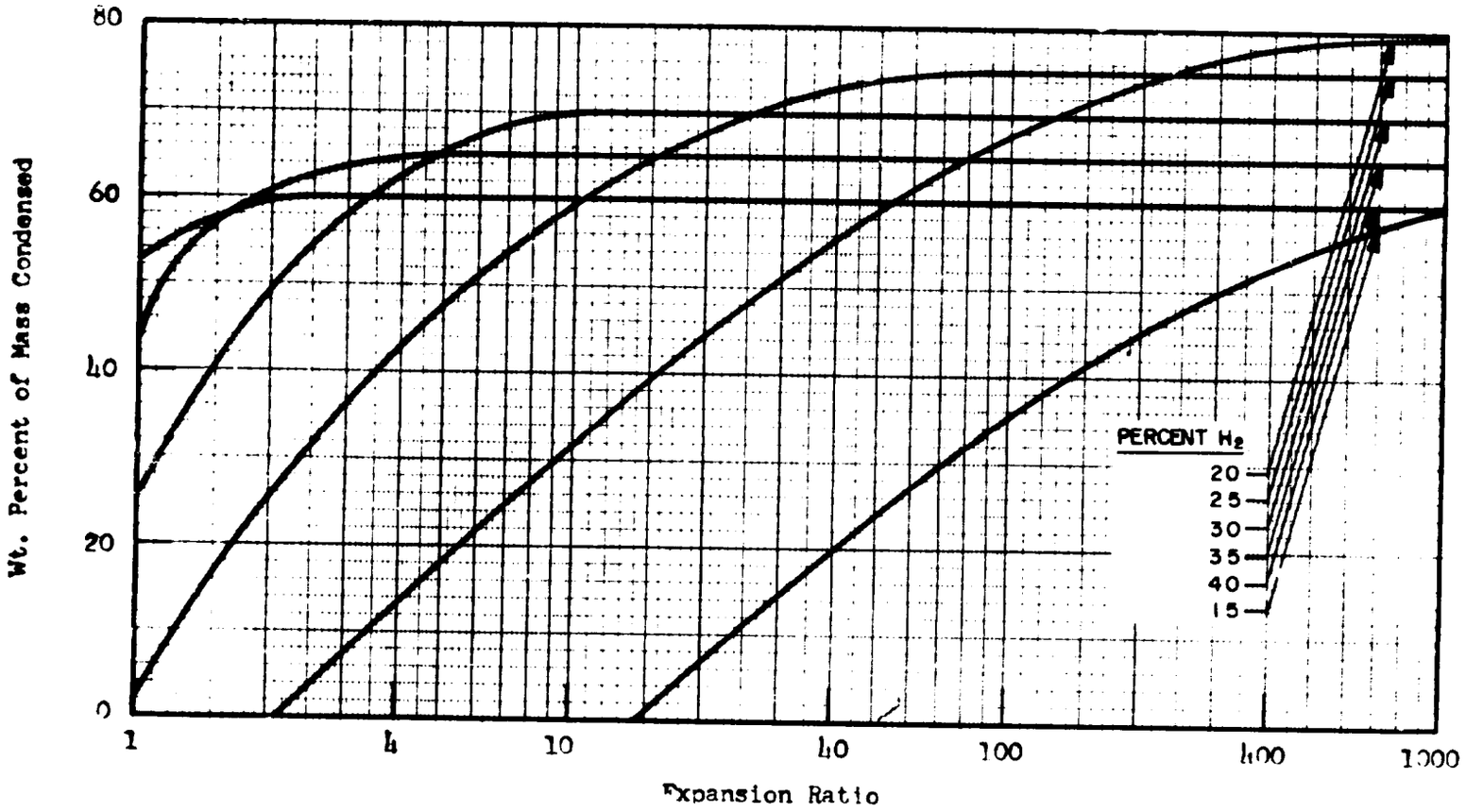

Figure 44 . Weight Percent of Condensed Phase in Nozzle as Function of Expansion Ratio at Indicated Percent Hydrogen. P_c = 1000 psia, F_2/Li M.R. = 2.74, LF_2(153 R)/LLi(960 R)/GH_2(537 R).

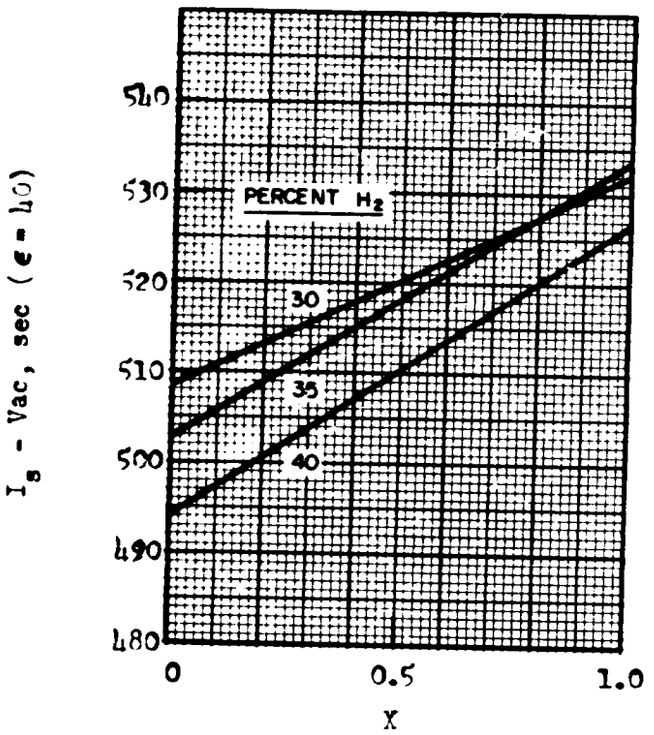

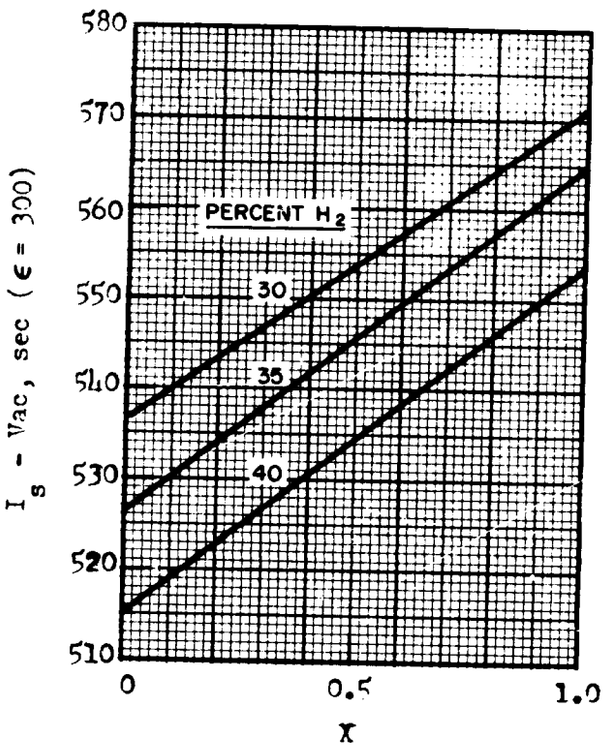

Figure 45. Effect of Incomplete LiF Condensation in Chamber on Vacuum Specific Impulse at ϵ = 40 and ϵ = 300. P_c = 500 psia, F_2/Li M.R. = 2.74. LF_2(153 R)/LLi(960 R)/GH_2(537 R).

$$X = \frac{\text{Actual wt. percent LiF condensed}}{\text{Theoretical wt. percent LiF condensed}}$$

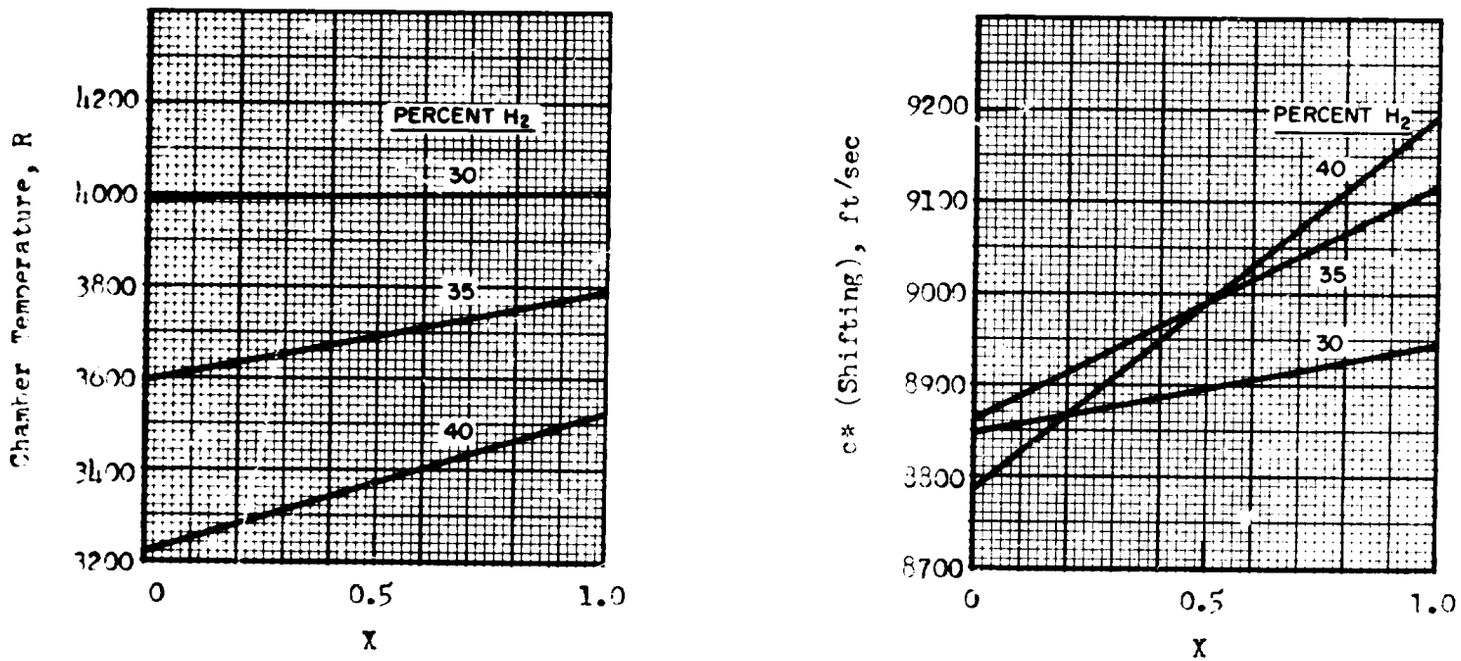

Figure 46. Effect of Incomplete LiF Condensation in Chamber on Chamber Temperature and c*. P_c = 500 psia, F_2/Li M.R. = 2.74. LF_2(153 R)/LLi(960 R)/GH_2(537 R).

$$X = \frac{\text{Actual wt. percent LiF condensed}}{\text{Theoretical wt. percent LiF condensed}}$$

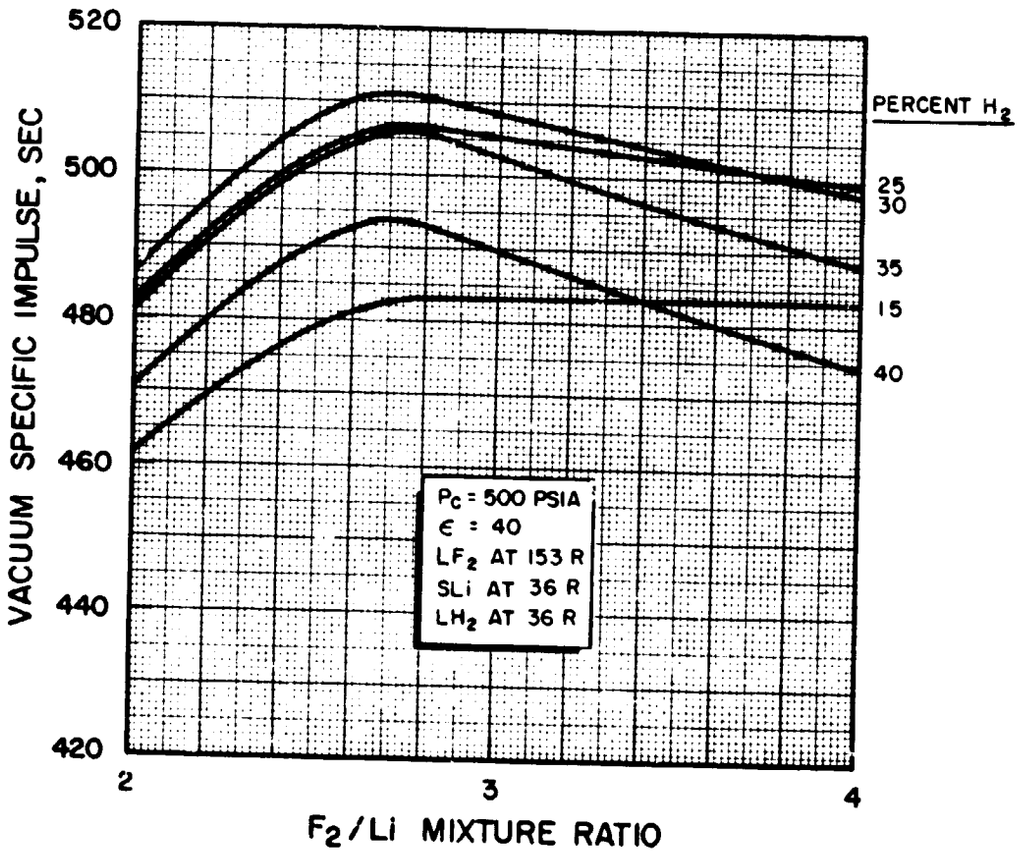

Figure 47. Variation of Vacuum Specific Impulse (Shifting Equilibrium) with F_2/Li Mixture Ratio at Indicated Percent Hydrogen, Chamber Pressure, and Expansion Ratio, LF_2(153 R)/SLi(36 R)/LH_2(36 R).

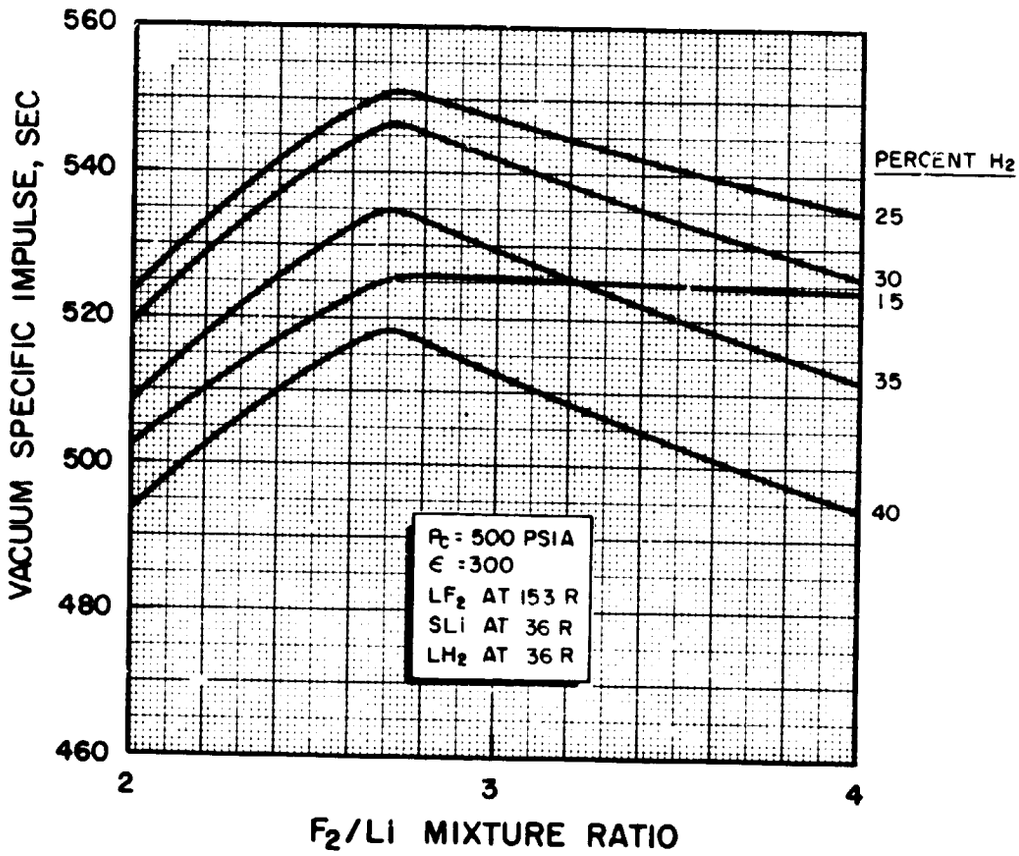

Figure 48. Variation of Vacuum Specific Impulse (Shifting Equilibrium) with F_2/Li Mixture Ratio at Indicated Percent Hydrogen, Chamber Pressure, and Expansion Ratio, LF_2(153 R)/SLi(36 R)/LH_2(36 R).

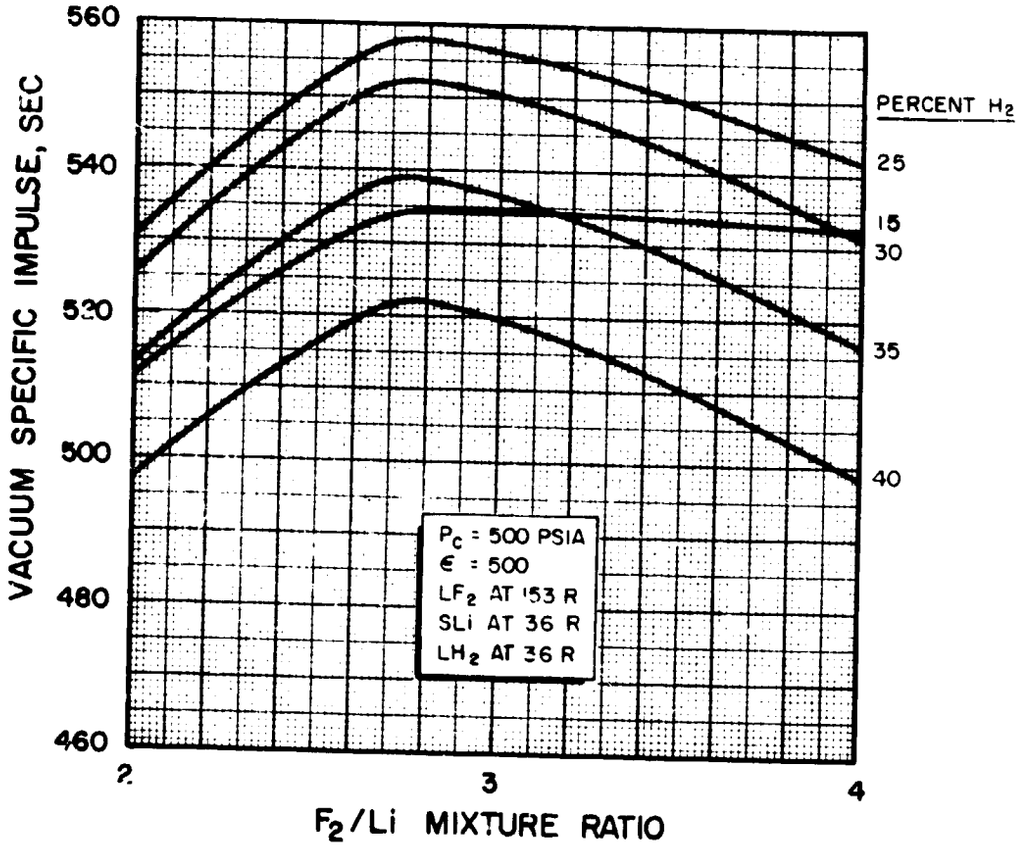

Figure 49. Variation of Vacuum Specific Impulse (Shifting Equilibrium) with F_2/Li Mixture Ratio at Indicated Percent Hydrogen, Chamber Pressure, and Expansion Ratio, LF_2(153 R)/SLi(36 R)/LH_2(36 R).

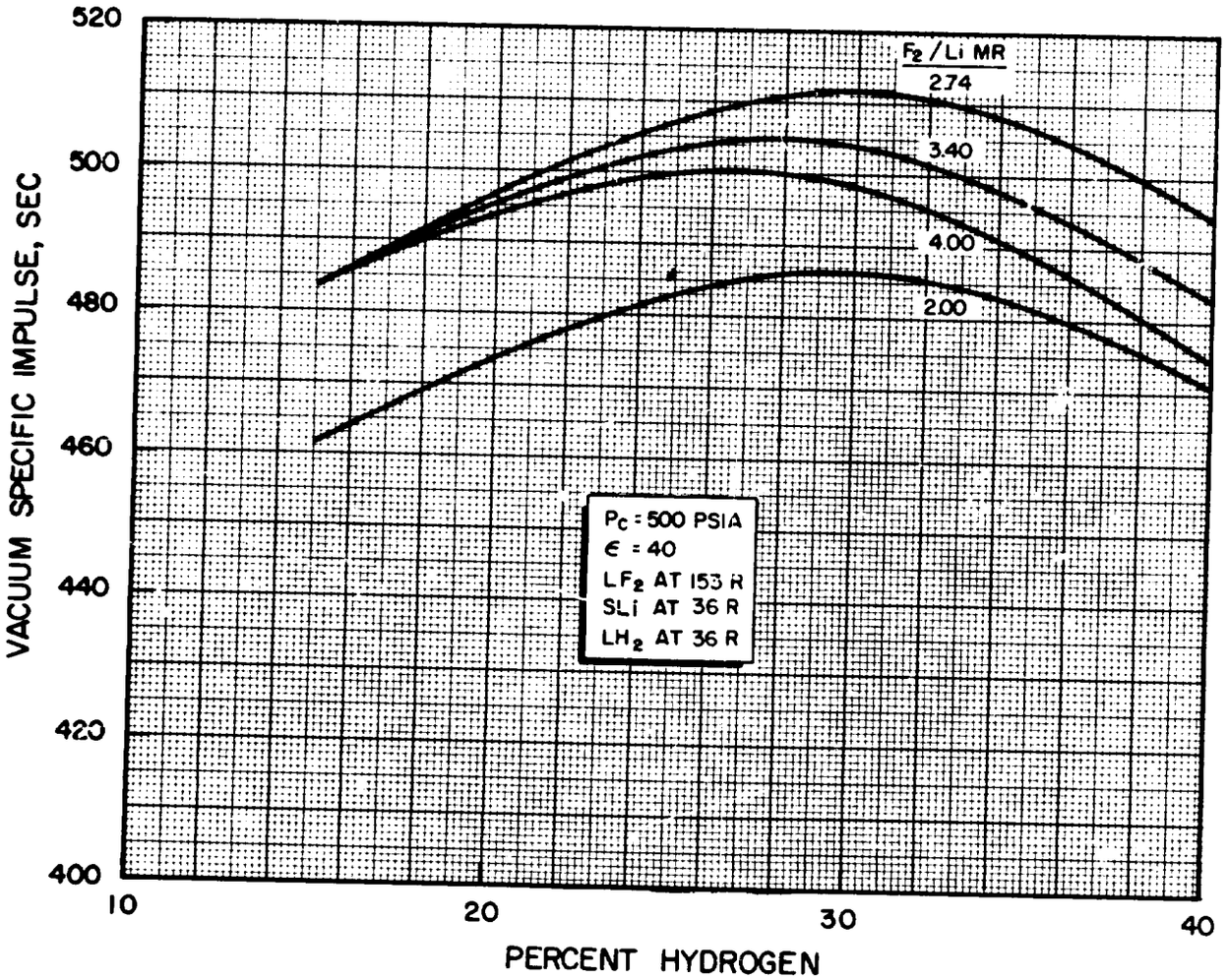

Figure 50. Variation of Vacuum Specific Impulse (Shifting Equilibrium) with Percent Hydrogen at Indicated F_2/Li M.R., Chamber Pressure, and Expansion Ratio, LF_2(153 R)/SLi(36 R)/LH_2(36 R).

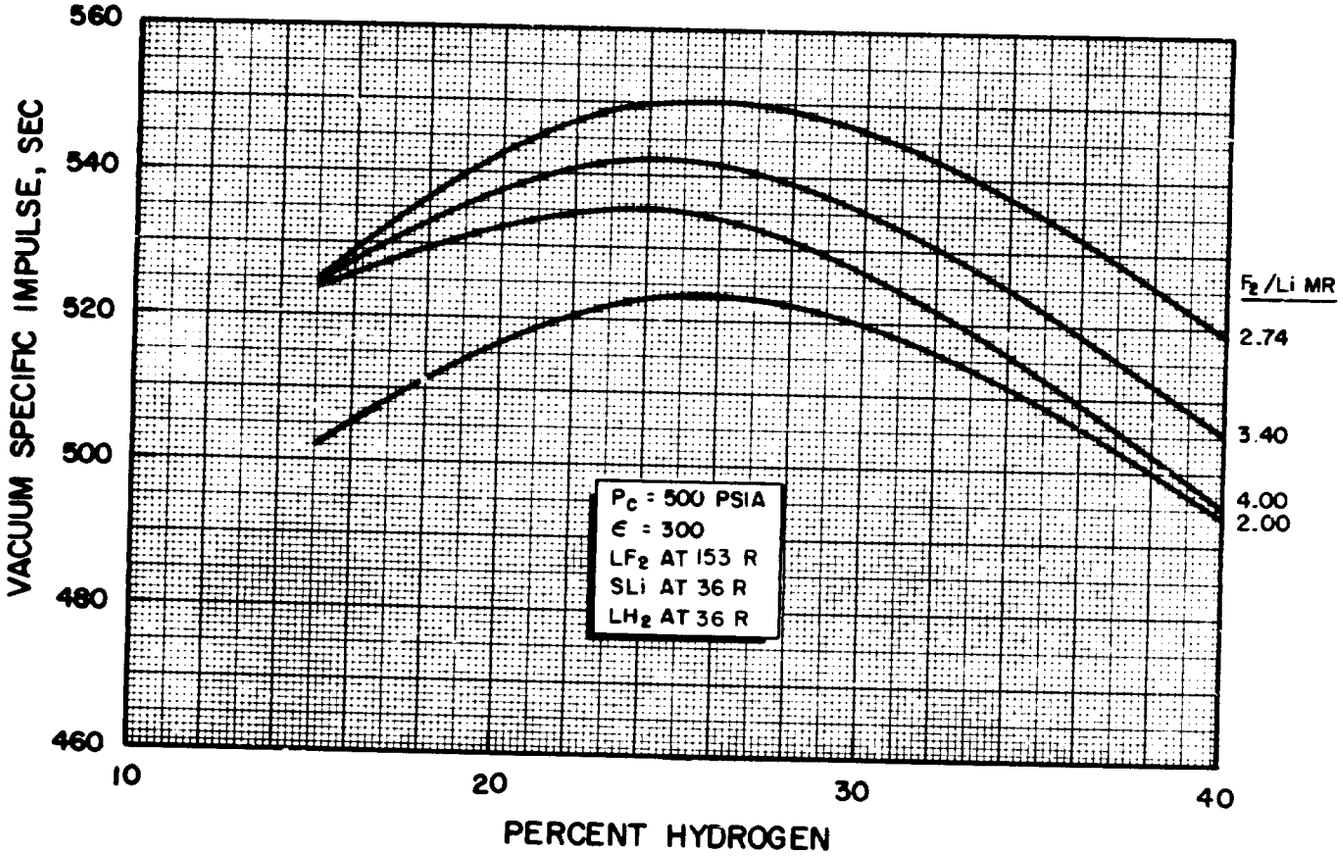

Figure 51. Variation of Vacuum Specific Impulse (Shifting Equilibrium) with Percent Hydrogen at Indicated F_2/Li M.R., Chamber Pressure, and Expansion Ratio, LF_2(153 R)/SLi(36 R)/LH_2(36 R).

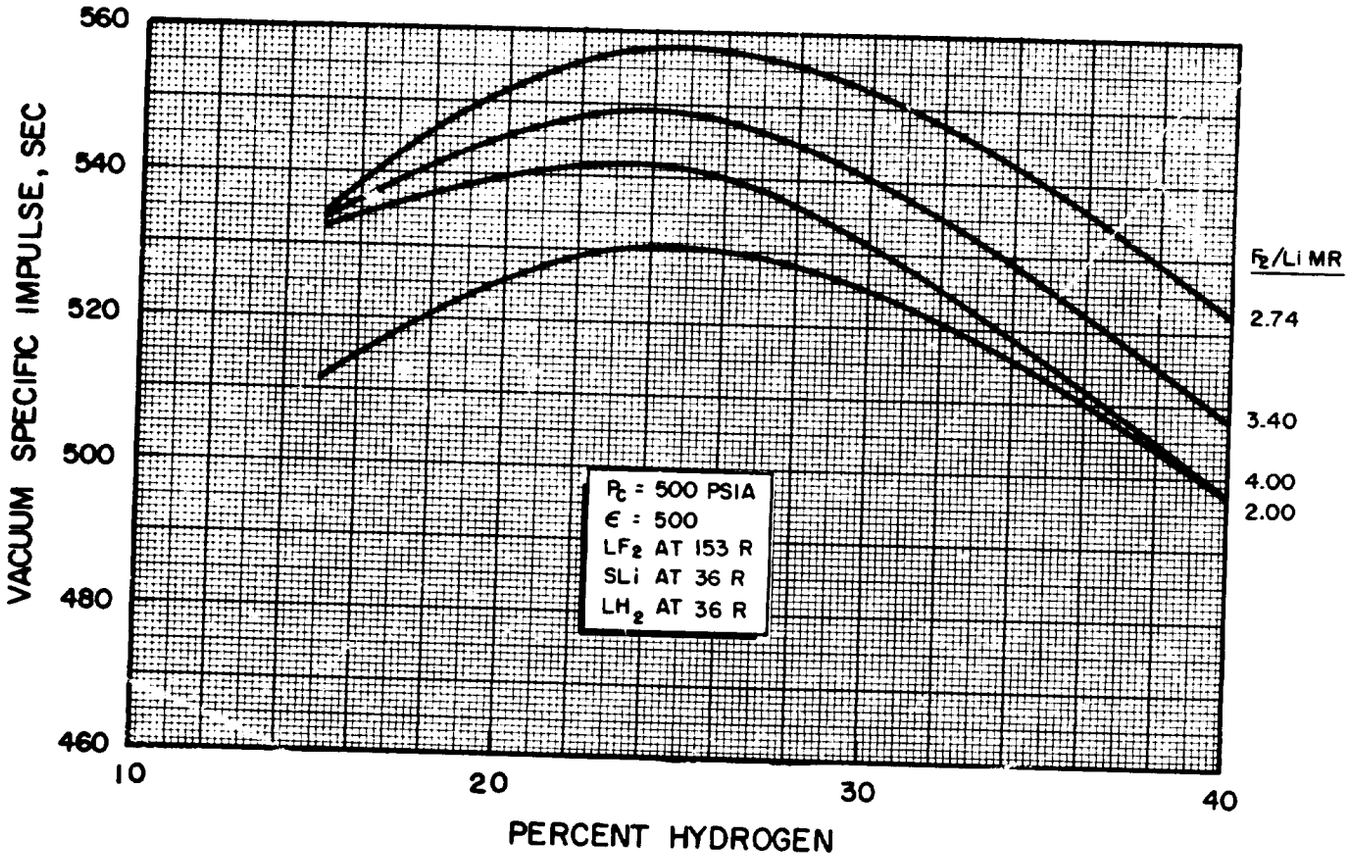

Figure 52. Variation of Vacuum Specific Impulse (Shifting Equilibrium) with Percent Hydrogen at Indicated F_2/Li Mixture Ratio, Chamber Pressure, and Expansion Ratio, LF_2(153 R)/SLi(36 R)/ LH_2(36 R).

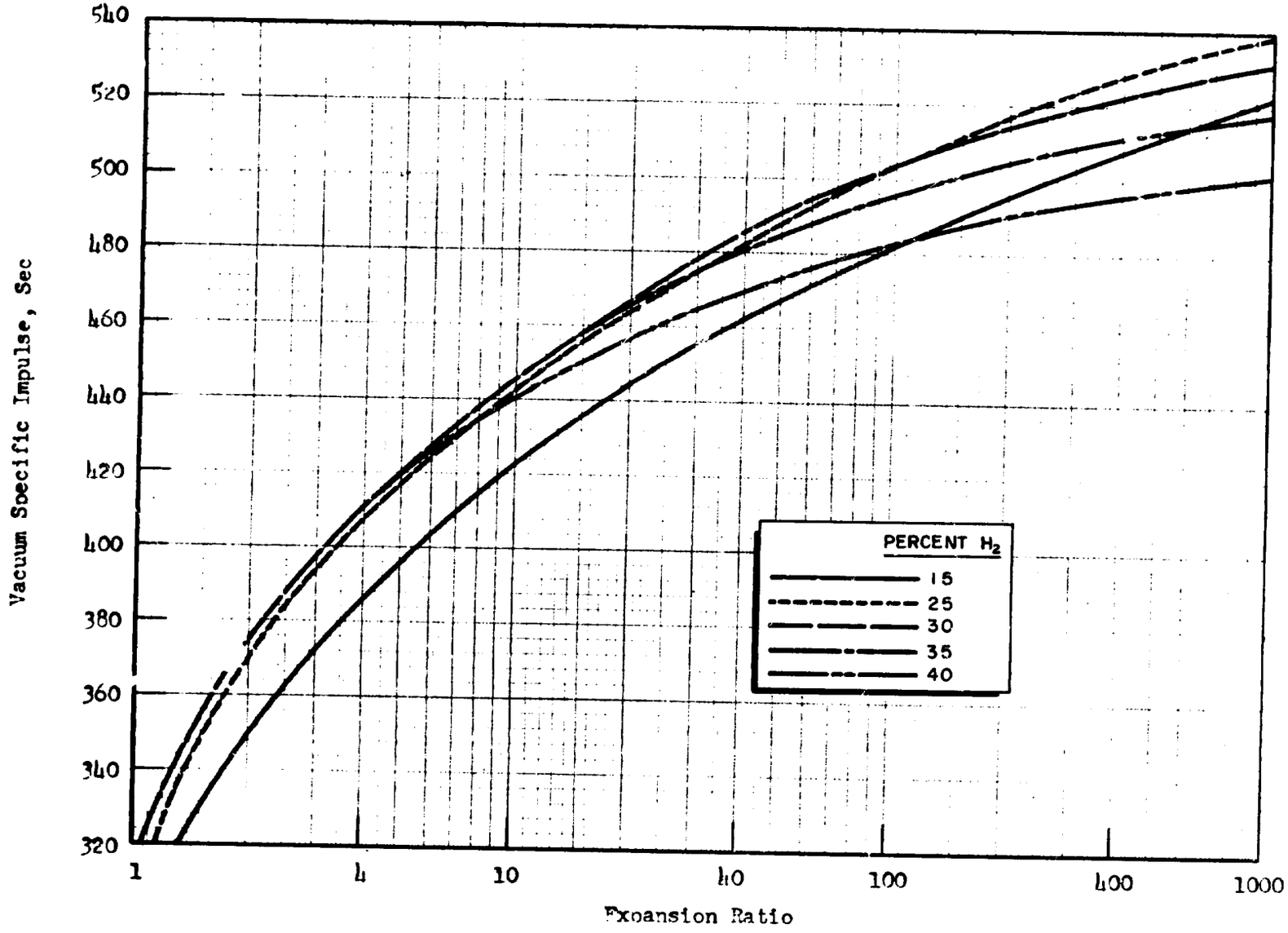

Figure 53. Vacuum Specific Impulse (Shifting Equilibrium) as Function of Expansion Ratio at Indicated Percent Hydrogen. P_c = 500 psia, F_2/Li M.R. = 2.00. LF_2(153 R)/SLi(36 R)/LH_2(36 R)[f].

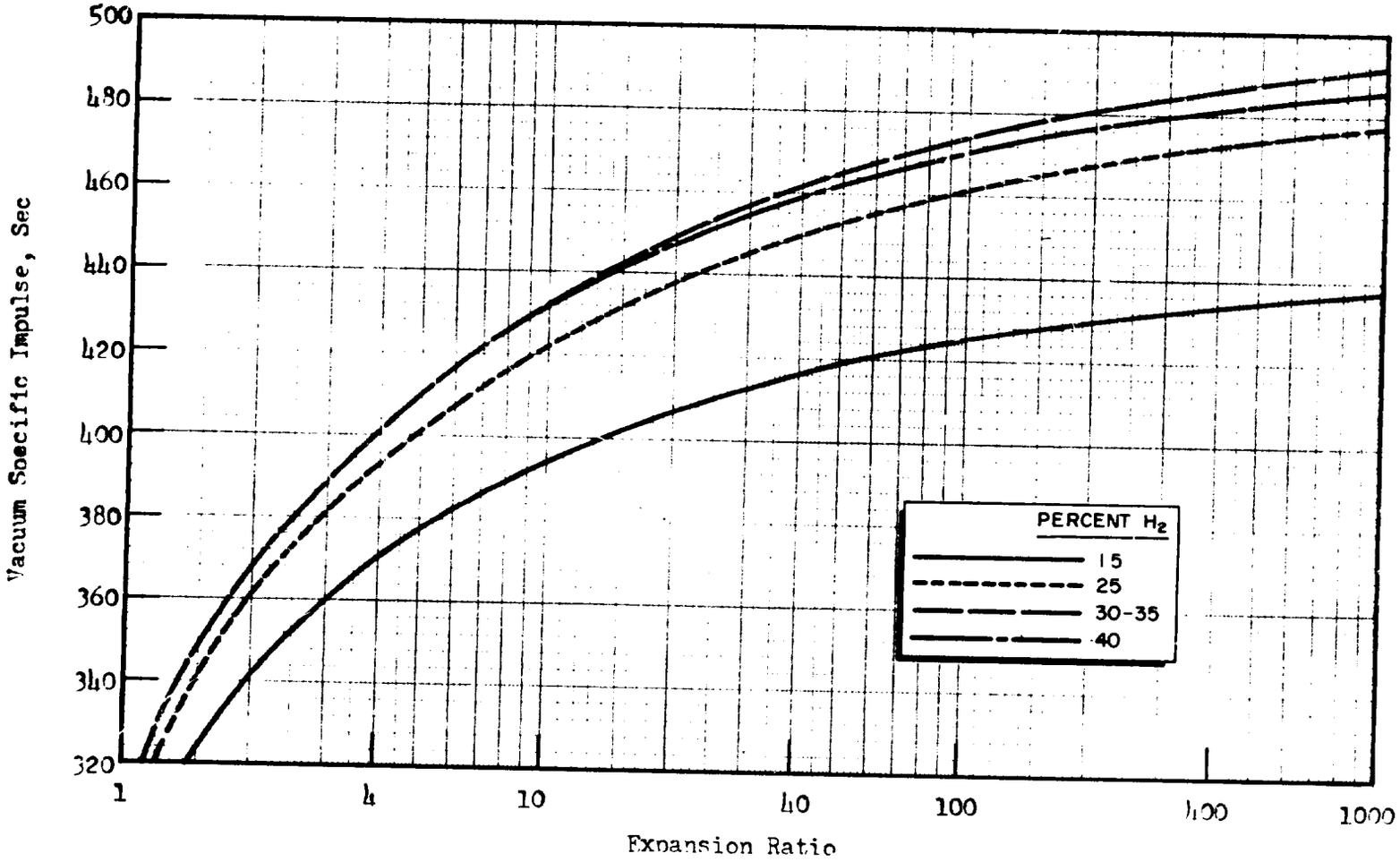

Figure 54. Vacuum Specific Impulse (Frozen Composition) as Function of Expansion Ratio at Indicated Percent Hydrogen. P_c = 500 psia, F_2/Li M.R. = 2.00. LF_2(153 R)/SLi(36 R)/LH_2(36 R).

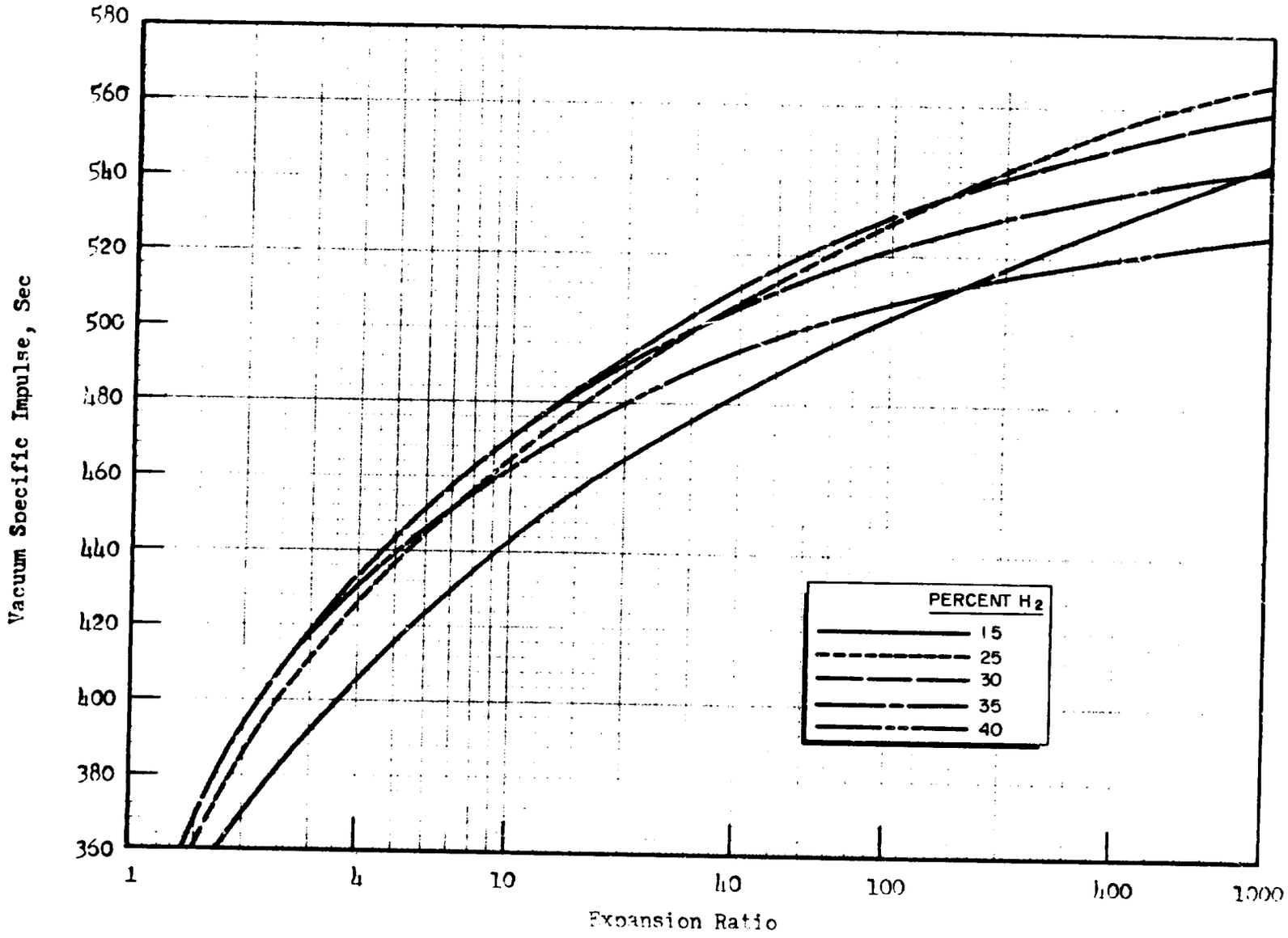

Figure 55. Vacuum Specific Impulse (Shifting Equilibrium) as Function of Expansion Ratio at Indicated Percent Hydrogen. P_c = 500 psia, F_2/Li M.R. = 2.74. LF_2(153 R)/SLi(36 R)/LH_2(36 R).

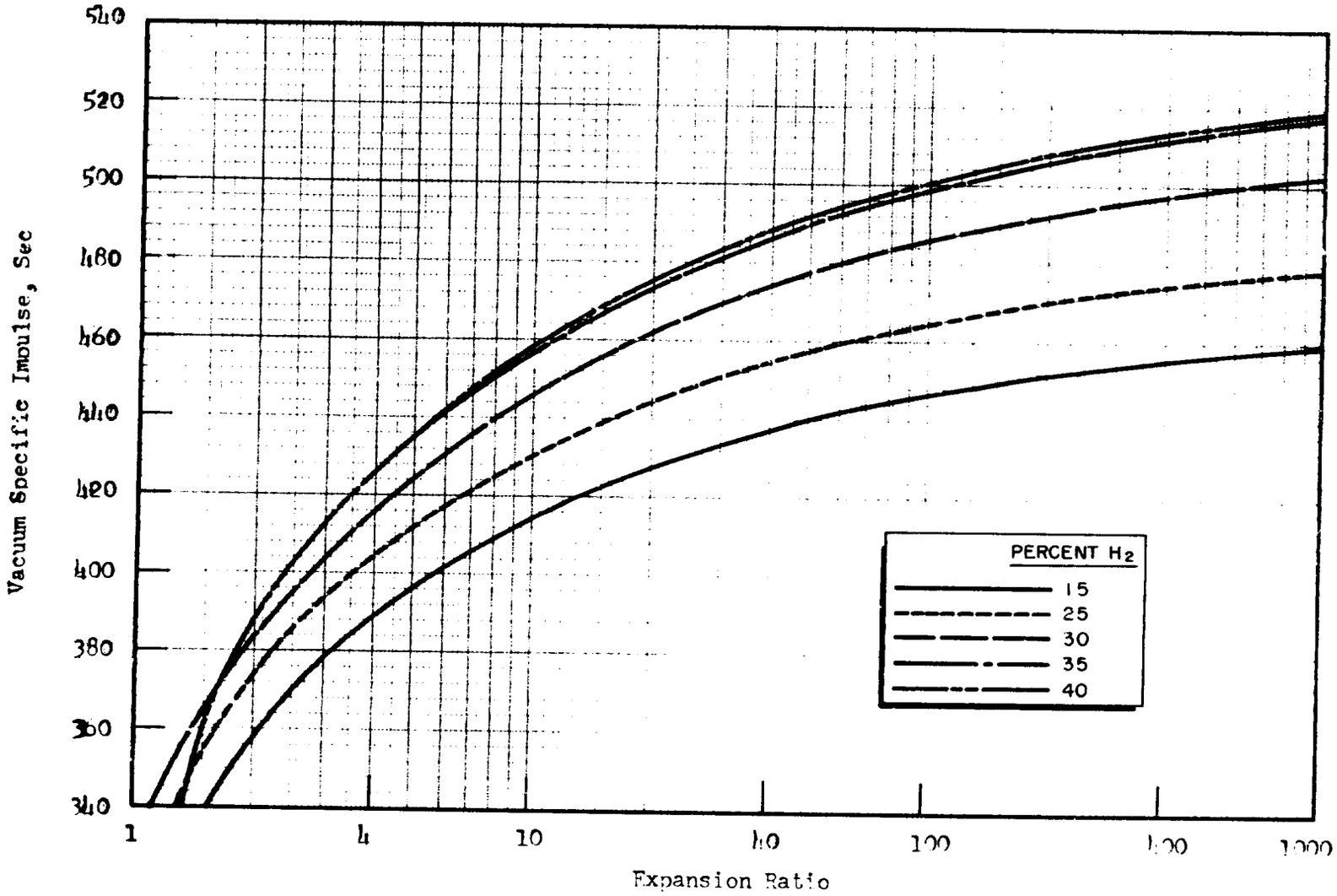

Figure 56. Vacuum Specific Impulse (Frozen Composition) as Function of Expansion Ratio at Indicated Percent Hydrogen, P_c = 500 psia, F_2/Li M.R. = 2.74. LF_2(153 R)/SLi(36 R)/LH_2(36 R).

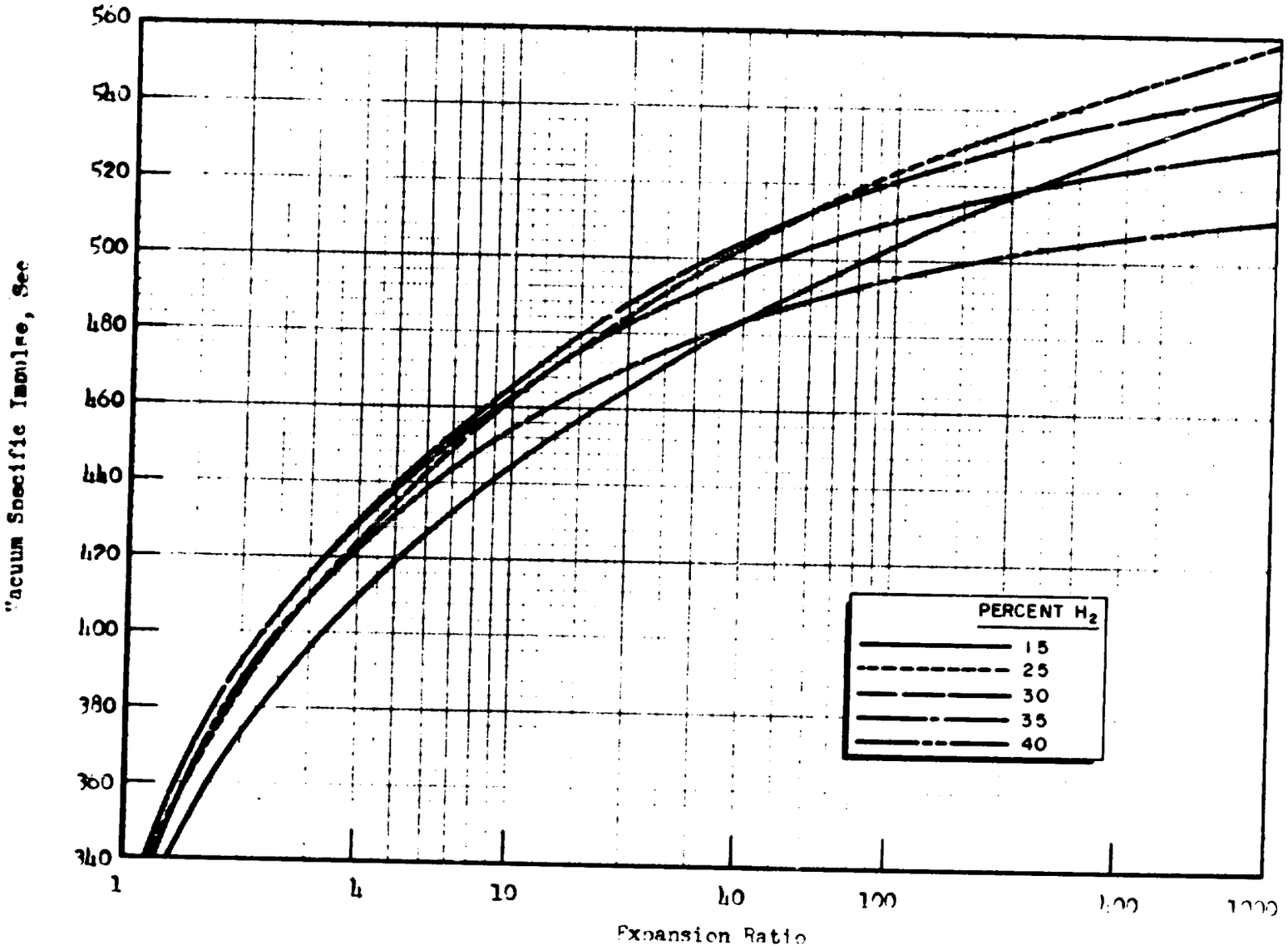

Figure 57. Vacuum Specific Impulse (Shifting Equilibrium) as Function of Expansion Ratio at Indicated Percent Hydrogen. P_c = 500 psia, F_2/Li M.R. = 3.40. LF_2(153 R)/SLi(36 R)/LH_2(36 R).

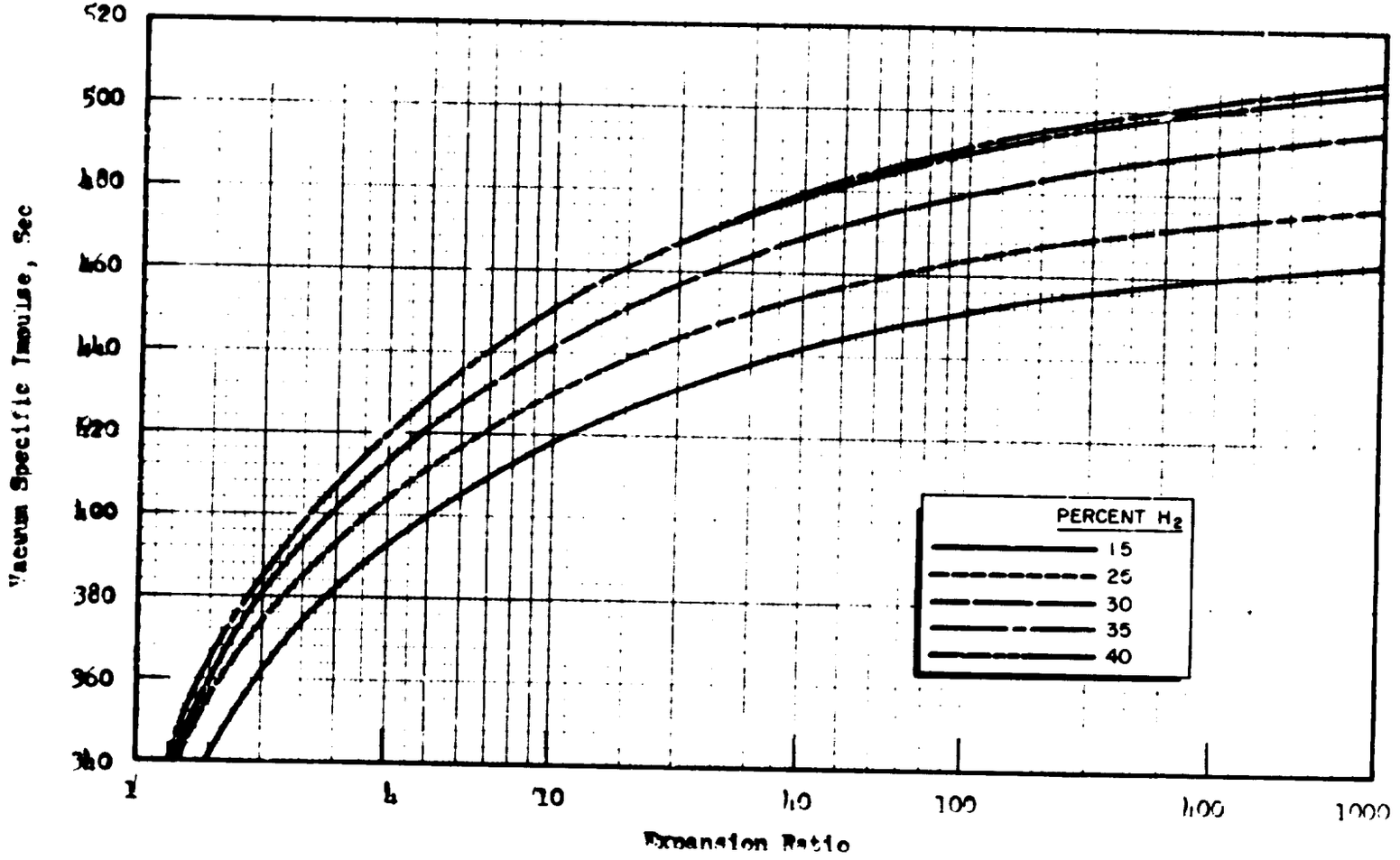

Figure. 58. Vacuum Specific Impulse (Frozen Composition) as Function of Expansion Ratio at Indicated Percent Hydrogen. P_c = 500 psia, F_2/Li M.R. = 3.40. LF_2(153 R)/SLi(36 R)/LH_2(36 R).

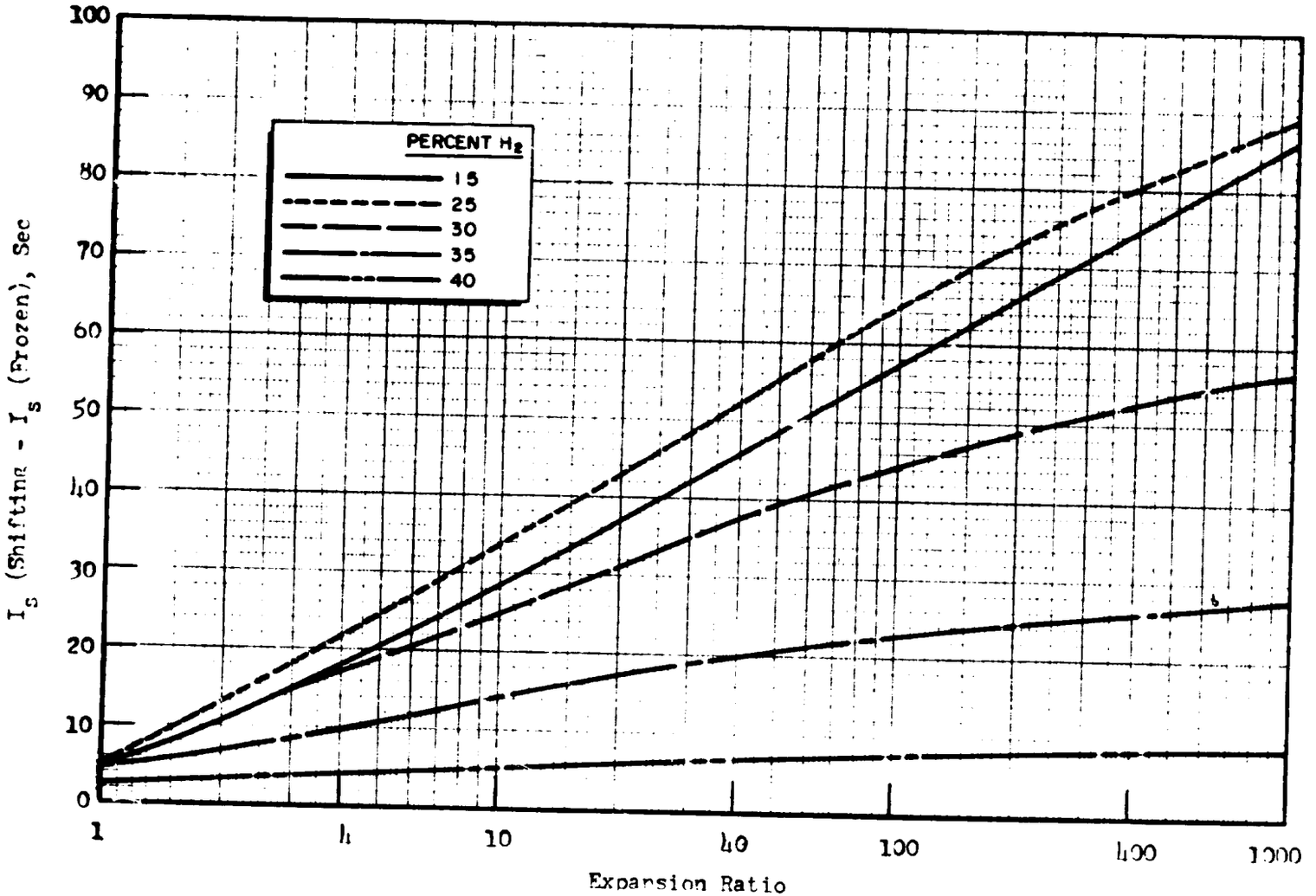

Figure 59. Difference between Shifting Equilibrium and Frozen Composition Vacuum Specific Impulse at Indicated Percent Hydrogen. P_c = 400 psia, F_2/[illegible] M.R. = 2.[illegible]. LF_2(153 R)/SLi(36 R)/LH_2(36 R).

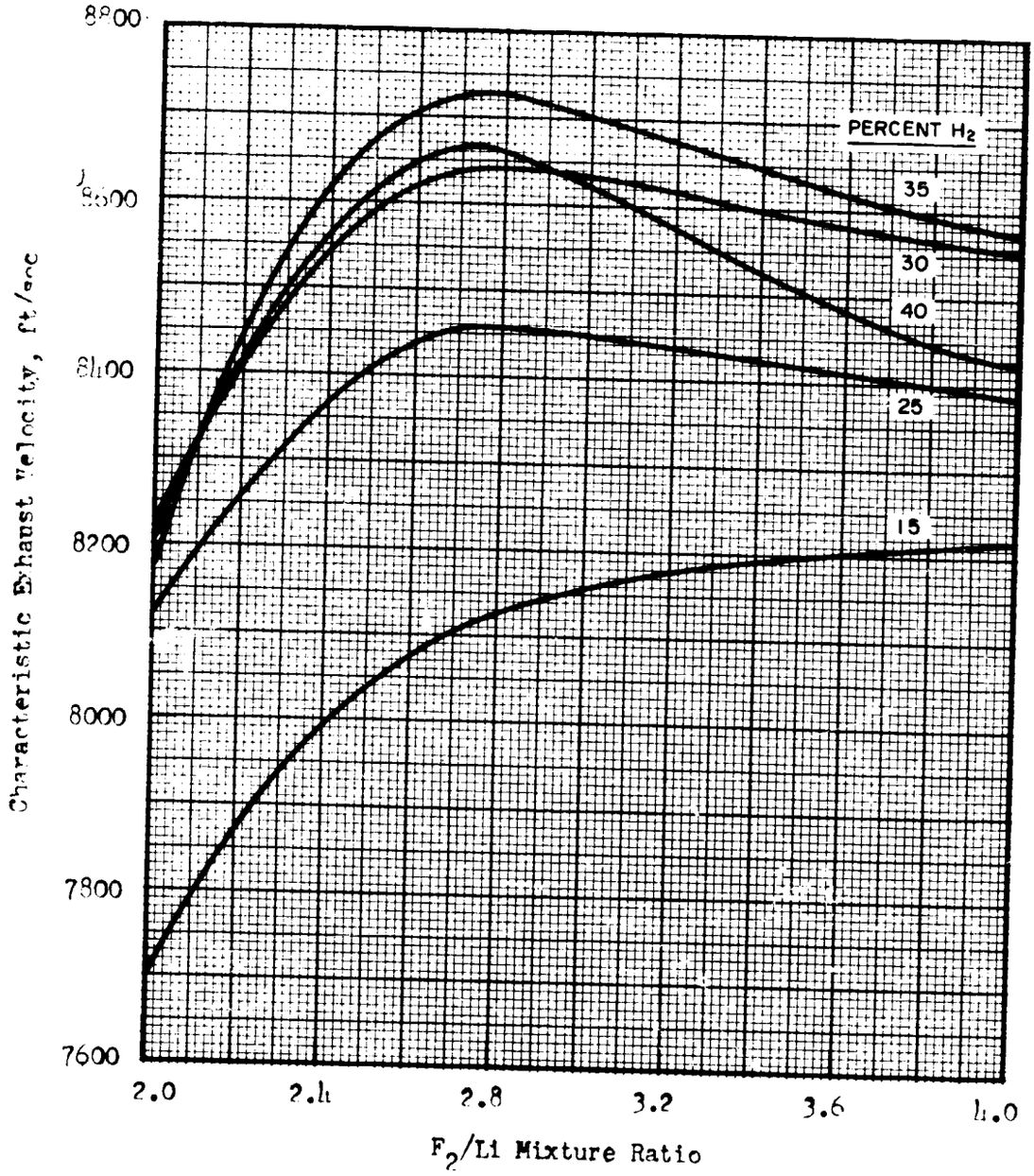

Figure 60. Variation of c* (Shifting Equilibrium) with F_2/Li Mixture Ratio at Indicated Percent Hydrogen, P_c = 500 psia.
LF_2(153 R)/SLi(36 R)/LH_2(36 R).

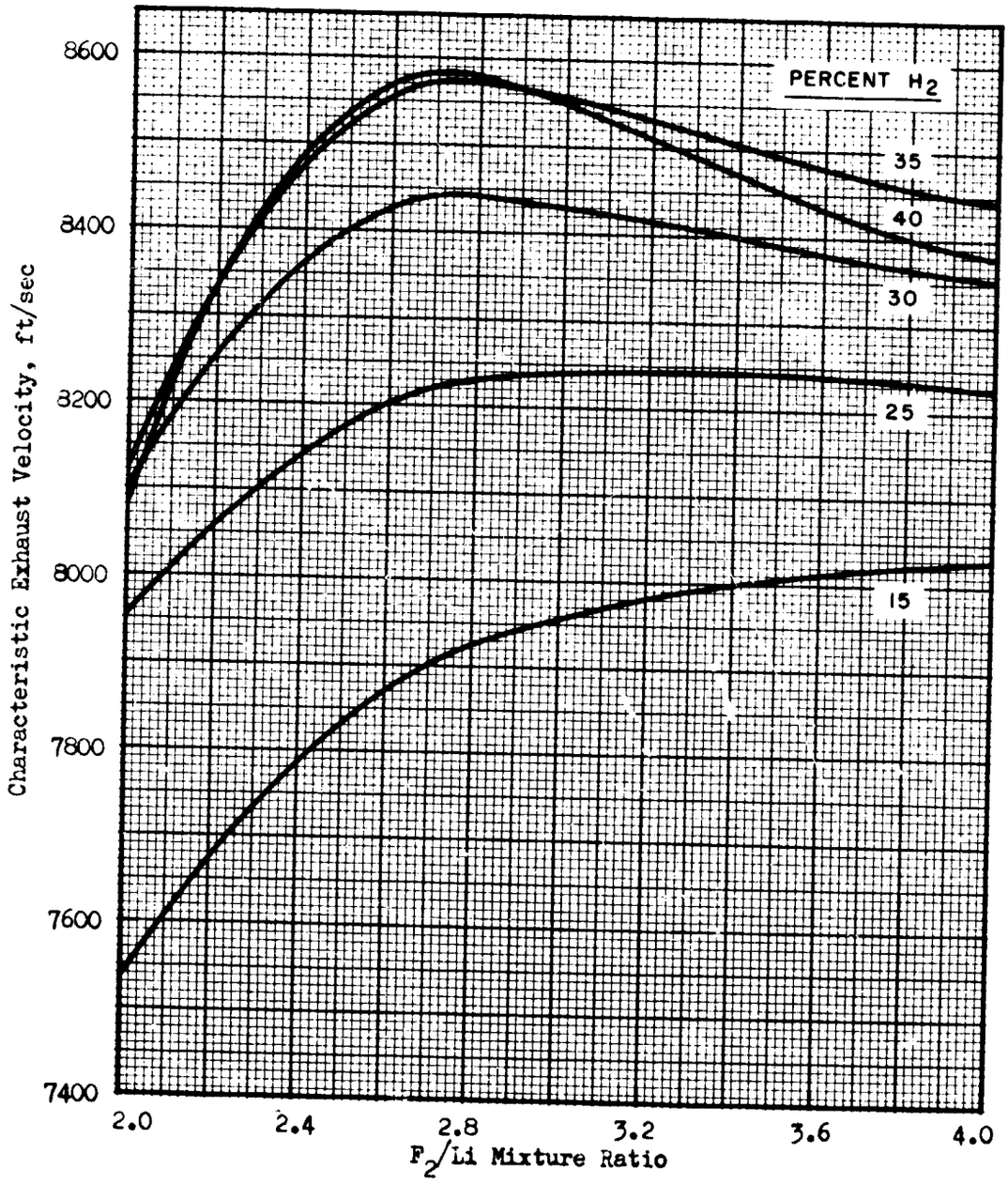

Figure 61. Variation of c* (Frozen Composition) with F_2/Li Mixture Ratio at Indicated Percent Hydrogen, P_c = 500 psia, LF_2(153 R)/SLi(36 R)/LH_2(36 R).

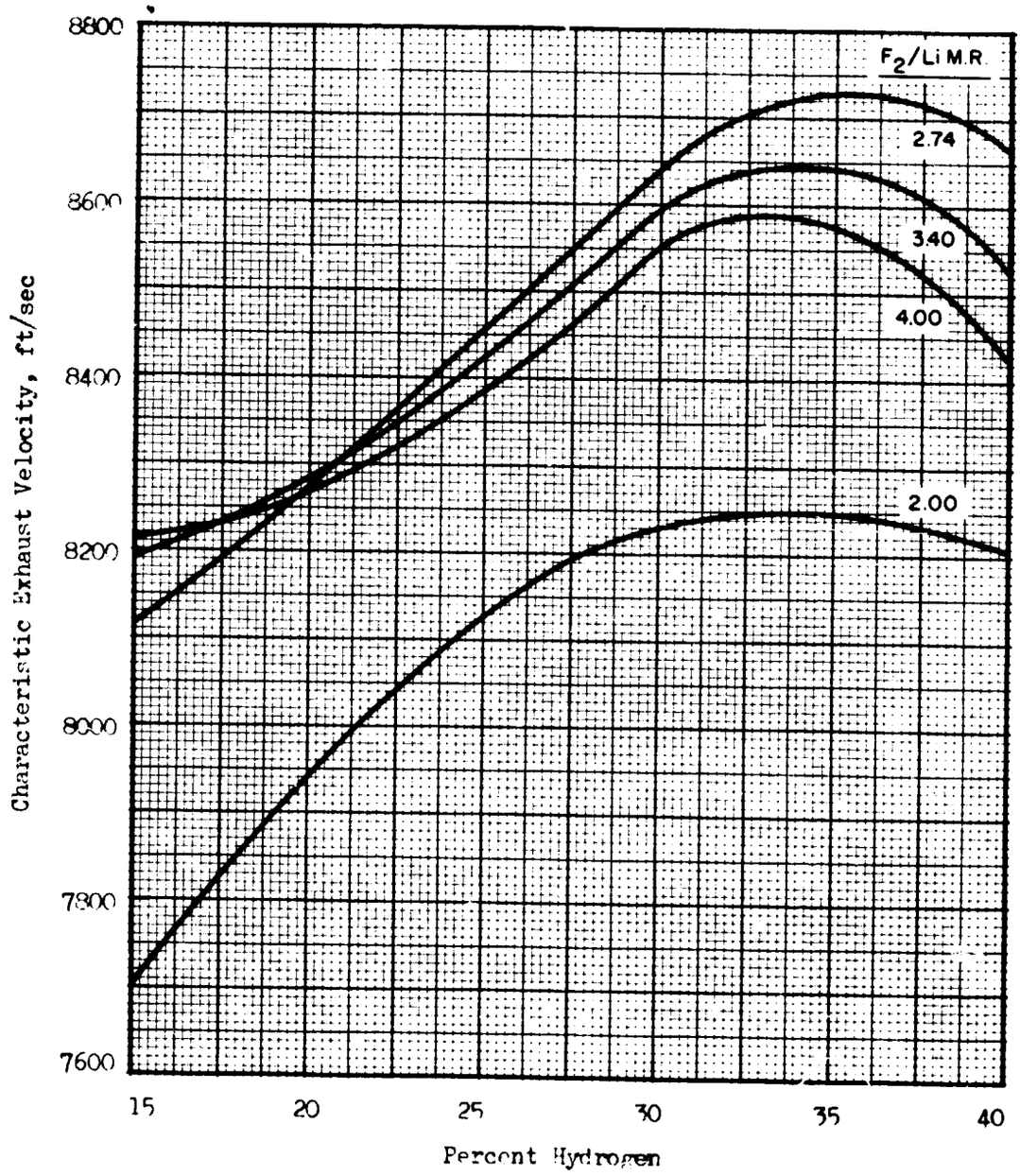

Figure 62. Variation of c* (Shifting Equilibrium) with Percent Hydrogen at Indicated F_2/Li Mixture Ratio, P_c = 500 Psia, LF_2(153 R)/SLi(36 R)/LH_2(36 R).

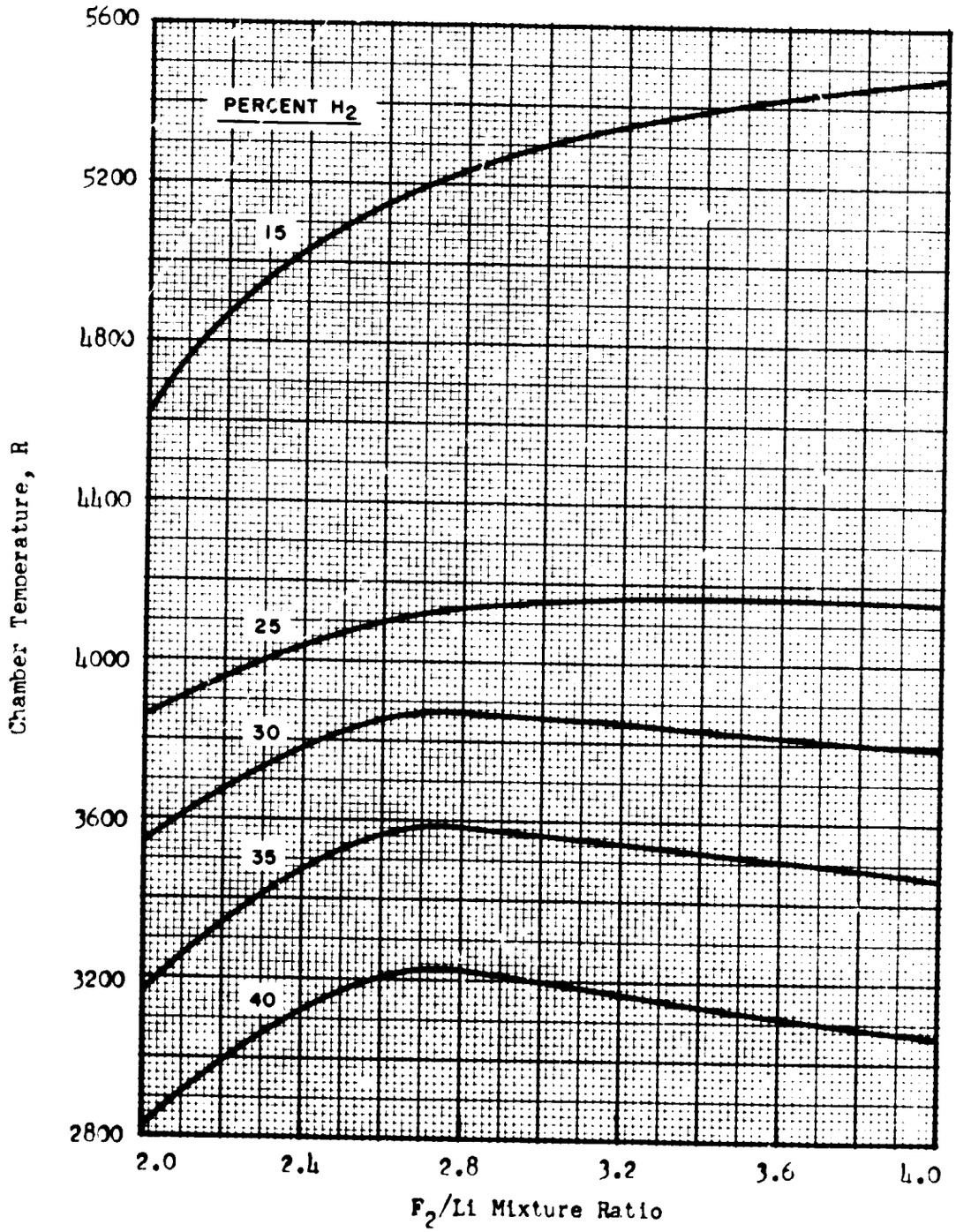

Figure 63. Chamber Temperature as Function of F_2/Li Mixture Ratio at Indicated Percent Hydrogen, P_c = 500 osia. LF_2(153 R)/SLi(36 R)/LH_2(36 R).

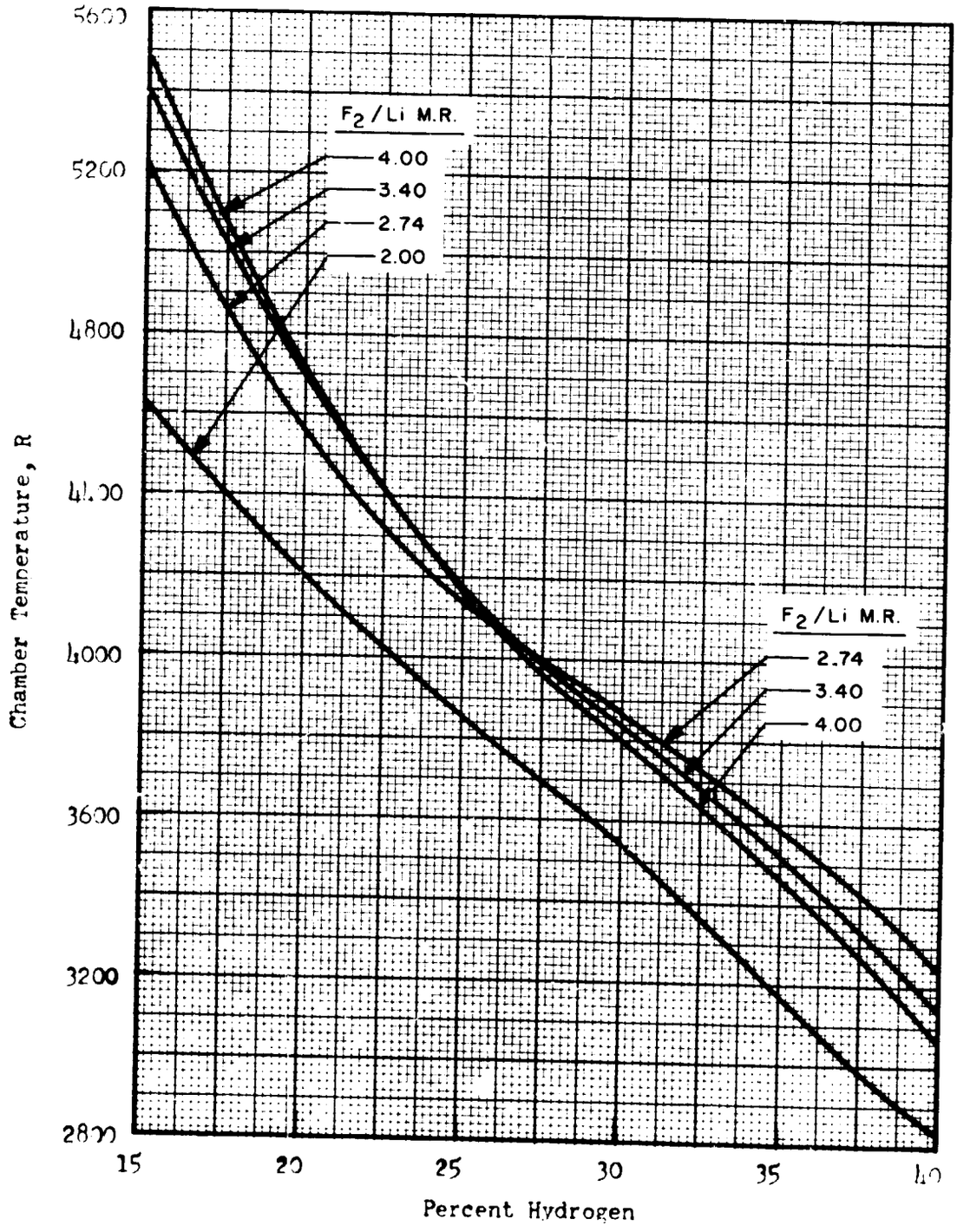

Figure 64. Chamber Temperature as Function of Percent Hydrogen at Indicated F_2/Li Mixture Ratio, P_c = 500 psia. LF_2(153 R)/SLi(36 R)/LH_2(36 R)

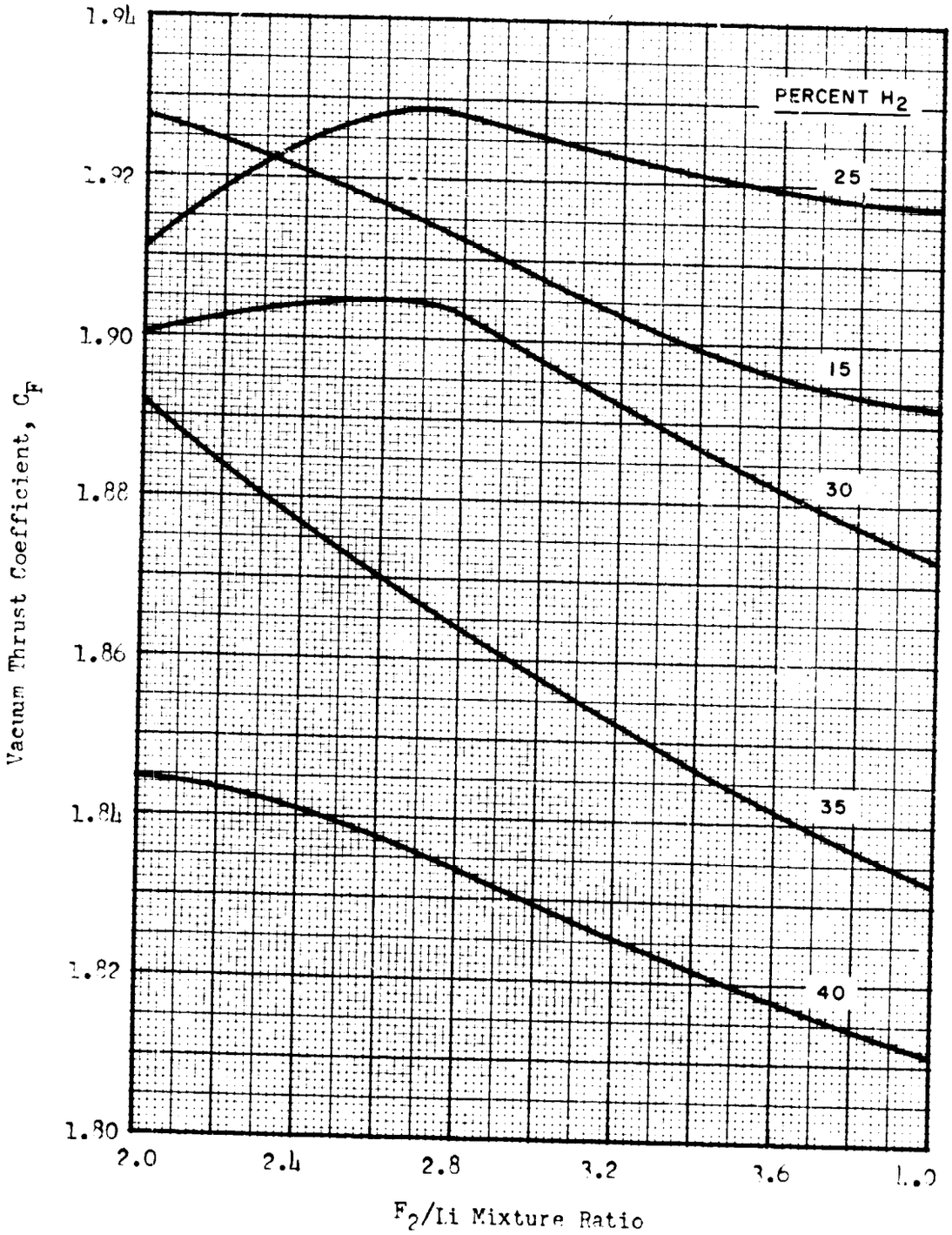

Figure 65. Vacuum Thrust Coefficient (Shifting Equilibrium) as Function of F_2/Li Mixture Ratio at Indicated Percent Hydrogen, P_c = 500 psia, ϵ = 40. LF_2(153 R)/SLi(36 R)/LH_2(36 R).

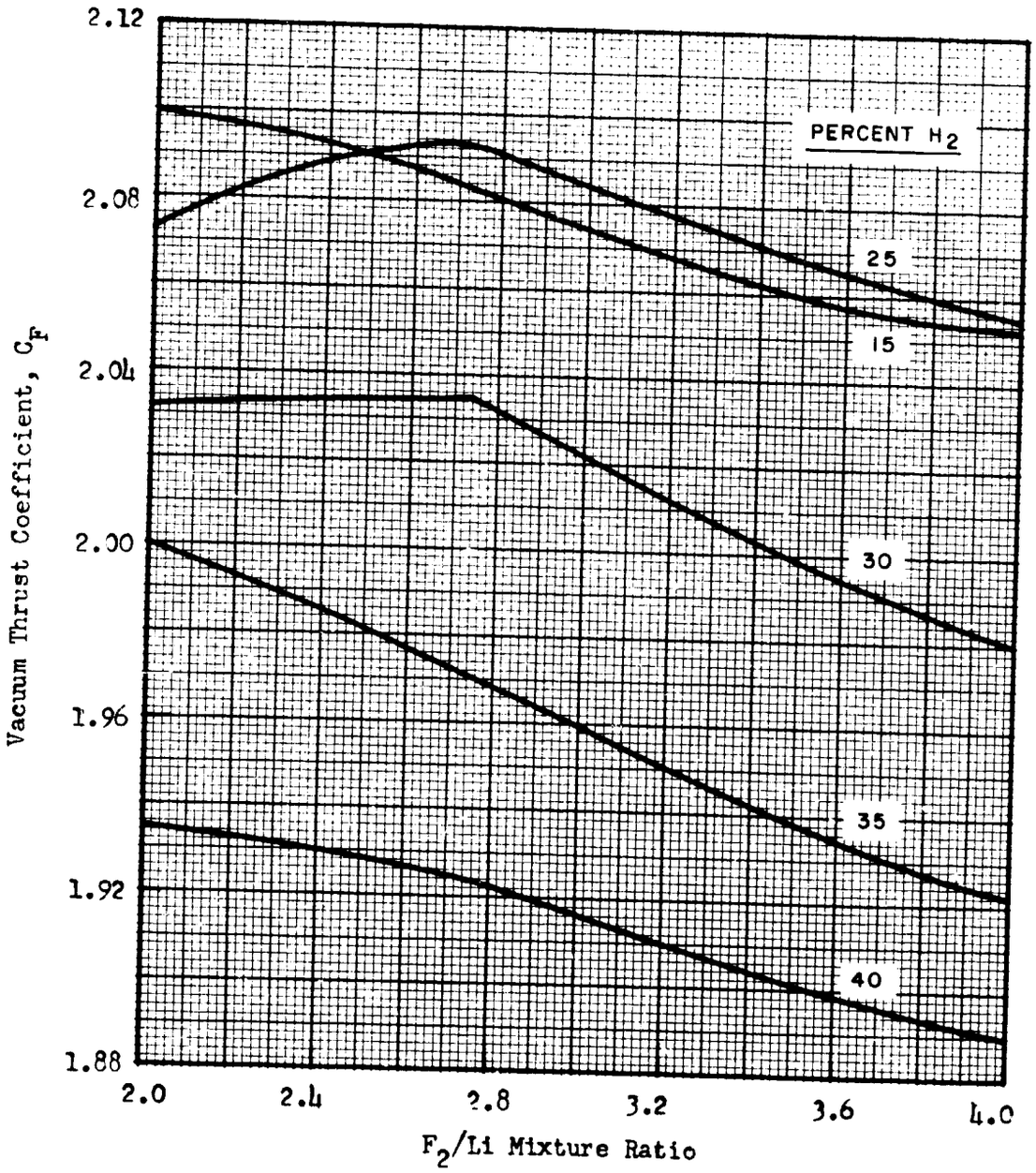

Figure 66. Vacuum Thrust Coefficient (Shifting Equilibrium) as Function of F_2/Li Mixture Ratio at Indicated Percent Hydrogen, P_c = 500 psia, ϵ = 300. LF_2(153 R)/SLi(36 R)/LH_2(36 R).

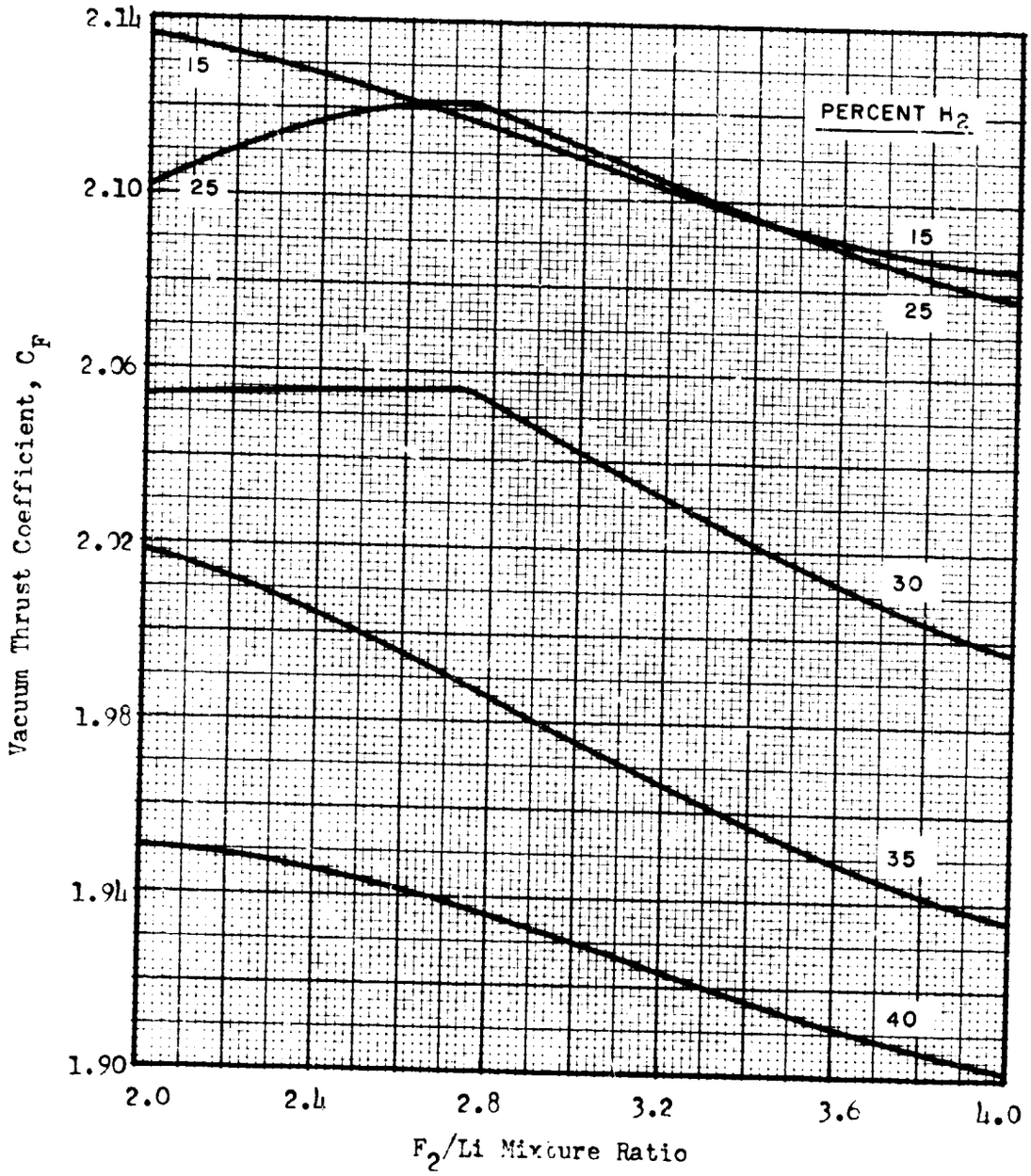

Figure 67. Vacuum Thrust Coefficient (Shifting Equilibrium) as Function of F_2/Li Mixture Ratio at Indicated Percent Hydrogen, P_c = 500 psia, ϵ = 500. LF_2(153 R)/SLi(36 R)/LH_2(36 R).

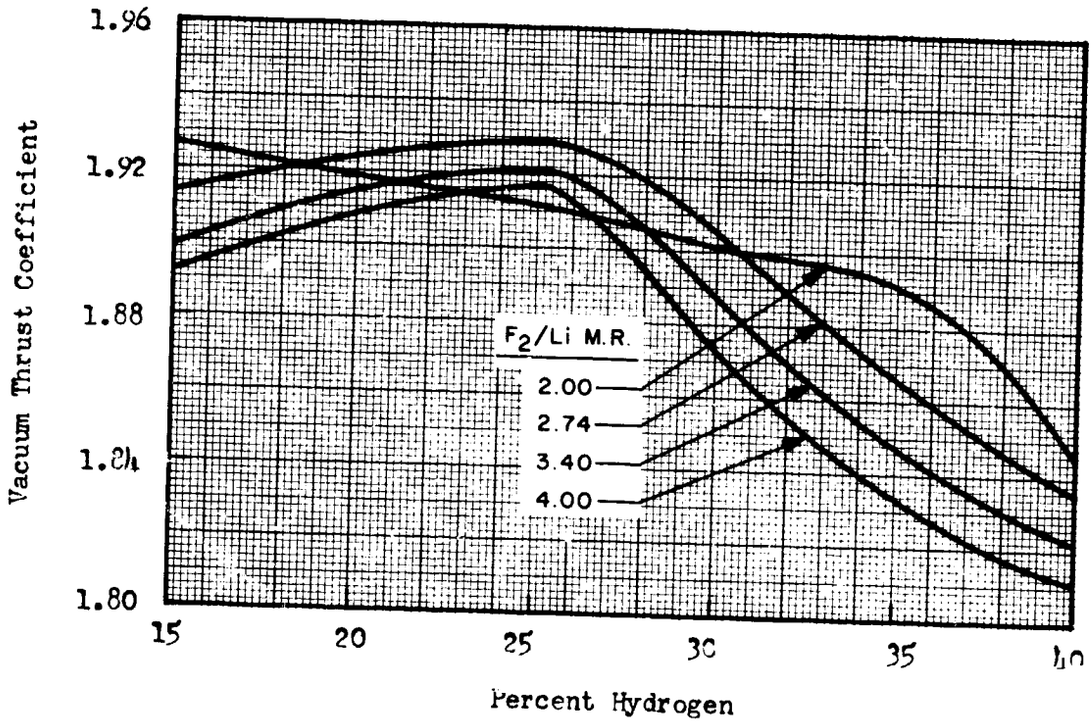

Figure 68. Variation of Vacuum Thrust Coefficient (Shifting Equilibrium) with Percent Hydrogen at Indicated F_2/Li M.R., P_c = 500 psia, ϵ = 40. LF_2(153 R)/SLi(36 R)/LH_2(36 R).

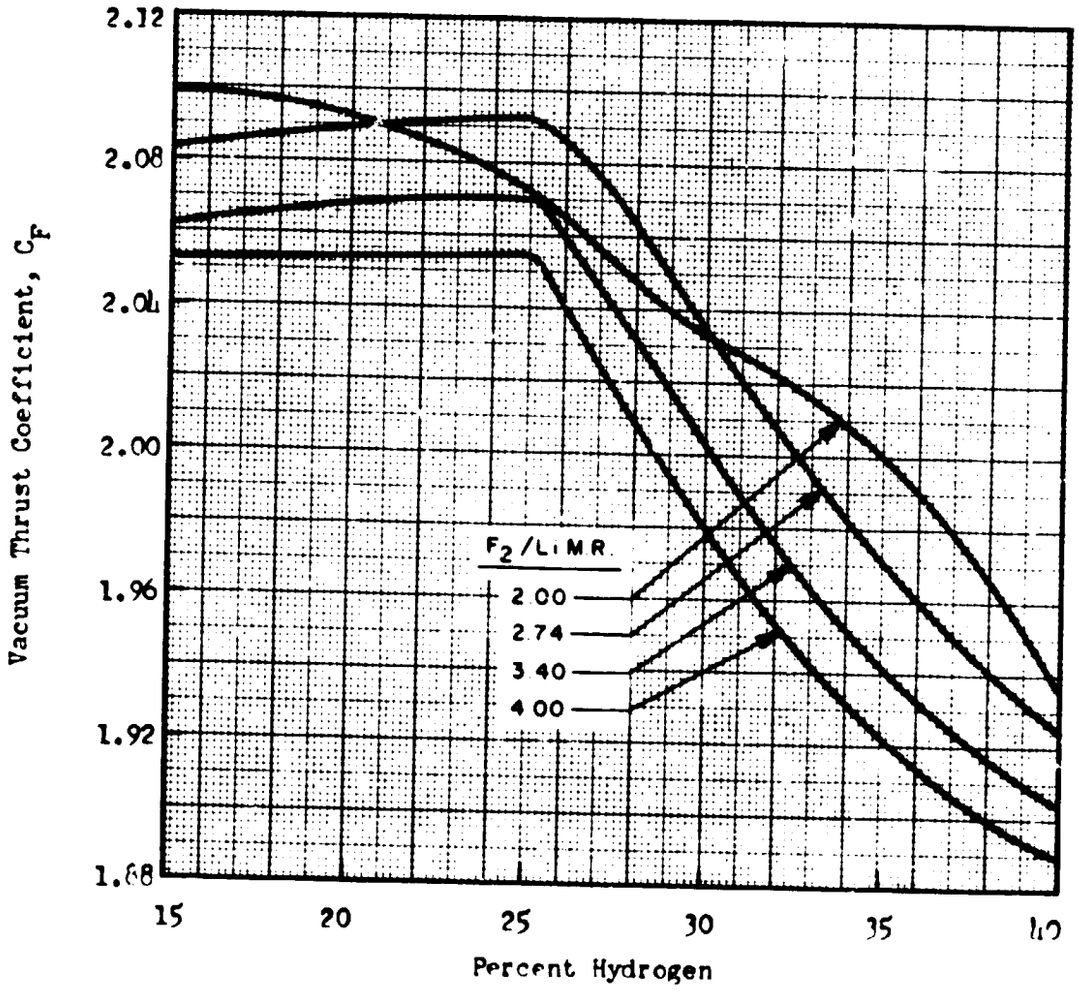

Figure 69. Vacuum Thrust Coefficient (Shifting Equilibrium) as Function of Percent Hydrogen at Indicated F_2/Li Mixture Ratio, P_c = 500 psia, ϵ = 300. $L\bar{F}_2$(153 R) / Li(36 R) / $L\bar{H}_2$(36 R).

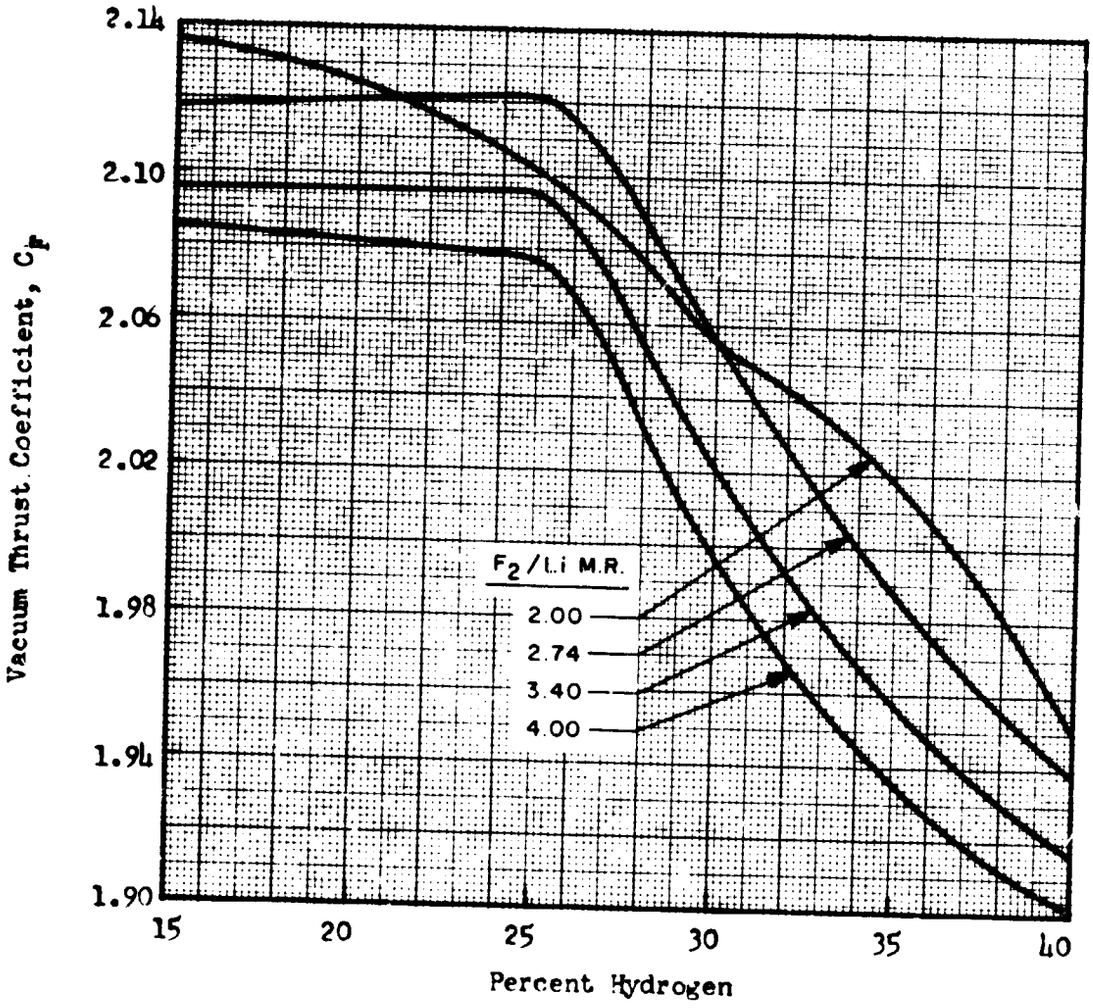

Figure 70. Vacuum Thrust Coefficient (Shifting Equilibrium) as Function of Percent Hydrogen at Indicated F_2/Li Mixture Ratio, P_c = 500 psia, ϵ = 500. LF_2(153 R)/SLi(36 R)/LH_2(36 R).

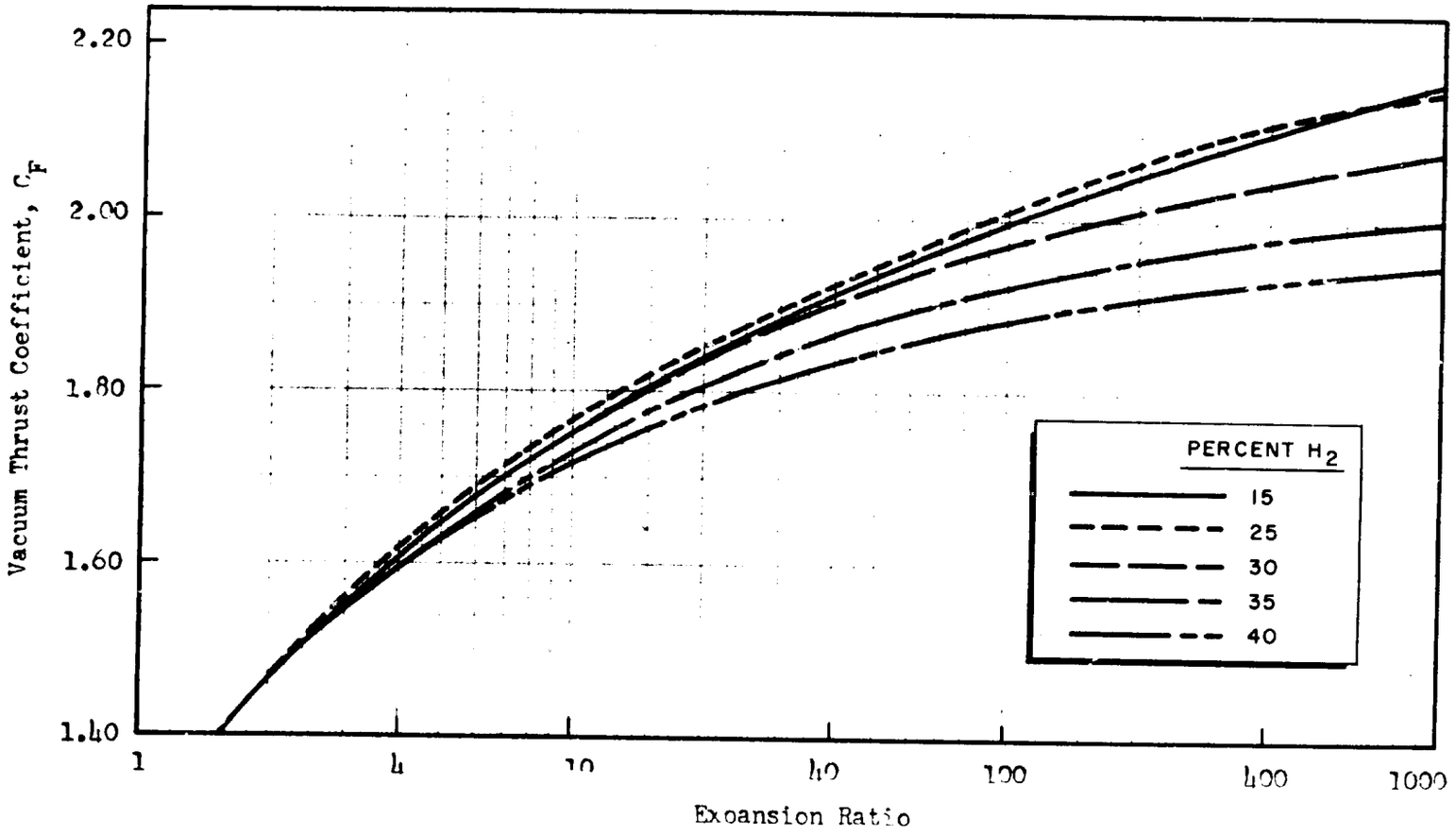

Figure 71. Vacuum Thrust Coefficient (Shifting Equilibrium) as Function of Expansion Ratio at Indicated Percent Hydrogen, P_c = 500 psia, F_2/Li M.R. = 2.74. LF_2(153 R)/SLi(36 R)/LH_2(36 R).

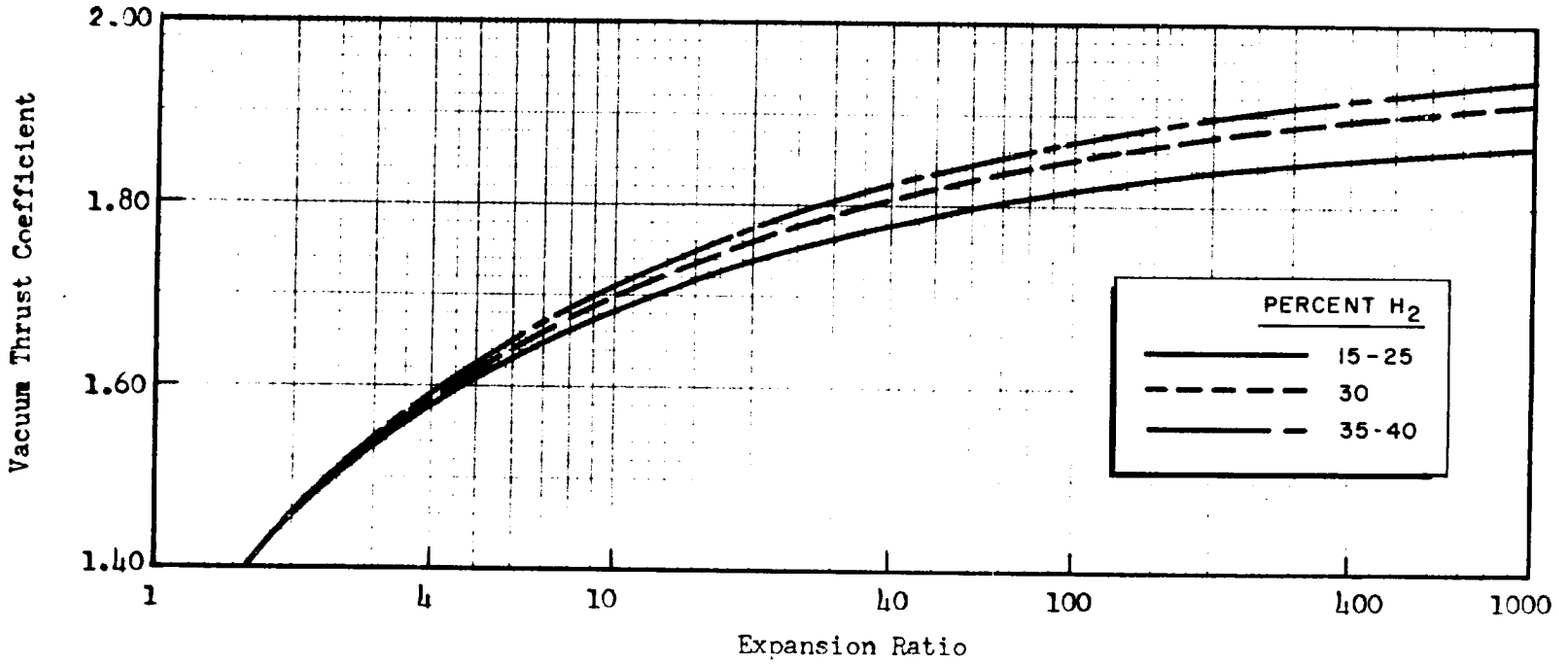

Figure 72. Vacuum Thrust Coefficient (Frozen Composition) as Function of Expansion Ratio at Indicated Percent Hydrogen, P_c = 500 psia, F_2/Li M.R. = 2.74. LF_2(153 R)/SLi(36 R)/IH_2(36 R).

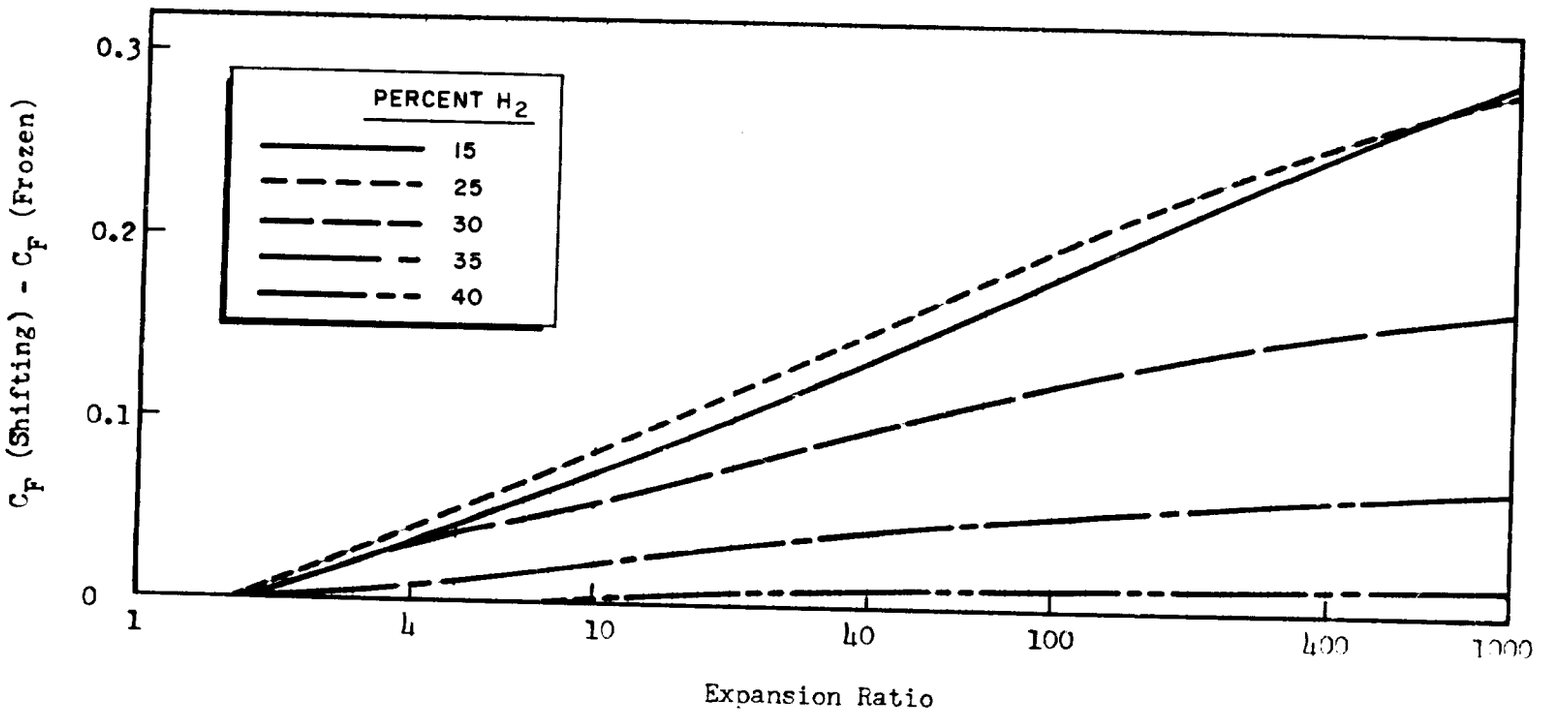

Figure 73. Difference Between Shifting Equilibrium and Frozen Composition Vacuum Thrust Coefficient at Indicated Percent Hydrogen, P_c = 500 psia, F_2/Li M.R. = 2.74. LF_2(153 R)/SLi(36 R)/LH_2(36 R).

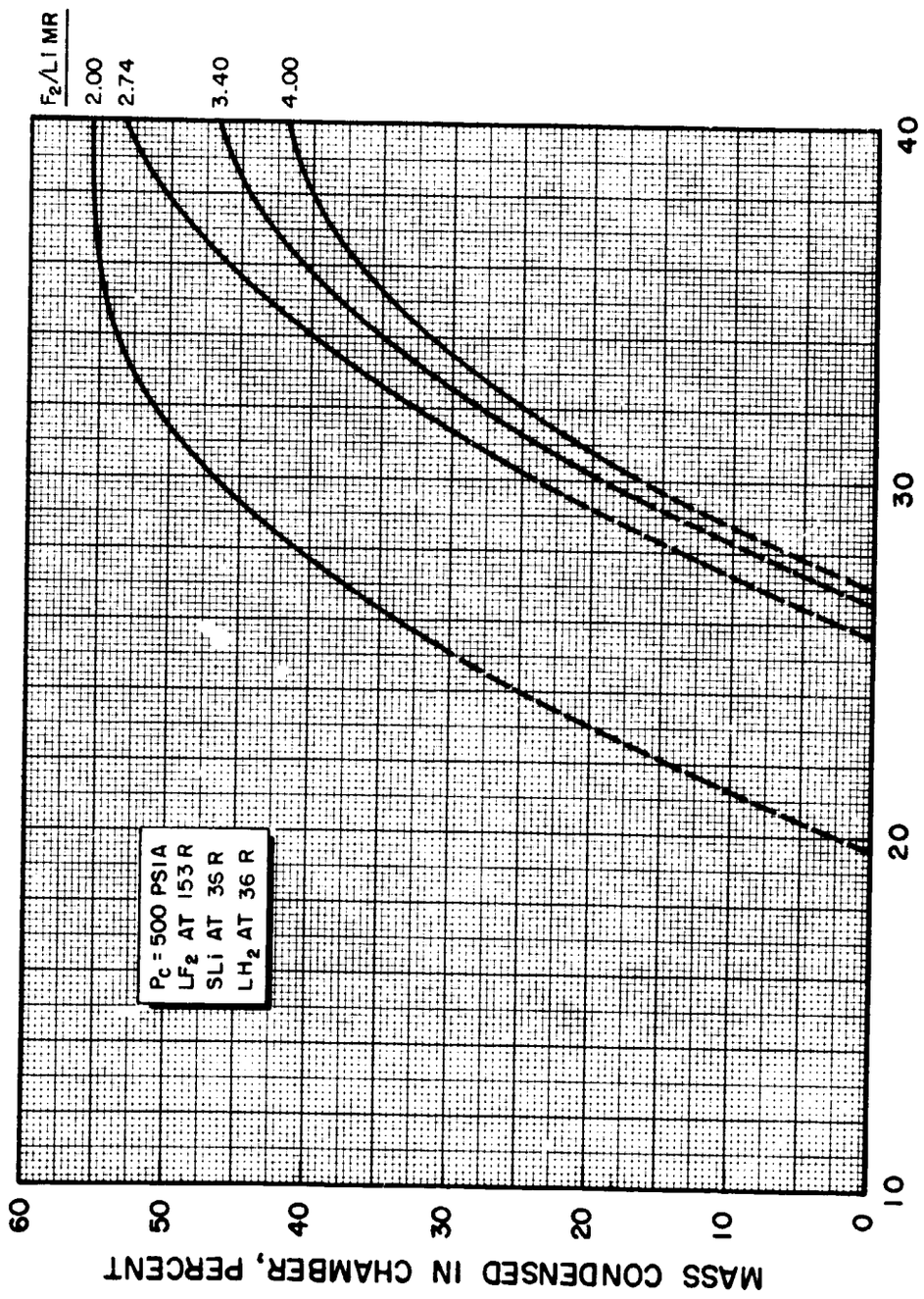

Figure 74. Weight Percent Condensed in Chamber as Function of Percent Hydrogen, at Indicated F_2/Li Mixture Ratio and Chamber Pressure, LF_2(153 R)/SLi(36 R)/LH_2(36 R).

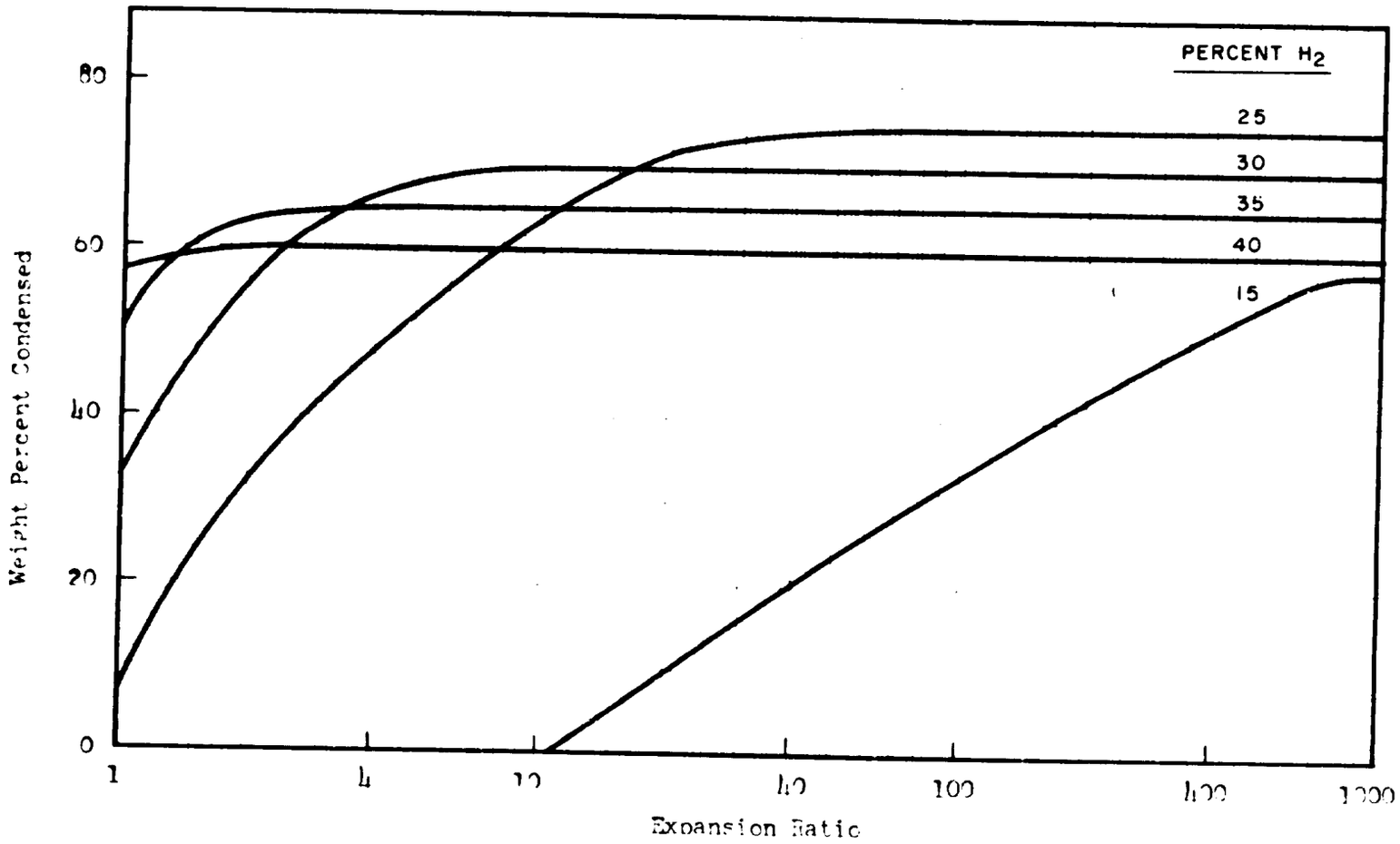

Figure 75. Weight Percent of Condensed Phase as Function of Expansion Ratio at Indicated Percent Hydrogen, P_c = 500 psia, F_2/Li M.R. = 2.74. $LF_2(153\ R)/SLi(36\ R)/LH_2(36\ R)$.

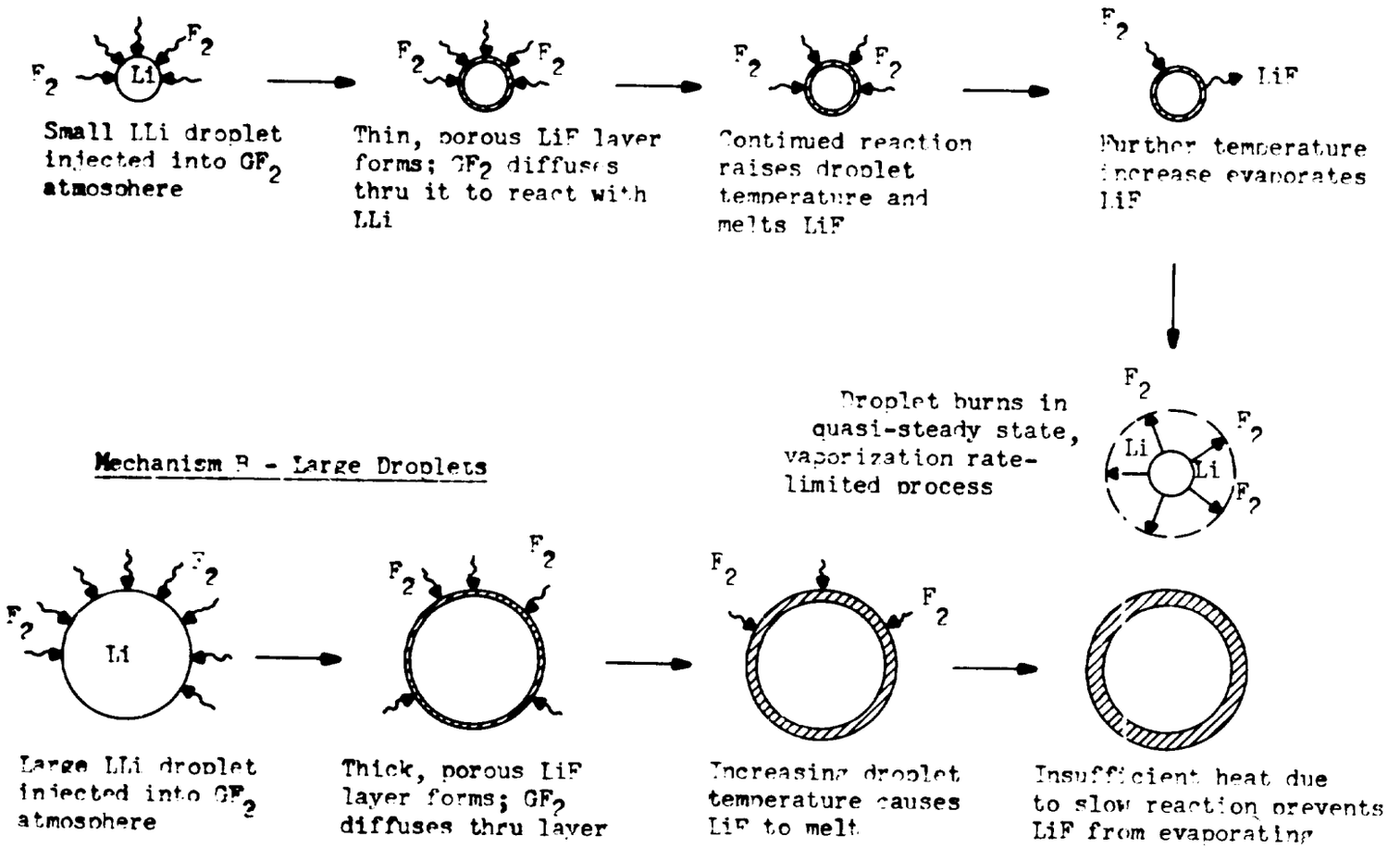

Figure 76. Ignition and Combustion Mechanisms of Liquid Lithium in Gaseous Fluorine.

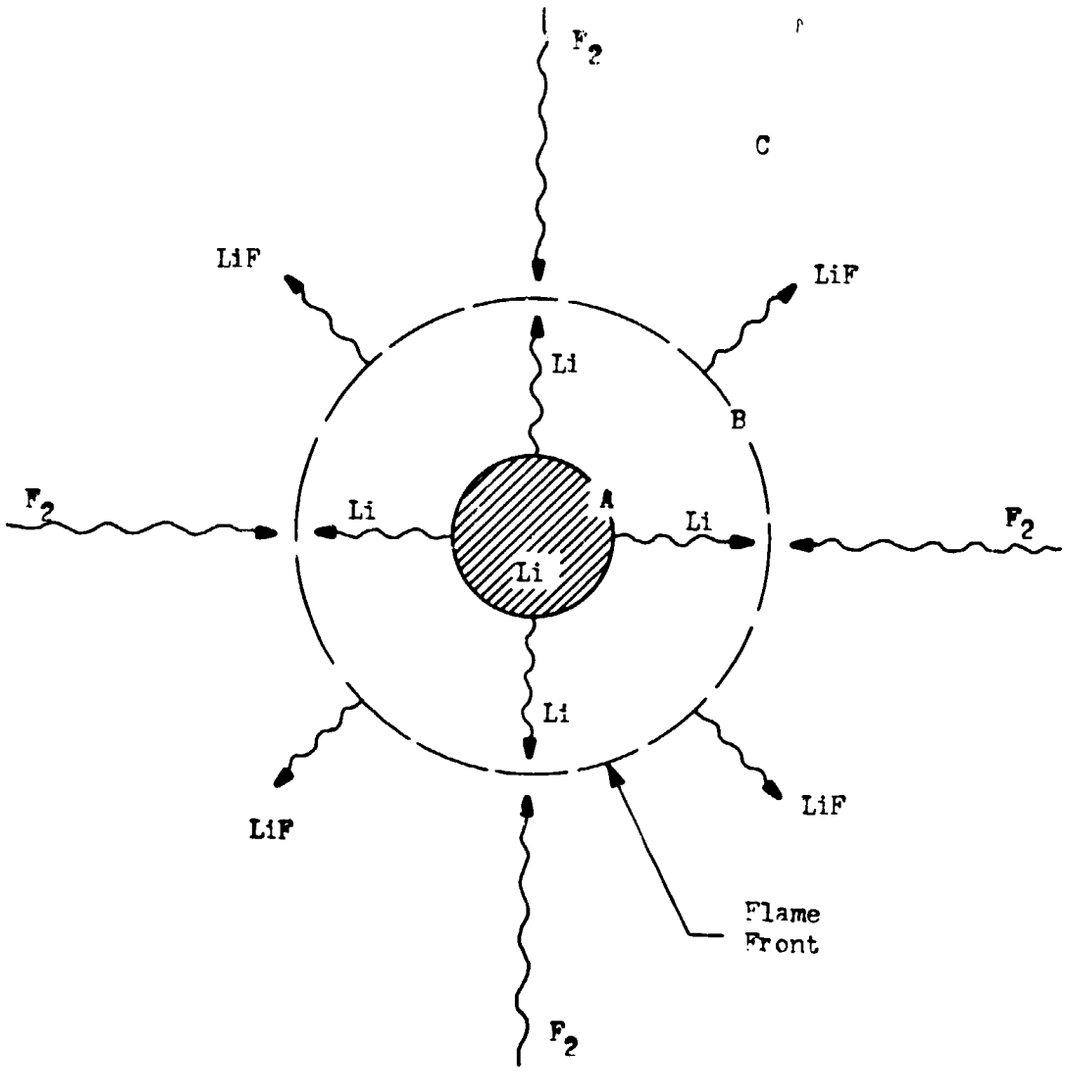

Figure 77. Simplified Schematic of Lithium Droplet Burning in Fluorine Atmosphere by Vaporization Rate-Limited Mechanism. (Lithium vapor diffuses away from the liquid droplet (A) to the flame front (B), where it reacts with fluorine. The LiF then diffuses outward.)

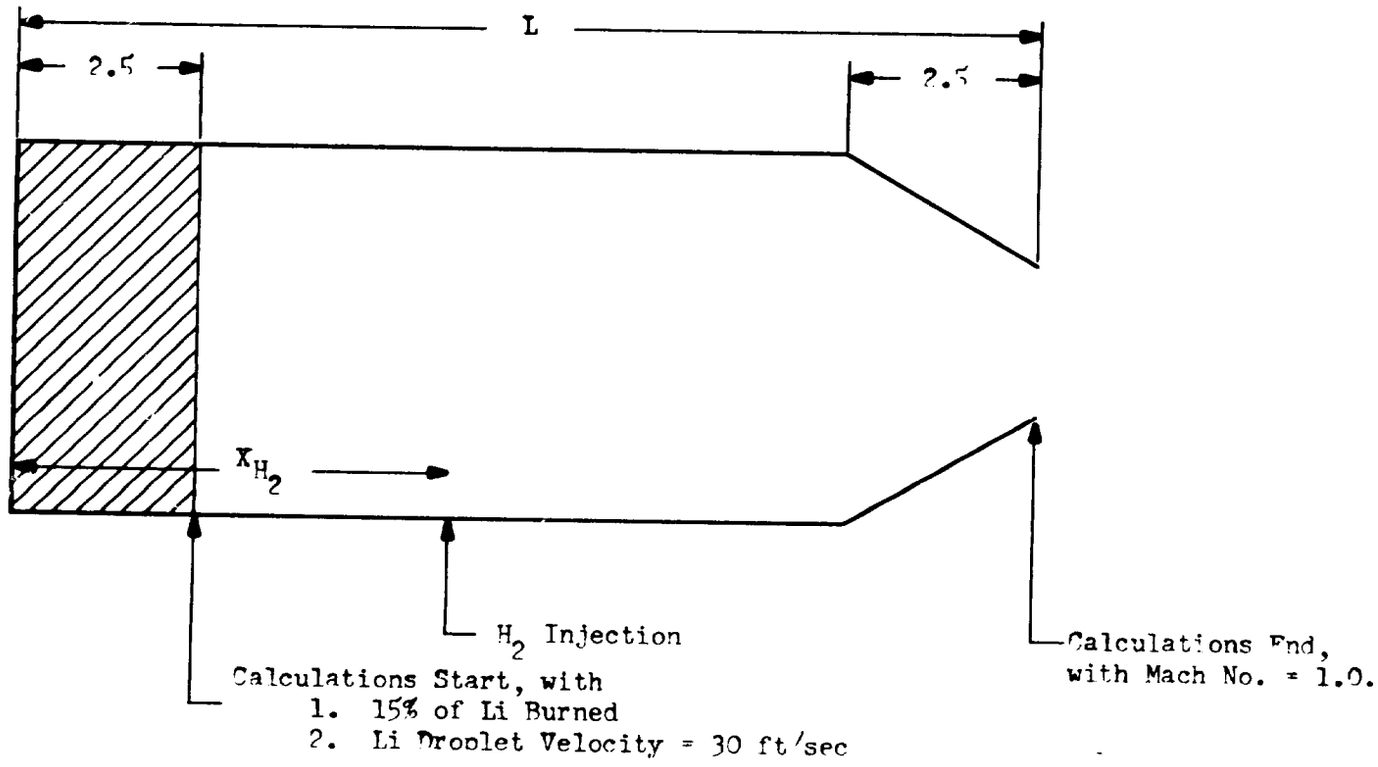

Figure 78. Chamber Geometry for Combustion Model Computations.

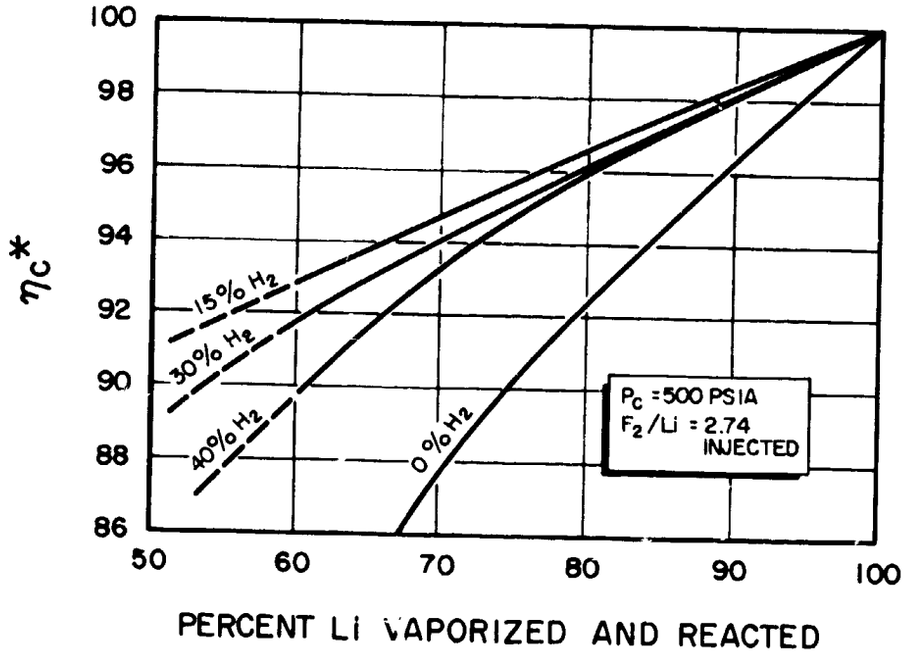

Figure 79. Calculated Variation of c* Efficiency with Percent Lithium Vaporized, at Indicated Percentages of Hydrogen. All Vaporized Propellants Assumed to be Completely Reacted.

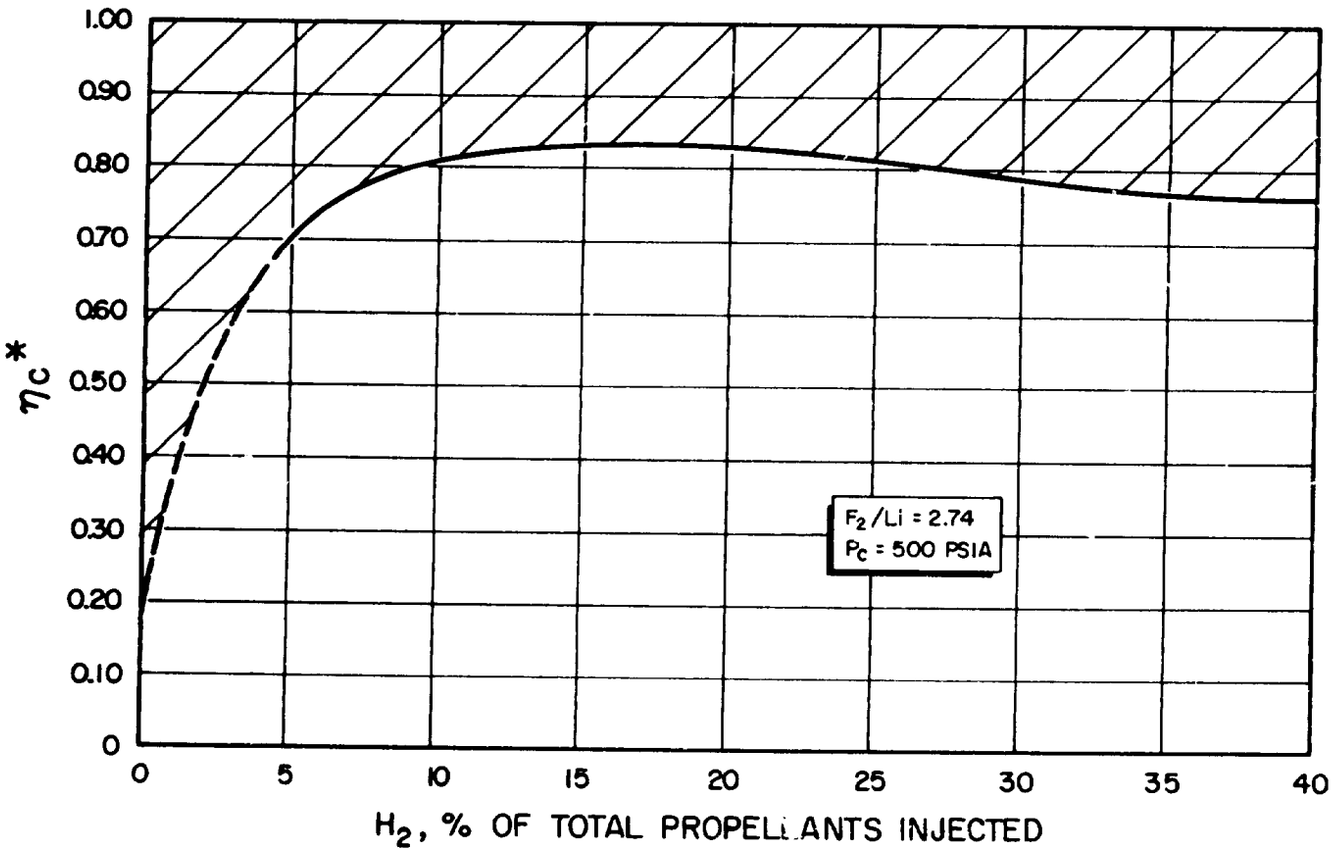

Figure 80. Calculated Range of c* Efficiency, Assuming Complete Reaction of Fluorine and Hydrogen but only Partial Reaction of Lithium. If No Lithium Reacts, c* Efficiency Is Represented by the Curved Line. With Partial Lithium Reaction, c* Efficiency Is in the Shaded Region.

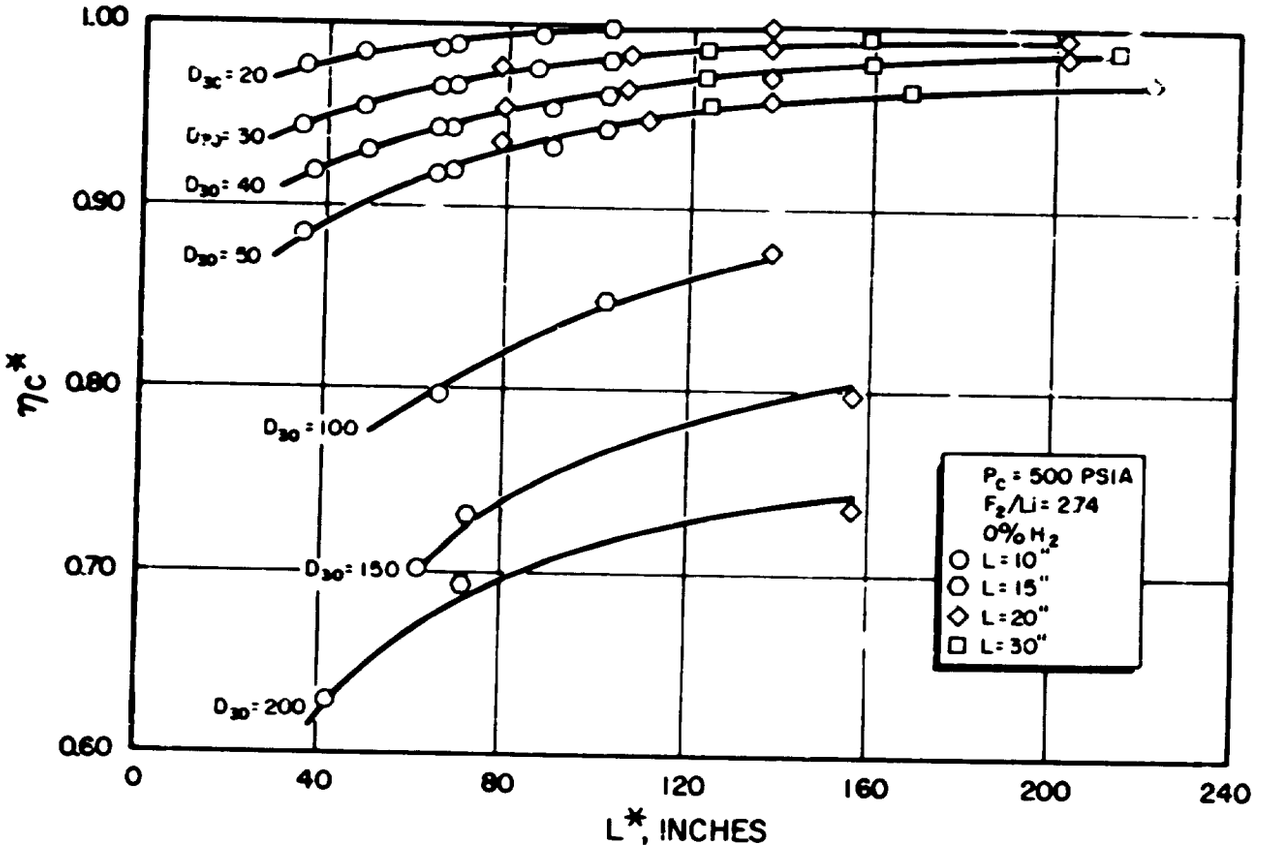

Figure 81. Calculated Variation of c^* Efficiency with L* for Indicated Volume Mean Lithium Droplet Diameters (in Microns). F_2/Li Combustion in Absence of Hydrogen.

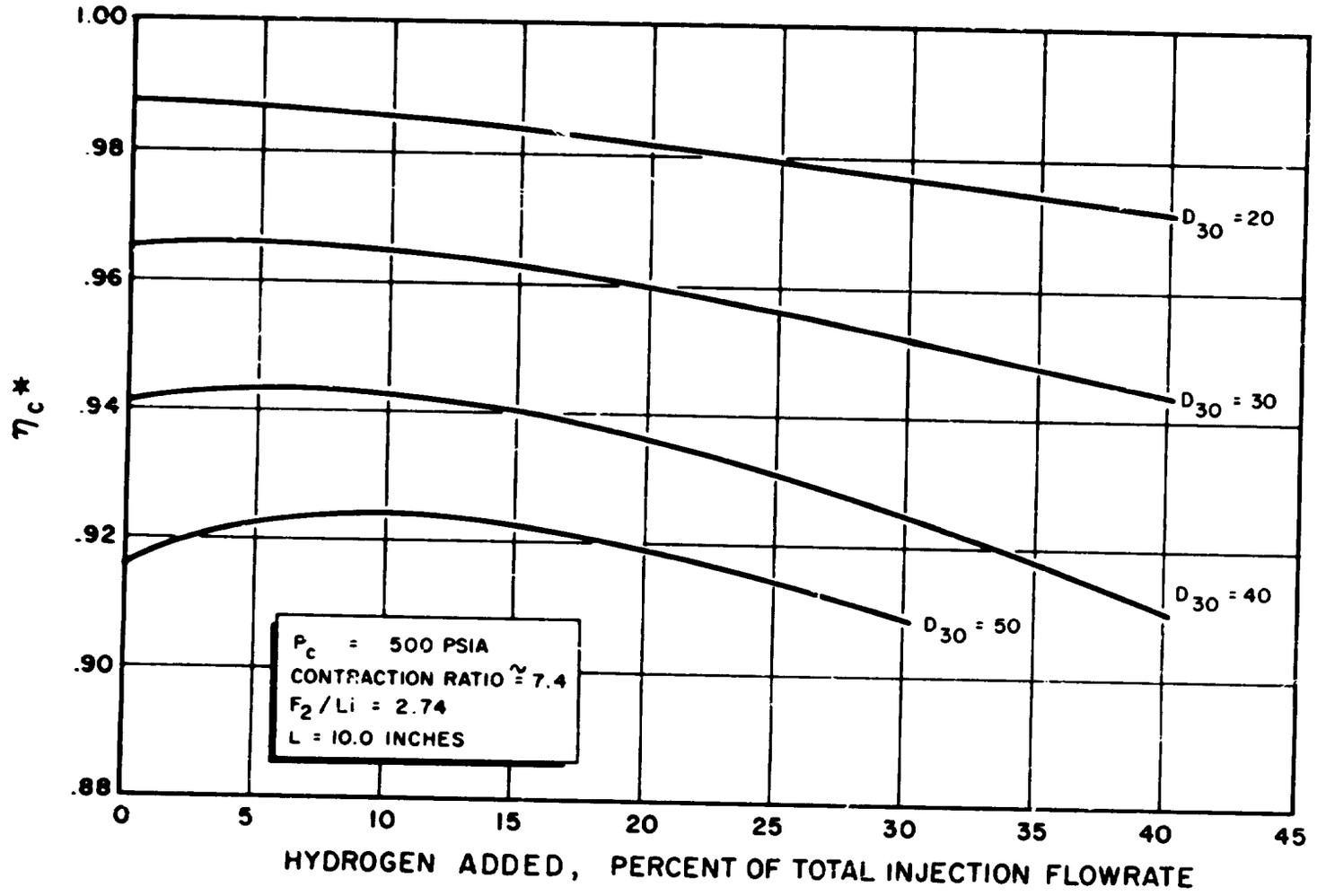

Figure 82 . Calculated Variation of c* Efficiency with Percentage Hydrogen, Added at Face of F_2/Li Injector, for Indicated Volume Mean Lithium Droplet Diameters (in Microns).

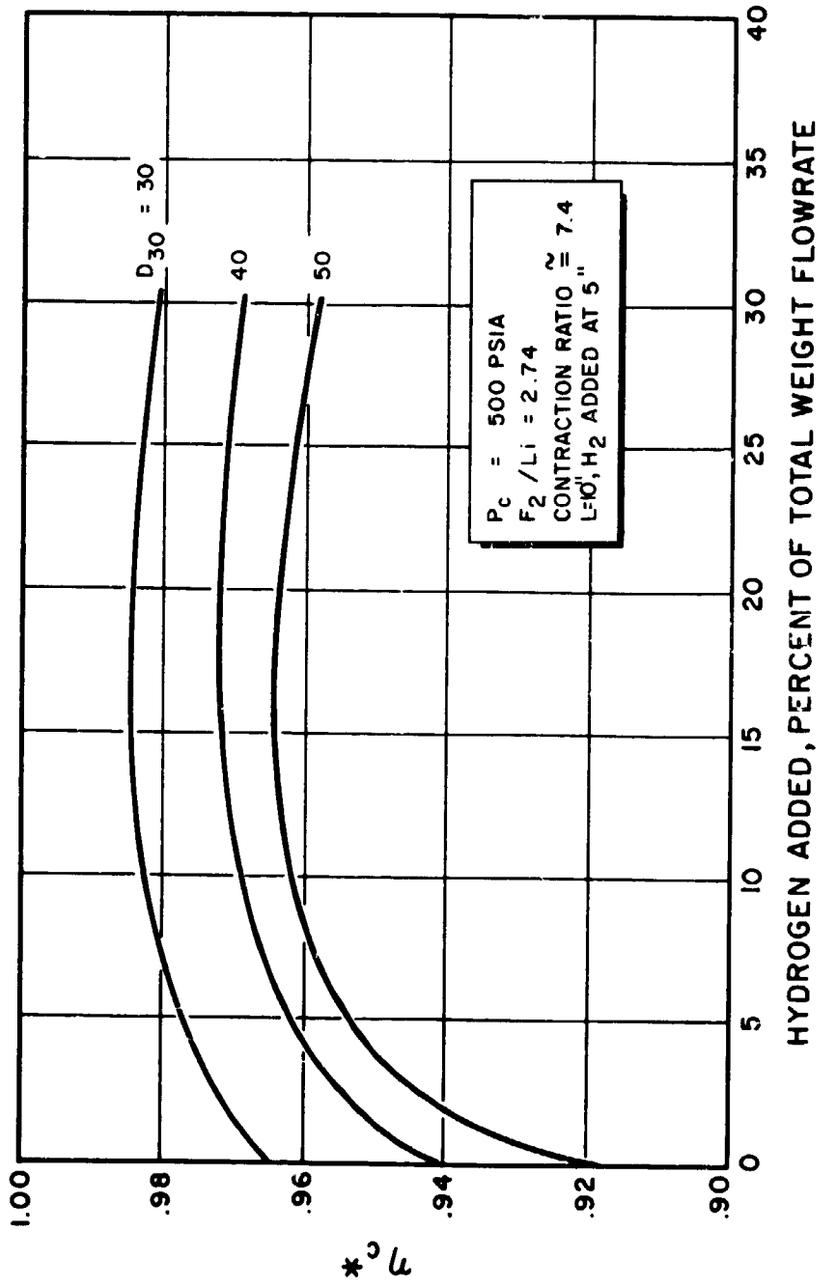

Figure 83. Calculated Variation of c* Efficiency with Percentage Hydrogen, Added at 5-inches from F_2/Li Injector Face in 10-inch Chamber, for Indicated Volume Mean Lithium Droplet Diameters (in Microns).

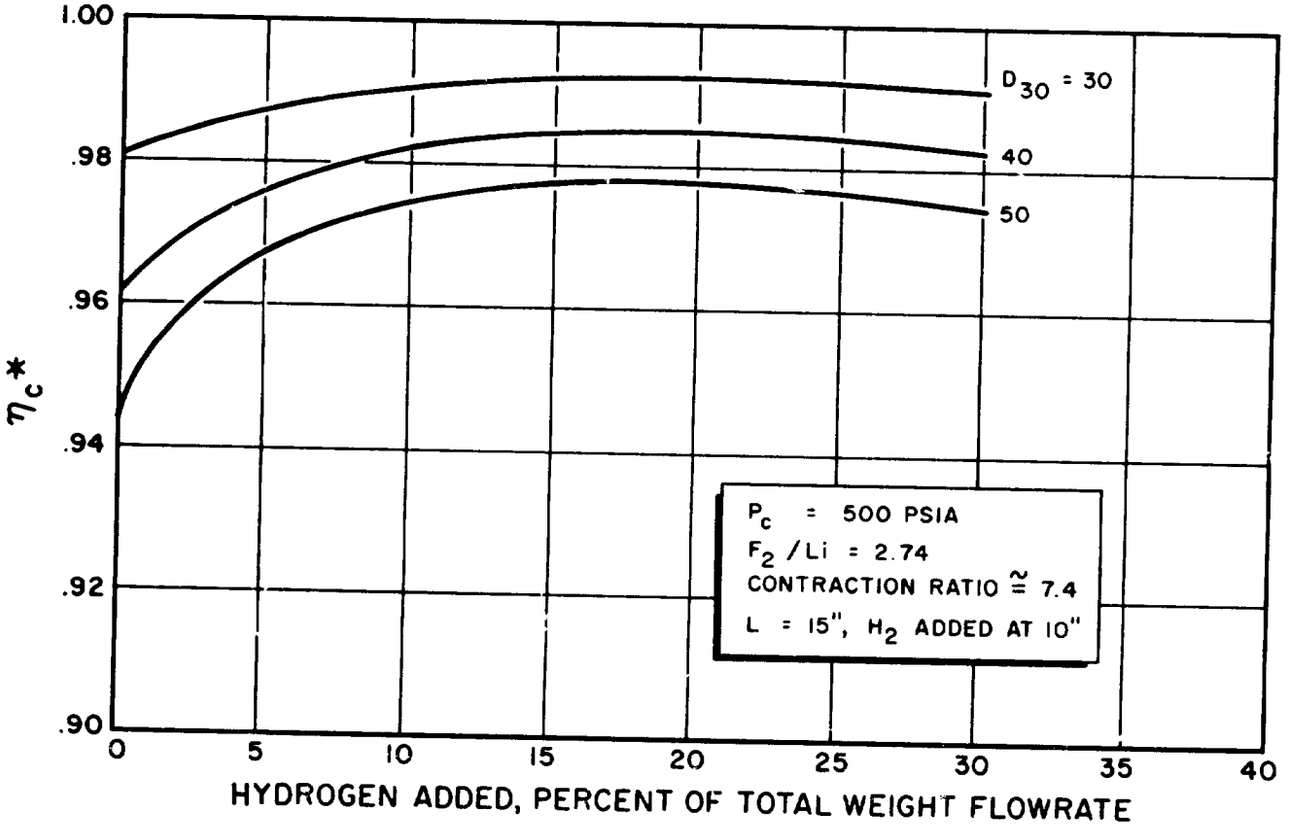

Figure 84. Calculated Variation of c* Efficiency with Percentage Hydrogen, Added at 10-inches from F_2/Li Injector Face in 15-inch Chamber, for Indicated Volume Mean Lithium Droplet Diameters (in Microns)

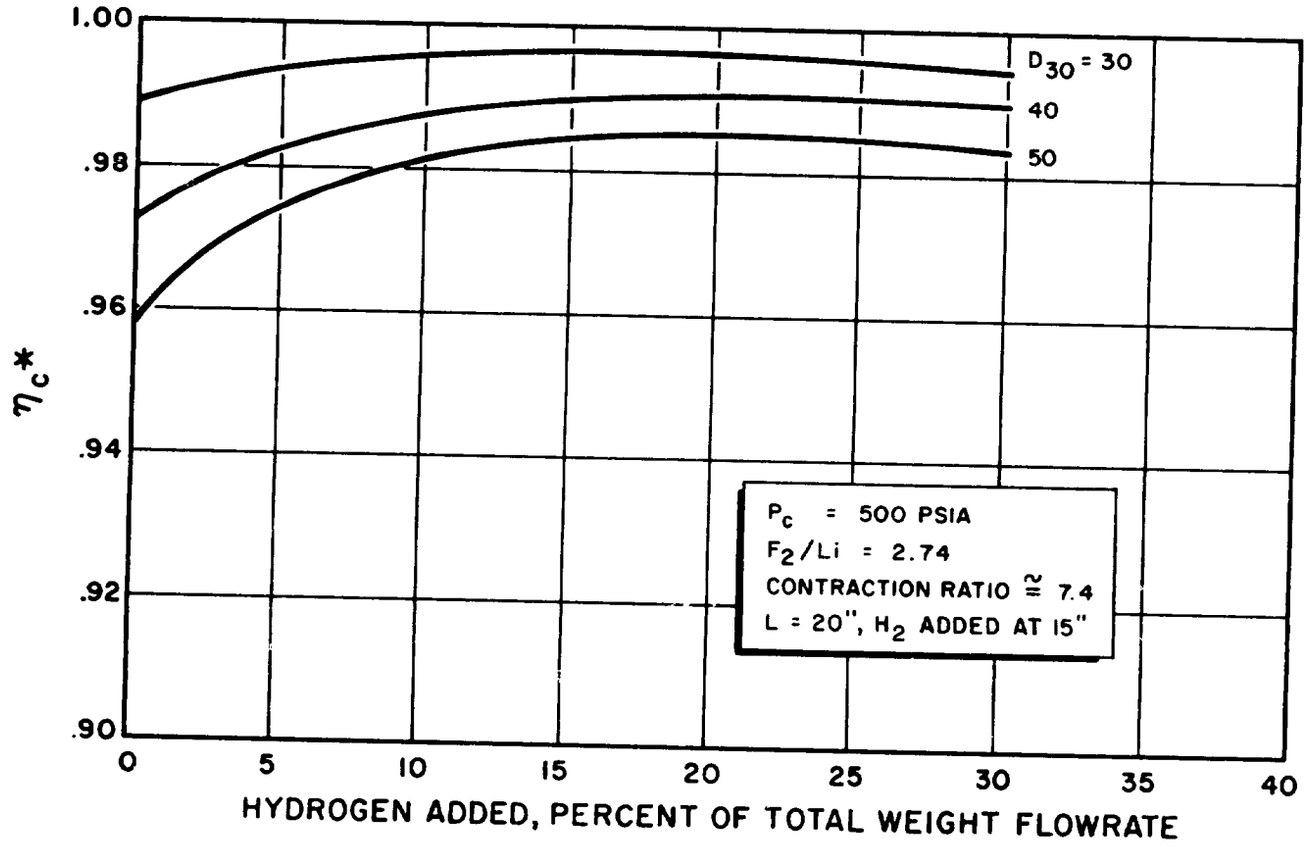

Figure 85. Calculated Variation of c* Efficiency with Percentage Hydrogen, Added at 15-inches from F_2/Li Injector Face in 20-inch Chamber, for Indicated Volume Mean Lithium Droplet Diameters (in Microns).

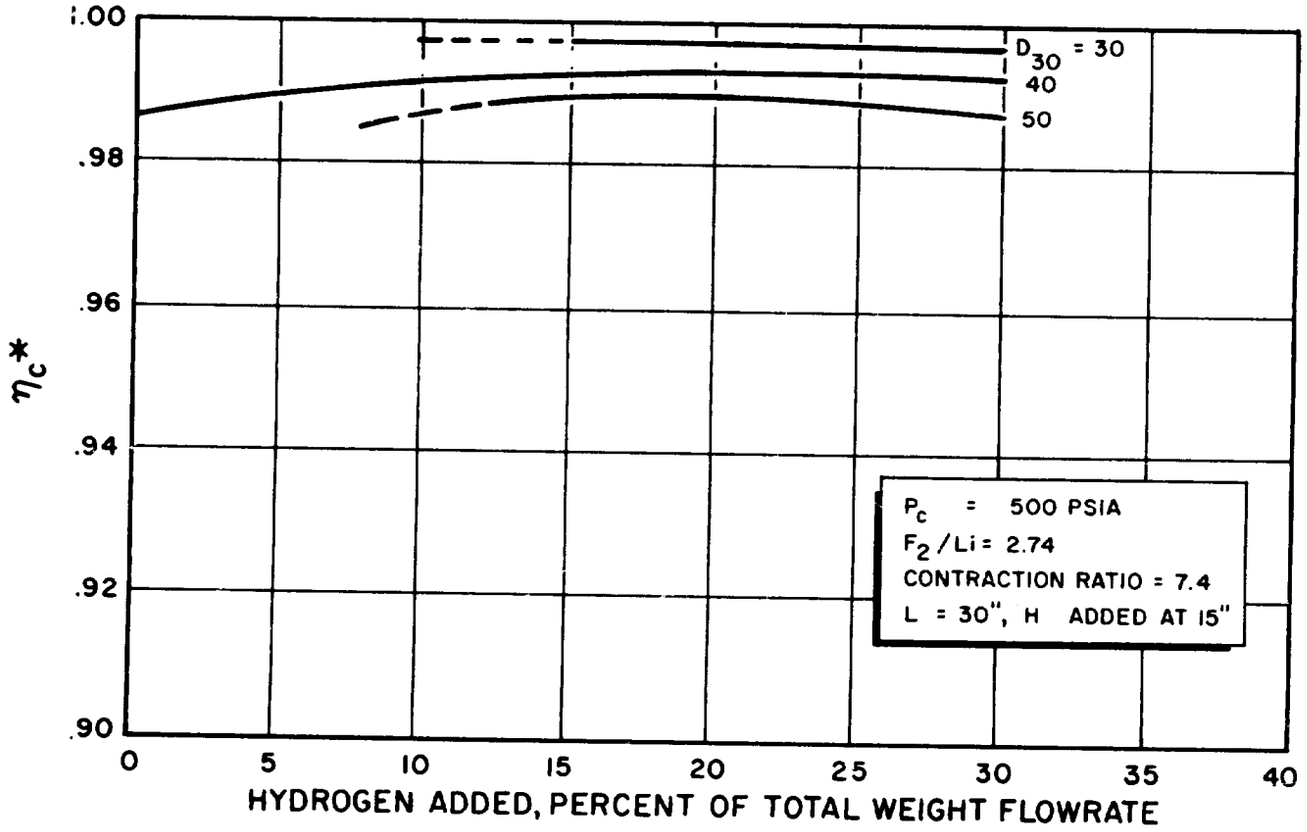

Figure 86. Calculated Variation of c* Efficiency with Percentage Hydrogen, Added at 15-inches from F_2/Li Injector Face in 30-inch Chamber, for Indicated Volume Mean Lithium Droplet Diameters (in Microns).

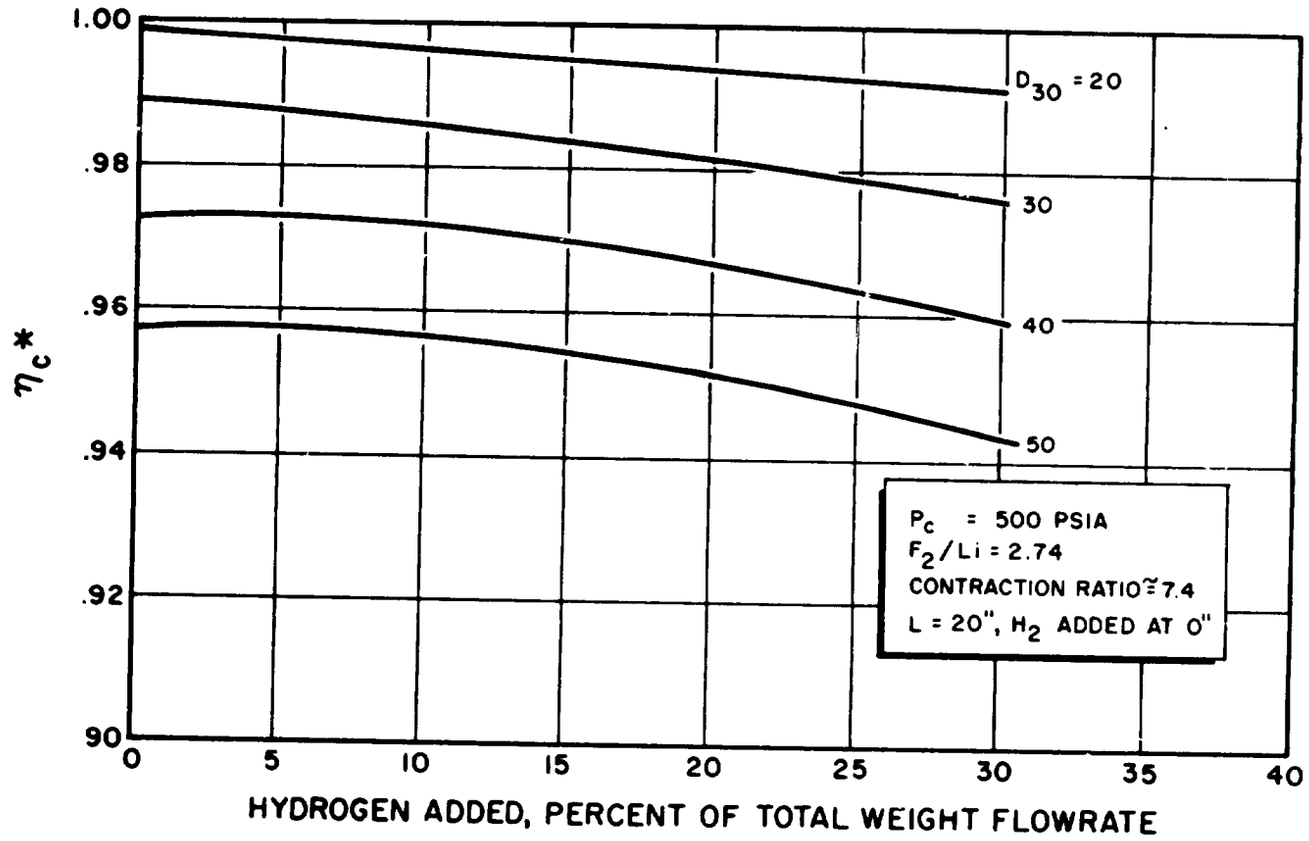

Figure 87. Calculated Variation of c* Efficiency with Percentage Hydrogen, Added at F_2/Li Injector Face in 20-inch Chamber, for Indicated Volume Mean Lithium Droplet Diameters (in Microns).

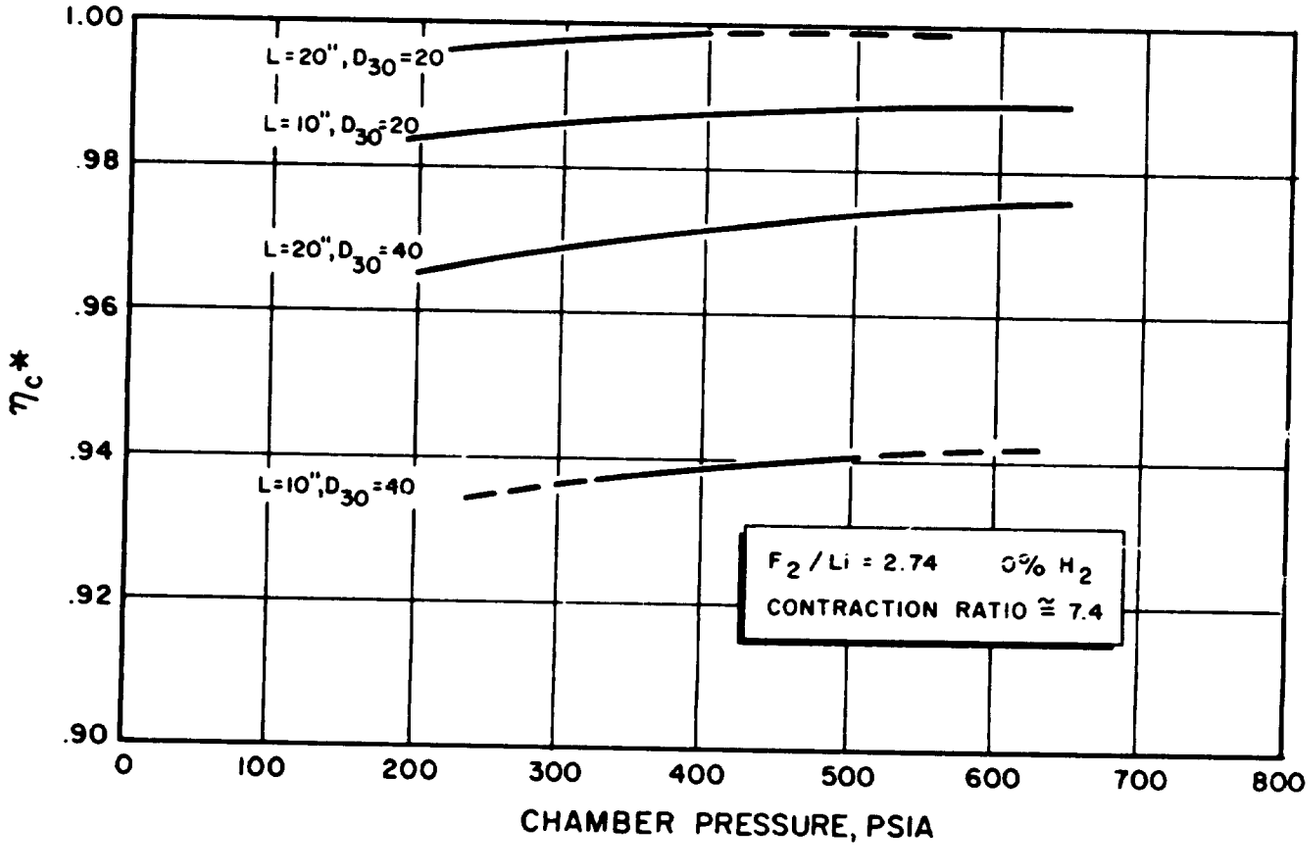

Figure 88. Calculated Variation of c* Efficiency with Chamber Pressure for OF_2/LLi Combustion at Indicated Chamber Lengths and Volume Mean Lithium Droplet Diameters (in Microns).

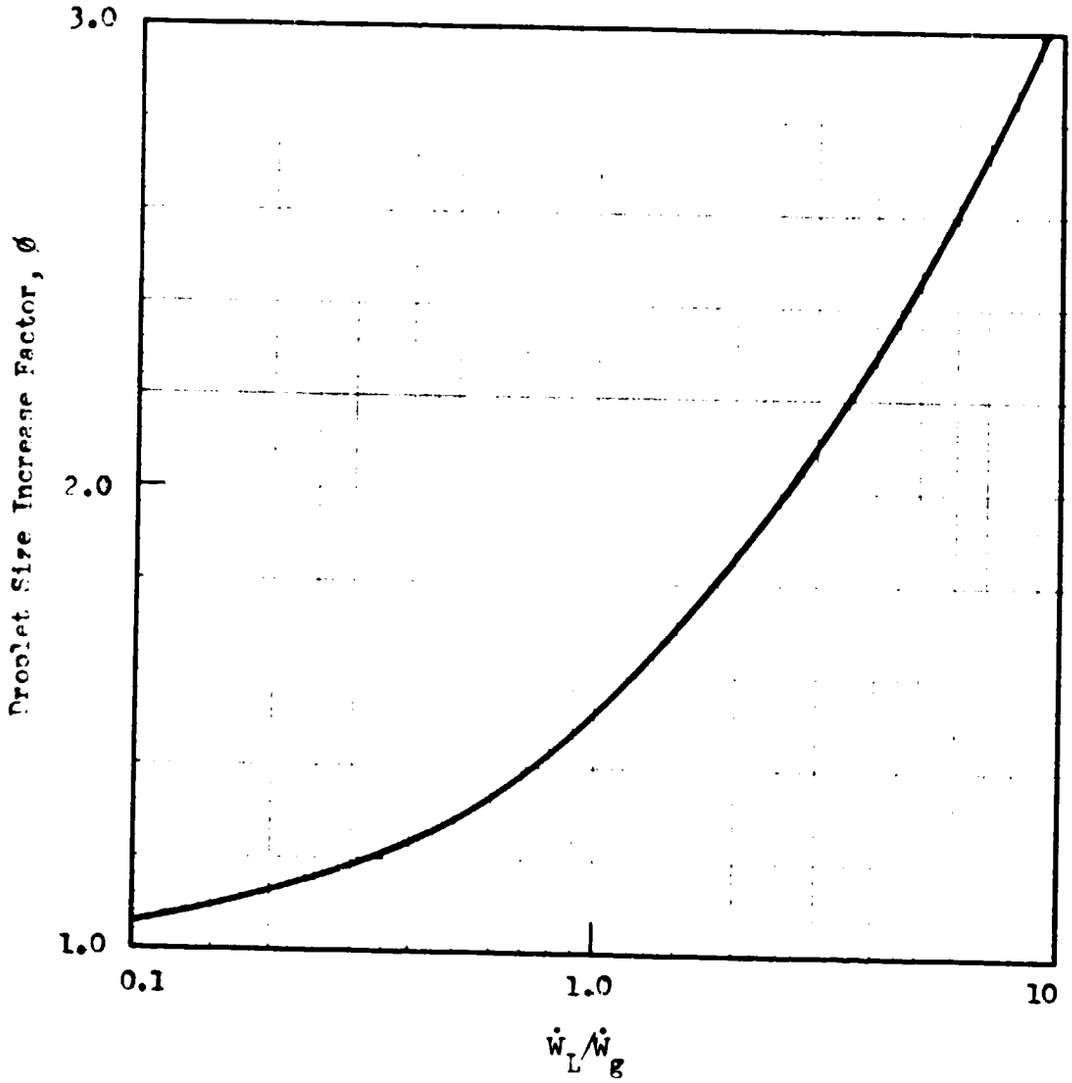

Figure 89. Variation of Ø (Equation 14) with the Ratio $\dot{W}_L/\dot{W}_g$.

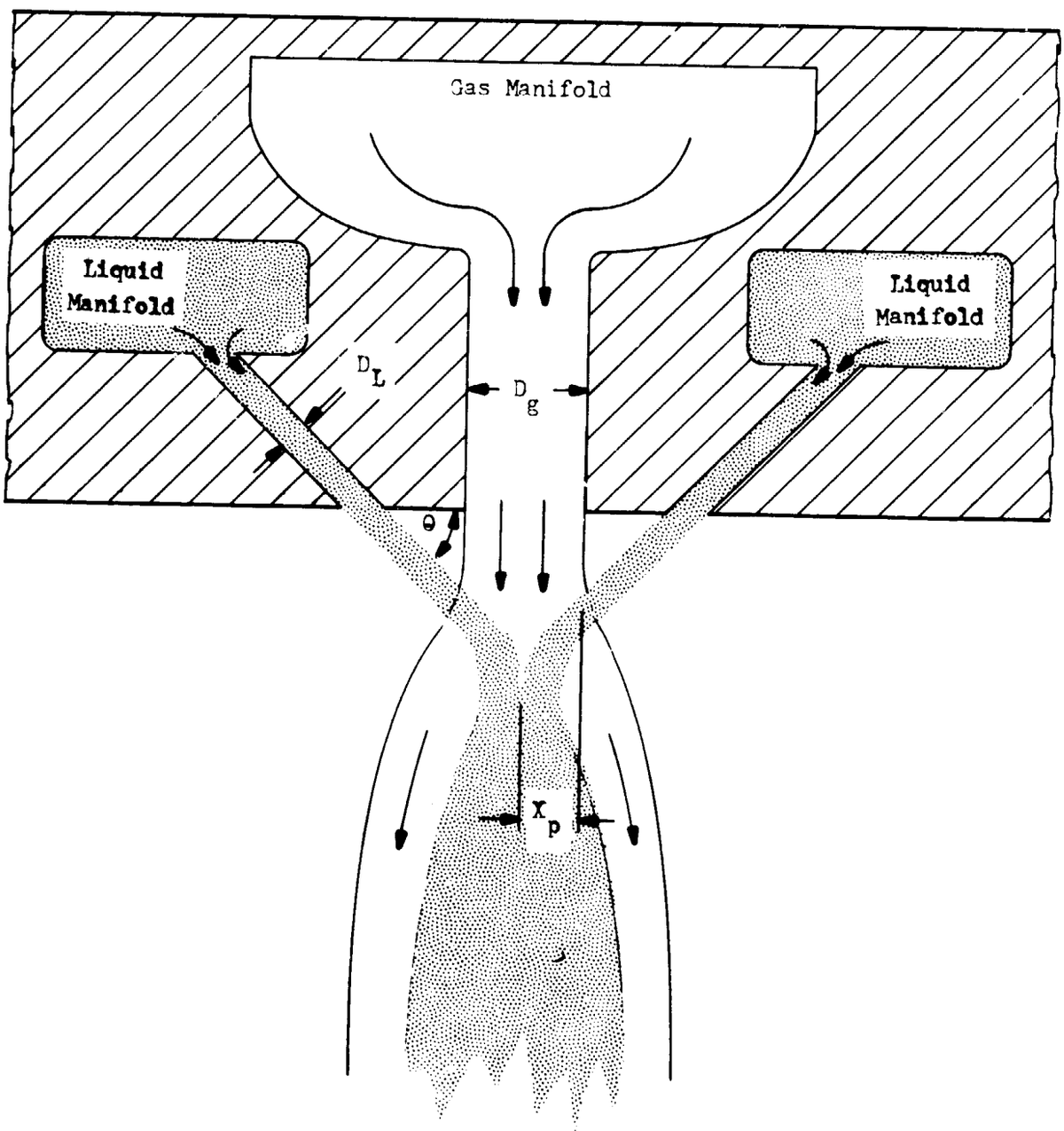

Figure 90. Gas-Liquid Interactions, Triplet Element.

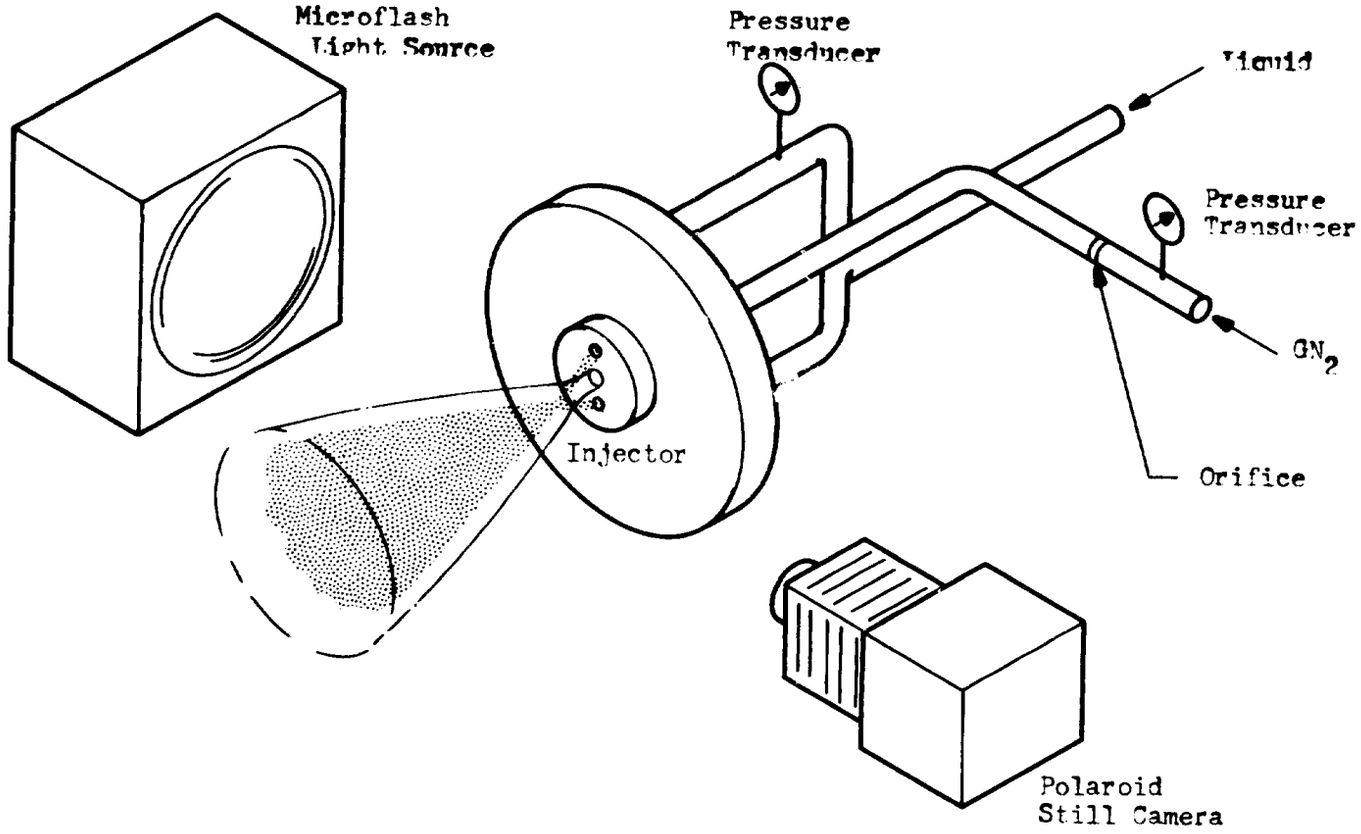

Figure 91. Schematic of Apparatus Used for Jet Penetration Studies.

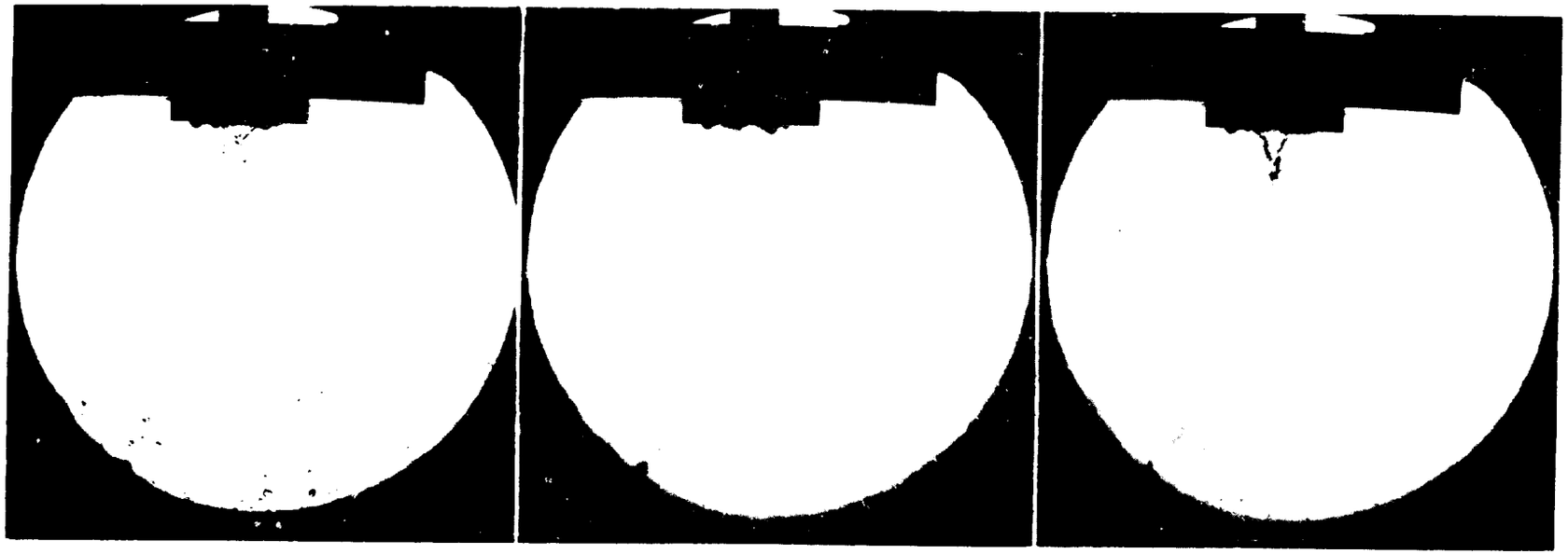

A	B	C
GN_2: 0 ft/sec	GN_2: 290 ft/sec	GN_2: 290 ft/sec
H_2O: 9 ft/sec	H_2O: 9 ft/sec	H_2O: 10.7 ft/sec

Figure 92. Penetration of Gas Jet by Liquid Streams. Triplet Element (0.060-inch Liquid Streams Impinging at 90-Degree Included Angle on 0.240-inch Showerhead Gas Jet).

(A) Water Impingement, No Gas

(B) Water with Insufficient Momentum to Penetrate Nitrogen

(C) Water with Just Enough Momentum to Penetrate to Center of Nitrogen Jet

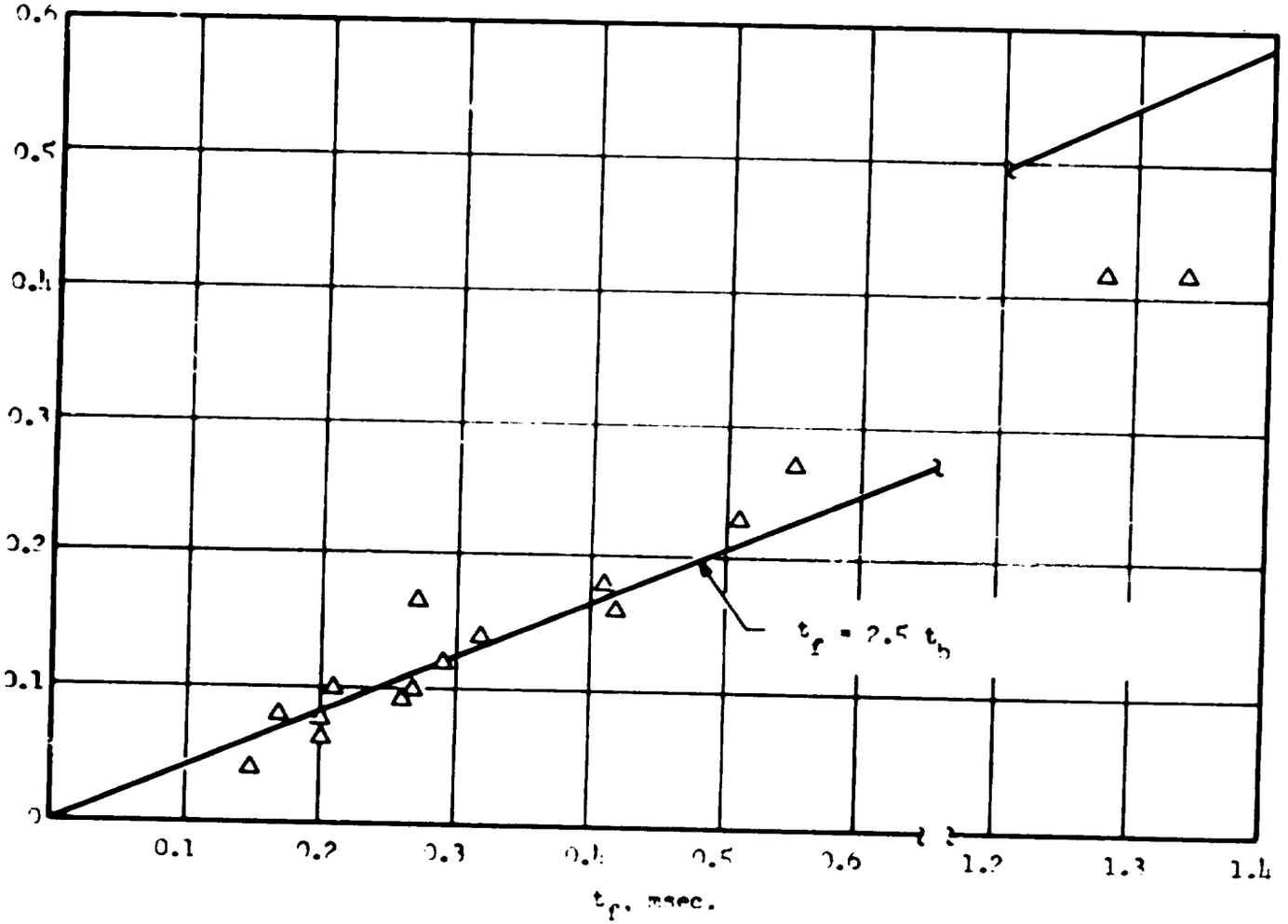

Figure 93. Correlation of Jet Penetration Data.

t_b - Droplet Break-up Time

t_f - Droplet Flight Time

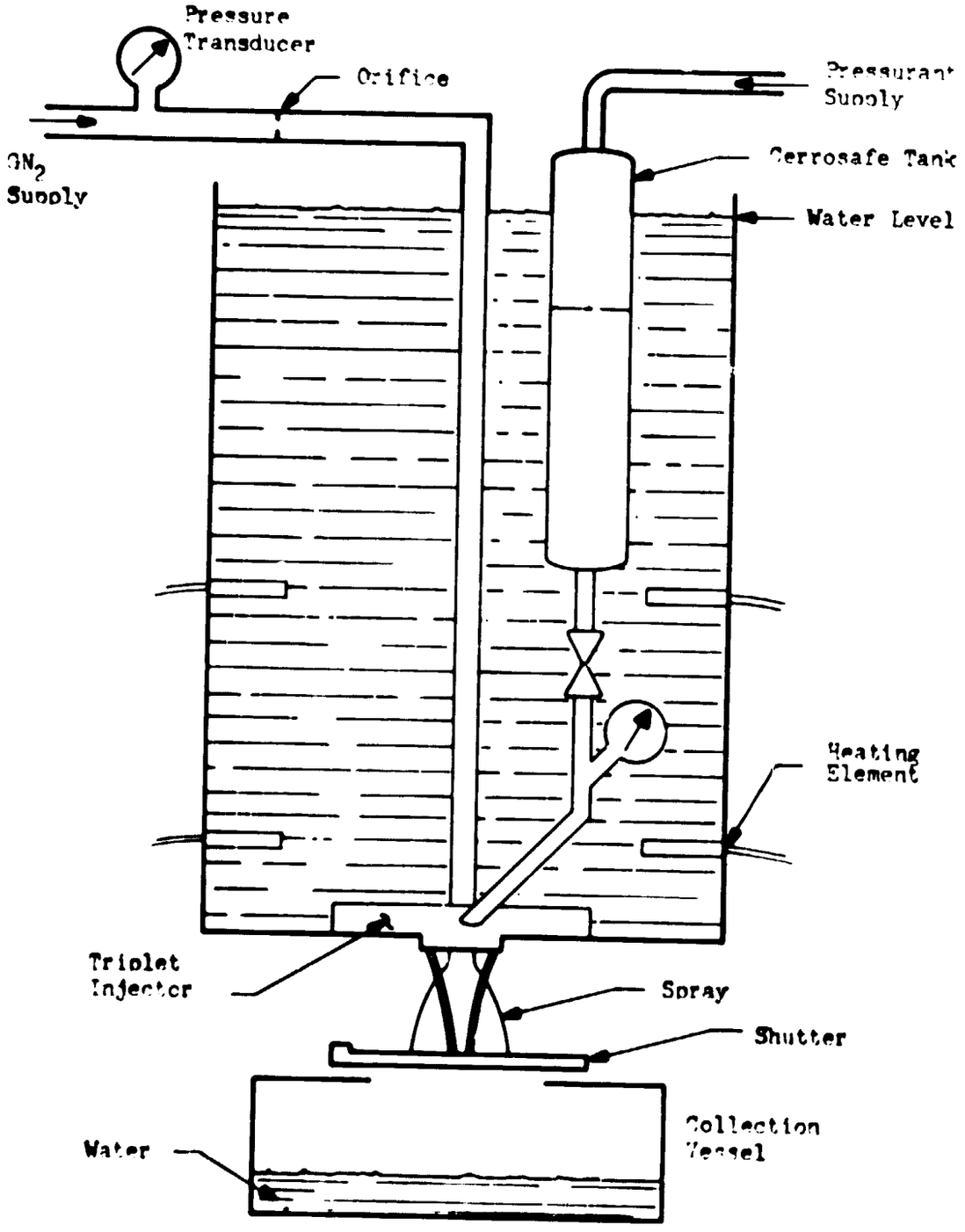

Figure 94. Schematic of Apparatus Used in Liquid-Metal Atomization Study.

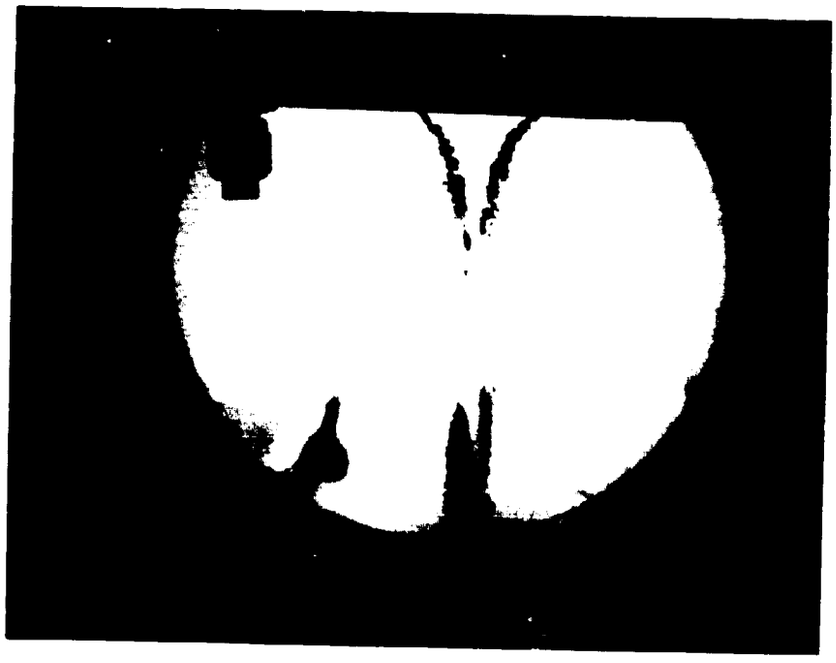

Figure 95. Atomization of Liquid Cerrosafe by GN_2 in Triplet Element.

Liquid Orifices: D = 0.060-inch

Gas Orifice: D = 1.50-inch,
V = 1,090 ft/sec

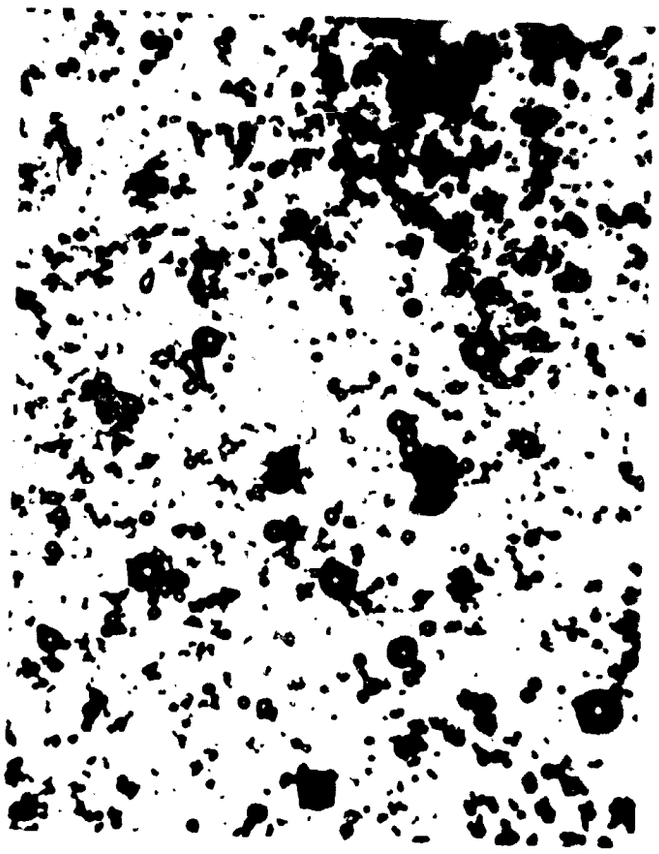

Figure 96. Photomicrograph of Solidified Cerrosafe Particles Collected During Test No. 49, 100X.

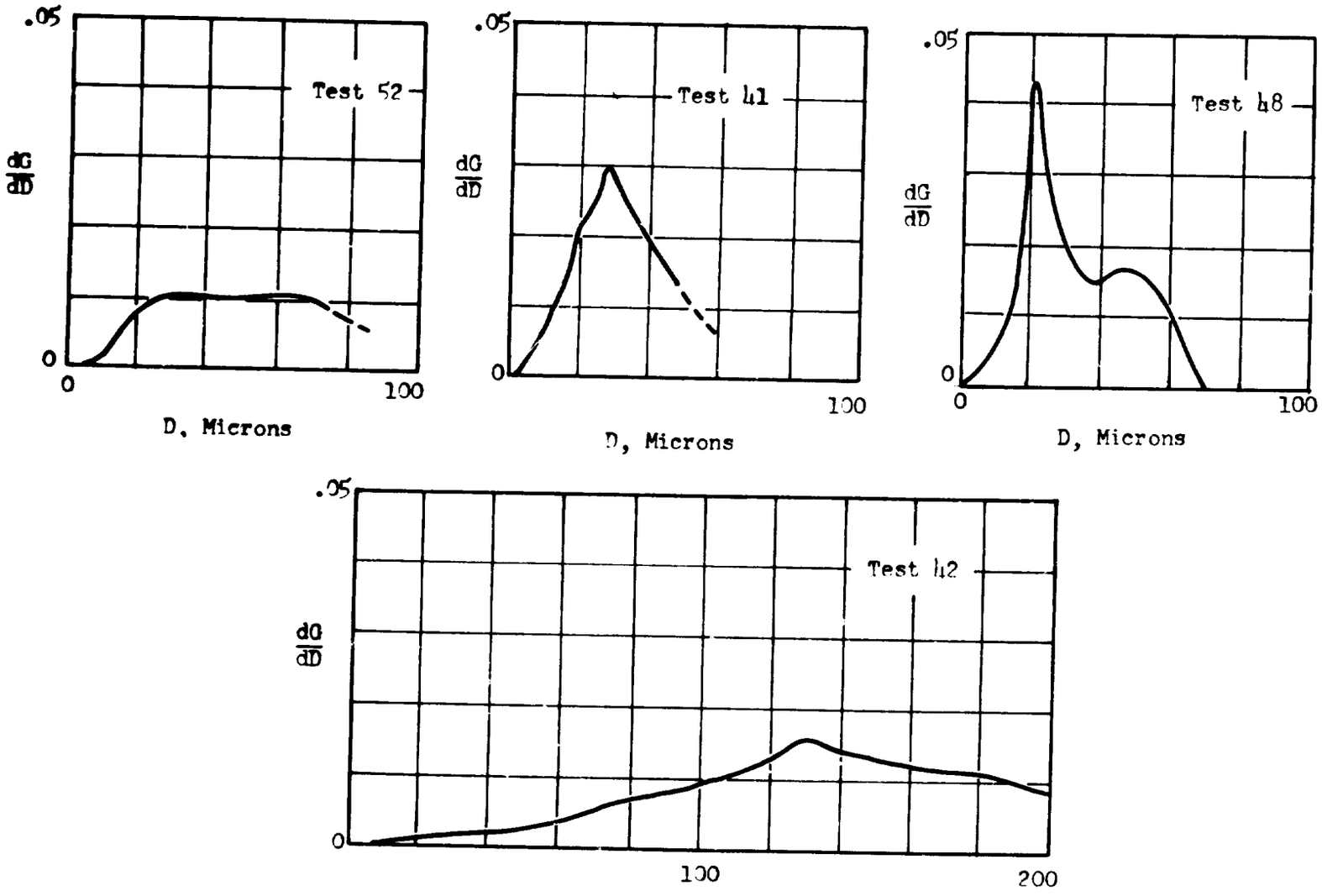

Figure 97. Experimental Droplet Distributions, Atomization of Liquid Cerrosafe.

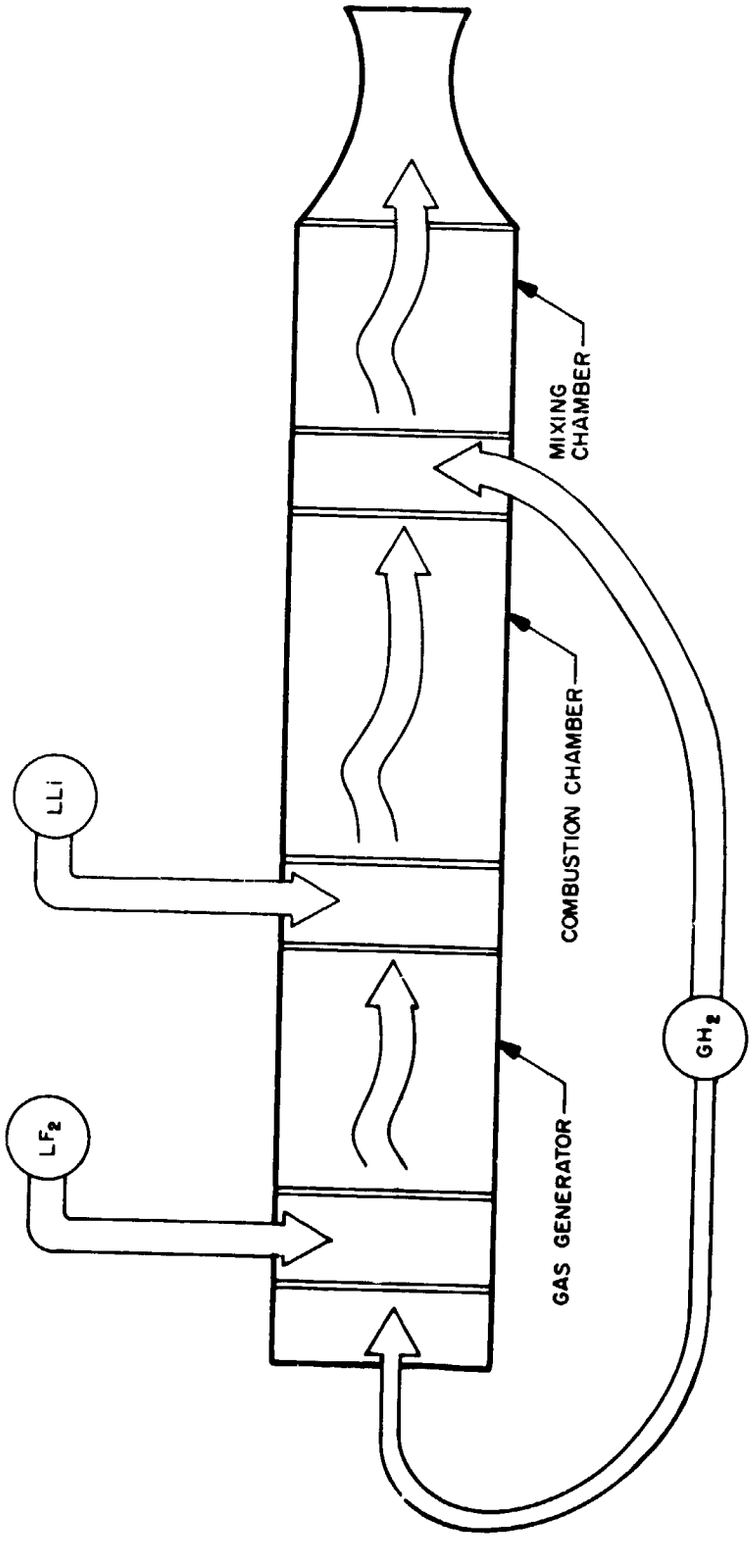

Figure 98. Conceptual Schematic of $LF_2/LLi/GH_2$ Thrust Chamber.

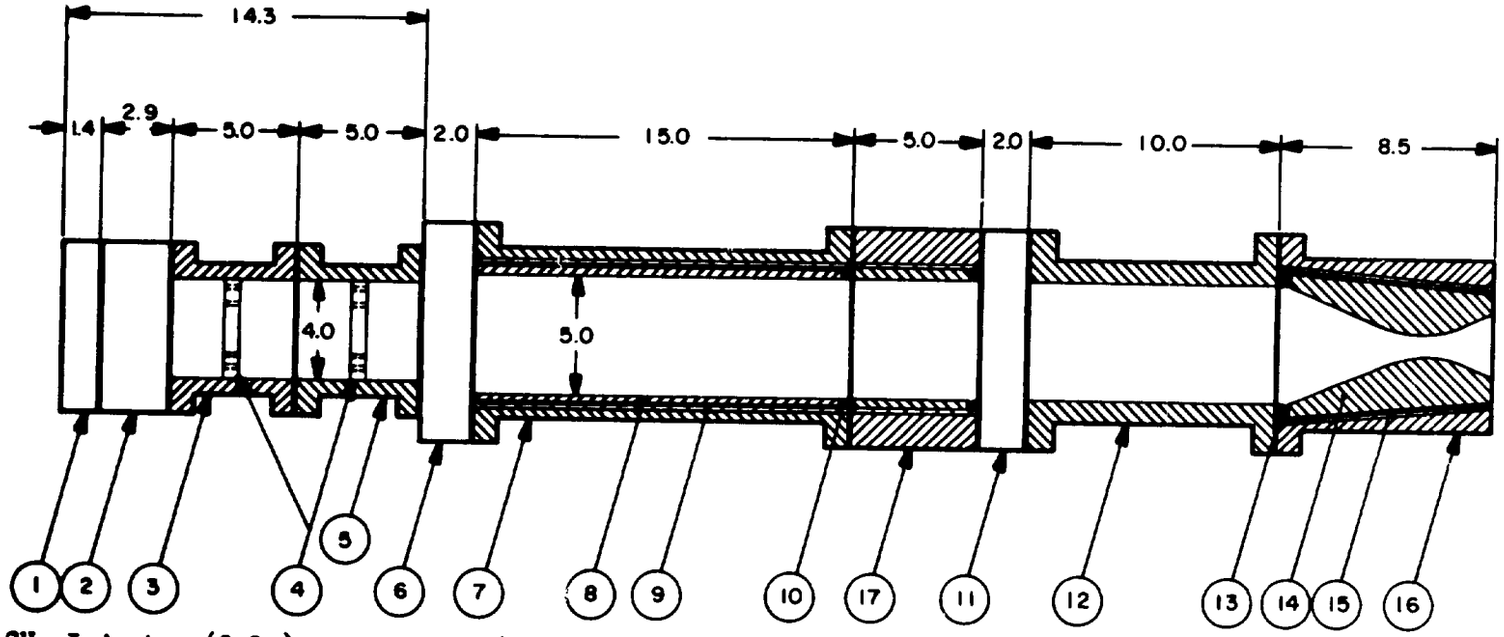

1. GH_2 Injector (G.G.)
2. LF_2 Injector
3. Combustion Chamber (G.G.)
4. Mixing Plate
5. Combustion Chamber (G.G.)
6. LLi Injector
7. Steel Shell
8. Graphite Liner
9. Asbestos Sheet
10. Graphite Washer
11. GH_2 Injector
12. Copper Mixing Chamber
13. Graphite Washer
14. Graphite Liner
15. Asbestos Sheet
16. Steel Shell
17. Second Chamber Section

Figure 99. Thrust Chamber Schematic.

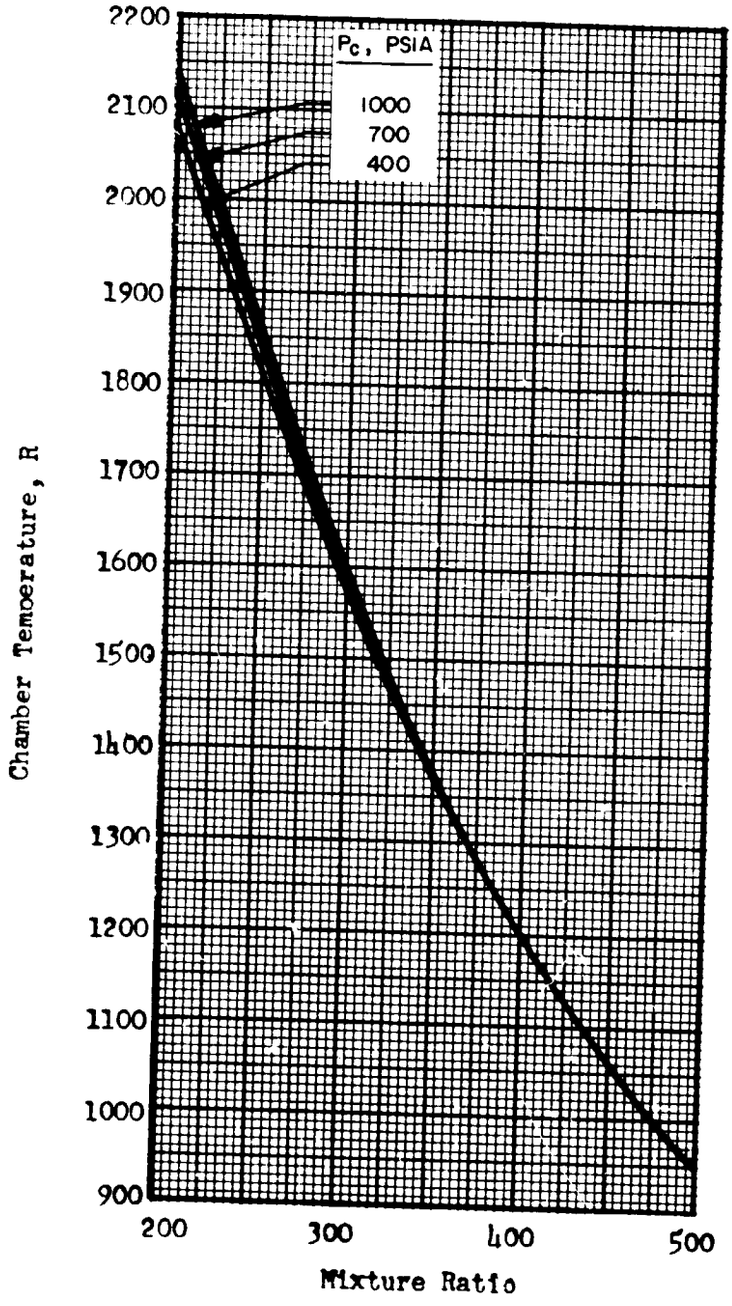

Figure 100. Variation of Chamber Temperature with Mixture Ratio at Indicated Chamber Pressures, LF_2(153 R)/GH_2(537 R).

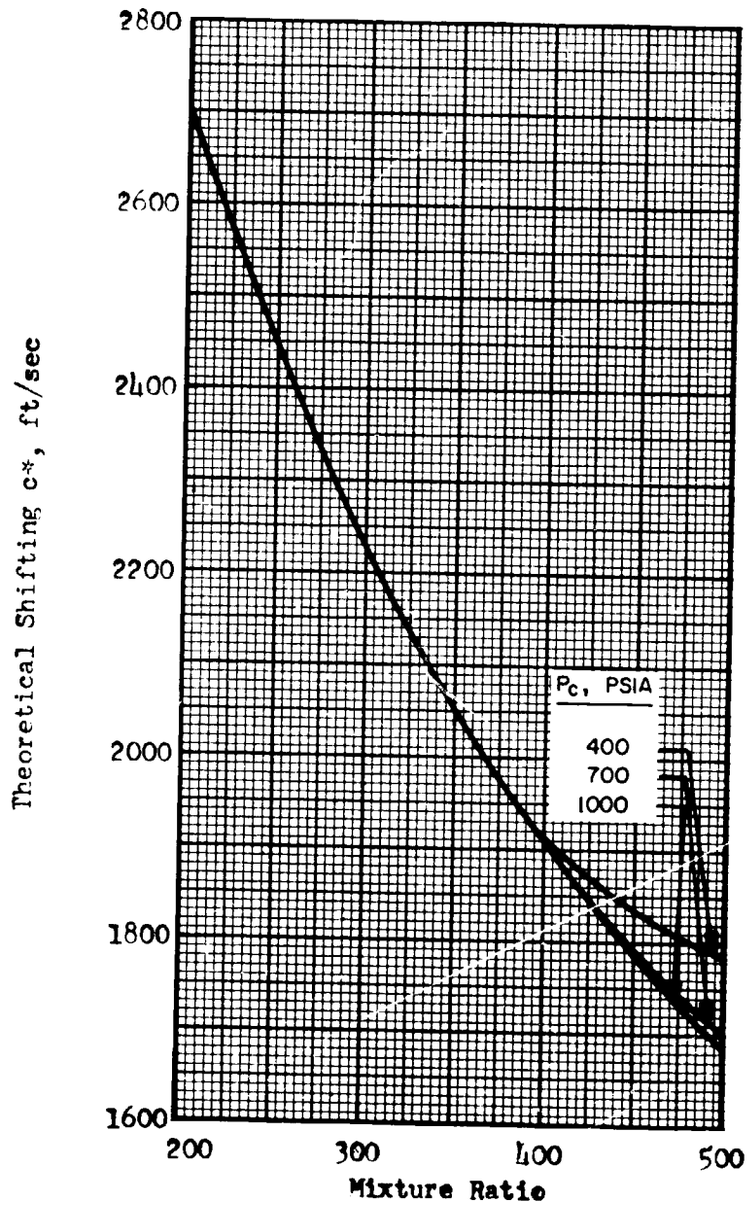

Figure 101. Variation of c* (Shifting Equilibrium) with Mixture Ratio at Indicated Chamber Pressures, LF_2(153 R)/GH_2(537 R).

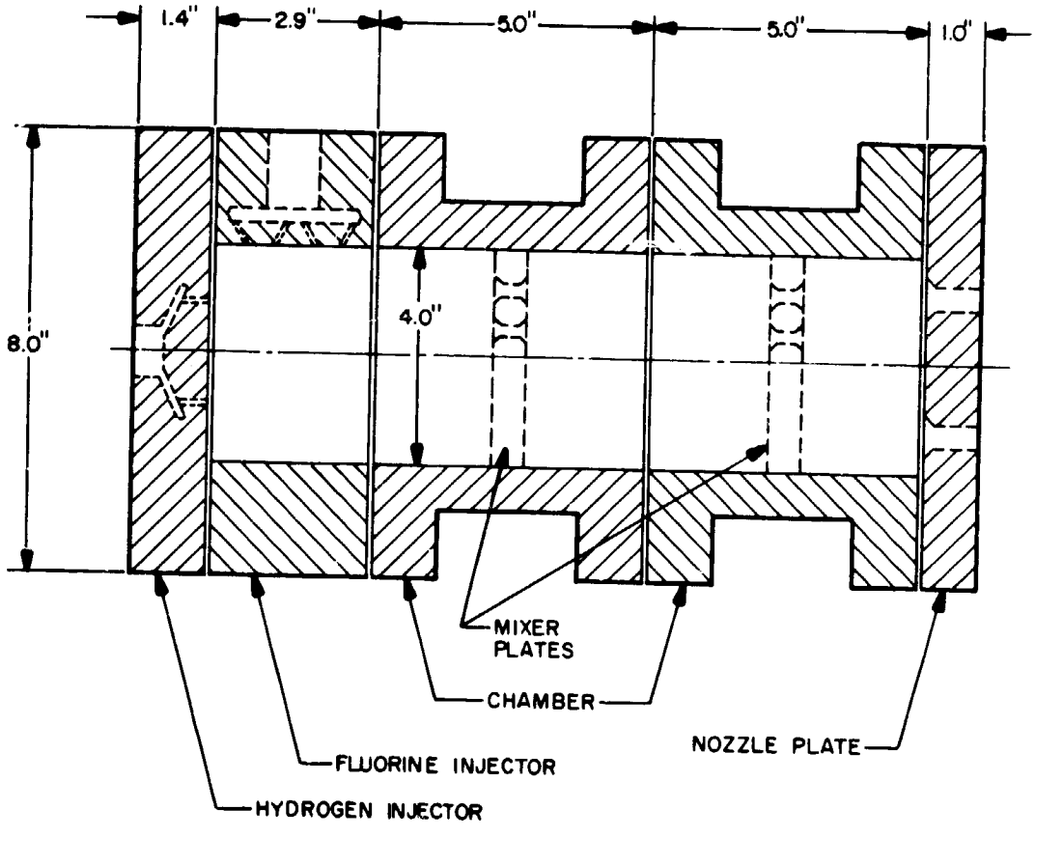

Figure 102. Gas Generator Assembly, Schematic.

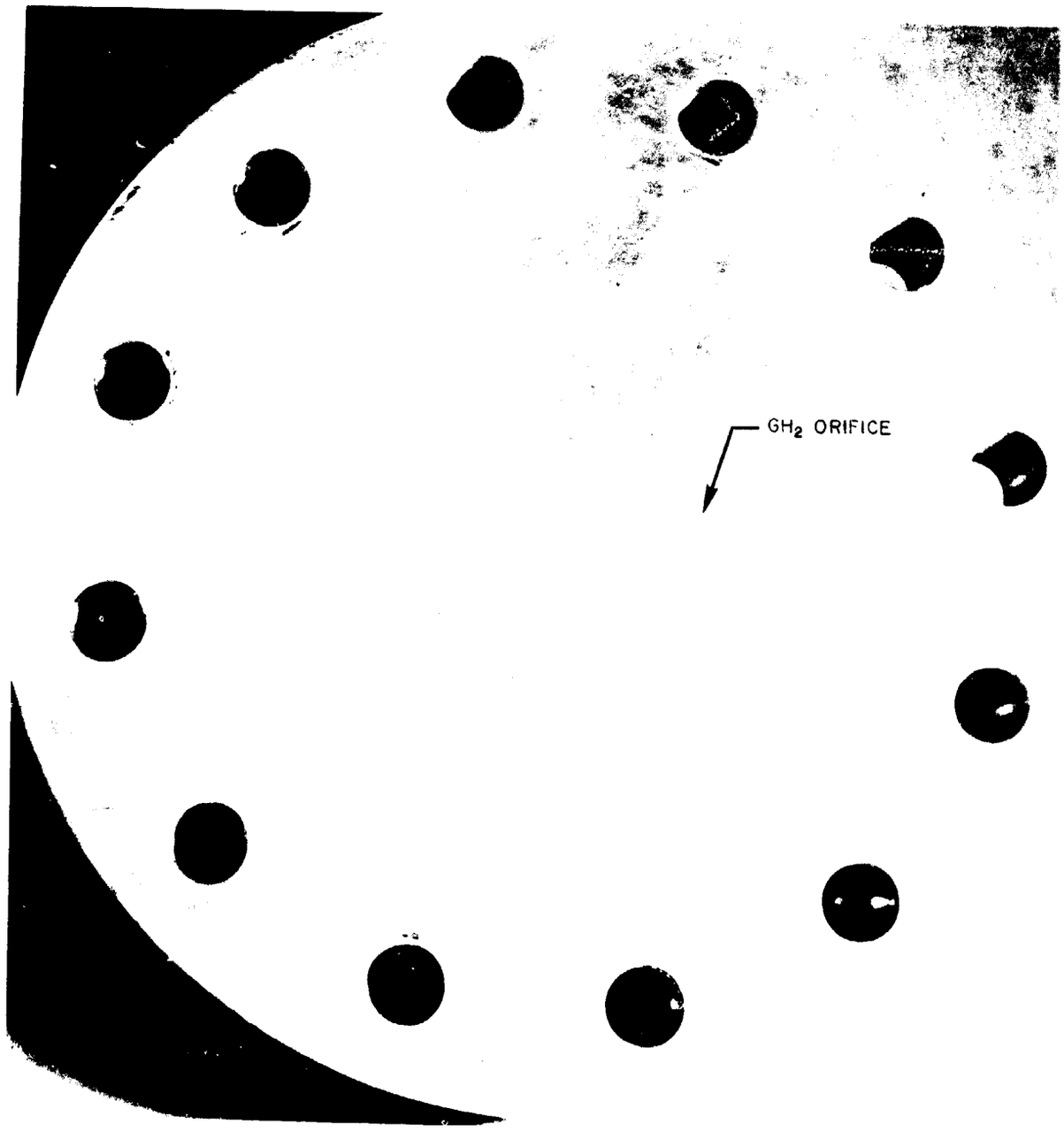

5AA26-10/10/66-S1C

Figure 103. Hydrogen Injector for Gas Generator, Face View, Showing Outlets of Nine 0.0135-inch Showerhead Orifices.

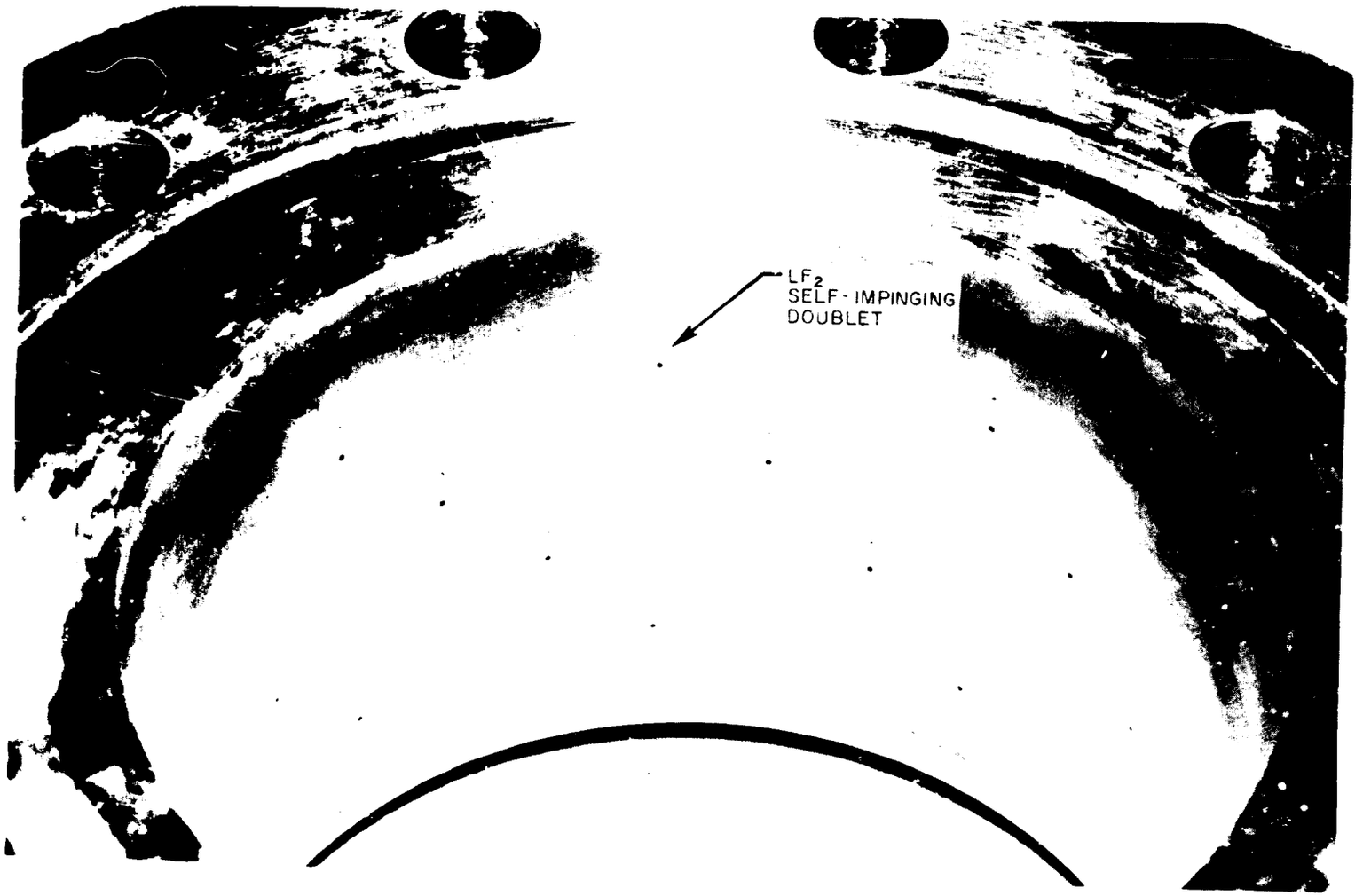

5AA26-10/10/66-S1B

Figure 104. Fluorine Injector for Gas Generator, Showing Self-Impinging Doublet Orifices (D = 0.026 inches) Around Inner Diameter.

5AA34-10 14 '66-S1B

Figure 105. Gas Generator Injector Combination Flowing Water and GN_2.

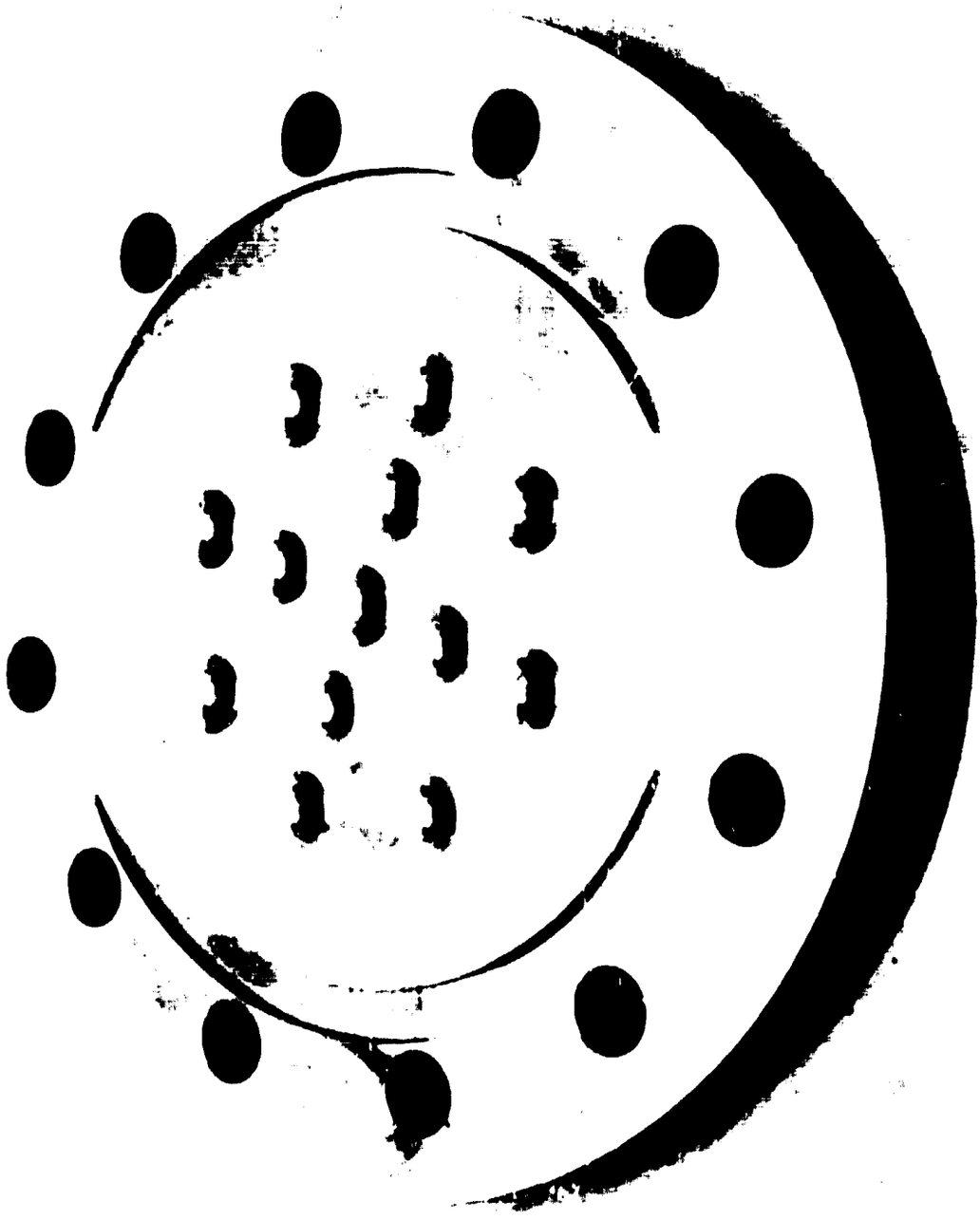

5AA26-10/10 66-81E

Figure 106. Gas Generator Nozzle Plate, View of Chamber Side Showing Exit Orifices.

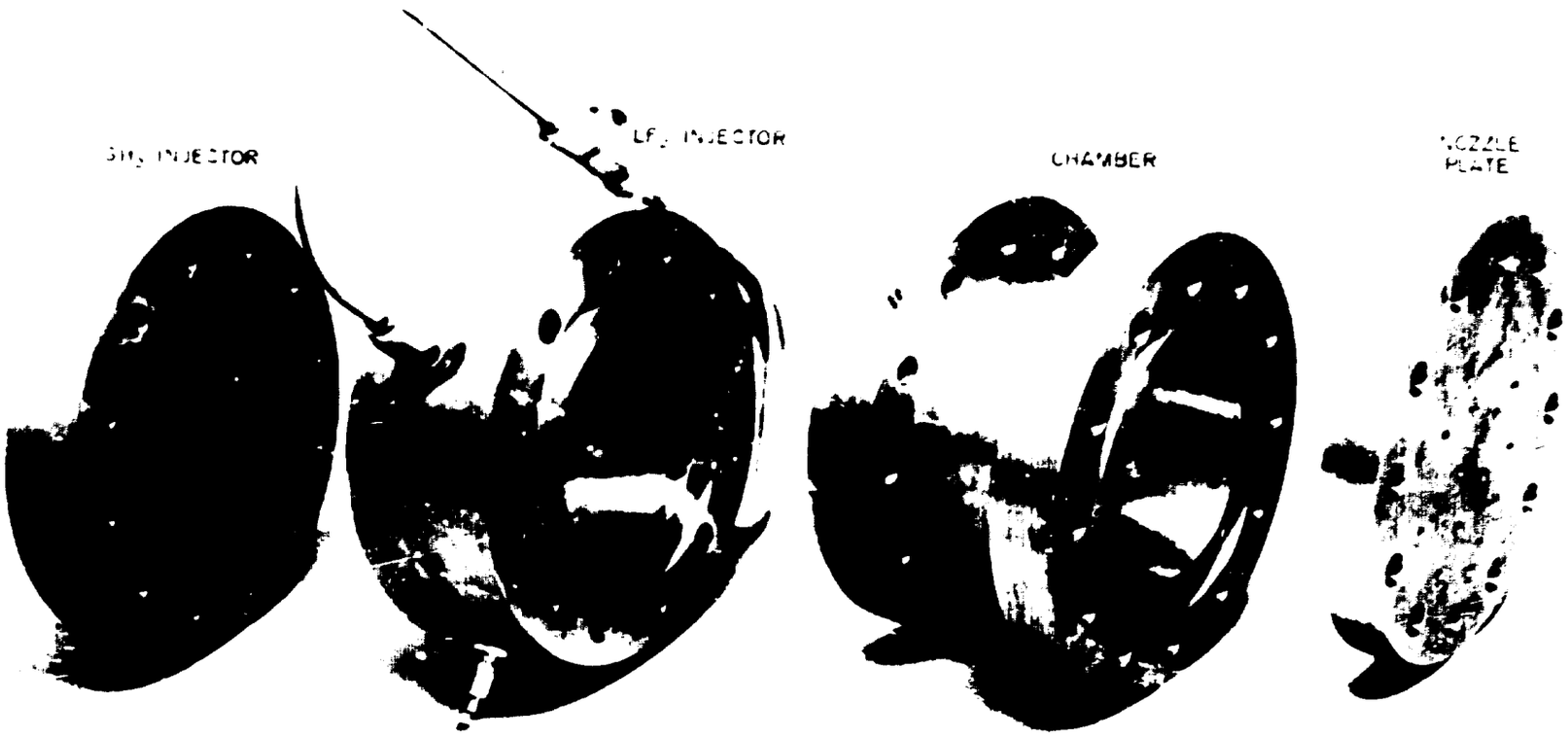

5AA-10 10 66-SIF

Figure 107. Gas Generator Components, Showing Order of Assembly.

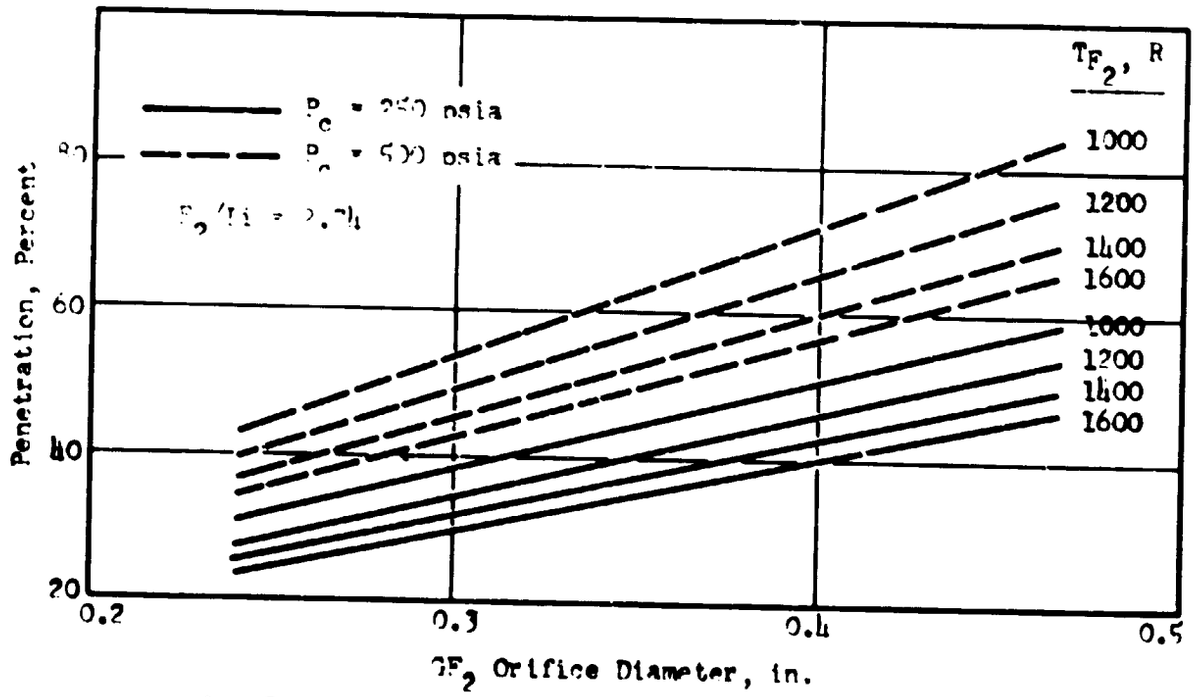

A. Penetration of OF_2 Jet by LLi Stream as Function of OF_2 Orifice Diameter at Indicated P_c and T_{F_2}.

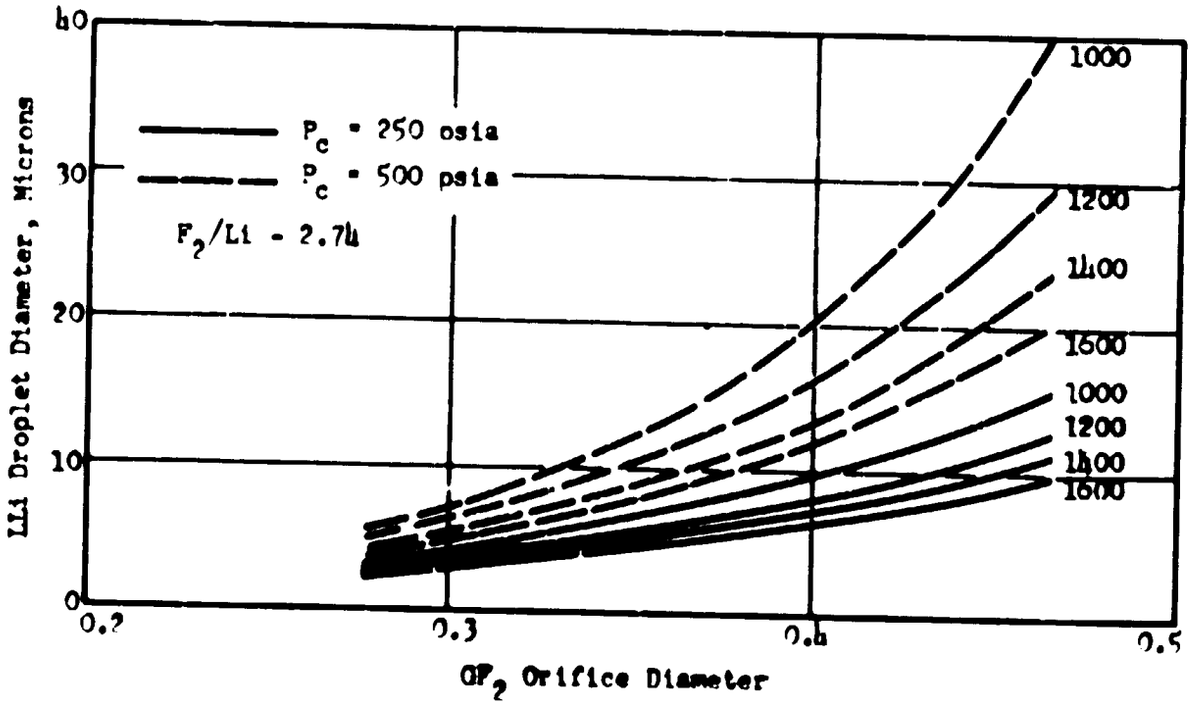

B. LLi Volume Mean Droplet Diameter as Function of OF_2 Orifice Area at Indicated P_c and T_{F_2} (Uncorrected for Poor Penetration or OF_2 Jet Spreading).

Figure 108. Interaction of Gaseous Fluorine Jet and Liquid Lithium Stream

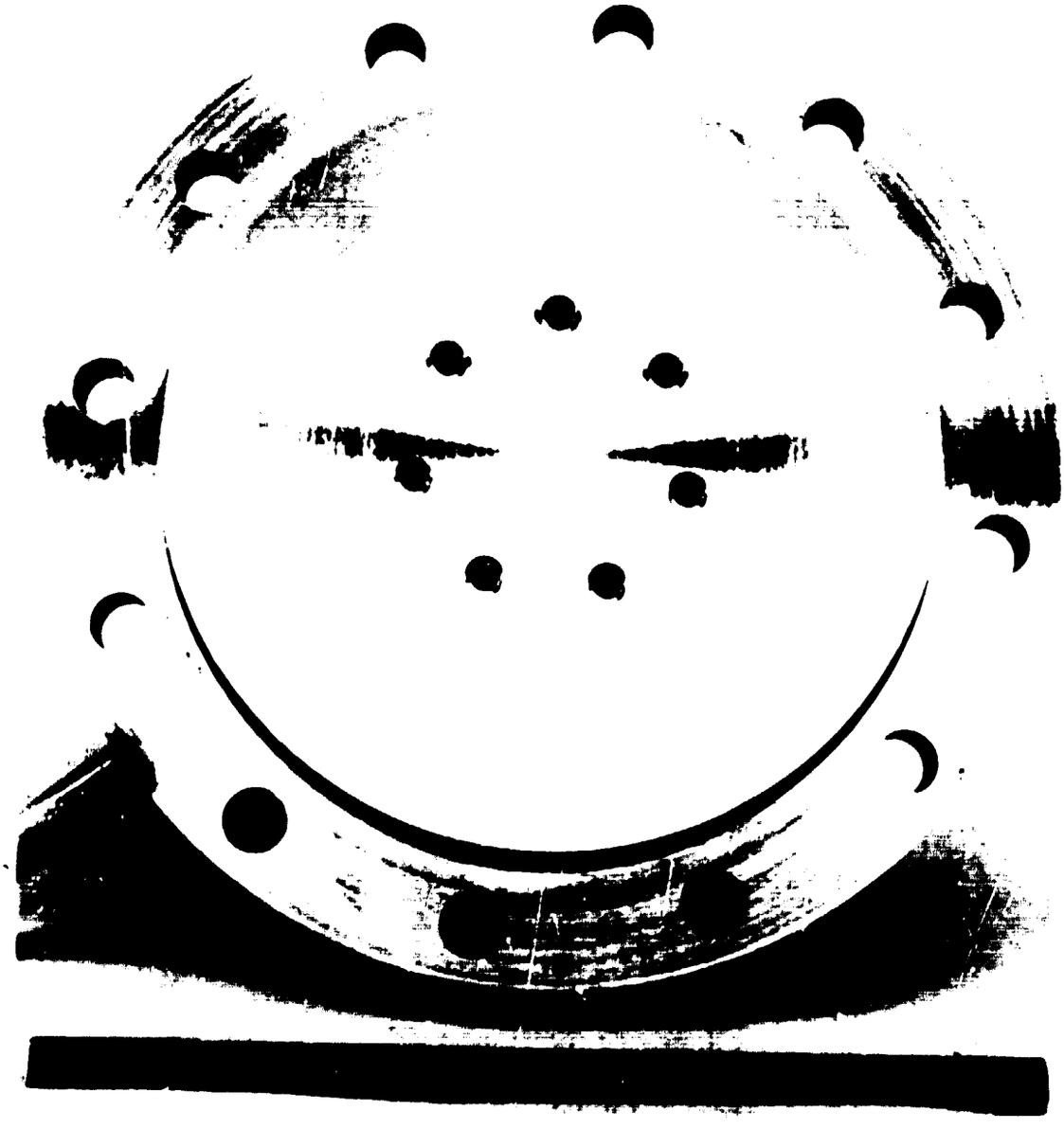

5AA33-4 21 67-S1C

Figure 109. Triplet Pattern Lithium Fluorine Injector, Gas Generator Side, Showing Inlets to GF_2 Orifices.

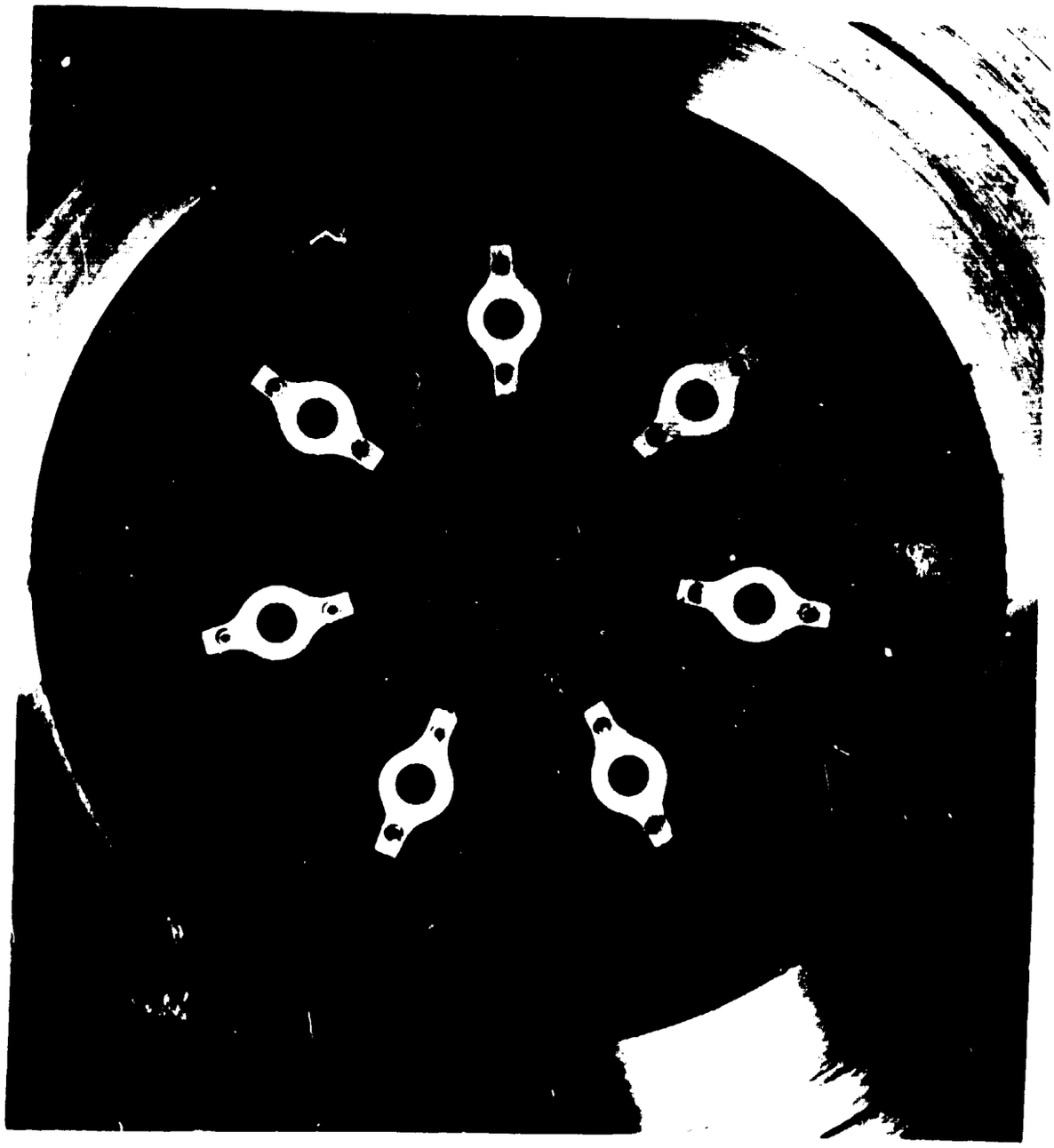

5AA34-4 24 67-81

Figure 110. Triplet-Pattern Lithium Fluorine Injector, Face View with Ablative Shield in Place.

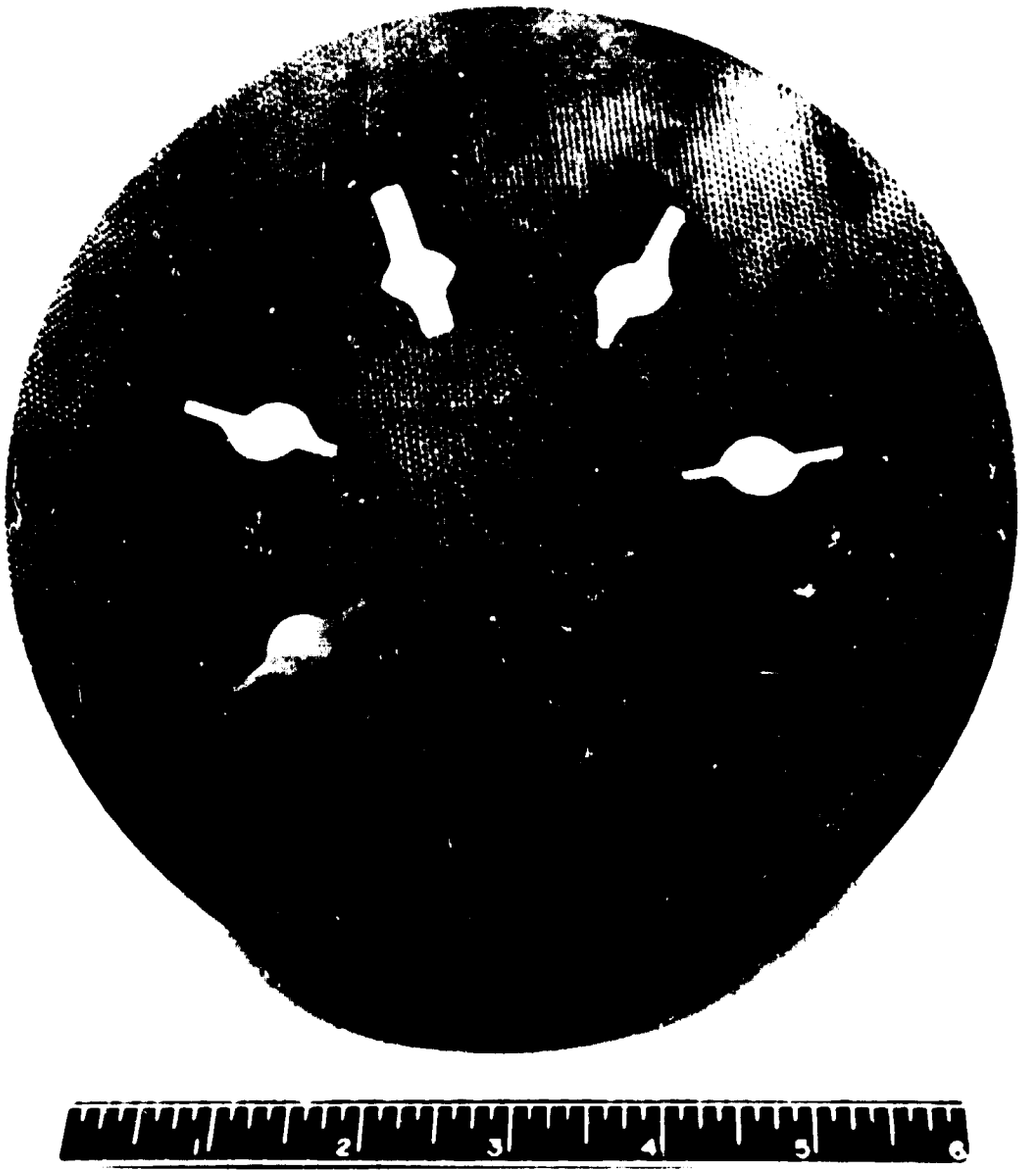

5AA33-4/21/67-SIG

Figure 111. Ablative Plate for Triplet-Pattern Lithium/Fluorine Injector, Face View.

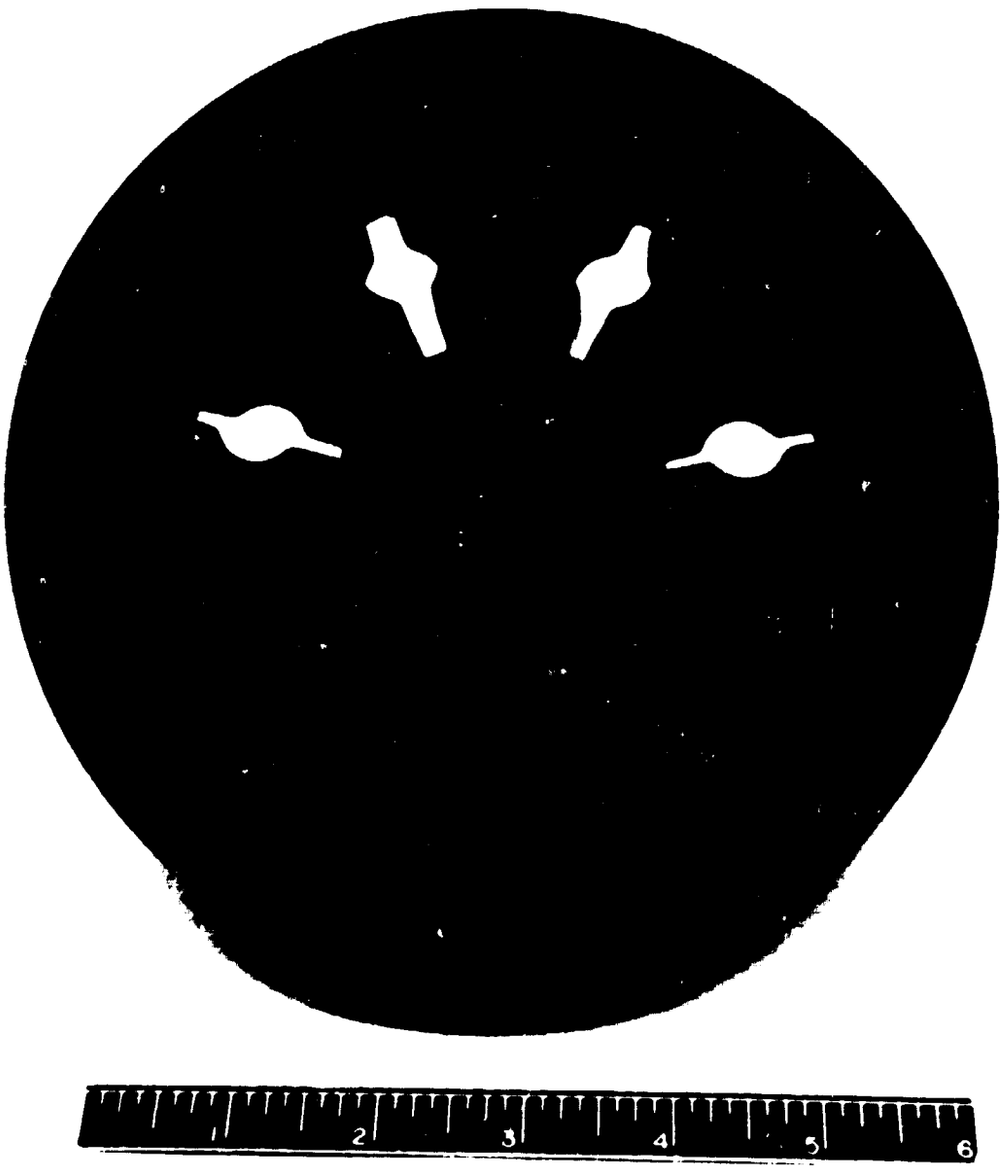

5AA33-4/21/67-SIF

Figure 112. Ablative Plate for Triplet-Pattern Lithium/Fluorine Injector, Back View.

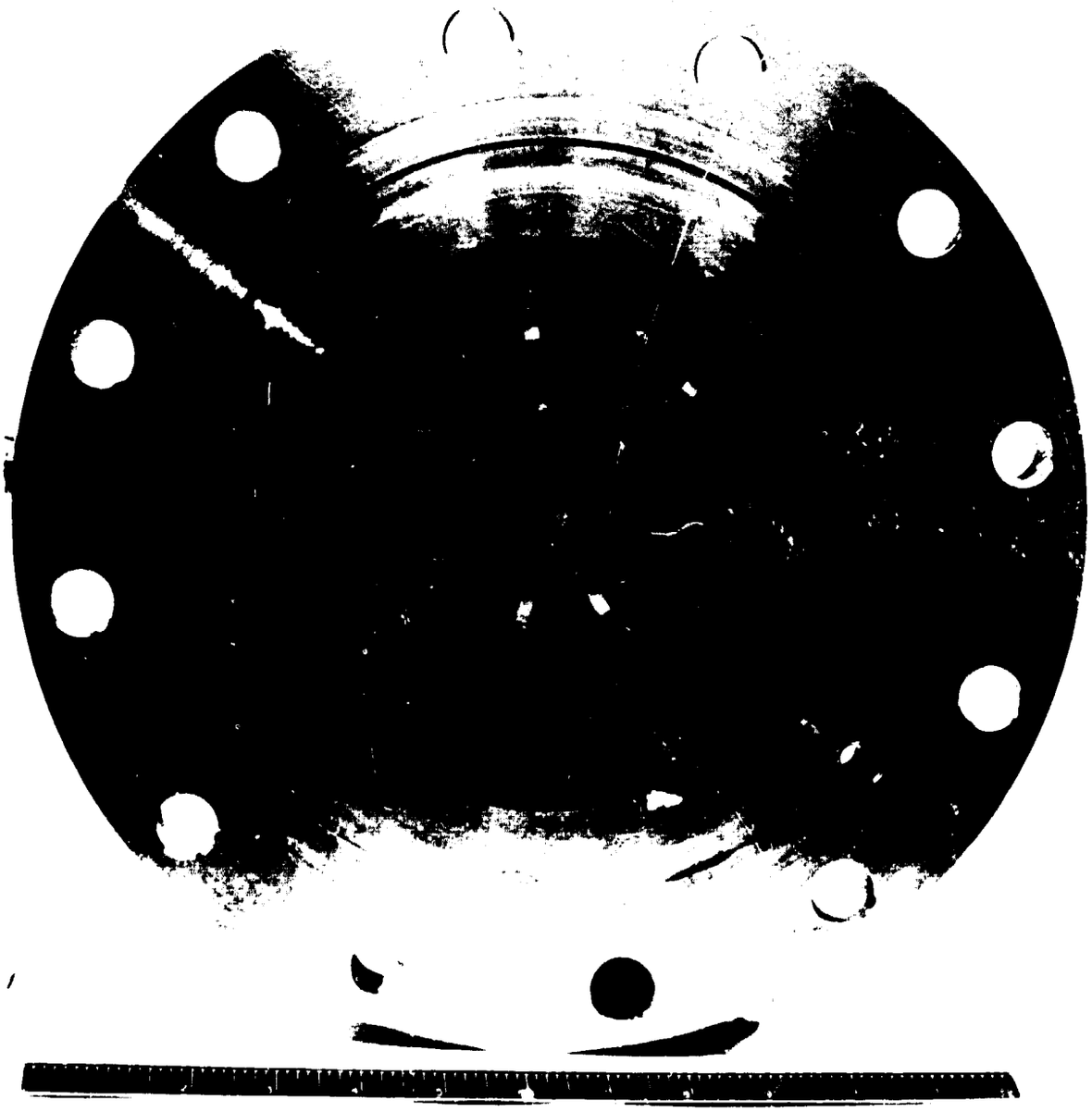

5AA33-4/21/67-SID

Figure 113. Triplet-Pattern, Lithium/Fluorine Injector, Face View Without Ablative Shield.

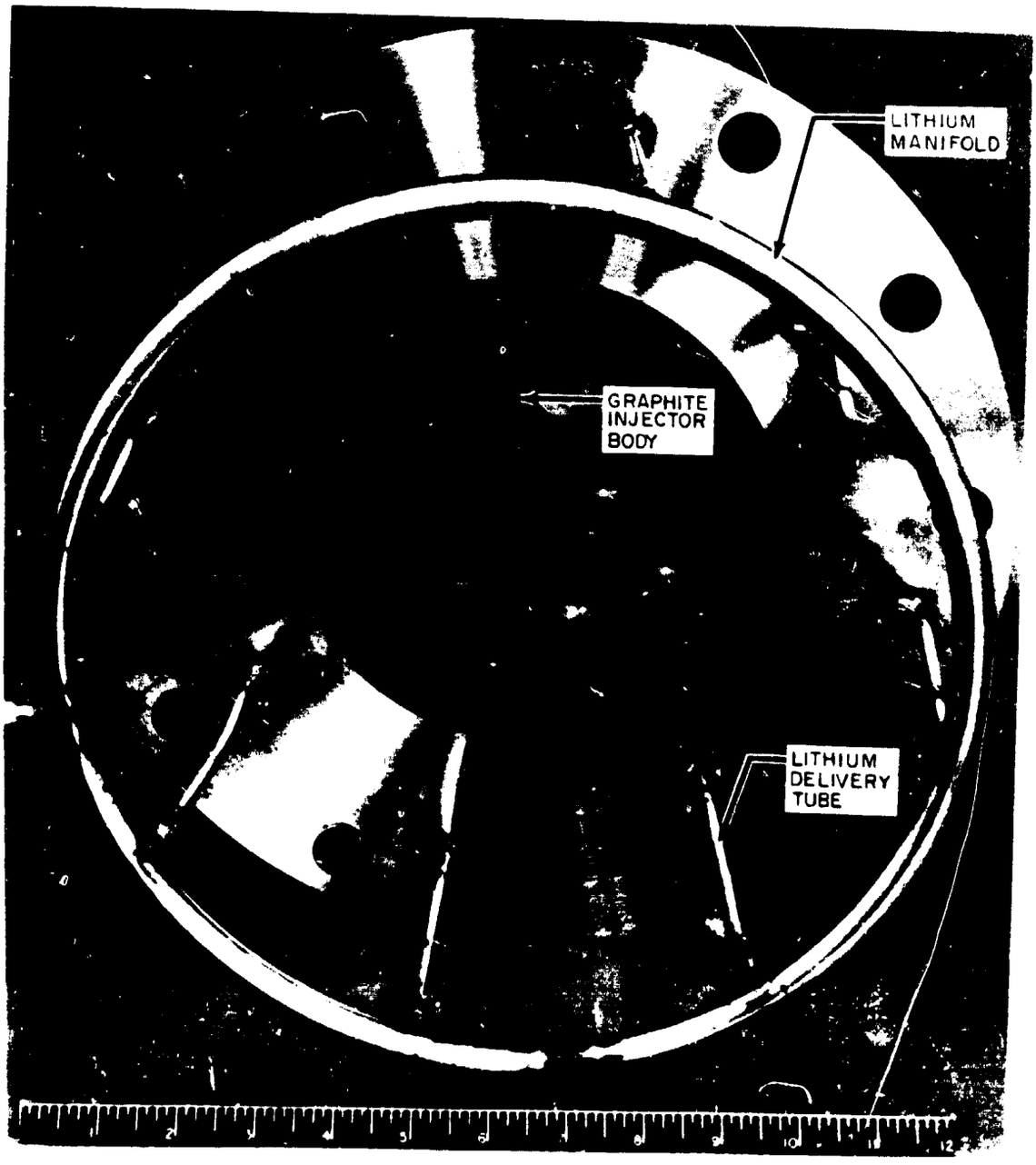

5AA34-7/14/67-SIA

Figure 114. Doublet-Pattern Lithium/Fluorine Injector and Lithium Manifold; Gas Generator Side, Showing Fluorine Orifice Inlets.

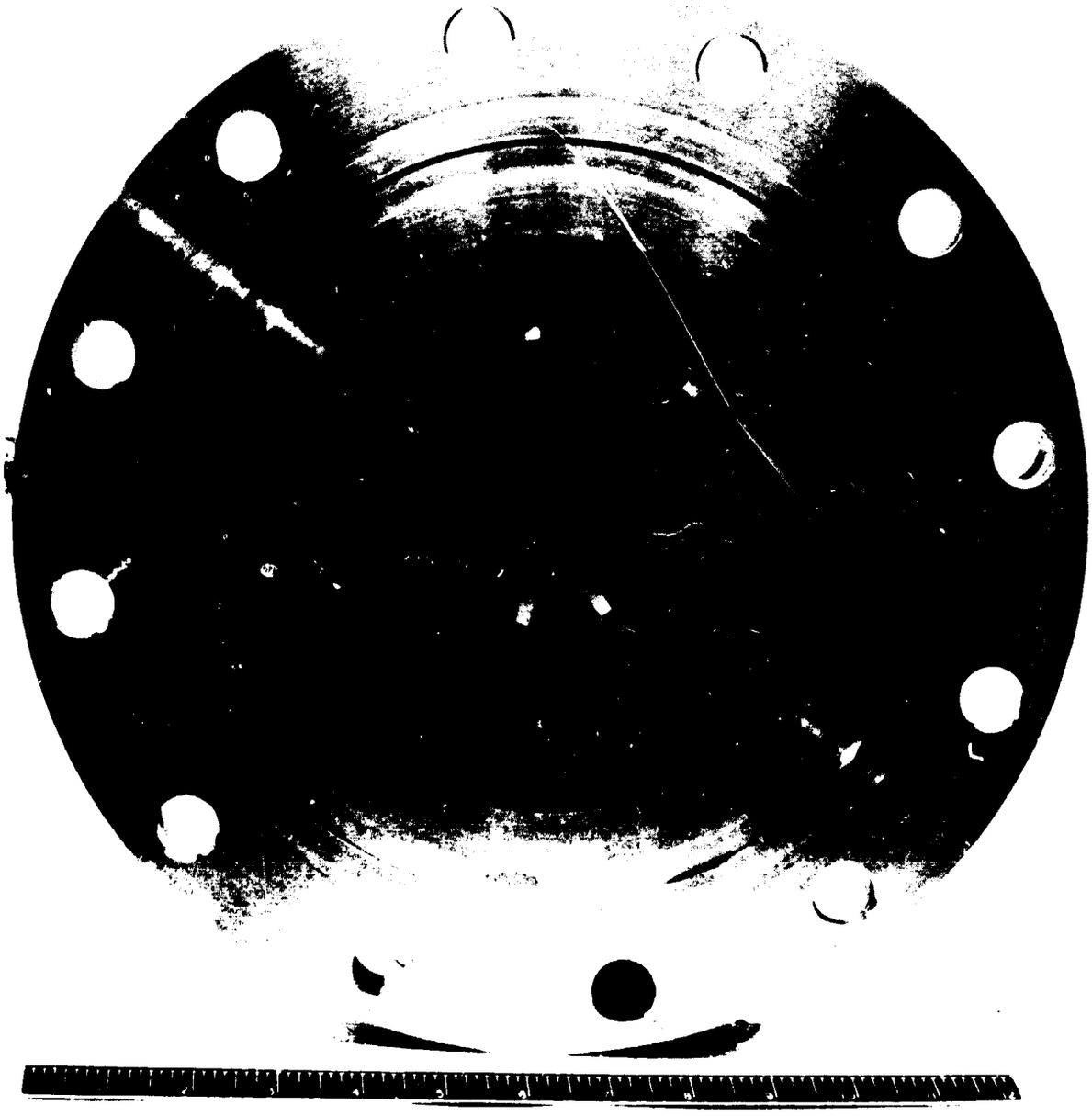

5AA33-4/21/67-SID

Figure 113. Triplet-Pattern, Lithium/Fluorine Injector, Face View Without Ablative Shield.

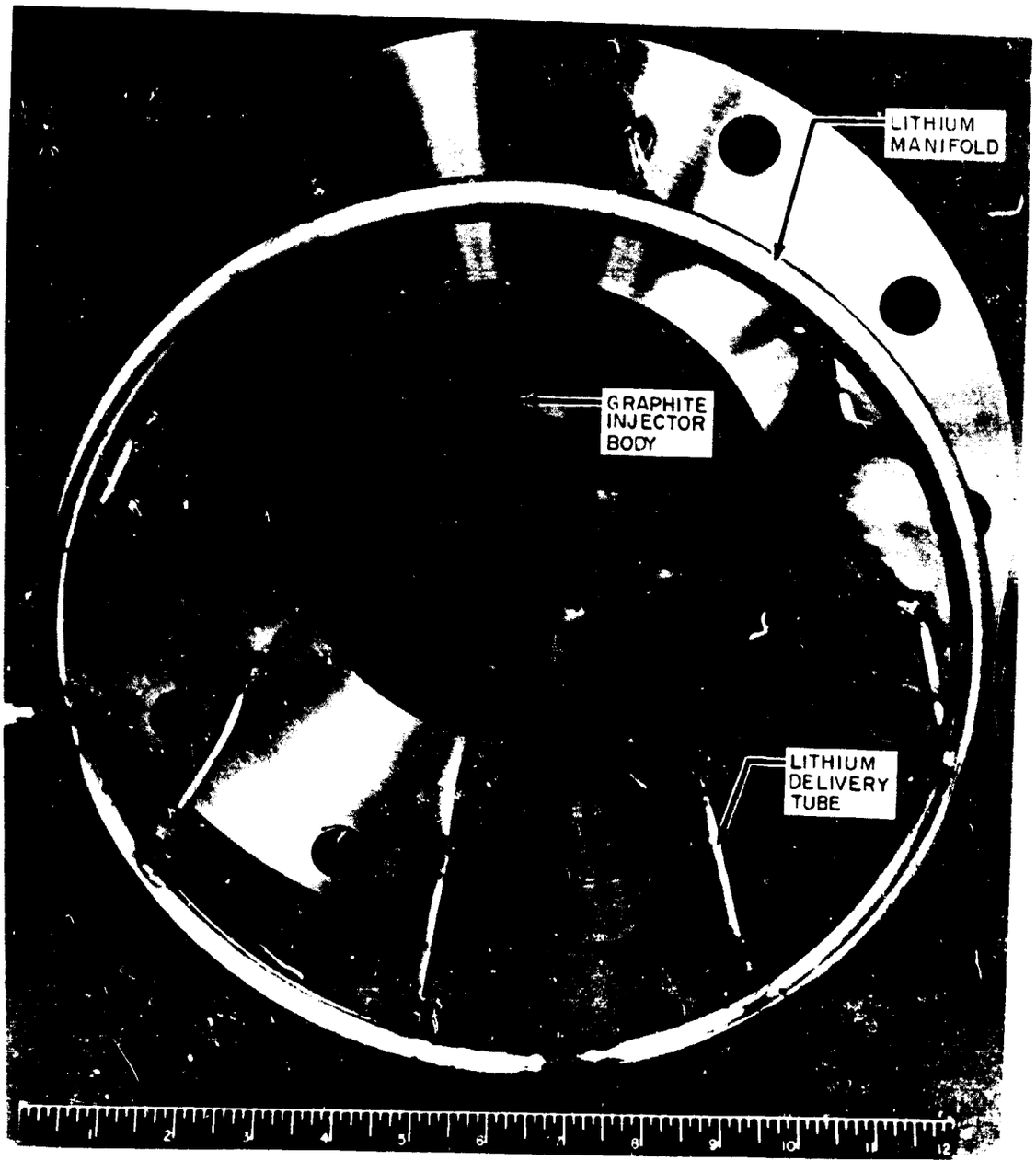

5AA34-7/14/67-SIA

Figure 114. Doublet-Pattern Lithium/Fluorine Injector and Lithium Manifold; Gas Generator Side, Showing Fluorine Orifice Inlets.

5AA34-7/14/67-SID

Figure 115. Doublet-Pattern Lithium/Fluorine Injector, Face View Showing Showerhead GF_2 Orifices and Outlets of Lithium Delivery Tubes.

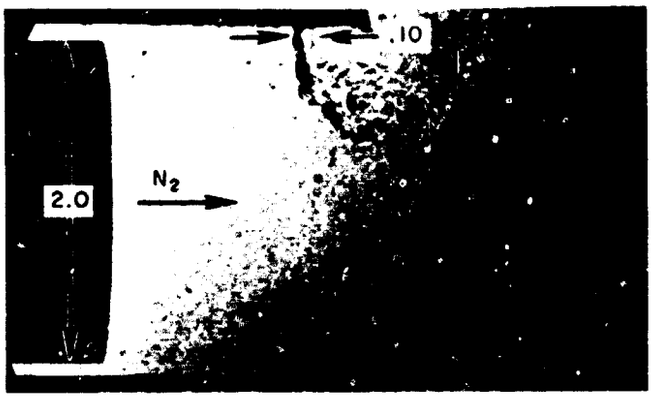

V_{He} = 650 ft/sec
V_{N_2} = 155 ft/sec

V_{He} = 1300 ft/sec
V_{N_2} = 155 ft/sec

Figure 116. Schlieren Photographs Showing the Penetration of Two 0.10-Inch Diameter Helium Streams Into a 2.0-Inch Diameter Nitrogen Stream.

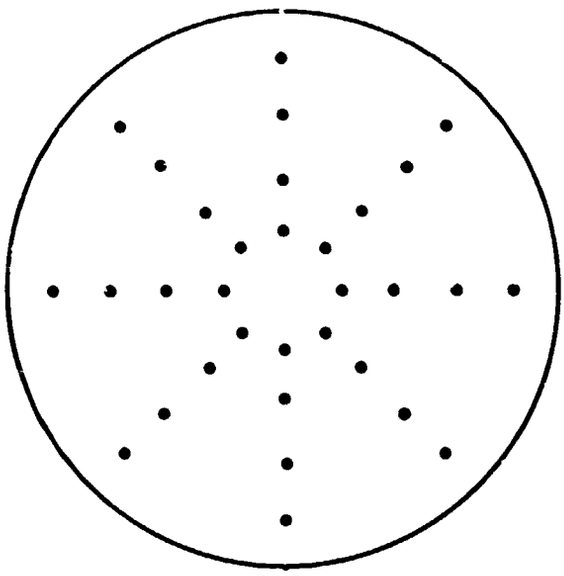

A. Impingement Points of 32 Pairs of Opposing Hydrogen Jets, Schematically Projected on a Single Plane

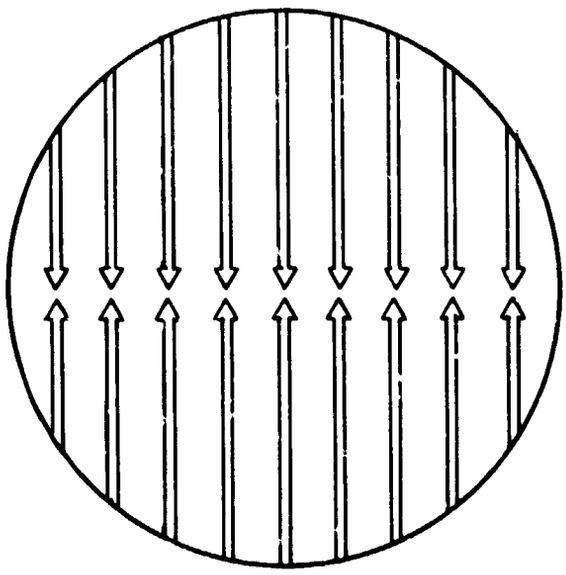

B. Schematic of One of Four Sets of Eight Pairs of Impinging Hydrogen Jets, Each Set in a Plane Successively Separated by 0.4 inch, and Successively Rotated 45 Degrees.

Figure 117. Hydrogen Injector Orifice Arrangement

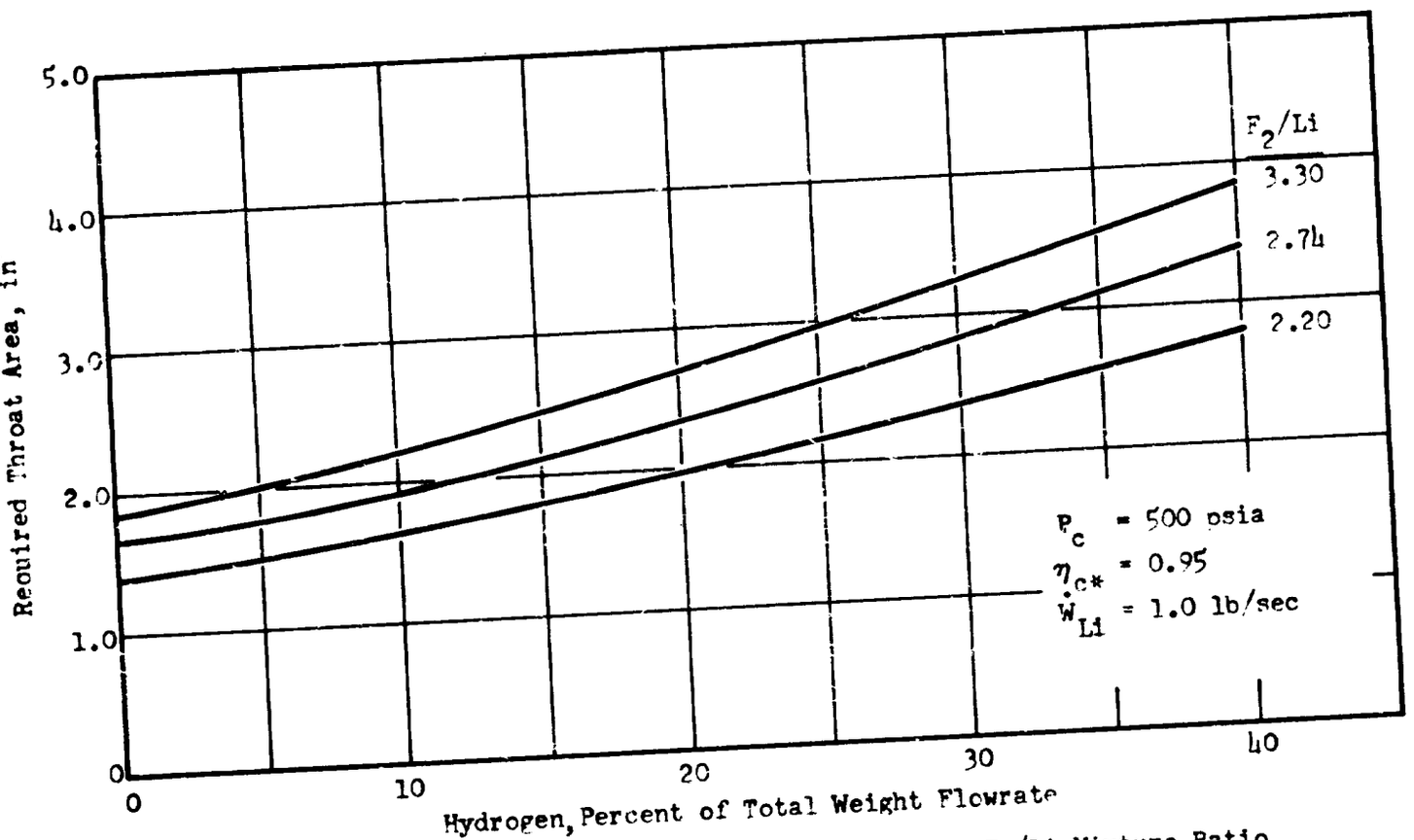

Figure 118. Throat Areas Required for Indicated F_2/Li Mixture Ratio and Hydrogen Percentage.

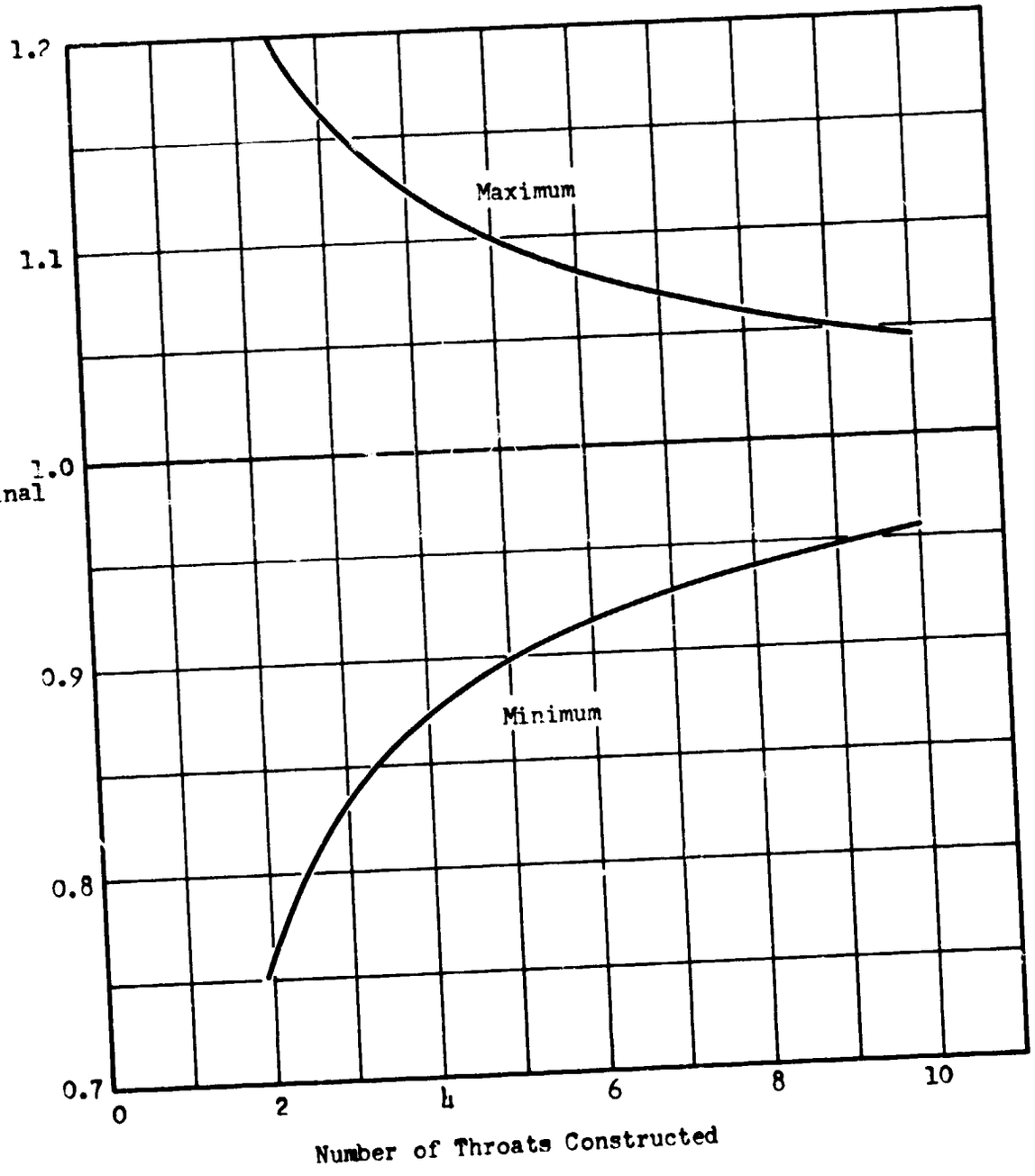

Figure 119. Variation of the Parameter $P_c/\dot{W}_{Li}$ with Number of Throats Constructed.

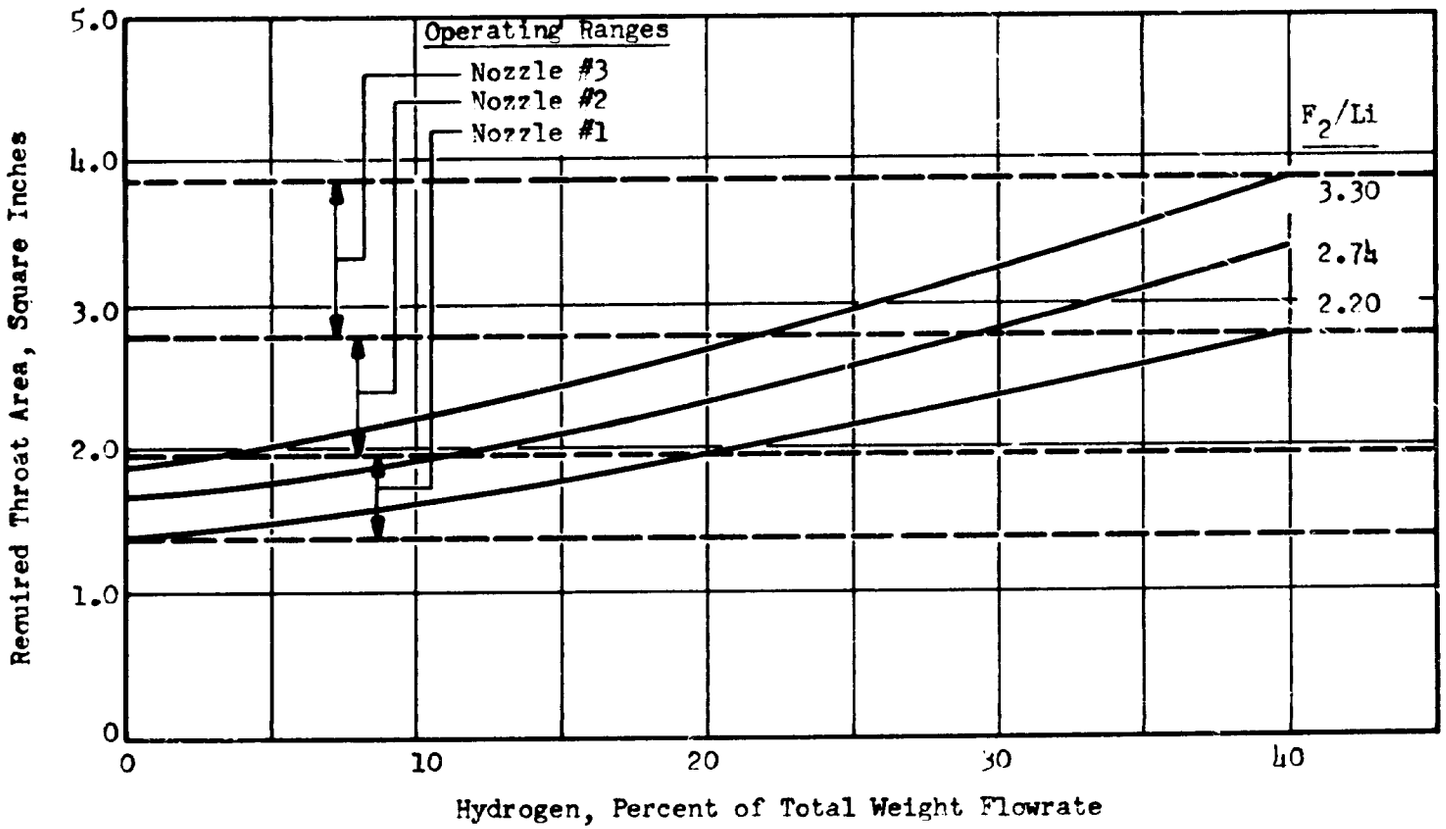

Nozzle	Throat Diameter	Contraction Ratio
1	1.48	11.5
2	1.74	8.3
3	2.05	5.9

Figure 120. Operating Ranges of Three Nozzles.

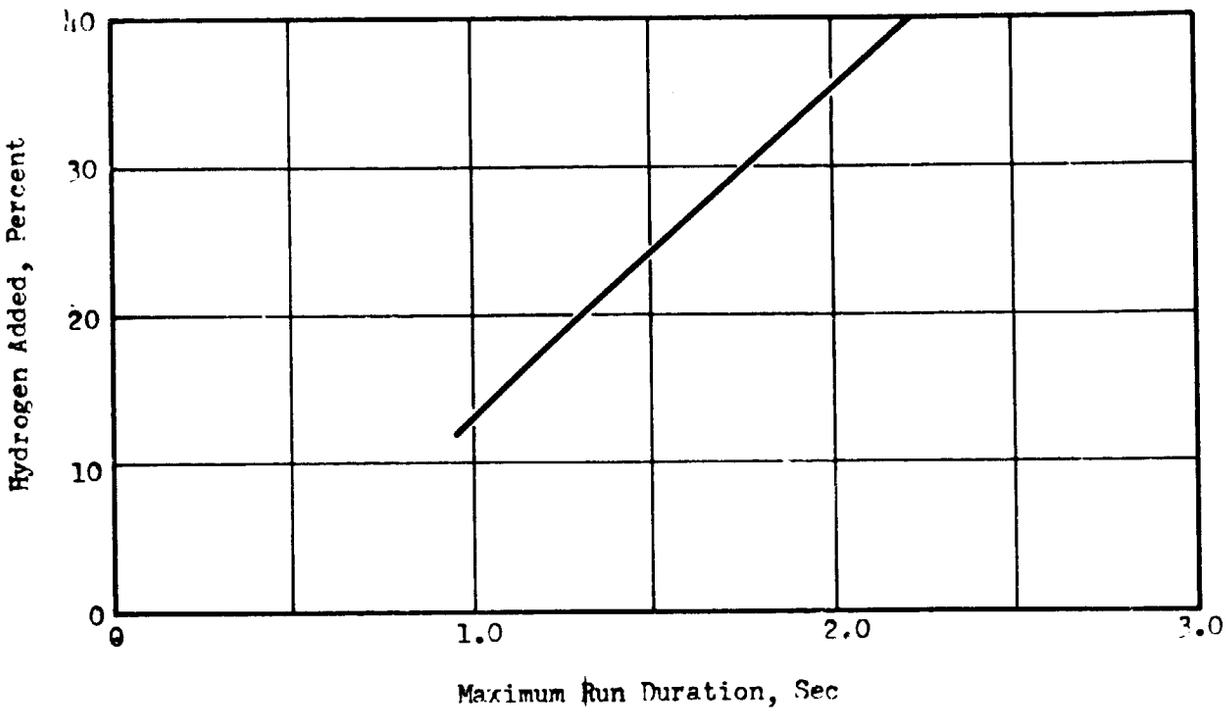

Figure 121. Maximum Run Duration of Copper Nozzle as Function of Hydrogen Percentage.

P_c = 500 psia

F_2/Li M.R. = 2.74

Initial Copper Temperature = 100 F

Maximum Surface Temperature at Run Termination = 1,250 F

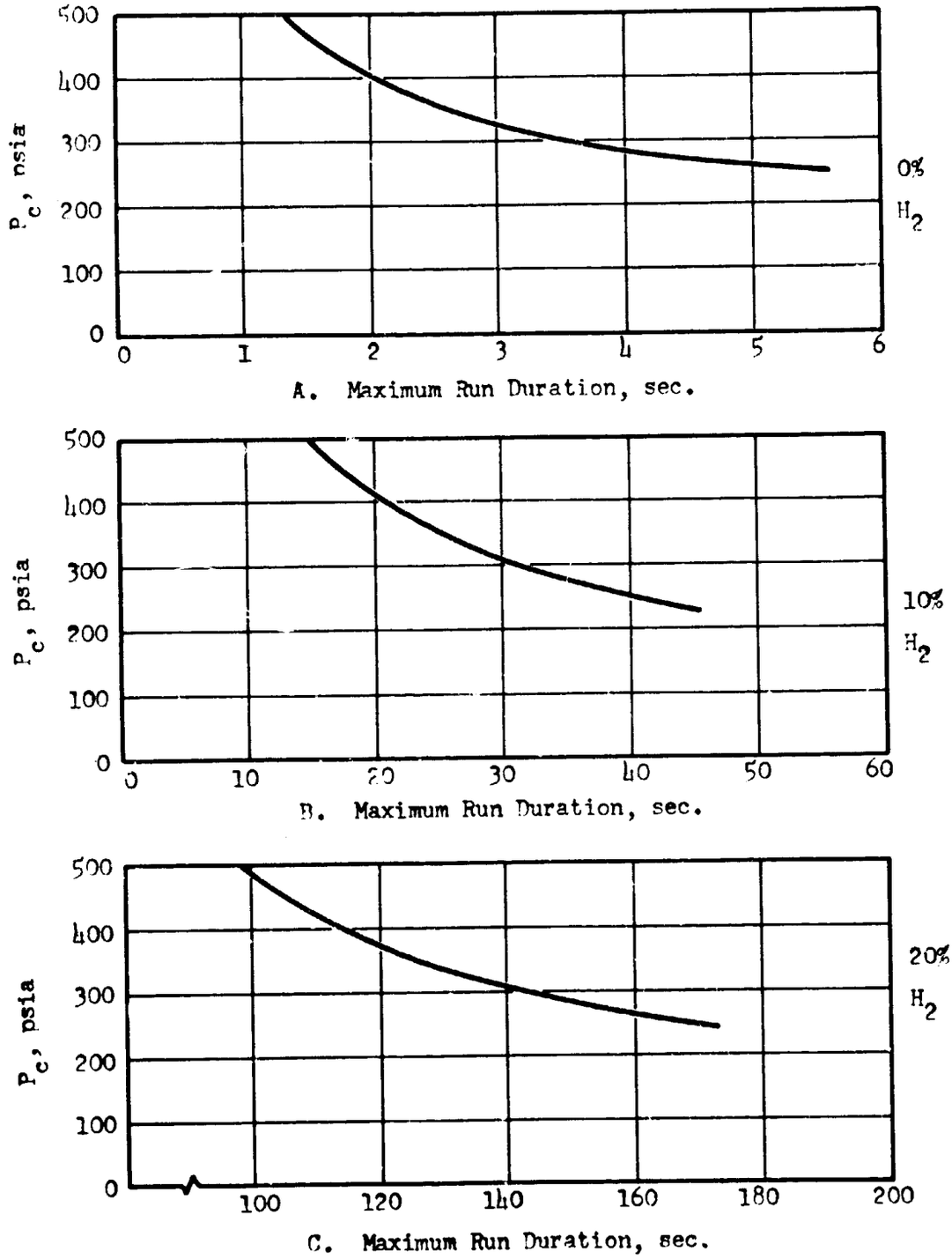

Figure 122. Maximum Run Durations of Graphite Nozzles at Indicated Hydrogen Percentage.
Initial Temperature = 500 F
Maximum Surface Temperature = 4000 F
F_2/Li Mixture Ratio = 2.74

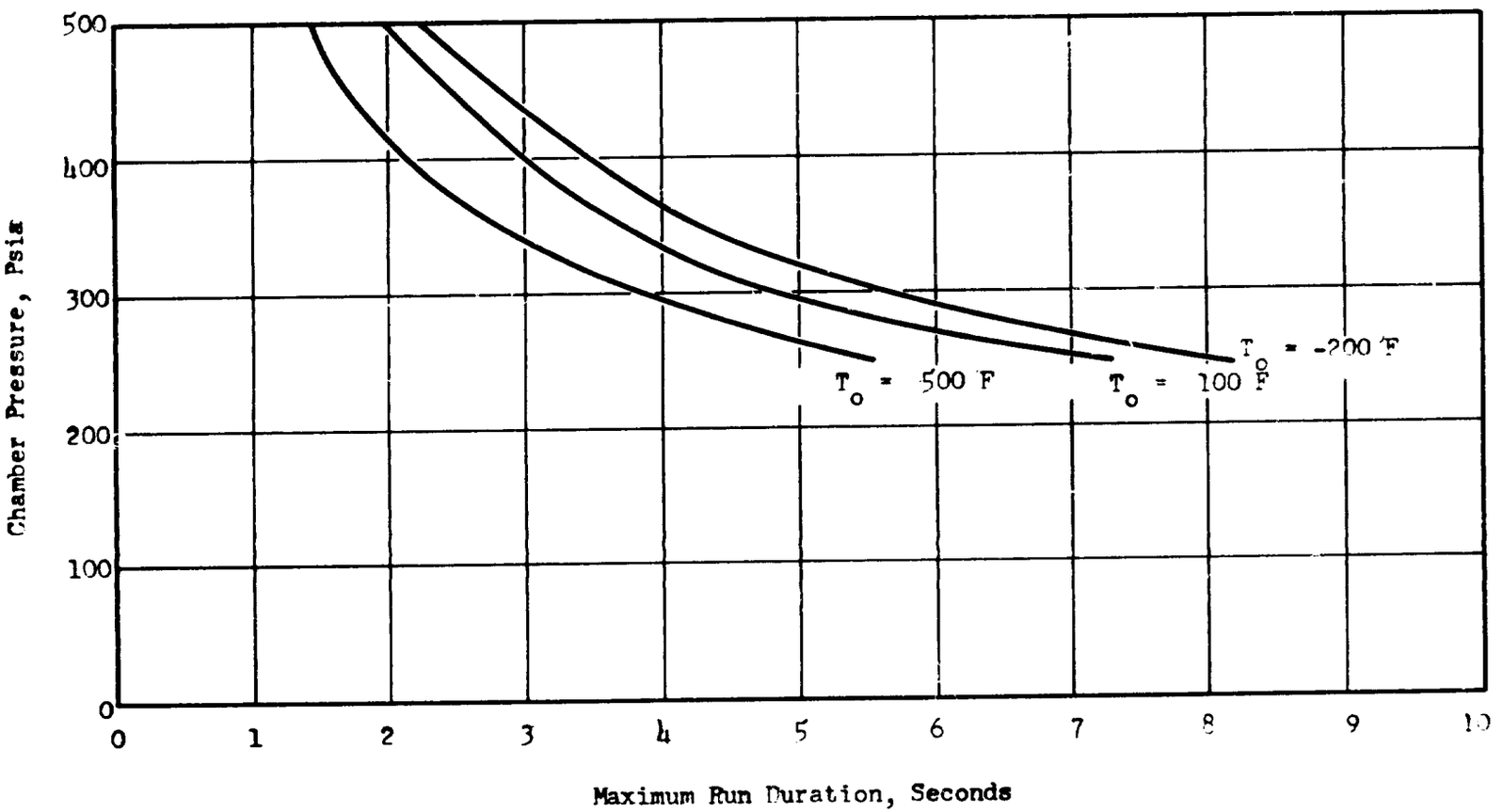

Figure 123. Effect of Initial Nozzle Temperature, T_o, on Maximum Run Duration (Nozzle Inside Surface Temperature at Run Termination = 4000 F). F_2/Li = 2.74, of H_2.

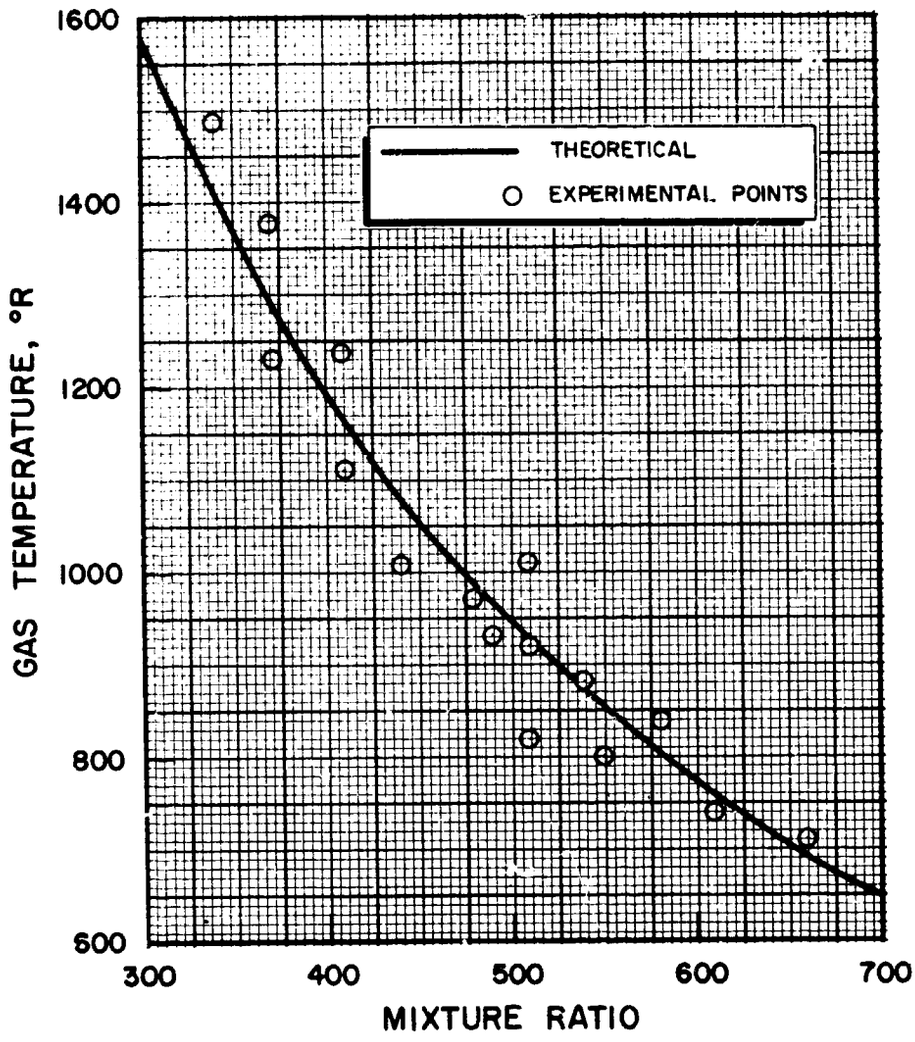

Figure 124. Experimental Variation of Gas Generator Chamber Temperature with F_2/H_2 Mixture Ratio, Compared to Theoretical Values. P_c = 300 ± 800 psia.

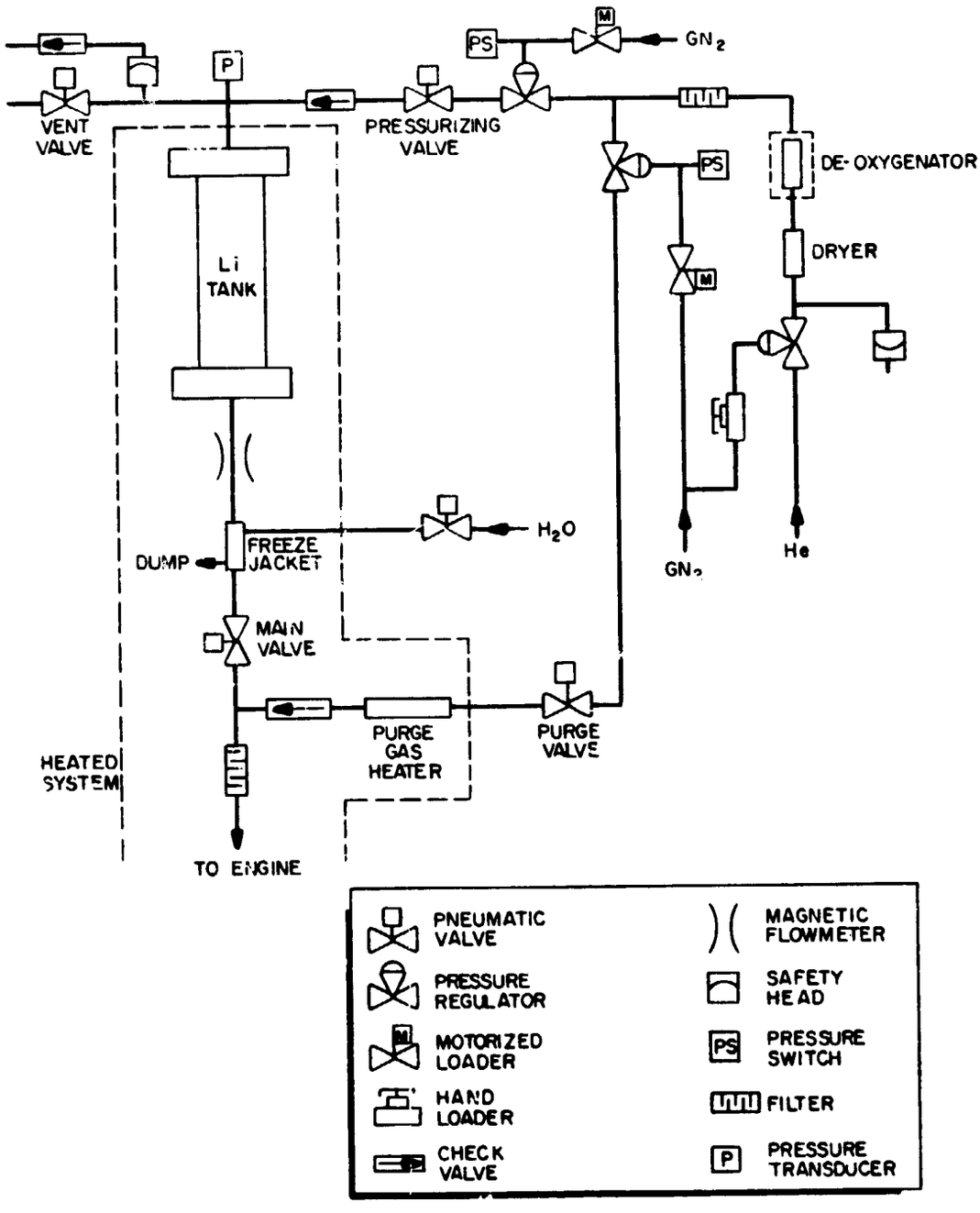

Figure 125. Liquid Lithium System, Schematic Flow Diagram.

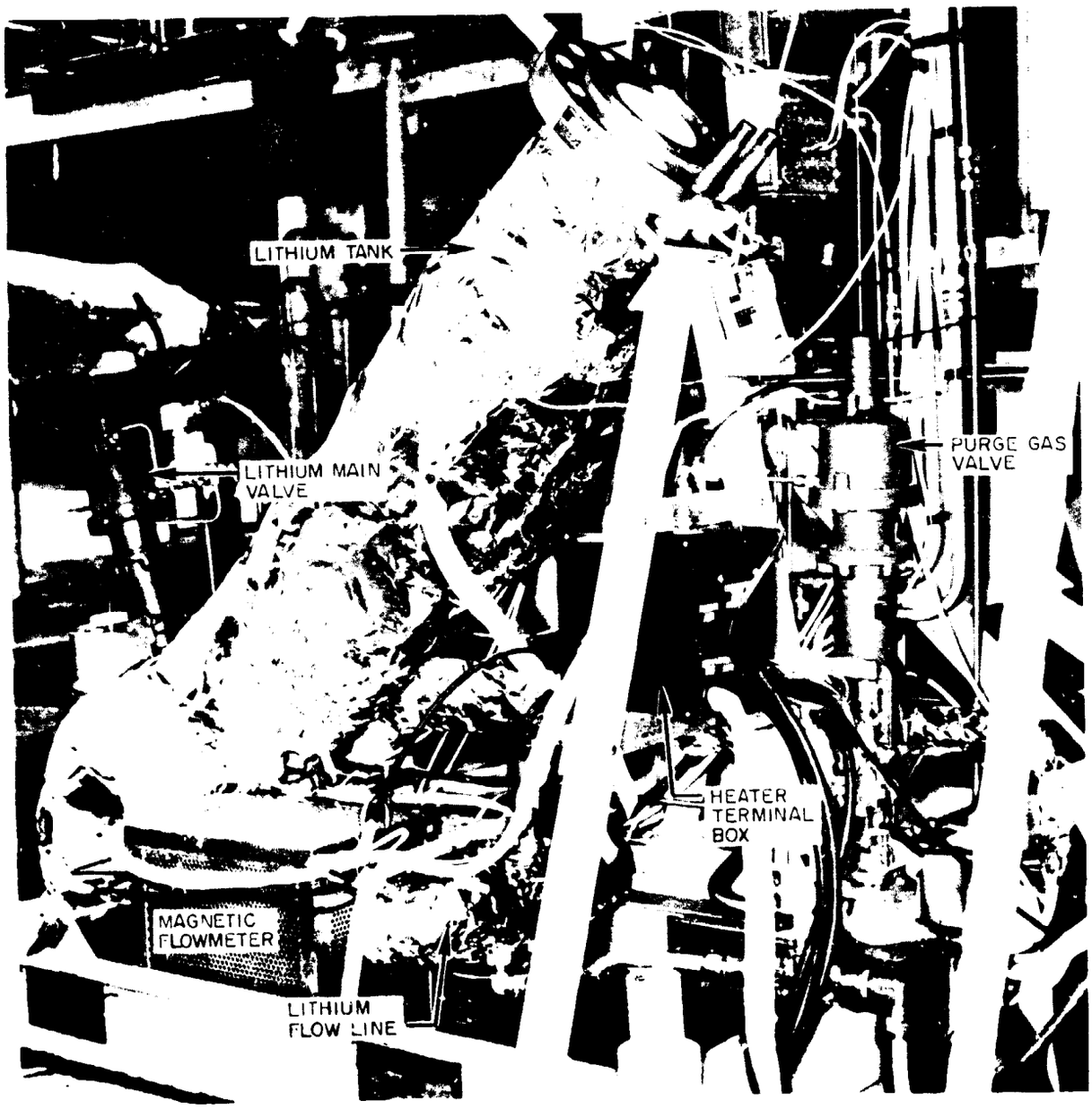

5AA91-12/22/66-SID

Figure 126. Liquid Lithium System, Side View, Upper Tank Flange Removed.

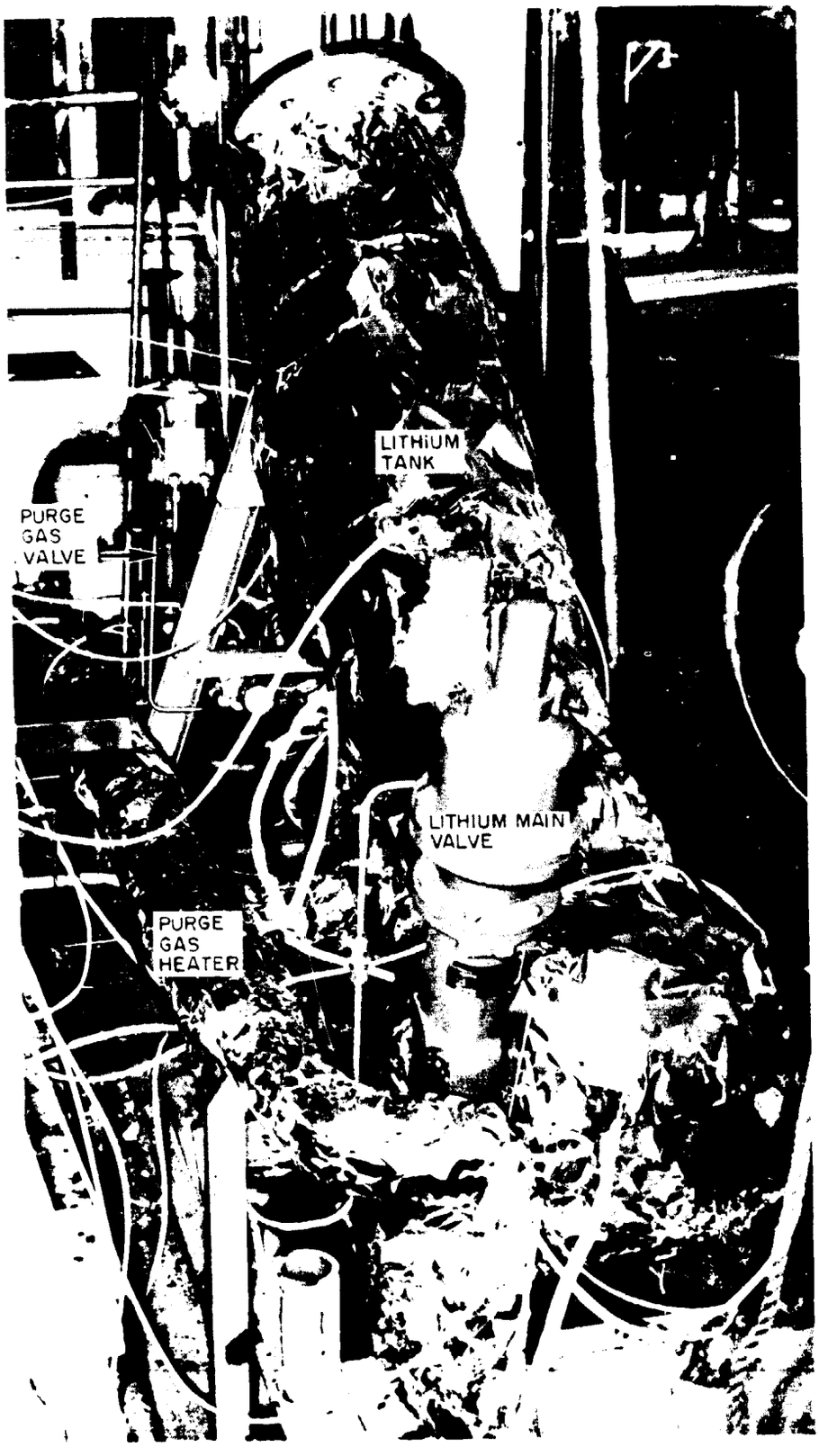

5AA91-12/22/66-SIA

Figure 127. Liquid Lithium System, Front View, Upper Tank Flange Removed.

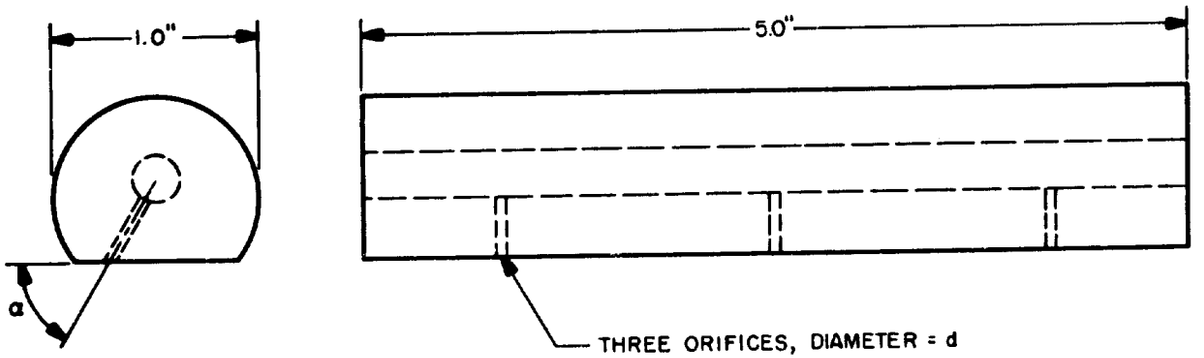

SEGMENT NUMBER	d	α
3	.031"	45°
7	.043"	30°
9	.043"	45°
13	.043"	90°

Figure 128. Test Segments Used for Study of Liquid Lithium Flow through Orifices.

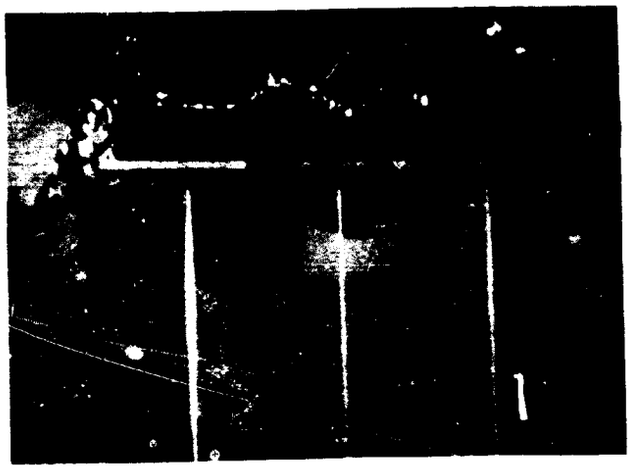

Figure 129. Liquid Lithium Flowing Through 0.043-Inch Showerhead Orifices at 0.07 lb/sec/orifice, ΔP = 250 psi.

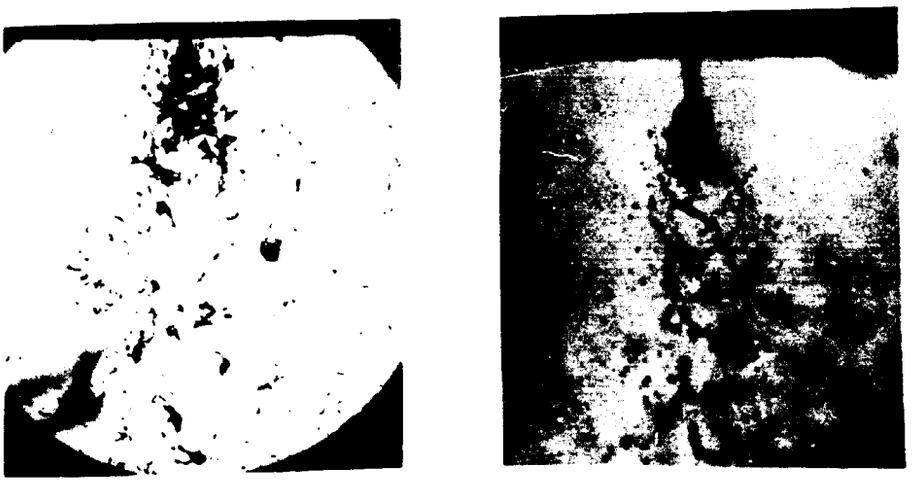

(A) (B)

Figure 130. Comparison of Liquid Metal Flows from Impinging Doublet Elements.

A. Cerrosafe, 0.060-inch orifices, ΔP = 100 psi, Field of View: 2" x 2".

B. Lithium, 0.043-inch orifices, ΔP = 250 psi, Field of View: 1" x 1".

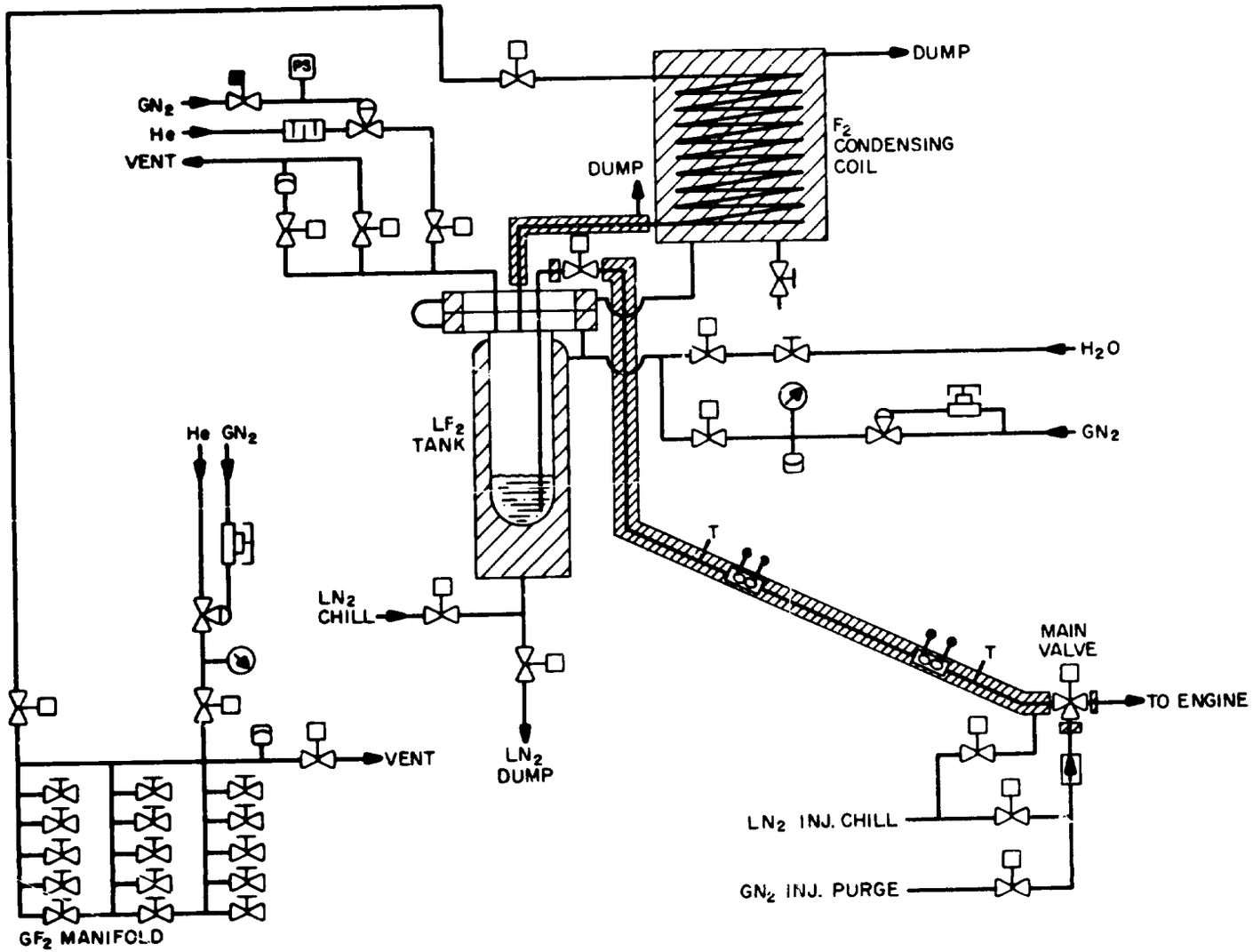

Figure 131. Schematic Flow Diagram of Peter Stand Fluorine Facility.

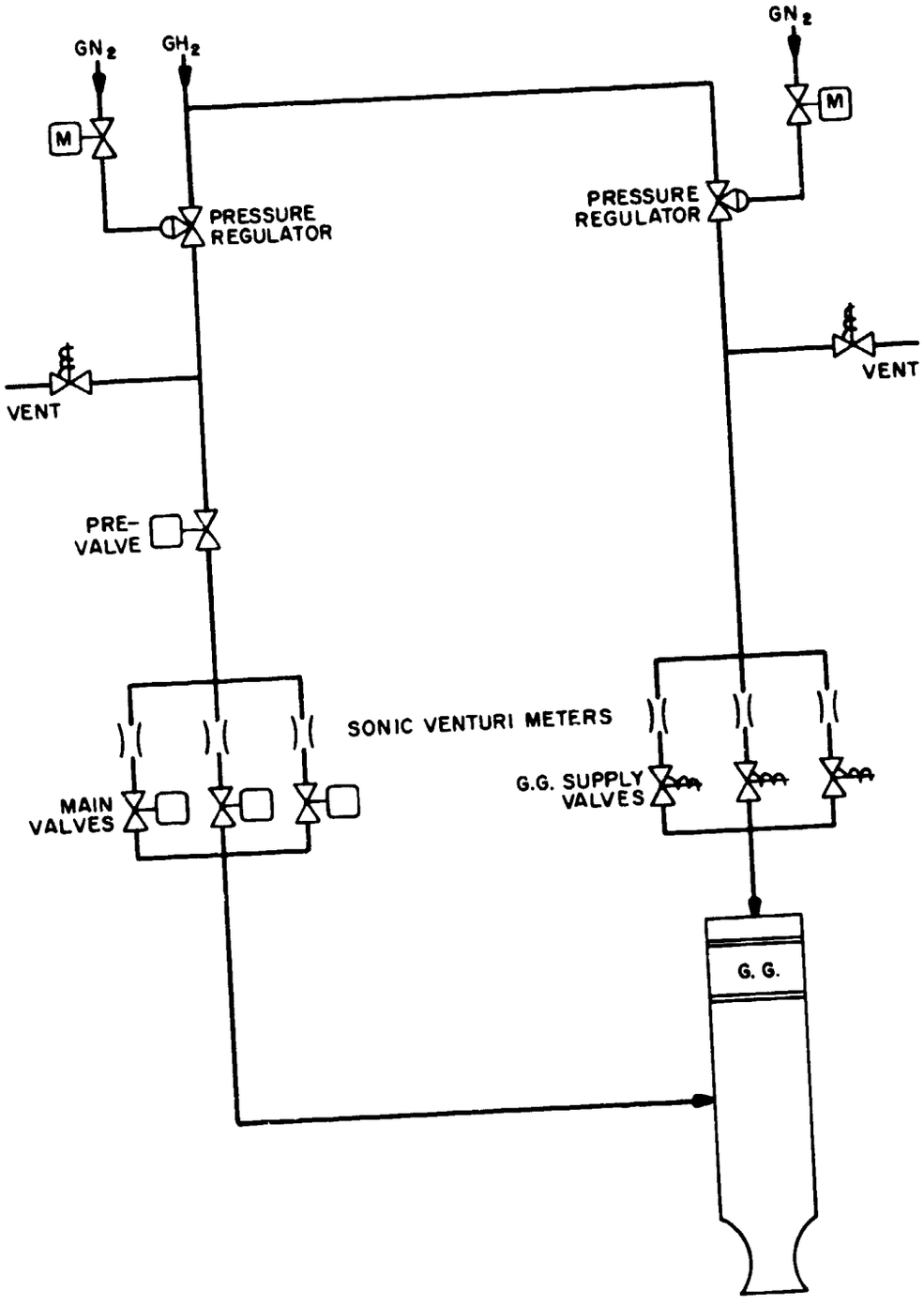

Figure 132. Schematic of Hydrogen Flow System, Showing Parallel Circuits in Both Main and Gas Generator Supply Branches.

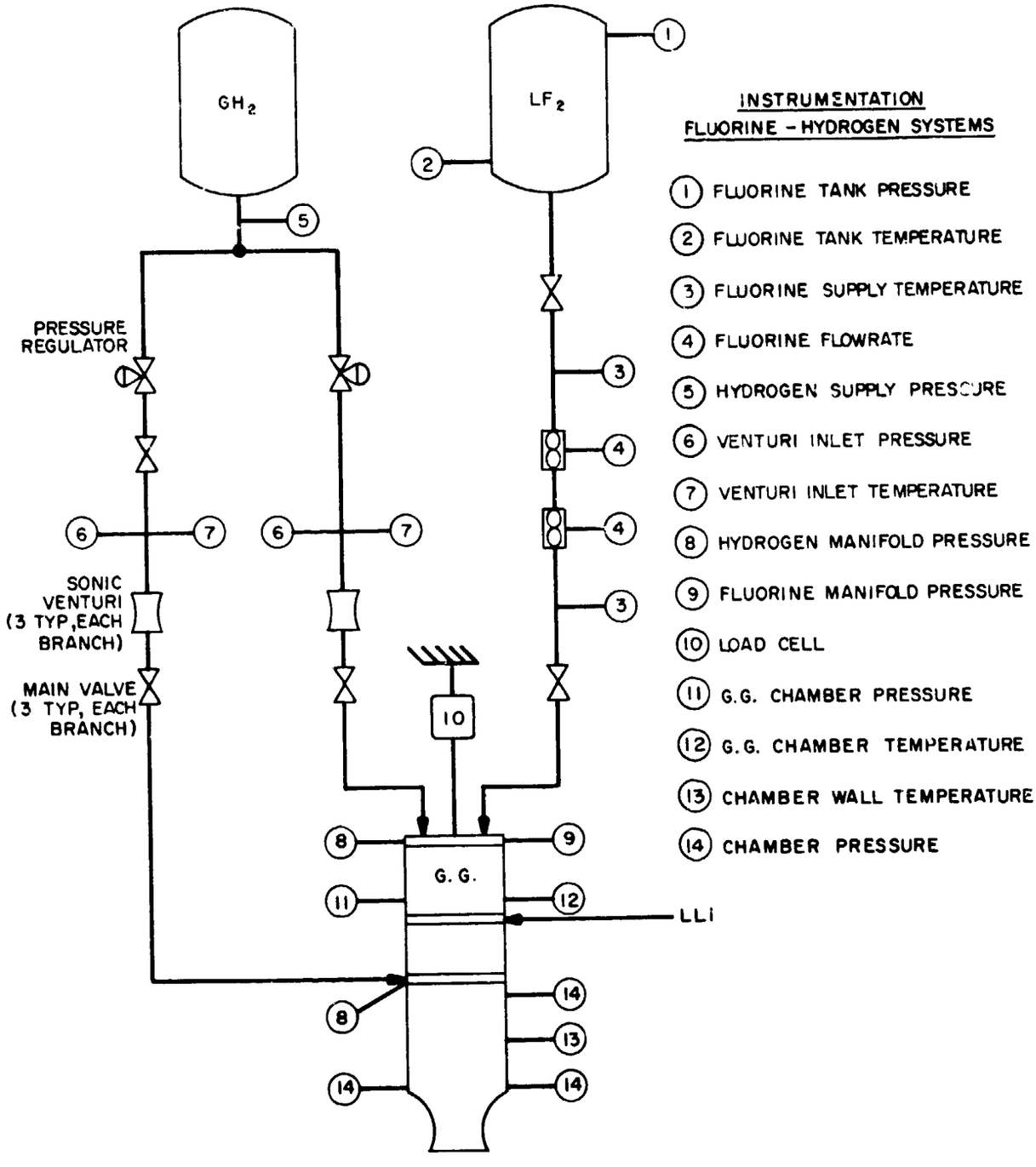

Figure 133. Schematic of Fluorine and Hydrogen Flow Systems, Showing Instrumentation Locations.

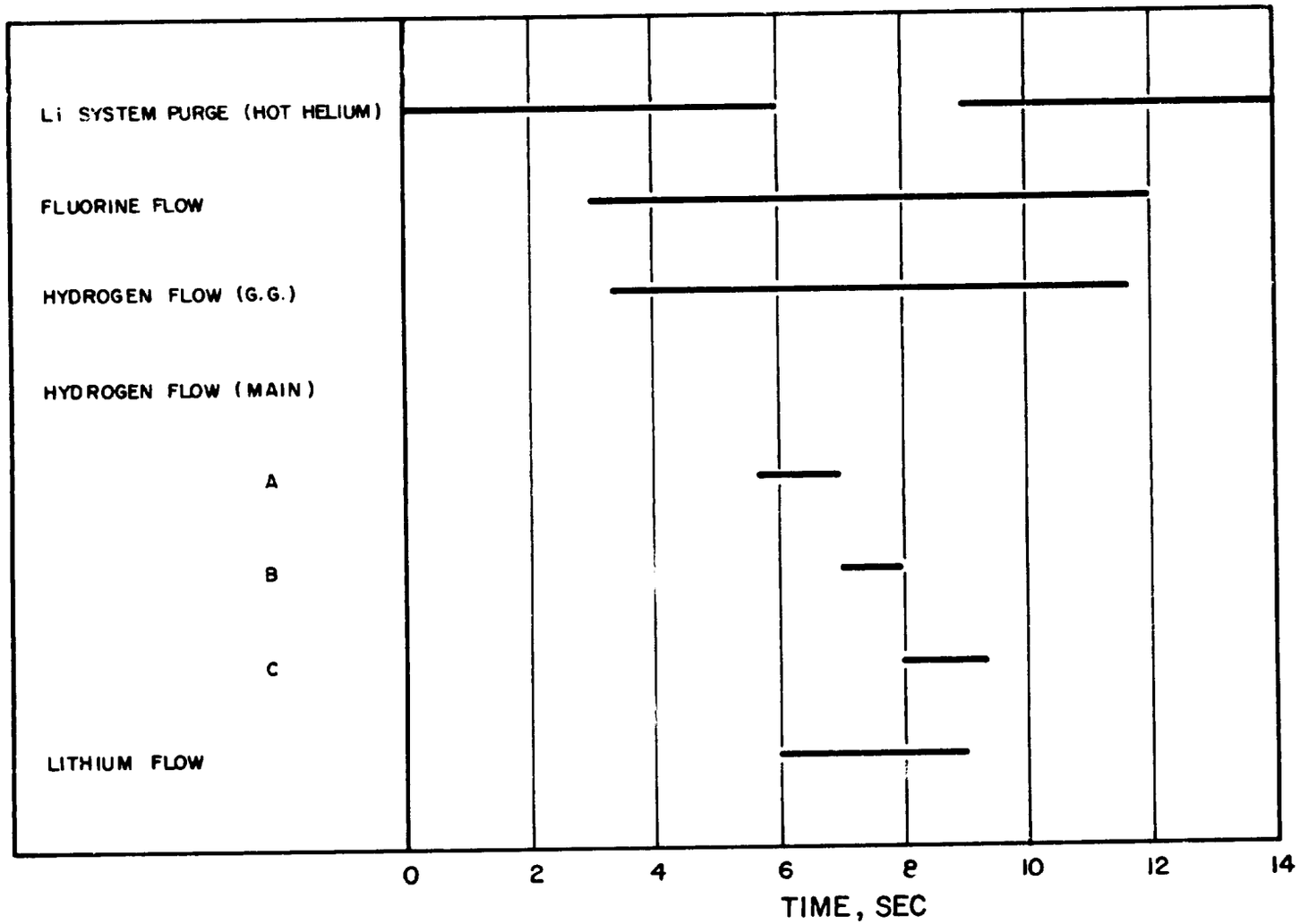

Figure 134. Typical Firing Sequence, Showing Timing of Propellant Flows and of Lithium Purge.

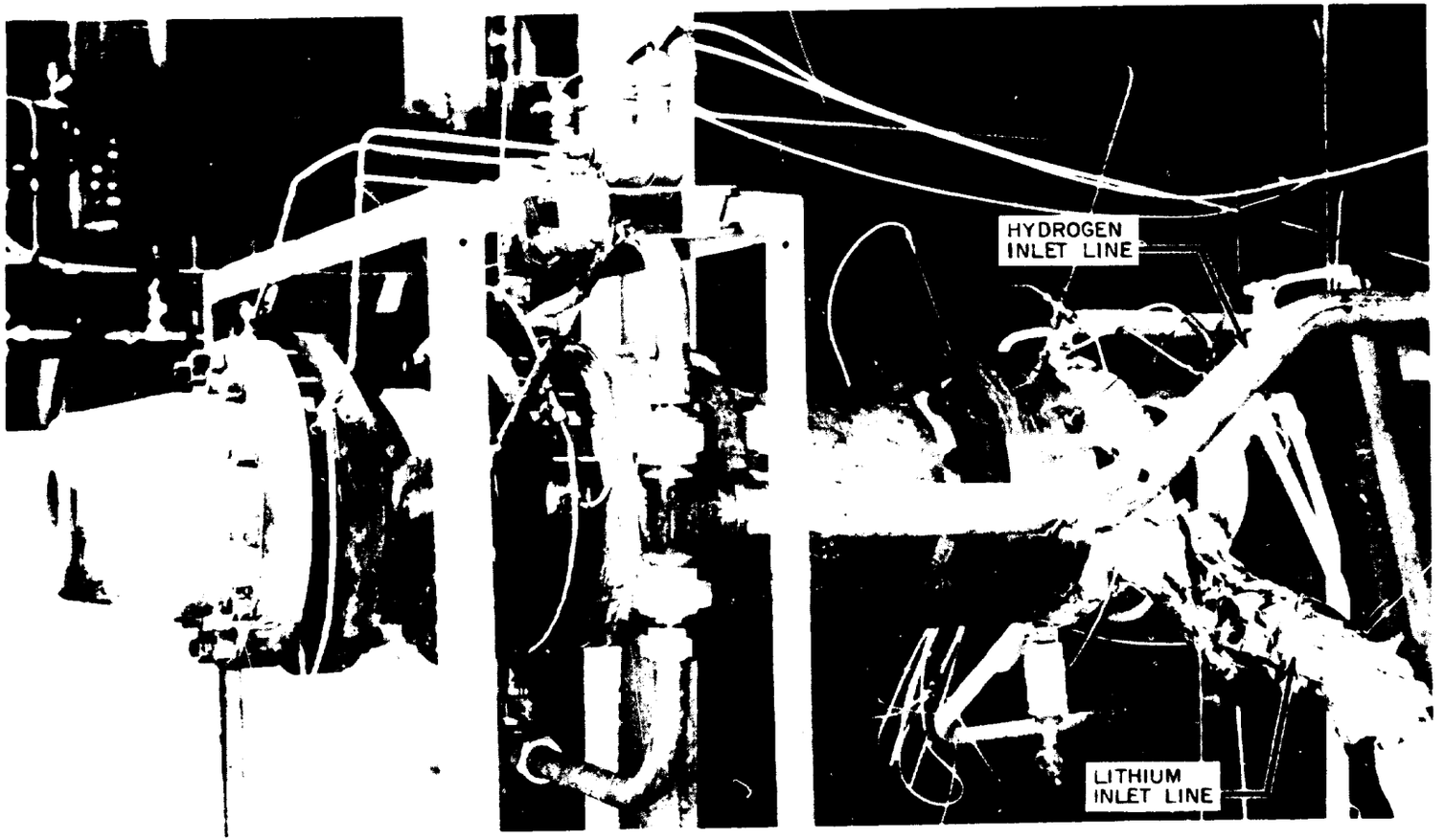

5AA36-9/1/57-SI

Figure 135. Thrust Chamber Mounted on Stand.

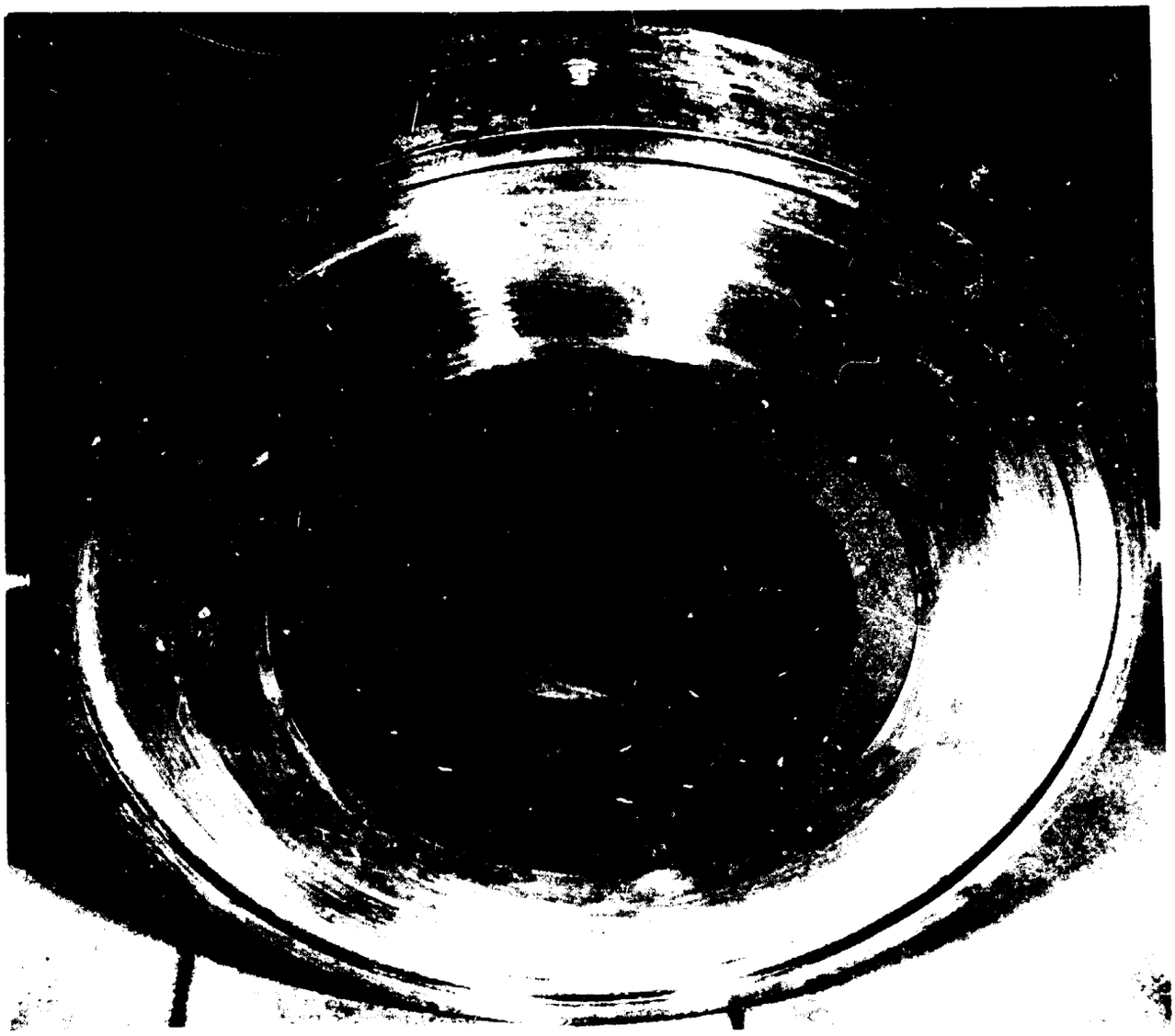

5AA33-9/6/67-SI

Figure 136. Hydrogen Injector for Main Hydrogen Flow. This Model Has A Graphite Core, in Which the Orifices Are Located, and a Copper Manifold.

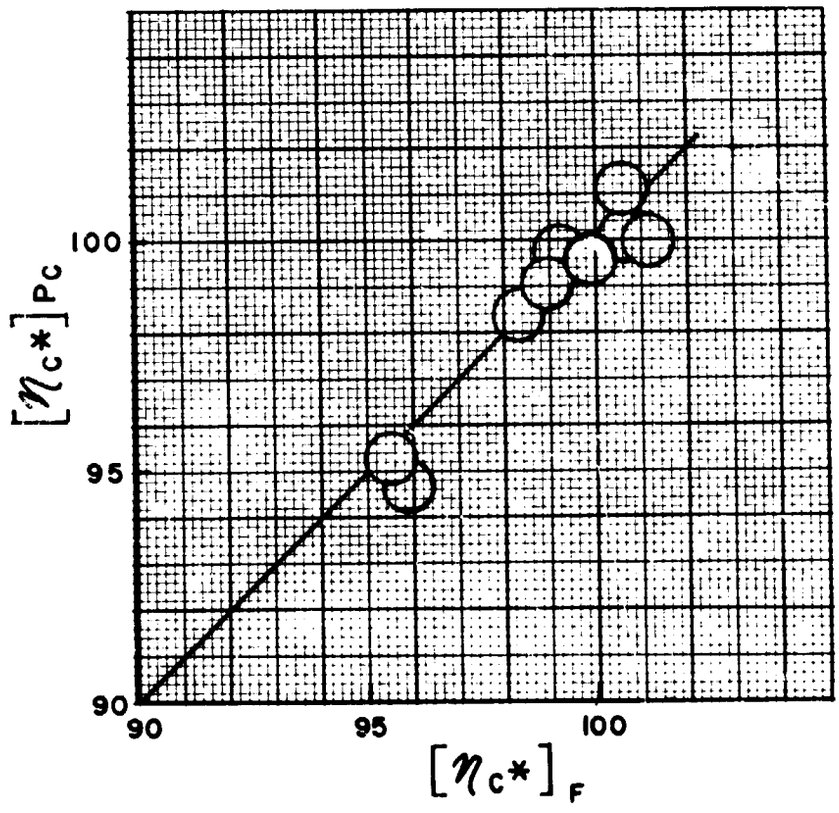

Figure 137. Comparison of Corrected c* Efficiencies Based on Measurements of Chamber Pressure and of Thrust. Straight Line Indicates Perfect Agreement.

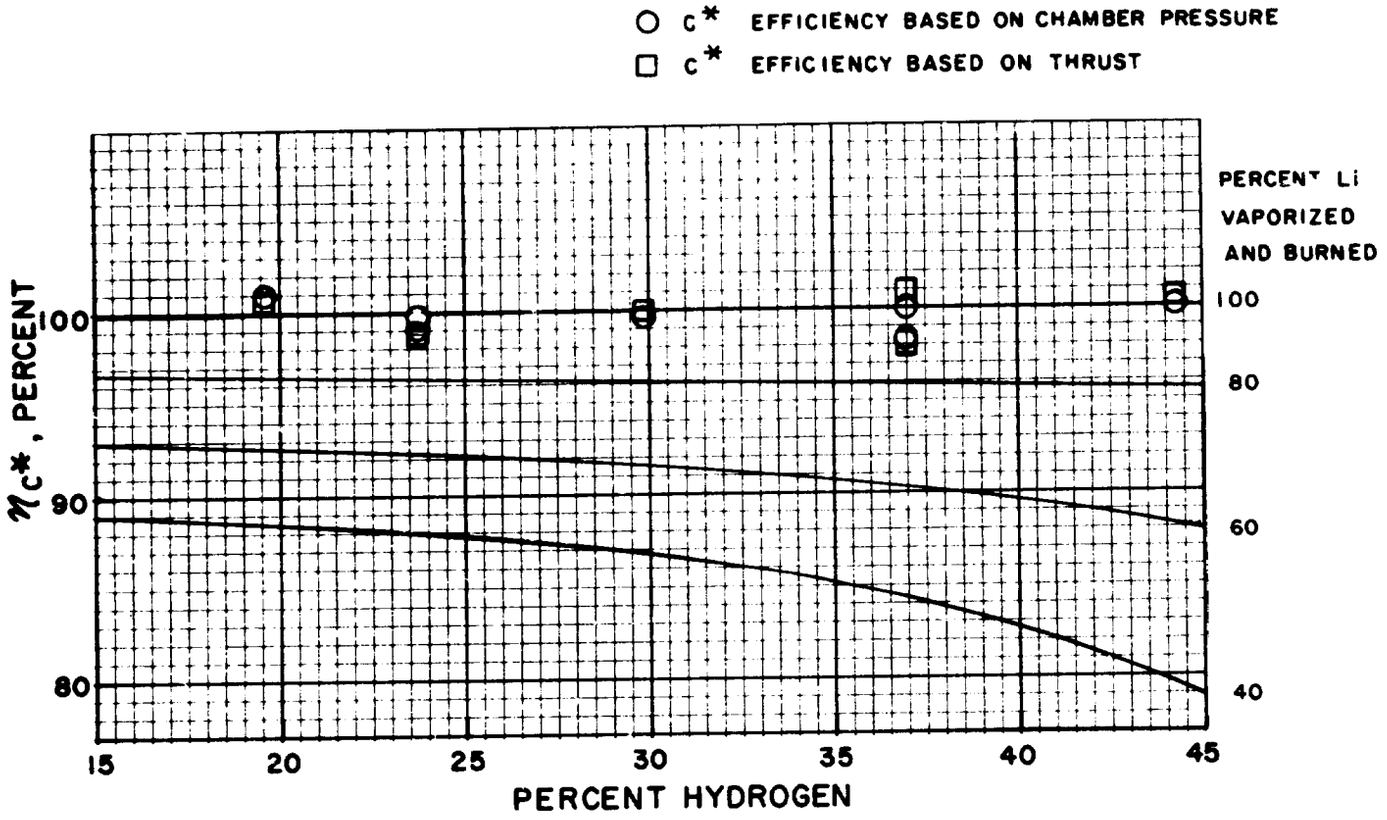

Figure 138. Predicted Variation of c* Efficiency with Percent Hydrogen as Function of Percent Li Vaporized. P_c = 500 psia, F_2/Li M.R. = 2.74. Experimental Data Points are Superposed.

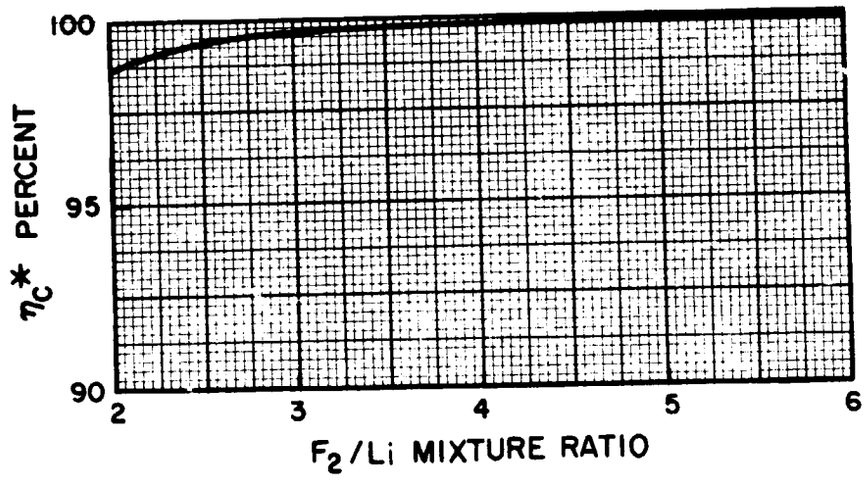

Figure 139. Predicted Variation of c* Efficiency with F_2/Li Mixture Ratio at Indicated Conditions.

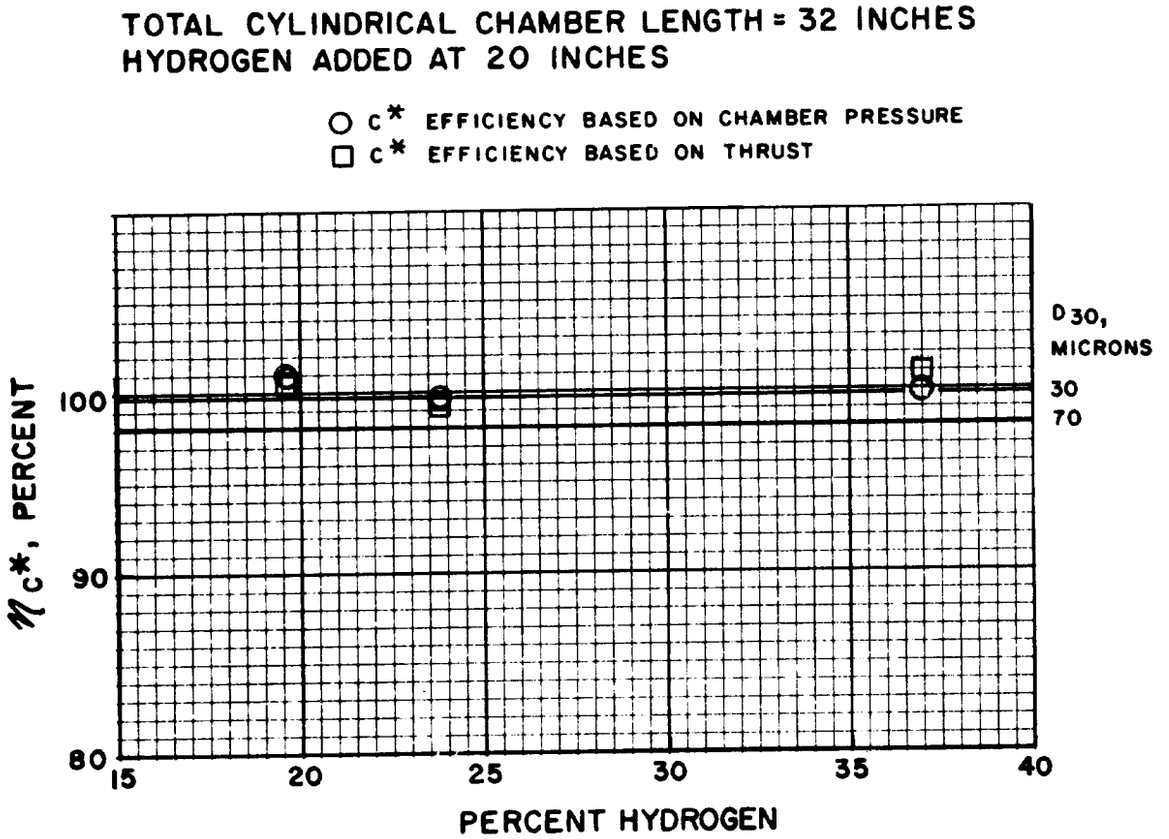

Figure 140. Experimental Data (Runs No. 6 and 7) Superposed on Predicted c* Efficiencies for Indicated Lithium Mean Droplet Diameters.

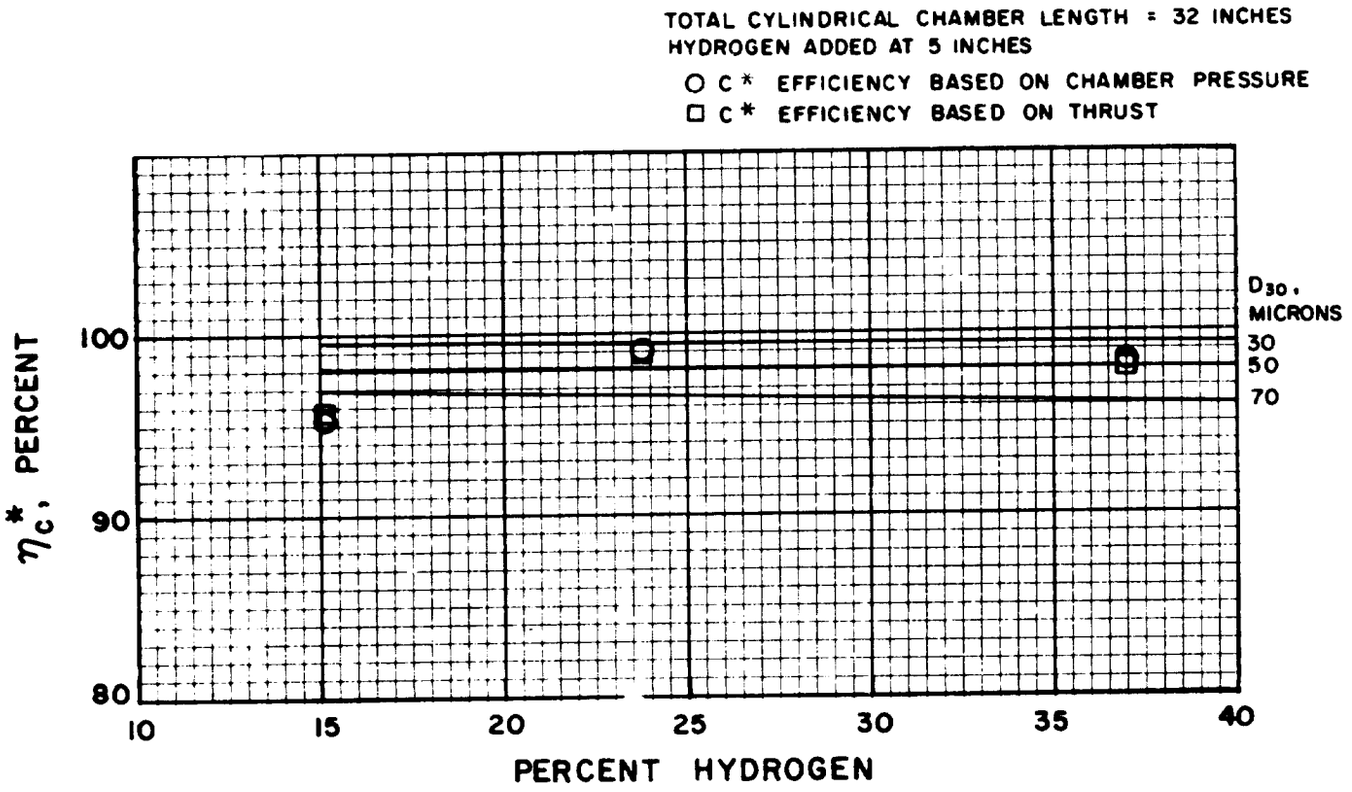

Figure 141. Experimental Data (Run No. 8) Superposed on Predicted c* Efficiency for Indicated Lithium Mean Droplet Diameters.

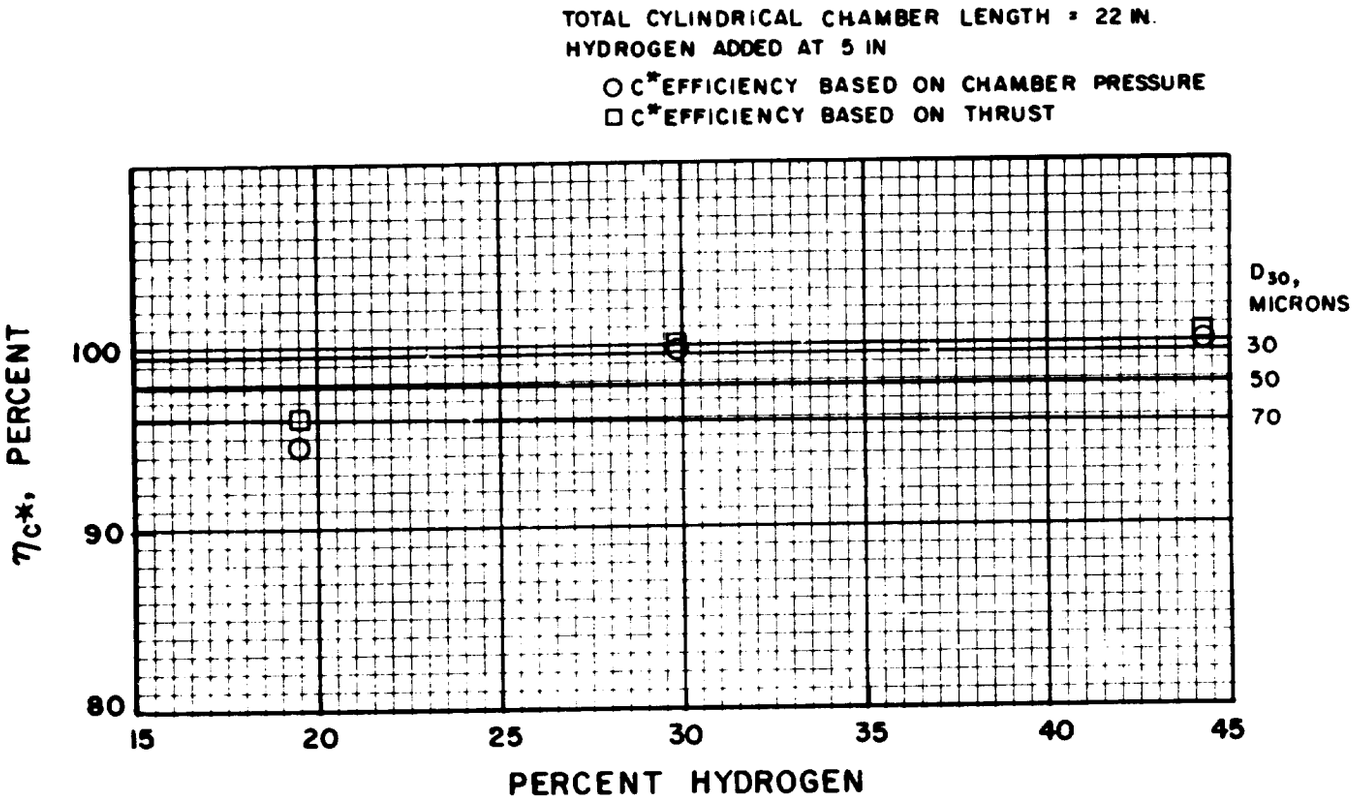

Figure 142. Experimental Data (Run No. 9), Superposed on Predicted c* Efficiencies For Indicated Lithium Mean Droplet Diameters.

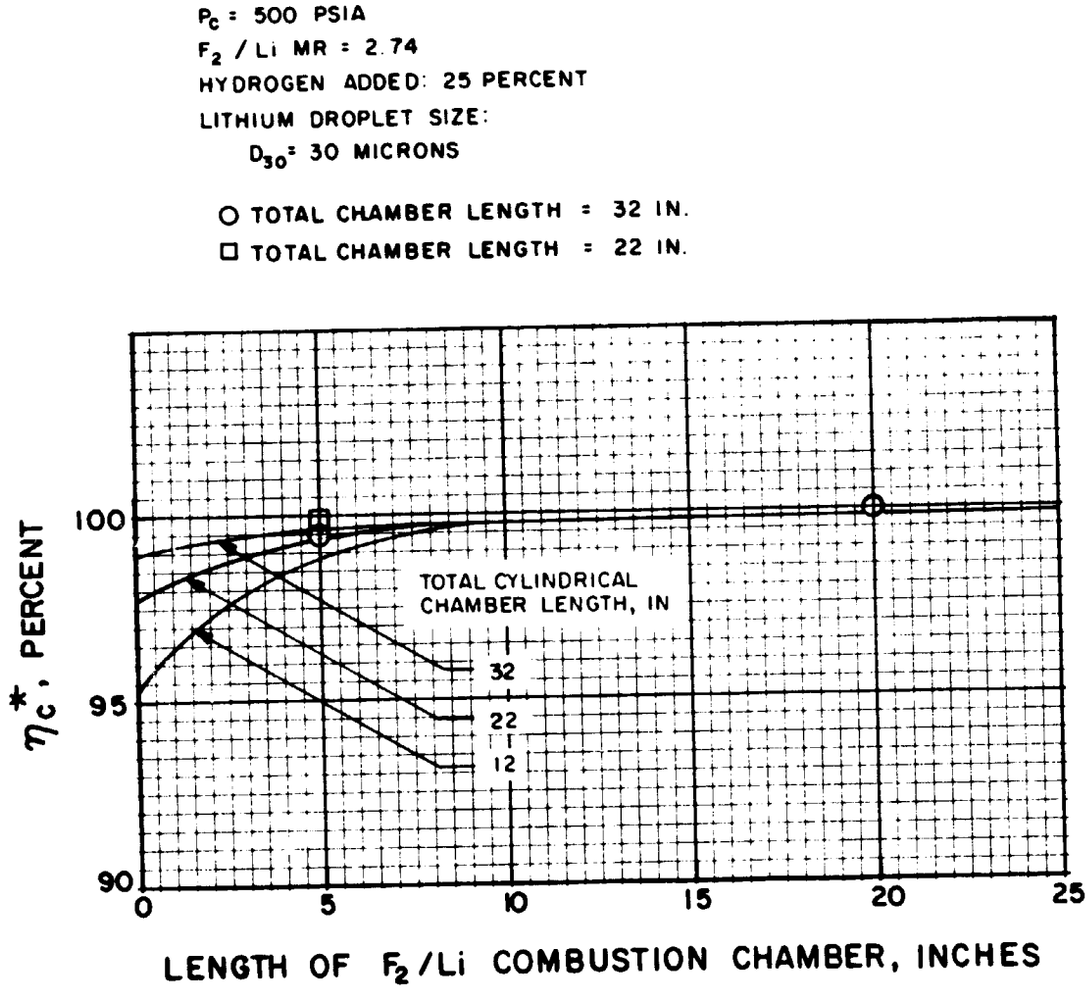

Figure 143. Experimental Data Superposed on Curves of Predicted c* Efficiency as a Function of Length of F_2/Li Combustion Chamber for Three Overall Chamber Lengths, at Indicated Conditions.

APPENDIX A

CALCULATION OF CORRECTED C* EFFICIENCIES

INTRODUCTION

The performance indices used in the present program were corrected c* efficiencies obtained independently from measurements of chamber pressure and of thrust. Details of the computational procedures and of the corrections applied are given in this appendix.

CORRECTED CHARACTERISTIC VELOCITY EFFICIENCY BASED ON CHAMBER PRESSURE

Characteristic velocity efficiency based on chamber pressure is defined by the following equation:

$$\eta_{c*} = \frac{(P_c)_o \ (A_t)_{eff} \ g_c}{(\dot{w}_T) \ (c*)_{theo}} \qquad \text{(A-1)}$$

where

$(P_c)_o$ = stagnation pressure at the throat, psia

$(A_t)_{eff}$ = effective thermodynamic throat area, $in.^2$

g_c = conversion factor (32.174 lbm-ft/lbf-sec^2)

$\dot{w}_T$ = total propellant weight flowrate, lbm/sec

$(c*)_{theo}$ = theoretical characteristic velocity based on shifting equilibrium, ft/sec

Values calculated from Eq. A-1 are referred to as "corrected" c* efficiencies because the factors involved are not measured directly, but are obtained by application of suitable corrections to measured parameters. Thus, stagnation pressure at the throat is obtained from measured static

pressure at start of nozzle convergence by assumption of isentropic expansion, effective throat area is estimated from measured geometric area by allowing for radius changes during firing and for nonunity discharge coefficient, and chamber pressure is corrected to allow for energy losses from combustion gases to the chamber wall by heat transfer and friction. Equation A-1 may therefore be written as follows:

$$\eta_{c^*} = \frac{P_c A_t g_c f_P f_{TR} f_{DIS} f_{FR} f_{HL}}{(\dot{w}_T)(c^*)_{theo}} \qquad (A\text{-}2)$$

where

P_c = measured static pressure at start of nozzle convergence, psia

A_t = measured geometric throat area, $in.^2$

g_c = conversion factor (32.174 lbm-ft/lbf-sec^2)

$\dot{w}_T$ = total propellant flowrate, lb/sec

$(c^*)_{theo}$ = theoretical c* based on shifting equilibrium calculations, ft/sec

f_P = factor correcting observed static pressure to throat stagnation pressure

f_{TR} = factor correcting for change in throat radius

f_{DIS} = factor correcting throat area for effective discharge coefficient

f_{FR} = factor correcting measured chamber pressure for frictional drag of combustion gases at chamber wall

f_{HL} = factor correcting measured chamber pressure for heat losses from combustion gases to chamber wall.

Methods of estimation of the various correction factors are described in the following paragraphs.

Pressure Correction (f_p)

Measured static pressure at start of nozzle convergence was converted to stagnation pressure at the throat by assumption of no combustion in the

nozzle and application of the isentropic flow equations. The shifting equilibrium specific heat ratio (γ) ranged from 1.20 to 1.26 for the experimental firings reported herein. At the applicable contraction ratio (5.95), the corresponding stagnation/static pressure ratios do not vary significantly; the same correction factor (f_p = 1.006) was therefore used for all of the firings.

Throat Radius Correction (f_{TR})

Temperature gradients produced in an uncooled nozzle wall by flow of hot combustion gases result in thermal stresses which affect throat radius. Consequently, the geometric throat diameter measured in an ambient-temperature nozzle is not the same as that which exists during firing. When firing begins, thermal penetration of the nozzle wall is small with respect to the wall thickness, hence the outer wall diameter is unchanged. The inner-wall material will therefore expand toward the center, resulting in a decrease in throat diameter. As heat penetrates throughout the nozzle wall, the outer diameter will also increase, allowing outward expansion of the inner portion and consequent increase in throat diameter. Hence, throat area during firing is a function of time, as well as of the physical properties of the throat material and the temperature and pressure of the combustion gases.

Calculations of throat radius change start with the transient thermal stress equations for a hollow cylinder (Ref. A-1). Various analyses based on these equations have been made. One which is applicable to relatively short-duration firings (Ref. A-2) assumes zero plastic stress, zero stress in the axial direction, a quadratic temperature distribution through the wall, circular throat and nozzle, and zero temperature and radius changes at the outer wall. The result is expressed as change in throat radius:

$$\Delta R_i = \alpha \left[\frac{1+\mu}{1-\mu}\right] \frac{(\theta_i - \theta_o)}{(R_o - R_i)^2} \left[\frac{R_o^2 R_i}{2} - \frac{2R_o R_i^2}{3} + \frac{R_i^3}{4} - \frac{R_o^4}{12R_i}\right] \qquad \text{(A-3)}$$

where

R_i = inner radius of wall

R_o = outer radius of wall

α = coefficient of linear expansion of wall material

μ = Poisson's ratio of wall material

θ_i = temperature at inner wall

θ_o = temperature at outer wall

Although graphite is not strictly an isotropic material, directional property variations are not large enough to significantly prevent application of Eq. A-3 . Inner-wall temperatures were estimated by the method of Ref. A-3. The throat area correction factor due to thermal shrinkage varied from 0.993 (at 40-percent H_2 addition) to 0.989 (at 15-percent H_2 addition).

Throat Discharge Coefficient Correction (f_{DIS})

The discharge coefficient is defined as the ratio of actual flowrate through the throat to the theoretical maximum based on the geometric throat area and one-dimensional, inviscid flow. Values of the discharge coefficient may be estimated either analytically or from correlations of the results of experimental studies of gas flow through nozzles. In the present program the ratio of the upstream wall radius at the throat to the throat radius was large (4:1) so that the discharge coefficient was very nearly unity and either of the two methods could be employed.

In a recent critical study of available theoretical analyses of nozzle flow (Ref. A-4), values of the throat discharge coefficient were presented as functions of nozzle wall/throat radius ratio and throat Reynolds number. For the applicable radius ratio (4) and Reynolds number (1×10^6 to 2×10^6),

the indicated value is 0.995. On the other hand, from correlations of experimental conical nozzle discharge coefficients obtained by various investigators (Ref. A-5) and the geometry of the present nozzle, a value of 0.993 is obtained. Agreement between the two values is good and the average was used as the correction factor: $f_{DIS} = 0.994$.

Frictional Drag Correction (f_{FR})

Calculations of c* based on chamber pressure are concerned with chamber phenomena up to the nozzle throat. Drag forces to this point are generally small enough to be considered negligible, particularly when the contraction ratio is fairly large as in the present case. Hence, the factor f_{FR} was taken to be unity.

Heat Loss Correction (f_{HL})

Heat transfer from the combustion gases to the walls of an uncooled thrust chamber results in loss of enthalpy and thus decreases chamber pressure and thrust. This enthalpy loss is substantially reduced in an ablative chamber and is effectively recovered in a chamber cooled regeneratively by one of the propellants, whose initial enthalpy is raised by the heat absorbed. To obtain a true indication of performance efficiency in an uncooled chamber, measured chamber pressure must be corrected by a factor which accounts for heat loss to the walls and to the injector face.

The three modes of heat transfer considered in estimating the heat loss rate to the thrust chamber walls were radiation, convection, and condensation. These heat transfer mechanisms were assumed to be uncoupled; other assumptions regarding the heat transfer modes were based on posttest observations of engine hardware.

Three separate regions are distinguishable in the experimental thrust chamber: (A) the gas generator section, (B) the lithium/fluorine combustion

section upstream of the hydrogen addition point, and (C) the chamber section downstream of the hydrogen injector.

In region A temperatures and flowrates are low enough so that heat losses to the chamber walls are negligibly small.

Combustion of lithium and fluorine in region B produces gas temperatures on the order of 9000 to 9800 R. In this region radiation from the gas cloud is by far the dominant mode of heat transfer. The meager emission data available for LiF and HF indicate that for the chamber geometry and pressure involved, the gas radiates as a continuum black body and that beam length is much shorter than any chamber dimension. Assuming unity view factor and black body emission, estimated radiation heat flux is approximately 26 Btu/in.^{2}/sec.

Confirmation of the order of magnitude of the heat flux in region B was obtained in the first $F_2/Li/H_2$ firing, in which an all-copper hydrogen injector was used. Postrun, the core of the injector was found to be burned away (graphite cores were therefore used in all subsequent firings). An estimate of the heat flux required to burn the copper core was made on the basis of its geometry, the cooling capability of the hydrogen flowing through it, and the time to failure. The value thus calculated was 29 Btu/in.^{2}/sec, which agrees with the estimate of radiation heat flux. Apparently total heat flux in region B (radiation plus convection) remains relatively constant at the indicated high level.

Heat flux in region C was estimated on the basis of response data obtained from thermocouples placed in the graphite liner one-half inch from the inner wall. The rates of temperature increase indicated by these thermocouples were used with Heisler transient conduction heat transfer charts to estimate the heat flux into the wall, which was found to be relatively constant at approximately 1.6 Btu/in.^{2}/sec. This value derives essentially from convection since radiation is negligible in this region and

contributions from condendation are small (observed LiF deposits on the wall were 0.01 to 0.03 inch thick).

Heat loss in the nozzle region was estimated from the Bartz equation (Ref.A-6); average heat flux in the converging section was approximately 2 Btu/in.^{2}/sec.

For each firing, heat losses to the chamber walls were computed for the various regions of the thrust chamber from the heat flux estimates given above. Total heat loss affecting the observed measurements of chamber pressure was then obtained by summation over the appropriate areas:

$$\mathcal{H} = \Sigma (q/A)A \qquad (A\text{-}4)$$

where

$\mathcal{H}$ = total heat loss

q/A = estimated heat flux over given region

A = area applicable to each q/A value

The enthalpy of the injected propellants was reduced by an amount equivalent to the total heat loss to the chamber walls, and performance calculations were made to determine theoretical values of c* under the modified conditions. While this procedure lumps all heat lost and confines it to the injection station instead of gradual loss along the chamber length, the difference is not significant as far as this application is concerned. Comparison of the modified values of c* with the corresponding original values provided a measure of the applicable correction factor, f_{HL}. Since heat flux in the F_2/Li combustion chamber represents by far the largest heat loss, the magnitude of the correction factor is a direct function of the length of that chamber. In the present series of data-producing firings, this length was either 20 inches (runs No. 6 and 7) or 5 inches (runs No. 8 and 9). With the 20-inch chamber, f_{HL} was ~ 1.07 ; with the 5-inch chamber, f_{HL} was ~ 1.02.

CORRECTED C* EFFICIENCY BASED ON THRUST

Specific impulse efficiency is defined by the following equation:

$$\eta_{I_s} = \frac{(F_{vac})}{(\dot{w}_T)\ (I_s)_{theo}} \qquad \text{(A-5)}$$

where

F_{vac} = measured thrust corrected to vacuum conditions by the equation: $F_{vac} = F + P_a A_e$

F = measured thrust, pounds

P_a = ambient pressure, psia

A_e = area of nozzle exit, $in.^2$

$\dot{w}_T$ = total propellant flowrate, lbm/sec

$(I_s)_{theo}$ = theoretical vacuum shifting-equilibrium specific impulse at applicable expansion ratio, lbf/lbm/sec

By application of suitable corrections to measurements of thrust made at sea level, corrected values of vacuum thrust may be obtained. With these values, which include allowances for all important departures from ideal flow, theoretical thrust coefficients may be used for calculation of c*. That is, C_F efficiency is 100 percent if there is no combustion in the nozzle, if chemical equilibrium is maintained in the nozzle expansion process, and if energy losses from the combustion products are accounted for.

Applicable corrections to measured thrust are specified in the following equation:

$$\eta_{c^*} = \frac{(F + P_a A_e)\ \varphi_{FR}\ \varphi_{DIV}\ \varphi_{HL}}{(\dot{w}_T)\ (I_s)_{theo}} \qquad \text{(A-6)}$$

where

F = measured thrust, pounds

P_a = ambient pressure, psia

A_e = area of nozzle exit, $in.^2$

$\dot{w}_T$ = total propellant flowrate, lbm/sec

$(I_s)_{theo}$ = theoretical vacuum shifting-equilibrium specific impulse at applicable expansion ratio, lbf/lbm/sec

φ_{FR} = correction for frictional losses

φ_{DIV} = correction for nozzle divergence

φ_{HL} = correction for heat losses to chamber and nozzle walls

The correction factors in Eq. A-6 were applied to vacuum thrust $(F + P_a A_e)$ instead of to measured site thrust (F) because, for convenience, the correction factors were calculated as changes in efficiency based on theoretical vacuum parameters so that the total correction was of the form $\Delta F/F_{vac}$.

Correction for Frictional Drag (φ_{FR})

This factor corrects for the energy losses caused by drag forces resulting from the viscous action of the combustion gases on the thrust chamber walls. Its magnitude, which is the integral of the local friction forces over the chamber inside wall, was estimated by a boundary layer analysis utilizing the integral momentum equation for turbulent flow. This analysis accounts for boundary layer effects from the injector to the nozzle exit by suitable description of the boundary layer profile and local skin friction coefficient. A computer program was used to carry out a numerical integration of the equation including effects of pressure gradient, heat transfer, and surface roughness. The program required a potential core solution of the nozzle flow which was obtained from the variable-property, axisymmetric method of characteristics calculation of the flow field outside the boundary layer; corresponding properties for the subsonic combustion chamber flow field were also calculated.

Computed values of φ_{FR} ranged from 1.007 to 1.009 for the conditions of the experimental firings.

Correction for Nozzle Divergence (φ_{DIV})

The one-dimensional theoretical performance calculations assume that flow at the nozzle exit is uniform and parallel to the nozzle axis. The correction factor, φ_{DIV}, allows for nozzle divergence (i.e., for nonaxial flow) and for nonuniformity across the nozzle exit plane. It was calculated from the standard equation (Ref. A-7):

$$\varphi_{DIV} = \left[\frac{1}{2} (1 + \cos \alpha) \right]^{-1} \qquad \text{(A-7)}$$

where α is the expansion angle (15 degrees in the present case). This gives $\varphi_{DIV} = 1.017$.

Correction for Heat Losses (φ_{HL})

The effect of heat loss to the chamber walls on measured I_s was determined by including this loss in the calculation of the theoretical values, as described above for the factor f_{HL}. Magnitude of φ_{HL} is directly dependent upon the length of the F_2/L_i combustion chamber; for the 5-inch chamber, φ_{HL} was about 1.02, and for the 20-inch chamber, φ_{HL} was about 1.08.

Summary

The correction factors applied are summarized in the following listing.

Applicable to $\left[\eta_{c^*}\right]_{P_c}$:

$f_p = 1.006$
$f_{TR} = 0.989$ to 0.993
$f_{DIS} = 0.994$
$f_{FR} = 1.000$
$f_{HL} = 1.017$ to 1.076

Applicable to $\left[\eta_{c^*}\right]_F$:

$\varphi_{FR} = 1.007$ to 1.009
$\varphi_{DIV} = 1.017$
$\varphi_{HL} = 1.019$ to 1.078

REFERENCES

A-1. Timoshenko, S. and J. N. Goodier, Theory of Elasticity, McGraw-Hill Book Company, New York, 1951.

A-2. TR-65-107, Performance Characteristics of Compound A/Hydrazine Propellant Combination, Prepared for Air Force Rocket Propulsion Laboratory, Edwards Air Force Base, California, by Rocketdyne, a Division of North American Aviation, Inc., Canoga Park, California, May 1965. CONFIDENTIAL.

A-3. Hatch, J. E., et al., Graphical Presentation of Difference Soultions for Transient Radial Heat Conduction in Hollow Cylinders with Heat Transfer at the Inner Radius and Finite Slabs With Heat Transfer at One Boundary, NASA Technical Report R-56, 1960.

A-4. Singer, H. A., Discharge Coefficients of Nozzles Having Sharp Throat Curvature, LAP 66-518, Rocketdyne, a Division of North American Aviation, Inc., Canoga Park, California, 18 October 1966.

A-5. Arbit, H. A. and S. D. Clapp, Fluorine-Hydrogen Performance Evaluation, Phase I, Part I: Analysis, Design, and Demonstration of High-Performance Injectors for the Liquid Fluorine-Gaseous Hydrogen Propellant Combination, NASA CR-54978, Prepared for NASA by Rocketdyne, a Division of North American Aviation, Inc., Canoga Park, California, July 1966.

A-6. Bartz, D. R., "A Simple Equation for Rapid Estimation of Rocket Nozzle Convective Heat Transfer Coefficients," Jet Propulsion, 27, 49-51, January 1957.

A-7. Sutton, G. P., Rocket Propulsion Elements, Third Edition, John Wiley & Sons, Inc., New York, 1963, p. 65.

APPENDIX B

MEASUREMENT ANALYSIS PROGRAM

INTRODUCTION

The primary purpose of a measurement analysis program is to provide a function which relates observed sensor outputs to estimates of corresponding system inputs, together with quantitative indications of the precision of this conversion. The function and the precision estimates are established on the basis of sensor calibration history, that is, upon a sequence of periodic calibrations of the sensor and its associated measuring and recording system against known inputs.

Because calibrations must of necessity be made at a time differing from the actual firing time by several hours to several days, the changes in random sensor error with time must be established. In the Random Walk measurement analysis program (Ref. B-1) this is accomplished by assuming that the input-output ratio at a particular input level performs a random walk in time which has normal distribution and variance. It assumes also that there is a random measurement error in the observed datum which is independent of the random walk and which is also normally distributed. Mathematical foundations and development of the program are given in Ref. B-2 and B-3 .

On the basis of the sequence of periodic calibrations, the Random Walk program provides the following:

1. A function, either linear or cubic, which converts observed system outputs into estimates of true system inputs

2. Coefficients of short-term and random walk variations as well as a combined value valid at specified times

3. A decision based upon the calculated coefficient of variation and a prespecified imprecision limit as to whether the sensor should be used as is, recalibrated immediately, or discarded, and the maximum allowable interval to next calibration

MEASUREMENT PROGRAM OUTPUT

A typical Random Walk computer program output is shown in Table B-1 . The first line of output gives the test stand name and number (Yoke, 0018), recording system (Beckman), transducer serial number (1641002), range (200 psi), ID number for data cards (018049), and the physical parameter being calibrated (P_c - 1A).

The next set of numbers ("Latest Output") is the most recent raw calibration data. On the left are the readings (in Beckman counts) for the listed calibration input steps ("Input"); on the right are the precalibrate throw zero (Z1), the calibrate throw reading (CT), the postthrow zero (Z2), the precalibration zero (Z3), the postcalibration zero (Z4), and the date of calibration ("Time").

The first two zeros (Z1 and Z2) are averaged and subtracted from the throw to get a reduced throw. For each calibration step, a linear interpolation is made between the last two zeros (Z3 and Z4) and the interpolated result is subtracted from the reading to get a reduced reading. Each reduced reading is then divided by the reduced throw to get a scaled output. All scaled output values from all calibrations in the system history are then listed ("Scaled Output") under the appropriate input pressures, with one calibration per line and its date ("Time") at the right of each line.

The next line gives the result of the second test, which checks whether or not the input-output model is consistent with the estimate of σ_m (the root-mean-square estimate for the calibration curve fit and σ_m should be approximately equal). If it is, then the model is labeled "SATISFACTORY"; if not, the model is labeled "UNSATISFACTORY," indicating a significant intercept or an error in the input data.

The following item indicates the ability of the system to meet the specified imprecision requirement. On the basis of the calibration data, three situations are recognized:

1. The system can never meet required precision, and should be replaced;
2. The system will fail the requirement within the next 2 days and should be recalibrated immediately; or
3. The system will meet the requirement up to a certain date (30 days maximum), on or before which it should be recalibrated. In this case, the estimated data reduction imprecision is given for test data taken 2 days after the most recent calibration and on the specified recalibration date.

The final item is a 2 by 2 matrix, denoted by R, which is used to estimate data reduction imprecision at any other time of interest and for any scaled output by the following expression:

$$P = \left[V + s^2 \left(h \sigma^2 + \sigma_m^2 \right) \right]^{1/2} \qquad \text{(B-1)}$$

where

P = estimated standard deviation for a reduced datum

s = scaled output

h = number of days after most recent calibration

V = matrix product: $(s, s^3)\ R \begin{pmatrix} s \\ s^3 \end{pmatrix}$

Application of the results of the measurement analysis program tc estimation of random experimental errors and to measurement reliability is given in Appendix C.

REFERENCES

B-1. Rothman, D.: Random Walk Program for Measurements Analysis of Static Systems, RM-1119-351, Rocketdyne, a Division of North American Aviation, Inc., Canoga Park, California, 25 January 1965.

B-2. Rothman, D.: A Random Walk Model for Non-Uniform, One-Parameter, Static, Linear Measurement Systems, RR-59-47, Rocketdyne a Division of North American Aviation, Inc., Canoga Park, California, 15 December 1959.

B-3. Rothman, D.: Gaussian Random Walk with Gaussian Measurement Errors, SORUM-63-9, Rocketdyne, a Division of North American Aviation, Inc., Canoga Park, California, 24 September 1963.

TABLE B-1

TYPICAL COMPUTER OUTPUT FOR TRANSDUCER CALIBRATIONS U
MEASUREMENT ANALYSIS PROGRAM

```
*       YOKE 0018          BKM    1641002       200       018049

*  LATEST OUTPUT
*
*     364      789     1103     1633     2162

*  INPUT

*      30       70      100      150      200

*  SCALED OUTPUT
*
*  0.1577   0.3706   0.5278   0.7932   1.0581                    8-
*  0.1577   0.3689   0.5265   0.7929   1.0572                    8-
*  0.1567   0.3704   0.5280   0.7923   1.0566                    7-
*  0.1556   0.3682   0.5283   0.7919   1.0565                    7-
*  0.1551   0.3692   0.5283   0.7924   1.0580                    7-
*  0.1570   0.3701   0.5276   0.7927   1.0578                    7-

*  MEASUREMENT VARIANCE IN INPUT-TO-SCALED OUTPUT  RATIO
*  RANDOM WALK VARIANCE IN INPUT-TO-SCALED OUTPUT  RATIO
*  RATIO OF SHORT-TERM VARIANCE TO RANDOM WALK VARIANCE
*  COEFFICIENT OF SHORT-TERM VARIATION
*  COEFFICIENT OF RANDOM WALK VARIATION
*  REQUIREMENT FOR COEFFICIENT OF VARIATION OF REDUCED DATA

*  SYSTEM NOW PASSES TEST FOR LINEARITY (TYPE I ERROR=.05).
*  DATA REDUCTION FORMULA IS

*                    (INPUT) = (1.8920E 02)*(SCALED OUTPUT)

*  ABOVE OUTPUT-INPUT MODEL IS SATISFACTORY (TYPE I ERROR=.05

*  SYSTEM SHOULD BE CALIBRATED ON OR BEFORE  9-19-65
*                                        COEFFICIENT OF VARIAT
*                                        COEFFICIENT OF VARIAT

*  DATA REDUCTION MATRIX            ( 2.40921E-02      0.
*                                   (
*                                   ( 0.               0.
```

=ALIBRATIONS USING RANDOM WALK
PROGRAM

018049 PC1A

Z1	CT	Z2	Z3	Z4	TIME
49	2046	49	49	49	8-20-65

TIME
8-20-65
8-13-65
7-27-65
7-27-65
7-27-65
7-27-65

RATIO	=	0.28773E-00	
RATIO	=	0.23258E-01	
ANCE	=	0.12318E 02	(DAYS)
	=	0.283	(PERCENT)
	=	0.0806	(PERCENT/DAY**.5)
CEO DATA	=	1.500	(PERCENT)

OR=.05).

OUTPUT)

ERROR=.05).

S
OF VARIATION OF REDUCED DATA ON 9-19-65 = 0.53 PERCENT
OF VARIATION OF REDUCED DATA ON 8-22-65 = 0.32 PERCENT

0.)
)
0.)

APPENDIX C

MEASUREMENT ERROR ANALYSIS

INTRODUCTION

Because it is not possible to measure the true value of any physical property or parameter, the error limits, or uncertainty interval, associated with any experimental measurement must be specified. It is the purpose of this appendix to indicate the reliability of the experimental determinations of performance efficiency by estimation of the errors inherent in the data acquisition processes and in the calculation procedures. This permits estimations to be made of the range within which, at a given confidence level, the true values of the measured or calculated parameters may be expected to fall.

If error be identified with departure of an experimental measurement from the "true" value, its magnitude can never be completely known; if it were known, it would become a correction which could be systematically applied. Hence, error limits can only be stated within probability limits. The estimation is made by an error analysis procedure which, in the present application, consists of the following steps:

1. Estimation of the uncertainty intervals in the individual transducers including the measuring systems in which they are used
2. Combination of the uncertainty intervals of duplicate or redundant sensors into an uncertainty interval for the measurement
3. Combination of the uncertainty intervals of several measurements (e.g., pressure, temperature, and flowmeter frequency) into an uncertainty interval for the parameter they determine (e.g., flowrate)

4. Combination of the uncertainty intervals of the measurements entering into calculation of the value of the desired variable (e.g., characteristic velocity) to estimate the uncertainty interval of the calculated result

Two types of errors are possible for any measurement:

1. Systematic errors. These are associated with the particular system, with the experimental techniques employed, or with the calibration procedures. They cannot be estimated by statistical methods, and are minimized primarily by careful calibration with the best available standards, by requirements for consistency and traceability of the experimental and calibration techniques, and by critical examination of experimental data.

2. Random errors. These arise from unpredictable and unknown variations in the experimental situation and are generally assumed to follow a normal distribution to permit simple statistical analysis. Error analysis is concerned only with random errors and implicitly assumes that systematic errors can be eliminated in a carefully conducted experimental program.

   From the properties of the normal, or Gaussian, distribution function, the probability of a system error exceeding ± 1 times the standard deviation (σ) is about 32 percent, the probability of exceeding ± 2 times the standard deviation is about 4.6 percent, and the probability of exceeding ± 3 times the standard deviation is about 0.3 percent. The value of y in a result expressed as $(x \pm y)$ is generally taken as 2σ, thus setting the confidence level at 95 percent so that the estimated odds of the true value of the result falling within the range $(x - y)$ to $(x + y)$ are 20:1.

SENSOR PRECISION

The precision of a measurement obtained as the output of a physical instrument or sensor is a quantitative estimate of the uncertainty associated with that measurement. This estimate is made by statistical analysis of the outputs of the sensor when repeatedly acted upon by known inputs. By sensor is meant not only the transducer itself but the complete system which converts the transducer signal to a numerical value of its physical parameter analog. The known inputs, of course, have uncertainty limits of their own, but for practical purposes it is assumed that they are accurate (i.e., identical to true values) within the limits required by the experimental situation. Ultimately, these inputs must be directly traceable to established standards, such as those of the National Bureau of Standards.

When a sensor is calibrated against known inputs, precision may be considered as the certification of an error band within the calibrated interval and within a given confidence level. Thus it provides a measure of "closeness to truth" of the reduced data. Precision may be numerically expressed as the standard deviation of a measurement, which has the same units as the measurement itself, or as the coefficient of variation, which permits valid comparisons between measurements in different units. Coefficient of variation (C_v) is the standard deviation expressed as a percentage of the mean, thus making it dimensionless:

$$C_v = 100 \frac{\sigma}{\mu} \qquad \text{(C-1)}$$

where

σ = standard deviation

μ = sample mean value

Pressure

The coefficients of variation of the pressure transducers were obtained by application of the Random Walk measurements analysis program to the calibration data, as discussed in Appendix B. The values obtained ranged from 0.1 to 0.4 percent, for static calibration made on a pressure manifold mounted on the thrust stand.

Other errors in pressure measurements may arise, in addition to the random, statistical uncertainty limits. Thus in the measurement of chamber pressures through a drilled wall tap, erroneous values of stream pressure may be indicated because of the effect of the hole itself upon the flow. The following estimated magnitudes (by percentage) of this tap error, which is a function of stream velocity, are based on experimental data obtained with water and gas (Ref. C-1):

(Mach No. $\simeq$ 0): 0.00
(Mach No. $\simeq$ 0.3): 0.05
(Mach No. $\simeq$ 1.5): 1.30

Coupling errors, arising from effects of the tubing joining the pressure taps to the transducers, are not significant in the present series of firings since precise dynamic or transient response pressure measurements were not required (Ref.C-2) and tubing lengths were not greater than 3 feet.

Thrust

Values of coefficient of variation obtained by application of the Random Walk measurement analysis program to thrust calibrations were in the range 0.3 to 0.8 percent. A possible source of error in the thrust measurements arose from the necessity of taking system prerun and postrun zeros with the

same degree of LF_2 inlet line chill and LLi inlet line heating that existed during the firings. On the basis of thrust calibrations made with inlet lines at varying temperatures (Ref. C-2), the estimated C_v value due to variation in zero readings is 0.1 percent.

Throat Area

Geometric throat diameter was measured with an expansion micrometer by two observers before and after every firing. Maximum coefficient of variation of the calculated areas was 0.3 percent.

Volumetric Flowrate

The coefficients of variation of the turbine flowmeters used to measure LF_2 flowrate were determined from calibration data. Observed C_v values, which refer only to flow bench water calibrations, were 0.1 percent for both meters. Corrections for thermal and viscosity effects in converting these calibrations to cryogenic LF_2 factors are discussed in another section of this report. In addition, however, there are unpredictable water-to-cryogenic calibration shifts (Ref. C-3) which introduce additional sources of error. The coefficient of variation arising from this source is approximately 0.5 percent (Ref. C-4).

Estimated C_v value for the magnetic flowmeter used for liquid lithium is 0.5, based on several calibrations of the electromotive force (emf) output.

Temperature

Resistance Temperature Sensors. The platinum resistance thermometers were precision calibrated by the manufacturer. These calibrations were checked by taking several emf readings with the sensors immersed in LN_2 and in LO_2

at atmospheric pressure; these were correct within the limits of readability with <0.02 percent coefficient of variation in a series of four measurements. Root-sum-square (RSS) error limits of these sensors based on specifications for repeatability, insulation, time lag, friction heating, and interchangeability were 0.1 percent. Voltage readout of the transducers was adjusted to calibration values by means of a standard decade resistance box with error limits of 0.2 percent.

Thermocouples. Iron-constantan thermocouples were used to measure temperatures of GH_2 in the venturi plena, and chromel-alumel thermocouples were used to measure lithium system temperatures. Because the latter were not involved in performance measurements, they will not be considered in this section. Estimated error to be expected with new iron-constantan thermocouple wire at ambient temperatures is 0.7 percent (Ref. C-1). Thermocouple calibrations were electrical only; i.e., the emf readout was adjusted on the assumption that thermocouple-generated electromotive forces correspond to standard values. Total estimated C_v is 1.0 percent.

COMBINED ERROR ESTIMATION

Redundant Measurements

Two independent transducers were used to measure most of the important parameters (except thrust) in order to increase measurement reliability. The most probable value of a redundant measurement is a weighted average in which the weight (W_i) assigned to an individual determination is given by

$$W_i = \frac{1}{\sigma_i^2} \qquad (C\text{-}2)$$

where σ_i is the standard deviation associated with the i^{tn} measurement and

σ_i^2 is the variance. The variance of the weighted mean, σ_m^2, is given by

$$\frac{1}{\sigma_m^2} = \sum_i \frac{1}{\sigma_i^2} \qquad \text{(C-3)}$$

Clearly the variance of the weighted mean is less than any of the individual variances; for example, in the particular case of two measurements with equal variances, the variance of the mean is half the individual variances.

Combined Measurements

The standard deviation of a parameter which is a function of two or more independent measurements is taken as the RSS of the standard deviations of the independent measurements. Thus LF_2 flowrate is a function of flowmeter frequency and fluorine temperature (assuming no significant error in conversion of fluorine temperature to equivalent density):

$$\dot{w}_o = \varphi(f, T_o) \qquad \text{(C-4)}$$

where

f = flowmeter frequency

T_o = oxidizer temperature

The standard deviation of the oxidizer flowrate is then:

$$\sigma_{\dot{w}_o} = \left[\sigma_f^2 + \sigma_{T_o}^2\right]^{1/2} \qquad \text{(C-5)}$$

In the same way the standard deviation of hydrogen flowrate, which is a function of measured pressure and temperature in the venturi plenum, is given by

$$\sigma_{\dot{w}_{H_2}} = \left[\sigma_{P_{H_2}}^2 + \sigma_{T_{H_2}}^2\right]^{1/2} \qquad \text{(C-6)}$$

where

$\sigma_{P_{H_2}}$ = standard deviation of GH_2 pressure measurement

$\sigma_{T_{H_2}}$ = standard deviation of GH_2 temperature measurement

Standard deviation is converted to coefficient of variation by Eq. C-1.

When several measured variables are combined algebraically to yield an experimental result, the standard deviation of the result, which takes into account the propagation of the individual errors, is given by

$$\sigma_R^2 = \left(\frac{\partial R}{\partial x_1}\sigma_1\right)^2 + \left(\frac{\partial R}{\partial x_2}\sigma_2\right)^2 + \ldots + \left(\frac{\partial R}{\partial x_n}\sigma_n\right)^2 \qquad \text{(C-7)}$$

where

σ_R = standard deviation of calculated result

$x_1, x_2, \ldots, x_n$ = measured variables

$R = \varphi(x_1, x_2, \ldots, x_n)$

$\sigma_1, \sigma_2, \ldots, \sigma_n$ = standard deviations of $x_1, x_2, \ldots, x_n$, respectively

The following example illustrates the application of this type of error analysis:

Run No. 8 (Step 1)

Chamber Pressure: $\sigma_{P_c} = 0.46$ psia

Calculated by Eq. C-1 and C-3 from calibration C_v values (0.28 and 0.13 percent) of the redundant sensors.

Throat Area: $\sigma_{A_t} = 0.03$ in.^{2}

Calculated from eight measurements of throat diameter.

Thrust: $\sigma_F = 12.1$ lbf

Calculated from RSS of calibration C_v (0.61 percent) and zero point variation C_v (0.10 percent).

Propellant Flowrate: $\sigma_{\dot{w}_T} = 0.04$ lb/sec

Calculated from the coefficient of variation of the individual flowrates: $C_v\left(\dot{w}_{LF_2}\right) = 0.35$ percent, $C_v\left(\dot{w}_{GH_2}\right) = 0.31$ percent, $C_v\left(\dot{w}_{LLi}\right) = 0.50$ percent.

Correction Factors: $\sigma_{C.F.} = 0.003$

Obtained from RSS of estimated variances of the individual corrections.

c*, Based on P_c: $\sigma_{c^*} = 41$ ft/sec

Obtained by application of Eq. C-7 to the expression

$$c^* = \frac{P_c A_t g_c (C.F.)}{\dot{w}_T} \tag{C-8}$$

where (C.F.) is the net correction factor.

The resulting expression is:

$$\sigma_{c^*}^2 = \left[\frac{A_t g_c (C.F.)}{\dot{w}_T}\sigma_{P_c}\right]^2 + \left[\frac{P_c g_c (C.F.)}{\dot{w}_T}\sigma_{A_t}\right]^2 + \left[-\frac{P_c A_t g_c (C.F.)}{\dot{w}_T^2}\sigma_{\dot{w}_T}\right]^2 + \left[\frac{P_c A_t g_c}{\dot{w}_T}\sigma_{C.F.}\right]^2 \tag{C-9}$$

Substitution of numerical values gives σ_{c^*}.

At the 95-percent (2σ) confidence level, this value of σ_{c^*} corresponds to an error band of approximately ±1.0 percent.

I_s Based on F: $\sigma_{I_s} = 2.2$ seconds

Obtained by application of Eq.C-7 to the expression

$$I_s = \frac{F\ (C.F.)}{\dot{w}_T} \tag{C-10}$$

where again (C.F.) is the net correction factor.

The resulting expression is:

$$\sigma_{I_s}^2 = \left[\frac{F}{\dot{w}_T}\,\sigma_{C.F.}\right]^2 + \left[\frac{C.F.}{\dot{w}_T}\,\sigma_F\right]^2 - \left[\frac{F\ (C.F.)}{\dot{w}_T^2}\,\sigma_{\dot{w}_T}\right]^2 \tag{C-11}$$

Substitution of numerical values gives σ_{I_s}. At the 95-percent (2σ) confidence level, the error band is observed I_s and therefore in c* based on thrust, is approximately ±1.3 percent.

DYNAMIC PRECISION

The estimates of expected standard deviations calculated above are based on static calibrations of pressure and thrust sensors, and hence may not be strictly applicable to the dynamic system represented by a firing thrust motor. It is generally assumed, however, that such calibration data may be extended without significant change to dynamic systems oscillating at very low frequencies and amplitudes, and that steady-state stable combustion is such a system.

REFERENCES

C-1. Dean, R. C., Jr., Aerodynamic Measurements, Gas Turbine Laboratory, Massachusetts Institute of Technology, Cambridge, Massachusetts, 1953.

C-2. Thomson, D. B., The Effect of Tubing on Dynamic Pressure Recording, TN-61-3, Rocketdyne, a Division of North American Aviation, Inc., Canoga Park, California, 28 February 1961.

C-3. Bucknell, R. L., "Calibration Systems and Turbine-Type Flow Transducers for Cryogenic Flow Measurements," Advances in Cryogenic Engineering, Vol. 8, Plenum Press, New York, 1963, 360-369.

C-4. Alspach, W. J. and T. M. Flynn, "Considerations when Using Turbine-Type Flowmeters in Cryogenic Service," Advances in Cryogenic Engineering, Vol. 10, Plenum Press, New York, 1965, 246-252.